Synthetic [C II] line emission maps of simulated interstellar medium

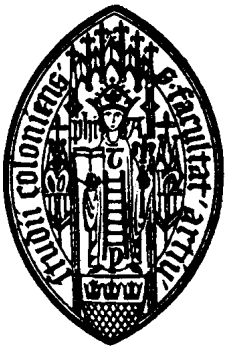

Inaugural – Dissertation

zur
Erlangung des Doktorgrades
der Mathematisch – Naturwissenschaftlichen Fakultät
der Universität zu Köln

vorgelegt von

Annika Franeck
aus Berlin-Pankow

Köln, 2018

Berichterstatter: Prof. Dr. Stefanie Walch-Gassner

Prof. Dr. Jürgen Stutzki

Tag der mündlichen Prüfung: 10. September 2018

“Hilf mir aus dem Rachen des Löwen,
und errette mich von den Einhörnern.”

Psalm 22,22

Abstract

In this thesis I analyse the synthetic [C II] emission from a slice of interstellar medium (ISM). The [^{12}C II] line emission is the fine structure transition in carbon ions. It is observed in several phases of the ISM, such as the molecular, warm, and ionized gas phases. By analysing the [^{12}C II] line emission in observations, one would like to estimate the star formation rate, and the fraction of molecular hydrogen in the studied objects. However, for those studies it is crucial to disentangle from which gas phase the [C II] line emission stems. We therefore study the [C II] line emission in 3D numerical simulations.

The underlying simulations represent *(i)* a piece of a galactic disc (SILCC-Project[1] Walch et al., 2015, Girichidis et al., 2016b), in which the ISM is stirred by the explosions of SNe; the positioning of the SNe determines the gas phases formed in the ISM. In a second setup, *(ii)* a forming molecular cloud before the onset of star formation (MC2) is simulated (SILCC-Zoom project Seifried et al., 2017). We carry out radiative transfer simulations with RADMC-3D (Dullemond, 2012) for the [^{12}C II] line emission. We expect the [^{12}C II] line emission to be observable for $I_{[^{12}\mathrm{CII}]} \geq 0.5$ K km s^{-1}, and find for MC2 that ∼20% of the total projected area is above this detection limit, contributing ∼80% to the total luminosity in [^{12}C II]. Thus, we conclude that molecular clouds before the onset of star formation are observable in [^{12}C II]. We find the [^{12}C II] emission to be optically thick, in the densest regions, ∼40% of the observable area for MC2. We estimate the emission line of the strongest hyperfine structure transition [^{13}C II] ($F = 2 - 1$) from the carbon ion isotope ^{13}C^{+} to use it as an optically thin analogue to [^{12}C II].

We analyse the distribution of the [^{12}C II] line emission in the SILCC setups, and find the vertical emission profiles to have in general a complex structure. In almost all simulations there is a dominant peak of the [^{12}C II] line emission from the molecular clouds located in the midplane. To characterize the distribution of the emission, we calculate its variance, and define the square root of the variance as a scale height. For most of the simulations the scale height is $\lesssim 100$ pc. We find the scale height to trace the outflowing component of the gas.

We study the origin of the [C II] line emission with the optically thin tracer [^{13}C II]. For the SILCC simulations we find the [C II] line emission correlated with the molecular gas phase. For the zoom-in simulation MC2, having a better spatial resolution, and no further feedback processes included, we find the [C II] line emission to stem from the atomic gas with physical properties as 43 K $\leq T \leq$ 64 K, 53 cm^{-3} $\leq n \leq$ 438 cm^{-3}, with a range of 16% to 44% of the hydrogen in molecular form, and a visual extinction A_V between $0.5 \leq A_V \leq 0.91$. We test further

[1] SILCC: Simulating the Life Cycle of molecular Clouds, project led by S. Walch

whether the result changes by the resolution of the simulation, and find the temperature range to be unaffected, whereas the number density and the fraction of molecular hydrogen change slightly. However, the overall conclusion holds for all zoom-in simulations.

We study the correlation between the integrated [^{12}C II] intensity with the column densities of the total gas, H, and C^+, and find the distributions to follow power-laws with slopes of ~0.7, 0.5, and 0.6, respectively. We define a $Y_{\rm CII}$ factor, which is the ratio between the column density of the total gas, and the integrated [^{12}C II] intensity. Estimated over the whole emission map, we find the median value as $Y_{\rm CII} \approx 1.1 \times 10^{21}$ cm^{-2} (K km s^{-1})$^{-1}$. In general it scales with $Y_{\rm CII} \propto I_{[^{12}{\rm CII}]}^{-0.3}$.

We analyse the line profiles by comparing them with two reference functions, a Gaussian and a Boxcar function, representing an optically thin and thick line. We define a Tauber value as the difference between the reference function and the line profile, normalized by the amplitude of the reference function. We find no specific tendencies for the Tauber values in the [^{12}C II] line. However, the values we obtain are comparable to Tauber values derived from observed data.

Finally, we carry out synthetic emission maps of the ^{12}CO (1–0), ^{13}CO (1–0), and C^{18}O (1–0) line emissions, and the H I 21 cm line. We calculate the H I line with different approaches for the spin temperature, and find the spin temperature to be equal to the kinetic gas temperature for most parts in the simulation. We compare the integrated [^{12}C II] and H I line emission, and find no correlation of these quantities in the observable range of [^{12}C II]. In a comparison of the synthetic [^{12}C II] and ^{12}CO (1–0) emission maps, we find a fraction of 80% of the total H_2 mass to be aligned with the observable ^{12}CO (1–0) line emission, and 90% with the observable [^{12}C II] line emission. Thus, about 10% of the H_2 mass is CO-dark H_2, and the remaining 10% of H_2 mass is not detected in the [^{12}C II] or the ^{12}CO (1–0) line.

Zusammenfassung

In der vorliegenden Arbeit geht es um synthetische Emissionskarten der [C II] Linie von Simulationen des interstellaren Mediums (ISM). Die [^{12}C II] Linie ist die Linie des Feinstrukturübergangs im Kohlenstoffion, und wird im Universum sowohl in der kalten, molekularen Gasphase, als auch in der warmen, ionisierten Phase beobachtet. Um mithilfe der [^{12}C II] aus Beobachtungen auf die Sternentstehungsrate, oder den Anteil von H_2 schliessen zu können, ist es wichtig zu verstehen, aus welcher Gasphase die beobachtete [^{12}C II] Emission stammt. Dies untersuchen wir in dieser Arbeit anhand von numerischen Simulationen.

Als Simulation verwenden wir dabei die *(i)* SILCC[2] Simulationen (Walch et al., 2015, Girichidis et al., 2016b), die das ISM in einem Teil einer Galaxiescheibe repräsentieren, und *(ii)* in einer zoom-in Simulation MC2 (SILCC-Zoom Projekt, Seifried et al., 2017), in der die Formation einer Molekülwolke untersucht wird. Wir berechnen von den fertigen Simulationen die Emissionskarten der [^{12}C II] Linie mit RADMC-3D (Dullemond, 2012). Wir erwarten, dass man die [^{12}C II] Linie ab einer Intensiät von 0.5 K km s^{-1}detektieren kann, und finden, dass ~20% der projizierten Gesamtfläche in MC2 beobachtbar sind. Diese beobachtbare Fläche trägt mit 80% zur Gesamtluminosität der [^{12}C II] Emission bei. Die [^{12}C II] Linie ist optisch dick über ~40% der beobachtbaren Fläche. Wir berechnen zusätzlich die [^{13}C II] ($F = 2 - 1$) Linie, welche die stärkste Linie der Hyperfeinübergänge im Kohlenstoffionenisotop $^{13}C^+$ ist, um ein optisch dünnes Äquivalent zur [^{12}C II] Linie zu erhalten.

In den SILCC Simulationen untersuchen wir die vertikale Verteilung der [^{12}C II] Strahlung um die galaktische Scheibe. In unseren Simulationen zeigt das Profil eine sehr komplexe Struktur. Das vertikale Emissionsprofil wird durch die starke Strahlung von den Molekülwolken aus der Galaxiescheibe dominiert. Wir quantifizieren die vertikale Verteilung der Emission, indem wir ihre Varianz berechnen. Die Wurzel aus der Varianz definieren wir als Skalenhöhe. Die Skalenhöhen sind in der Grössenordnung von $\lesssim$ 100 pc für die meisten Simulationen, und bilden ein Maß für das ausströmende Gas aus der Galaxiescheibe.

Ein Hauptanliegen dieser Arbeit besteht in der Charakterisierung des Gases, welches die [C II] Linie emittiert. Dies untersuchen wir mit der optisch dünnen [^{13}C II] Linie. In den SILCC Simulationen finden wir einen Zusammenhang zwischen der [C II] Emission und der molekularen Gasphase. In der besser aufgelösten Simulation MC2 kommt die [C II] Linie aus Gas mit Temperaturen zwischen 43 K $\leq T \leq$ 64 K, mit Teilchenzahldichten zwischen 53 cm^{-3} $\leq n \leq$ 438 cm^{-3}, in denen zwischen 16% und 44% des Wasserstoffs als H_2 vorliegt, und das eine visuelle Extinktion

[2]SILCC: Simulating the Life Cycle of molecular Clouds, geführt von S. Walch

zwischen $0.5 \leq A_V \leq 0.91$ hat. Folglich stammt die [C II] Emission aus der atomaren Gasphase, in dem sich H im Übergang zu H_2 befindet. Diese Schlussfolgerung finden wir bei anderen Auflösungen und anderen Simulationen bestätigt.
Wir untersuchen weiterhin den Zusammenhang zwischen der integrierten [^{12}C II] Intensität und der Säulendichte des gesamten Gases, H und C^+. In allen drei Fällen lässt sich dieser mit einem Potenzgesetz beschreiben. Wir definieren weiterhin einen $Y_{\rm CII}$ Faktor als Verhältnis zwischen der Säulendichte und der [^{12}C II] Intensität. Der $Y_{\rm CII}$ Faktor skaliert im allgemeinen mit der [^{12}C II] Intensität als $Y_{\rm CII} \propto I_{[^{12}{\rm CII}]}^{-0.3}$.
Schließlich berechnen wir Emissionskarten bei den Wellenlängen der H I 21 cm Linie und den ^{12}CO (1–0), ^{13}CO (1–0), C^{18}O (1–0) Linien. Die H I Linie berechnen wir mit verschiedenen Annahmen für ihre Spintemperatur; das Ergebnis zeigt dass die Spintemperatur in großen Teilen der Simulation identisch mit der kinetischen Temperatur des Gases ist. Wir finden keine Korrelation der integrierten H I und [^{12}C II] Intensität im beobachtbaren Bereich von [^{12}C II]. Dies kann mit der optischen Tiefe der Linien zusammenhängen, als auch ein Hinweis darauf sein, dass die H I Linie aus einem grösseren Bereich als das [C II] emittierende Gas stammt. Weiterhin untersuchen wir welcher Massenanteil von H_2 entlang von Sichtlinien von [^{12}C II] und ^{12}CO (1–0) existiert. Im Bereich des beobachtbaren ^{12}CO (1–0) liegen 80% der H_2 Masse, und im beobachtbaren [^{12}C II] Bereich 90% der H_2 Masse. Folglich sind 10% der H_2 Masse CO dunkles Gas, und weitere 10% weder in [^{12}C II] noch in ^{12}CO (1–0) detektierbar.

Contents

List of Figures

List of Tables

Preamble

Everything is about time. The time that we have on Earth is a gift. To use it in the way we want, a pleasure. To struggle with it, exhausting. It turns back to pleasure, whenever we realise that time is a gift. Dear reader, I wish that you have the chance to experience this. This time is yours, use it as yours.

If you wish, you can take the time to learn about the things in the Universe. About star forming regions, about molecular clouds. I used the last four years to investigate where the [C II] line emission comes from.
"What is that?" You may ask with interest.
It is the fine structure emission line that we observe from carbon ions. If we could see the interstellar medium at wavelengths of $\lambda = 157.74$ μm, we would see it as a bright disc. And that is made up of molecular clouds, where stars will form. The even brighter regions are those clouds that already contain stars. The stars heat the gas in their surrounding, and this ionizes even more carbon atoms. Layers dominated by photons form whenever the radiation penetrates regions of dense gas. We call them "photon dominated regions" (PDRs). The photons ionize the gas. Therefore, the PDRs contain a large amount of carbon ions, so that they are bright in the [C II] line emission.
"How do you know about the [C II] line emission?" You might ask with interest.
We need instruments to see the [C II] line. We sent balloons with instruments into the sky to look above the blanket of atmosphere, that blocks the emission before it reaches Earth's surface. We take planes to fly a bit higher and to see [C II] more precisely. We sent rockets up into space to come more close to the objects we study.
"Is this what you are doing?" You ask.
No. We started being fascinated by the observations. And we want to understand the interplay of the gas in the interstellar medium exposed to different environments. That is why we started building models. We combine what we know about flowing gas, what we know about the chemistry within the gas. Sometimes we even let it interact with magnetic fields. We tell all this to the computer and ask the computer to tell us the story about the scenario we just described with maths. And then we get a story in the form of a simulation. I take these stories and try to interpret them. I ask another program to predict how the scenario looks like in the light of the [C II] line emission. And this I take for doing my analysis.
"What do you analyse?"
We want to understand more precisely the origin of the [C II] line emission. We first need to understand this in our models. We then want to help interpreting the observations, and see whether the [C II] line emission can be used to count stars or estimate the dark gas in the interstellar medium. We are curious how the [C II]

emission is distributed. This work builds up on answer to these questions. I invite you to read this book.

1

Introduction

To ponder on the nature of the world in which we live, is probably one of the fundamental questions that occupies humans. One aspect of this is to wonder about the things that exist beyond the Earth, the things that we call the Universe. Throughout history people have used the methods they had to study the world around the Earth. With the naked eye one can see the stars, and if the night is dark enough, identify the Milky Way on the sky, which, as we learned, is the Galaxy that we live in. Nowadays, we build instruments to observe the Universe with a better resolution than our eyes, and at wavelengths outside the visible spectrum. With the information we gained, our picture of the Universe has changed. By studying it in more detail, we aim to build a consistent picture of the Universe; in the past we understood it in a framework of stories and mythology; nowadays our story is written in science.

1.1 The Milky Way

The Milky Way consists of a thick and a thin disc of stars, and a concentration of gas and dust in an extreme disc (Buser, 2000). In its centre is a bulge, hosting a black hole. The Milky Way is embedded in a halo of stars, and a halo of dark matter. A sketch of it is presented in Fig. 1.1, taken from Buser (2000, fig. 1 therein). The halo consists of stars and tenuous gas, with a radius of about ~100 kpc (Buser, 2000). The stars in the halo belong to an older population compared to the stars in the disc (Weigert et al., 2016). The disc components have a radius of ~15 kpc. The total mass of the Milky Way within that radius is expected to be $\sim 10^{11}\ M_\odot$, distributed in stars ($\sim 5\times10^{10}\ M_\odot$), dark matter ($\sim 5\times10^{10}\ M_\odot$), and interstellar gas ($\sim 7\times10^{9}\ M_\odot$ Draine, 2011). Seen from our perspective on Earth, we experience the Milky Way as a bright band of emission. A view of the Milky Way at different

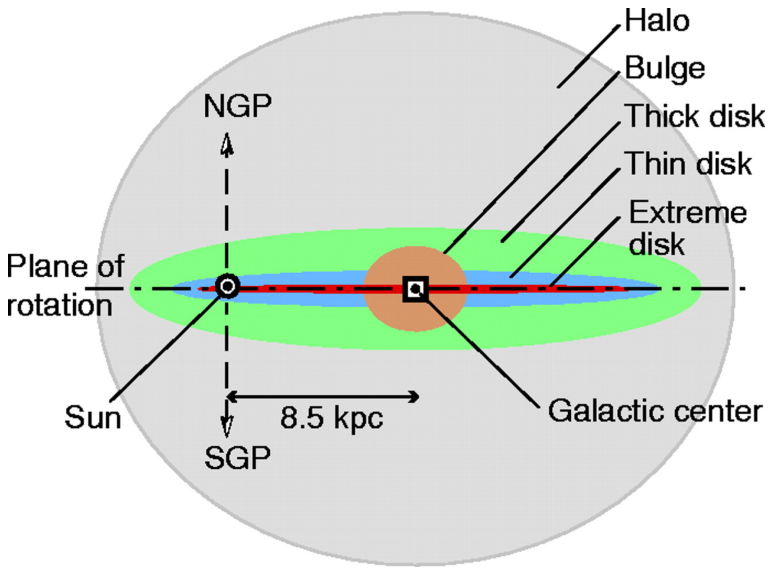

Figure 1.1: Sketch of the composition of the Milky Way, taken from Buser (2000), fig. 1 therein. The Milky Way consist of a thin and a thick disc, with a concentration of gas and dust in the extreme disc, and a bulge in the galactic centre. The Milky Way is embedded in a halo of stars and dark matter. The direction of the north and south galactic poles are indicated with NGP and SGP, respectively.

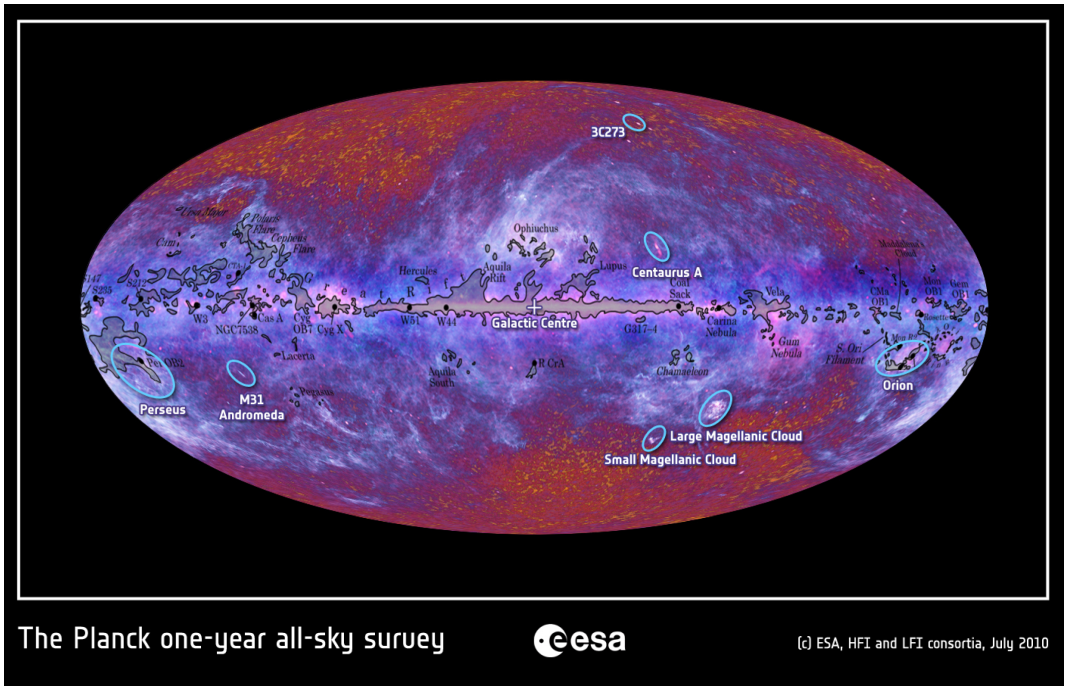

Figure 1.2: The Milky Way, seen with the Planck satellite in a wavelength range of 30 to 857 GHz, thus detecting the emission from gas and dust in the galactic plane. The contours indicate the CO emission (Dame et al., 2001), used to identify molecular clouds (credit: ESA, footnote 1).

wavelengths is shown in Fig. 1.2 (credit: ESA[1]). The Milky Way is not an isolated system. The Milky Way might interact with its closest neighbours: the Small and Large Magellanic clouds (SMC, LMC), or the Andromeda Galaxy M31. These are marked in Fig 1.2.

The disc consists of stars and the gas and dust between the stars, called the interstellar medium (ISM). Its structure shows spiral arms. The gas in the disc is composed of atomic, molecular, and ionized gas. These components are not equally distributed, neither in the vertical nor horizontal dimension, but are commonly found in well separated stable phases. The molecular gas peaks at a molecular ring at a radius of $\sim$ 4.5 kpc. Atomic gas, on the other hand, has a flat distribution, and dominates in the outer part of the Milky Way (Tielens, 2005). Although there is no sharp boundary of the Galaxy, its dimension can be estimated by observations of its gas and star components. Considering the gas measured in atomic hydrogen (H I) or transition lines of CO, the radius of the Milky Way is about 15 kpc, and its thickness, as defined as the point when the density of the gas drops by 50%, is about $z_{1/2} \approx 250$ pc. Since the vertical height is much smaller than the radius, the disc is called "thin /disc" (Draine, 2011). Our solar system is positioned at a radius of $\sim$ 8.5 kpc from the centre of the Galaxy. In addition, there are observational indications e.g. of H I and CO (May et al., 1993, Dickey & Lockman, 1990) and of the stellar component (Carney & Seitzer, 1993, Momany et al., 2006), that the galactic disc is warped.

As habitants of the Milky Way it is challenging to get a concrete picture of our own Galaxy. However, there are other galaxies found with Milky Way like properties. Two such examples, shown in Fig. 1.3, are the galaxy NGC 891 seen edge-on[2], while NGC 1232 is seen face on[3] (Hughes et al., 2015, Weigert et al., 2016). The galaxy NGC 891 has a distance of $\sim$ 9.77 Mpc (Karachentsev et al., 2004), and thought to be similar to the Milky Way with respect to its morphology and physical properties (Madden et al., 1994). It has a size of 13.1′, which corresponds to a physical size of $\sim$ 37 kpc at its distance. NGC 1232 is at a distance of $\sim$ 22 Mpc, with a diameter of about $\sim$ 43 kpc, which is almost twice the diameter of the Milky Way (Möllenhoff et al., 1999, Nasonova et al., 2011).

1.2 The interstellar medium

The interstellar medium consist of gas and dust, with a gas to dust mass ratio of roughly 100. The gas in the ISM of the Milky Way consists of ~73% hydrogen and

[1]This picture is taken from http://sci.esa.int/planck/47341-selected-galactic-and-extragalactic-sources-in-the-microwave-sky-as-seen-by-planck/ (credit:ESA).

[2]The picture is taken from https://www.spektrum.de/alias/wunder-des-weltalls/ngc-891-in-der-andromeda/1551412 (credit: Franz Klauser)

[3]The picture is taken from https://www.eso.org/public/germany/images/eso9845d/(credit: ESO)

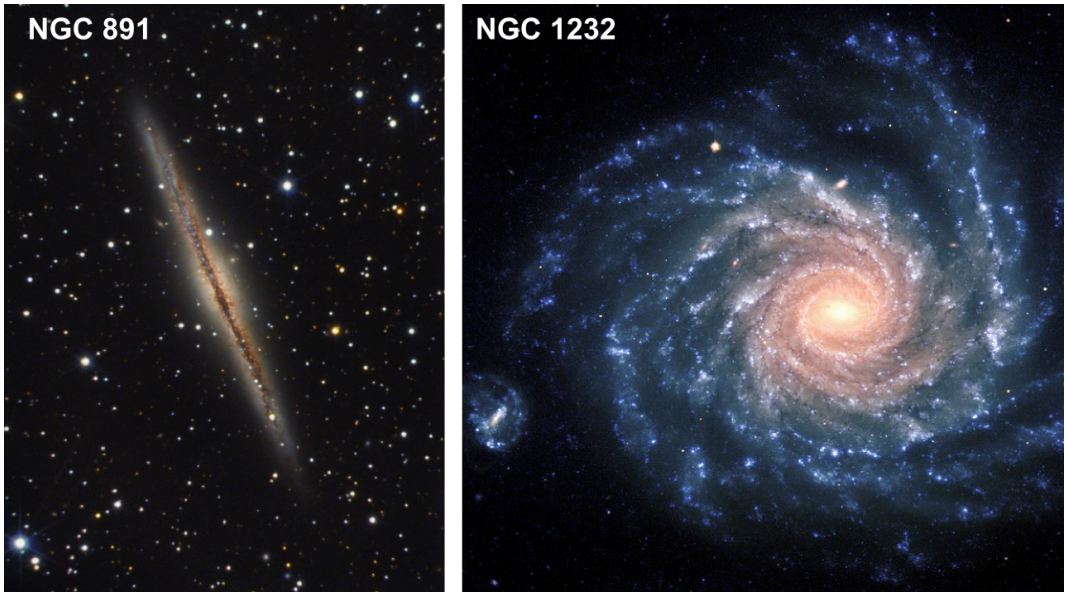

Figure 1.3: Presentation of the Milky Way like galaxies NGC 891 (left, credit: Franz Klauser, footnote 2) and NGC 1232 (right, credit: ESO, footnote 3). The picture of NGC 1232 is composed of three individual pictures, showing the ultraviolet, blue, and red light. In the centre of NGC 1232, there are old, red stars, while in the spiral arms mostly young, blue stars are present.

$\sim$27% helium. Elements with an atomic number of $Z \geq 3$ contribute to about $\sim$1%, but have a great impact on the chemistry in the gas (Draine, 2011).

1.2.1 Processes in the ISM

Depending on the density, temperature and composition of the gas, it is heated and cooled by different processes. We describe here shortly the important processes for the different regimes of the gas.

Heating in the ISM

Different processes yield to the heating of the gas. Their contributions can be summarized in a heating rate Γ, which measures how much energy (in erg) and time (in s^{-1}) is transferred to the gas. In general, the coupling of radiation to the ISM is the dominant heating source. There are contributions from synchrotron emission, the cosmic microwave background, infrared (IR) emission from dust, and from stars, with O- and B-type stars producing ultraviolet (UV) and far-UV radiation. In the proximity of stellar sources, the contribution from the stars dominates. All contributions can be summarized in an interstellar radiation field (ISRF). The strength of the UV radiation field is often expressed in units of G_0, which is the Habing field defined as $G_0 = 1.2 \times 10^{-4}$ erg cm^{-2} s^{-1} sr^{-1} (Habing, 1968, Tielens, 2005).

Radiation can cause photoionization or the photoelectric effect in gas and dust (Tielens, 2005). The energy of the radiation is then transferred to thermal energy

of the reaction products, which is the electron and a remaining charged particle. Further energy transfers can happen via elastic collisions. Photons with energies $h\nu \geq 13.6$ eV can ionize hydrogen. In an energy range of $11.2\,\mathrm{eV} \leq h\nu \leq 13.6\,\mathrm{eV}$, carbon is ionized. Photons with even lower energies, $5\,\mathrm{eV} \leq h\nu \leq 11.2\,\mathrm{eV}$, interact with polycyclic aromatic hydrocarbon molecules (PAHs) and dust grains by the photoelectric effect. Likewise, the radiation can interact with molecules. They can cause photodissociation of molecules, such as H_2. This process is important in atomic and molecular gas. The absorption of an UV photon can excite H_2 to a higher electronic state. This can decay to a vibrational excited electronic ground state, while the energy difference is transferred to the surrounding gas. Via collision or emission of radiation, the vibrational excited state can further decay. This process is called vibrational heating (Stahler & Palla, 2005). Further, if gas and dust are well coupled, interactions between dust and gas particles can take place. If the temperature of the gas is lower than the temperature of the dust, the interaction of gas particles bouncing off a dust grain results into the heating of the gas (Tielens, 2005).

Interactions of gas and dust with cosmic rays lead to heating. Cosmic rays are charged, relativistic protons, with an admixture of heavy elements and electrons with energies in the range of 10 to 10^{21} MeV (Tielens, 2005). Cosmic rays with energies below 10^9 MeV are believed to originate from particle accelerations within the magnetized shocks created by supernova remnants. Cosmic rays with even higher energy are probably extragalactic in origin (Stahler & Palla, 2005). Cosmic rays can interact with molecular hydrogen by exciting it to a higher electronic state, that leads to dissociation. H_2 is ionized in this process, providing a secondary electron that can further interact with the gas, e.g. by ionizing the gas, or by scattering, which can yield to the excitation of another H_2 molecule. In a similar manner, atomic hydrogen can be ionized by cosmic rays, producing a secondary electron, that in turn can interact with the gas (Stahler & Palla, 2005).

Heating can also occur due to mechanical processes in the ISM (Tielens, 2005). Gravitational contraction of a dense cloud is one example, where the compression of the gas results in an increase of the temperature. This is important in the collapse phase of molecular cloud cores. Movements within the gas can contribute to the heating. If the gas is partially ionized, the influence of magnetic fields can yield to a small velocity difference between the ions and neutrals in the gas. The movement of neutrals and ions then cause friction, that heats the gas. This process is called ambipolar diffusion. Further, the ISM is turbulent. Following the theory of Kolmogorov (1941), turbulence is injected on large spatial scales, and decays towards smaller scales. On the dissipation length scale, which is determined by the viscosity of the ISM, the energy is converted into heat. Additionally, shock waves convert supersonic motion into heat. A source for those shocks are SN explosions (Tielens, 2005).

Different heating processes dominate at different density ranges of the gas. In the ionized medium, the heating is dominated by photons with high energies (≥ 13.6 eV), that cause the ionization of atomic hydrogen. In the atomic medium, the photo dissociation of small molecules is important for the heating of the gas. This process

can take place if dense gas is illuminated by strong far-UV fields. In the warm neutral medium the photo-electric effect is dominant at high densities, while the heating due to cosmic rays and X-rays are important at high densities. In the dense medium, cosmic rays can penetrate the gas, and their influence is important for the heating of this gas.

Cooling in the ISM

The gas of the ISM looses energy when photons from its constituents are emitted. Although the abundance of species with $Z > 2$ is about 1% of the mass, line transitions in these atoms, and the molecules formed from these elements have a large impact on the cooling of the gas. Hydrogen and helium act as important collisional partners for the heavier species and dust grains, exciting internal degrees of freedom (Stahler & Palla, 2005). According to the chemical composition of the gas, which is dependent on the gas temperature and density, molecules, atoms, or ions, their interaction with electrons, and dust contribute to the cooling of the gas.

In ionized gas, cooling dominantly takes place due to the excitation of low-lying electronic states of heavy ions, such as O^{++} or N^{+}, resulting in their fine-structure transition. Ions can contribute to the cooling by recombining with electrons. In such a free-bound transition the electron looses energy by emitting a photon. Charged particles in the gas interact via the Coulomb force, and by this emitting a photon. This emission is called bremsstrahlung or free-free emission (Tielens, 2005). Ionized hydrogen contributes to the cooling of the gas by free-bound and free-free transitions.

The atomic gas phase is mainly cooled by fine structure transitions in C^{+} or in O. To excite these species to the higher electronic level, H and H_2 are important collisional partners in the denser gas regions. However, since some species like carbon, sulphur, or siliceous (C, S, Si) have an ionization potential below 13.6 eV, there exist also free electrons in the atomic gas phase, so that collisions with these can likewise excite C^{+} or O (Stahler & Palla, 2005, Tielens, 2005). Further, atomic hydrogen can be excited. A transition to its ground state takes then place by emitting a Lyman α photon. This process is called Lyman-α cooling (Tielens, 2005).

In the molecular gas, carbon and oxygen no longer exist separately, but form CO. Due to collisions, the rotational levels of CO are excited, and a transition to the ground state takes place by emitting a photon. Since the lower lying CO rotational transitions of carbon are optically thick, the emitted photons are trapped within the molecular gas, moving via diffusion, and only escape at the cloud surface (Stahler & Palla, 2005). Further cooling takes place due to interaction of the gas with dust grains. Collisions between the gas and the dust grains reduce the kinetic energy of the gas, and result in lattice vibrations of the dust, that decay by the emission of a photon. These photons contribute to the infrared continuum emission (Tielens, 2005).

To measure the cooling of the gas, a cooling rate Λ is used, which expresses

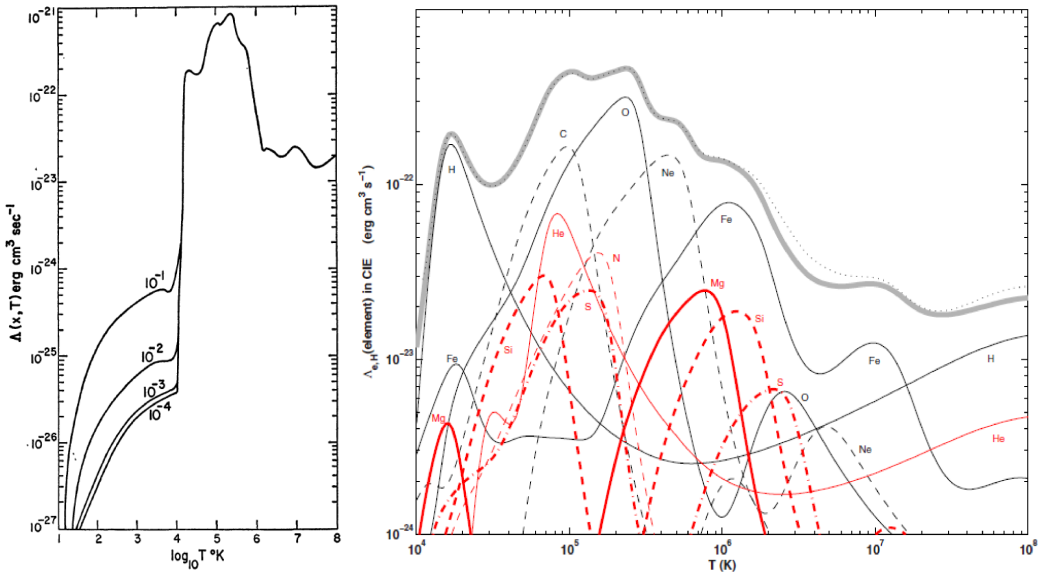

Figure 1.4: Interstellar cooling function $\Lambda(x, T)$, as presented in Dalgarno & McCray (1972) in their fig. 2 (left). The fractional ionization is denoted by x, and indicated at each line. The right panel shows the cooling curve with the contribution from the different elements as presented by Gnat & Ferland (2012), fig. 3 therein.

how much energy (in erg), integrated over a certain volume element (in cm^3), is transferred to the environment over time (in s^{-1}). The processes described above can be summarized in cooling curves, as done in e.g. Dalgarno & McCray (1972), Sutherland & Dopita (1993) and Gnat & Ferland (2012). Figure 1.4 shows the cooling curve for the atomic gas phase as a function of the temperature in the optically thin limit. In the left panel the curve is presented for a larger range of temperatures between 10 K and 10^8 K. The different lines indicate the cooling curves for different degrees of ionization in the gas. For $T \leq 10^4$ K the gas is mainly cooled by fine structure transitions. Depending on the degree of ionization in the gas, the efficiency in the cooling changes.

The right panel of Fig. 1.4 shows the contribution from the different elements to the cooling curve for $T \gtrsim 10^4$ K. It is assumed that the gas is in collisional ionization equilibrium. At temperatures of $T \sim 2 \times 10^4$ K, cooling is dominated by hydrogen Lyman-α cooling. Carbon cools most efficient at $T \sim 10^5$ K, followed by oxygen at $T \sim 3 \times 10^5$ K. Further, cooling by neon ($T \sim 5 \times 10^5$ K) and iron ($T \sim 1.5 \times 10^6$ K and 10^7 K) takes over. As fewer electrons are bound to their atoms, the less efficient the cooling becomes, so that the cooling curve drops above 10^5 K (Tielens, 2005). For temperatures larger than 10^7 K, the cooling is dominated by thermal bremsstrahlung due to the fully stripped ions (Gnat & Ferland, 2012, Tielens, 2005).

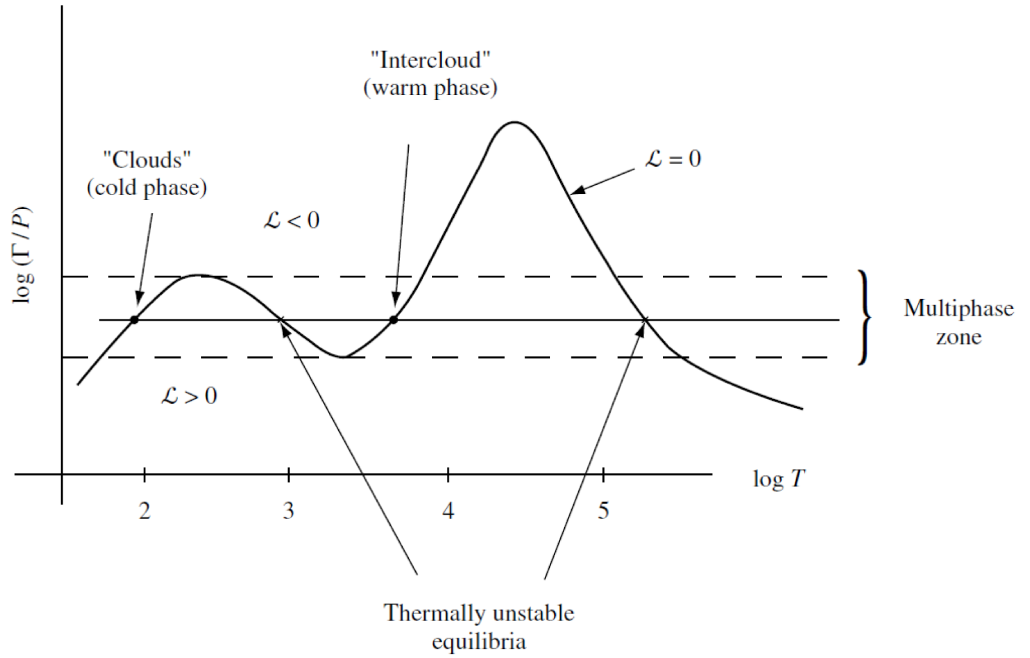

Figure 1.5: Schematic representation of the equilibrium curve ($\Lambda/(kT)$), illustrating the resulting two phases of the ISM (credit: Tielens, 2005, , fig. 8.1 therein, taken from Shull et al. 1987). Above the curve, heating exceeds cooling, and below the curve, cooling dominates. The horizontal line indicates a constant heating rate and constant pressure. The intersection points of the cooling curve with the horizontal line are the equilibrium points, from which two are stable and two are unstable, so that multiple phases coexist.

1.2.2 Phases of the ISM

Although one might expect the gas to be present at any region in the temperature-density phase space, most of it is constrained to narrow temperature-density regions, known as the phases of the ISM. These phases are determined by the balance between the cooling, Λ, and heating, Γ, which can be expressed in

$$\mathcal{L} = n^2\Lambda - n\Gamma. \tag{1.1}$$

Given that heating and cooling depend on the density and temperature of the gas, it is possible to find conditions of temperature and density, where $\mathcal{L} = 0$. This is also known as the equilibrium curve. As a consequence of this equilibrium curve, the two phase model of the ISM is derived. A schematic illustration is shown in Fig. 1.5. In that model, the phases of the cold neutral medium (CNM), forming the molecular clouds, and the warm neutral medium (WNM) and warm ionized medium (WIM), present in the intercloud gas, coexist in thermal and pressure equilibrium. For these assumption the two-phase model predicts the CNM at temperatures around 50 K and number densities around 60 cm^{-3}, and a WNM with $T \sim 7500$ K and $n \sim 0.4$ cm^{-3} (Tielens, 2005).

Caused by supernova (SN) explosions turbulent energy is injected to the ISM, and the gas is heated. This results in the formation of an additional very hot, and

tenuous gas phase, with $T \sim 10^6$ K and $n \sim 10^{-3}$ cm^{-3}. This is the hot intercloud medium, or hot ionized medium (HIM), present in a SN driven ISM. Due to its low density, the radiative cooling does not work efficiently in this gas phase. Thus, it coexist with the CNM, WNM and WIM, but is not in thermal equilibrium. The HIM, WNM and WIM, and CNM together build the three-phase model of the ISM, also called McKee-Ostiker model (McKee & Ostriker, 1977). The CNM is expected to mainly exist in the galactic disc, but might extend to some distance from the disc midplane due to the turbulent cloud velocity dispersion. The HIM, WNM and WIM are expected to form the low halo, while the HIM is found towards higher latitudes (Tielens, 2005).

There are different schemes to classify the gas phases in greater detail. Draine (2011) distinguishes between the following phases:

- Coronal gas (or hot ionized medium, HIM), which is shock-heated gas, mostly ionized and with $T \geq 10^{5.5}$ K and $n_{\mathrm{H}} \sim 0.004$ cm^{-3}.
- H II gas, which predominantly forms around massive O-type stars. These stars emit photons in the ultraviolet regime, that ionize hydrogen. This gas is at temperatures of $T \sim 10^4$ K and densities n_{H} between 0.2 and 10^4 cm^{-3}.
- Warm H I gas (or warm neutral medium, WNM), which is mostly atomic gas, with $T \sim 5 \times 10^3$ K and $n_{\mathrm{H}} \sim 0.6$ cm^{-3}.
- Cool H I gas (or cool neutral medium, CNM), is likewise atomic gas, but at lower temperatures of $T \sim 100$ K and higher densities of $n_{\mathrm{H}} \sim 30$ cm^{-3}.
- Diffuse H_2 gas, in which the shielding in the gas is sufficient that H_2 can form. This gas has temperatures of $T \sim 50$ K and densities of $n_{\mathrm{H}} \sim 100$ cm^{-3}.
- Dense H_2 gas, with T between 10 and 50 K and n_{H} between 10^3 and 10^6 cm^{-3}, which forms gravitationally bound clouds. In those clouds stars can form.

An alternative, more simplified classification is provided in Mihalas & Binney (1981), and used in Walch et al. (2015). Here, the gas is distinguished between

- hot gas, mostly from SN remnants ($T \geq 3 \times 10^5$ K),
- warm-hot, ionized gas (8×10^3 K $< T < 3 \times 10^5$ K),
- warm atomic and partly ionized gas (300 K $\leq T \leq 8 \times 10^3$ K),
- thermally stable cold gas ($T < 300$ K),
- very cold and dense gas, most likely in molecular form ($T < 30$ K).

1.2.3 Molecular clouds

Molecular clouds are characterized by their higher densities and thus, lower temperatures compared to the embedding material. The classification of molecular clouds into groups has no strict limits. However, one approach is to distinguish the molecular clouds by its visual extinction A_V (Stahler & Palla, 2005, Snow & McCall, 2006, Draine, 2011):

- Clouds with a low visual extinction ($A_V \sim 1$) are "diffuse clouds". They have typical total gas number densities between ~100 and 500 cm^{-3}, temperatures around $T \sim 50$ K, and masses of $M \sim 50\ M_\odot$. Their sizes are about 3 pc.
- Translucent molecular clouds have a slightly larger visual extinction ($A_V \sim 2$), typical number densities of 500 to 5000 cm^{-3}, and temperatures of 10 to 50 K (Snow & McCall, 2006).
- Clouds with masses of $M \sim 10^5\ M_\odot$, visual extinction of $A_V \gtrsim 2$, on scales of $L \sim 50$ pc can be classified as "giant molecular clouds" (GMC). They have number densities of about $n \sim 100$ cm^{-3}, and temperatures about $T \sim 15$ K.
- Clouds with visual extinctions around $A_V \sim 5$ are dark clouds. They have smaller dimensions compared to the GMCs ($L \sim 10$ pc), and smaller masses ($M \sim 10^4\ M_\odot$), while their total number densities are around $n \sim 500$ cm^{-3}, and the temperatures of $T \sim 10$ K are slightly smaller than in GMCs.
- Due to gravitational collapse in molecular clouds, dense cores can form. These are of small dimension ($L \sim 0.1$ pc), and have visual extinctions of $A_V \sim 10$. Their number densities are about $n \sim 10^4$ cm^{-3}, and their temperatures are about $T \sim 10$ K. It is within these cores where star formation takes place.
- Infrared dark clouds are characterized by a high visual extinction of $A_V \sim 10$ to 100, so that they are opaque even at 8 μm (Draine, 2011).

As a result of the shielded gas, the intensity of the far-UV radiation is reduced within molecular clouds, and the gas-phase chemistry is mainly driven by cosmic ray ionization (Tielens, 2005). Due to the low temperatures, atoms and molecules from the gas phase freeze out on the surface of dust grains, forming an ice mantle around them. Thus, chemical species and molecules are depleted from the gas phase. This changes the chemistry in the gas phase, as well as introduces the ice as a further chemical reaction component, since now interaction between the gas phase and the solid state takes place (Tielens, 2005).

In dense regions molecular clouds can gravitationally collapse and from protostars, whose feedback likewise influences the energy balance of the gas as well as its chemical composition. Massive stars (O- and B-type) can influence the ISM by stellar winds, and their radiation. A typical GMC survives around 3×10^7 yr, before it is destroyed by the winds of its stars (Stahler & Palla, 2005). Further, the UV radiation of the embedded stars evaporate the ice mantles of the dust grains and ionize the surrounding gas. In the transition regions from the ionized to the molecular gas phase, photon-dominated regions (PDRs) evolve (Hollenbach & Tielens, 1999). The far-UV radiation ($6\,\mathrm{eV} < h\nu < 13.6\,\mathrm{eV}$) from the stars is no longer sufficient to ionize hydrogen, but it still dominates the chemistry of the gas and ionizes species with ionization potentials below that of hydrogen. Carbon is one species, that becomes ionized in those PDRs. Thus, PDRs are observable in the emission line from C^+, which is a fine structure emission line [C II].

Often, the molecular clouds do not exist in isolation, but form large cloud complexes. In galaxies, these are situated within the galactic disc. In Fig. 1.2 the contours mark emission from the ^{12}CO (1–0) line, indicating the molecular clouds. One example is Orion, shown in Fig. 1.6 (Kong et al., 2018, fig. 5 therein), which is a

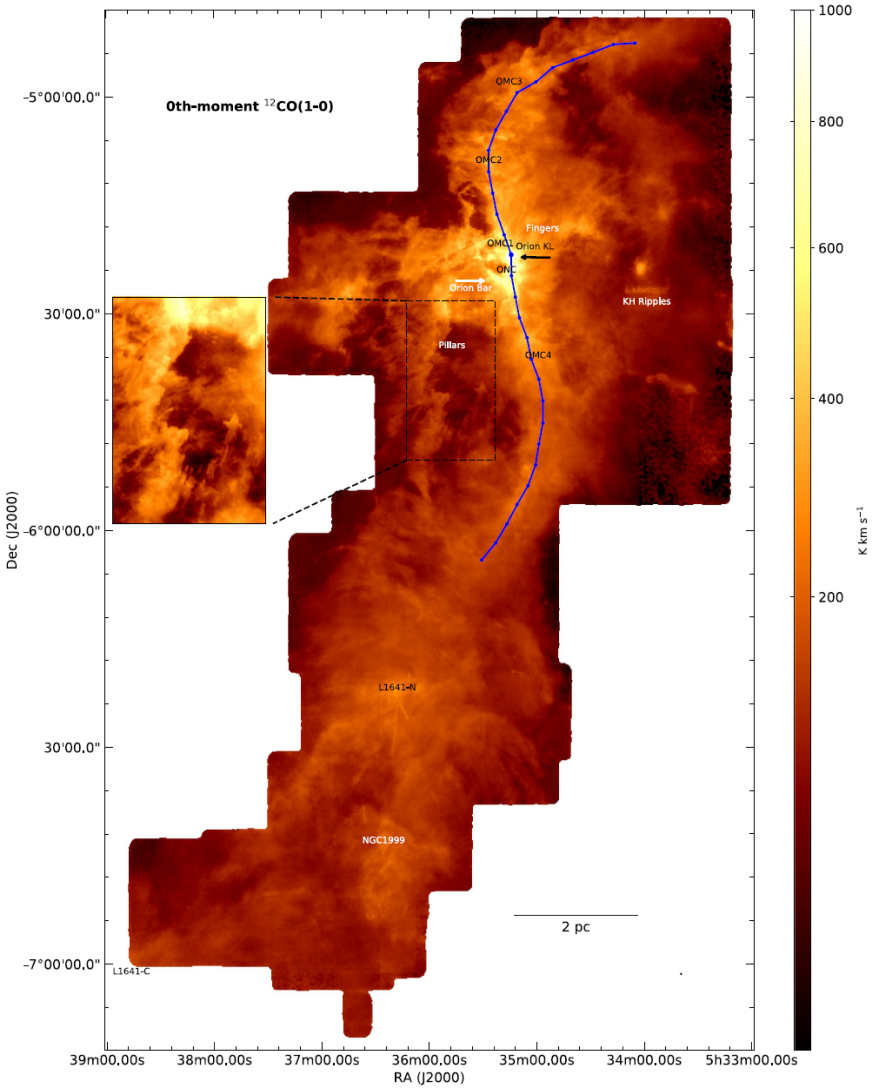

Figure 1.6: Orion molecular cloud in the integrated ^{12}CO (1–0) intensity (over the velocity range of 2.5 - 15 km s^{-1}), as presented by Kong et al. (2018), fig. 5 therein.

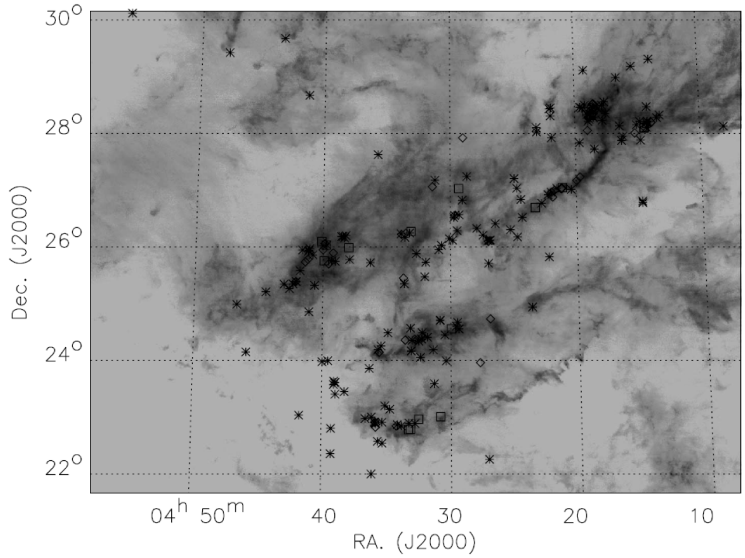

Figure 1.7: Taurus molecular cloud complex, as presented in Goldsmith et al. (2008) in fig. 14 therein. The grey colours show the H_2 column density. The symbols mark the position of the stars. Diamonds indicate diffuse, extended sources, squares indicate Class I or younger stars, asterisks indicate T Tauri stars (see Goldsmith et al., 2008).

star forming molecular cloud complex at a distance of 450 pc (Genzel & Stutzki, 1989). It contains OB-type stars, and thus, it is suitable to study the formation of stars, filaments, and the influence of stellar feedback on the ISM. Due to its active star formation, Orion is also used to study the chemistry and structure of PDRs (e.g. Andree-Labsch et al., 2017).

Another example is Taurus, a well studied molecular cloud (Goldsmith et al., 2008), situated in our proximity, with a distance of about ∼140 pc (∼126 pc), according to Elias (1978) (Hartigan & Kenyon, 2003, respectively). A study of the region within a field of 100 deg^2 in ^{12}CO and ^{13}CO rotational transition $J = 1 - 0$ was done by Goldsmith et al. (2008). Figure 1.7 shows the Taurus molecular cloud complex (Goldsmith et al., 2008, fig. 14 therein). Assuming that Taurus is at a distance of about 140 pc, (10 deg)^2 correspond to ∼(24 pc)^2. They find a complex structure of the molecular cloud, with filaments, ridges, blobs, and holes. They estimate the mass of Taurus with their observations, and find a mass of about 2.35×10^4 $M_\odot$. Half of this mass is present in regions with total gas column densities $N \leq 2.1 \times 10^{21}$ cm^{-2}. Star formation takes place in Taurus since about 10 Myrs, where most of the stars were formed during the last 3 Myrs (Palla & Stahler, 2002, Goldsmith et al., 2008).

Regions of molecular cores in infrared dark clouds (IRDC) and cold, massive, molecular clouds were studied with *Herschel* as part of the Earliest Phases of Star Formation (EPOS) key program (Ragan et al., 2012). They analysed with the *Herschel* PACS[4] instrument the emission at 70, 100, and 160 μm, and with SPIRE the

[4]PACS stands for Photoconductor Array Camera and Spectrometer, and is an instrument onboard *Herschel*.

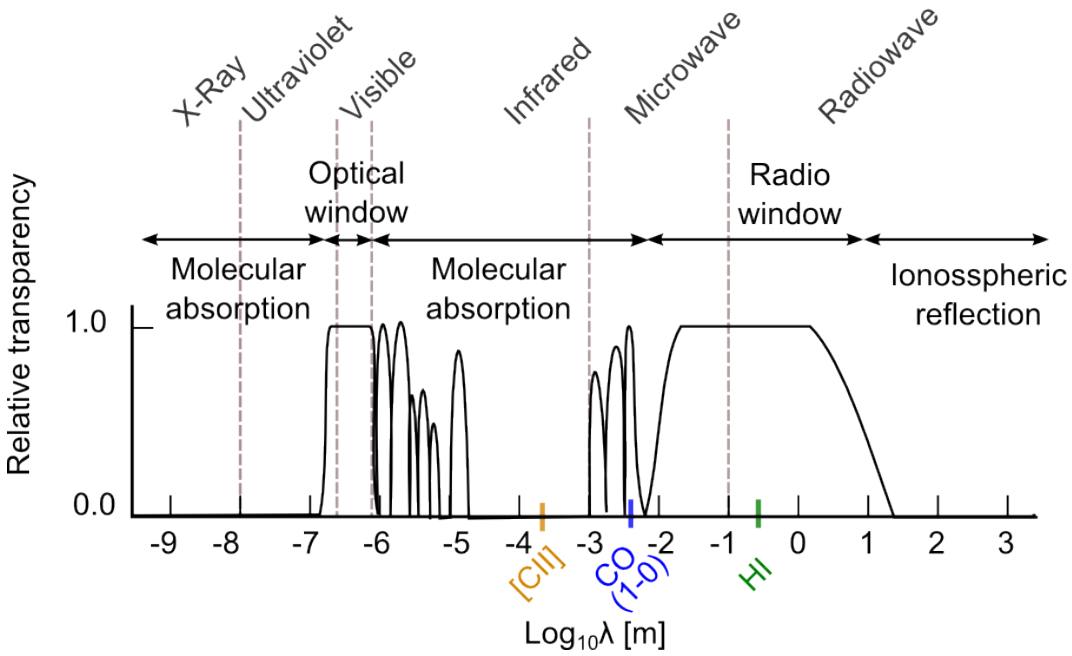

Figure 1.8: Plot showing the relative transparency of the atmosphere of the Earth as a function of wavelengths. This plot is inspired by Carroll & Ostlie (2006), fig. 6.25 therein. Note, that the transparency is also influenced by the height above the sea level. Therefore, this is only a sketch. Additionally, wavelengths of the [C II] line emission, the H I 21 cm line, and the ^{12}CO $(1-0)$ line emission are indicated on the x-axis.

emission at wavelengths of 250, 350, and 500 μm. Ragan et al. (2012) find the core population to have a median temperature of 20 K, while their masses and luminosities span four to five orders of magnitude. Some of those IRDCs are further analysed by Beuther et al. (2014) in studies of carbon lines, finding the atomic carbon to CO mass ratio to be low (between 7% and 12%), with smaller values for regions more quiet in star formation. According to Beuther et al. (2014), the [C II] line emission traces the environment around the dense gas, and is sensitive to the external UV field.

1.3 Radiation detected from the ISM

Whether the radiation from space can be detected on Earth, depends on the transparency of the atmosphere at their wavelengths (e.g. Weigert et al., 2016). A sketch of the Earth's atmosphere's transparency is presented in Fig. 1.8 (drawn after Carroll & Ostlie, 2006, fig. 6.25 therein). The transparency of radiation through the atmosphere is in general likewise dependent on other factors, e.g. the height above the sea level, air humidity, and temperature. Therefore, Fig. 1.8 has to be interpreted as a sketch of the transparency for average conditions on Earth. Wavelengths below $\lambda \lesssim 300$ nm are absorbed by the atmosphere due to the ionisation of elements, Rayleigh-scattering on electrons in the atmosphere, and absorption from O_3 and O_2

in the ozone-layer of the atmosphere. Between 300 nm $\lesssim \lambda \lesssim$ 1 μm, in the optical wavelengths, radiation can pass unimpeded through the atmosphere. This is the so-called "optical window". In the near-infrared light ($\lambda \lesssim 10$ μm) there are lots of small ranges in wavelengths in which radiation can transmit through the atmosphere. These ranges are bordered by absorptions from molecules, mostly by H_2O and CO_2 absorptions. The absorptions are more frequent at smaller wavelengths, such that the atmosphere absorbs the emission for $\lambda \gtrsim 20$ μm. In the submillimeter wavelength range, the atmosphere becomes more transparent again, and radiation with wavelengths between 1 mm $\lesssim \lambda \lesssim$ 10 m can be detected from Earth. However, for even higher wavelengths, the radiation is totally reflected by the ionosphere of the atmosphere.

In addition, the wavelengths of the [C II] line emission, the H I 21 cm line, and the ^{12}CO (1 − 0) line emission are indicated on the x-axis of Fig. 1.8. The H I 21 cm line, and the ^{12}CO (1 − 0) line emission are detectable with ground-based instruments, since their wavelengths are in the radio- and submillimetre wavelength ranges, respectively. Thus, it is comparably easy to carry out large scale observations for these lines.

1.3.1 Carbon monoxide, CO

Carbon monoxide (CO) is a main component of molecular clouds. It is observable via its rotational transitions in the wavelength range of microwaves. Its low-lying rotational transitions are at mm wavelengths (Flower, 2001). As indicated in Fig. 1.8, these transitions can be observed by ground-based telescopes, and thus, they are easily accessible for observations. In the context of molecular clouds, CO transitions are detected in Taurus, Orion and many more. Further, large scale surveys of the CO transitions of the Milky Way exist, e.g. Dame et al. (2001, see Fig. 1.2).

About 20% of hydrogen atoms are in form of H_2, but it is observationally difficult to access, since it has no permanent dipole moment, and therefore no allowed dipole transition. Therefore, CO is usually used to estimate the abundance of H_2 in molecular clouds. CO is assumed to form in dense molecular gas, well shielded from ionizing and dissociating radiation, and therefore, it is expected to be found in the same regions as H_2. Shetty et al. (2011a,b) numerically studied the ability of CO to trace H_2, finding that the conversion factor between the CO emission and the H_2 abundance depends on metallicity, density and background radiation of the molecular cloud. This is in agreement with observations analysed by Genzel et al. (2012). Furthermore, in regions of less dense molecular clouds, CO is not formed, or is efficiently photo-dissociated by UV radiation at low metallicities and therefore the H_2 gas is invisible in the CO intensity signal. This gas is called CO–dark H_2, following the work of Grenier et al. (2005). For regions fulfilling these conditions, CO is no longer a good tracer of H_2, and therefore a different tracer is needed. The

emission line of C^+ might be a good candidate.

1.3.2 Ionized carbon, [C II]

Carbon ions can be present in molecular and atomic gas, since only 11.6 eV are needed to ionize carbon atoms. For comparison, the ionization potential of hydrogen is at 13.6 eV. Beyond that, carbon ions can still be present in the ionized gas phase, since 24.4 eV are necessary to ionize C^+ even further (Goldsmith et al., 2012, Pineda et al., 2013, Kapala et al., 2015). The carbon ion has a fine structure transition [C II] at a wavelength of $\lambda = 157.741$ μm, corresponding to a frequency of $\nu = 1900.537$ GHz. This line emission is a dominant cooling line in the ISM (Tielens & Hollenbach, 1985, Klessen & Glover, 2016), and thus, one of the brightest far-infrared lines observed. The [C II] line emission can originate from various phases in the ISM and it is therefore not trivial to disentangle its origin. In the Milky Way, the [C II] line emission accounts for 0.1 – 1% of the total infrared emission (Stacey et al., 1985).

The [C II] line emission has its wavelength in the far-infrared range, where molecular absorption in the atmosphere hinder ground based observations. Therefore, one has to use instruments at high altitudes for the detection of the [C II] line emission. This can be done by instruments installed on balloons, telescopes on air planes, and on satellites. A list of some important surveys with their spatial and spectral resolution is given in Table 1.1, and some of their main results described later in Section 1.4 (see also Pineda et al., 2013, Langer et al., 2014b).

Since the [C II] line emission can originate from several phases of the ISM, among them the molecular gas phase, one would like to use the [C II] line emission as a tracer for H_2 gas in regions where CO is not present (CO-dark H_2, e.g. Wolfire et al., 2010, Langer et al., 2014b). Once stars have began to form, carbon can be ionized by the radiation of these newborn stars, and bright [C II] line emission can be observed in connection with stellar radiation feedback in various studies (e.g. Beuther et al., 2014, Goicoechea et al., 2015). Therefore, one would like to use the [C II] line emission likewise as a tracer for the star formation (De Looze et al., 2011, 2014, Herrera-Camus et al., 2015, Kapala et al., 2015). However, for all these questions it is crucial to understand what fraction of the [C II] emission originates from each of the ISM phases.

1.3.3 Atomic hydrogen, H I

Hydrogen is the most abundant element in the ISM. About ~60% of it is in form of atomic hydrogen (Tielens, 2005). Atomic hydrogen emits radiation via its hyperfine structure transition at $\lambda = 21$ cm. Its spontaneous transition probability is very

small, with 2.9×10^{-15} s^{-1}, meaning that a spontaneous transition takes place around once every 11 million years. However, since it is present in large amounts in the ISM, the H I 21 cm line can be observed. This line was first theoretically predicted by van de Hulst (1945), and observed for the first time by Ewen & Purcell (1951). Within the Milky Way, it was mapped within the different Galactic Plane surveys (e.g. Taylor et al., 2003, McClure-Griffiths et al., 2005, Stil et al., 2006). Across the northern hemisphere, H I was mapped in The H I, OH, Recombination Line Survey (THOR Bihr et al., 2015, Beuther et al., 2016).

Studies of the H I 21 cm line emission are used to e.g. investigate the structure of the galaxies (O'Brien et al., 2010), like its spiral arms, and radius, as well as to study the chemical evolution of the gas. Further, the rotation curve within galaxies are observed with H I observations. Another field of investigations are the H I self absorption features within the H I line profiles, being subject of research in the THOR survey (Bihr et al., 2015).

1.4 [C II] Surveys

During the past decades several [C II] line emission studies were carried out and were used to analyse from which regions in a galaxy and from which phase of the ISM the emission originates. A list of some important surveys is given in Table 1.1 (see also Pineda et al., 2013, Langer et al., 2014b).

- With the balloon–borne surveys BIRT (Balloon–borne Infrared Telescope) and especially BICE (Balloon–borne Carbon Explorer), the [C II] line emission has been studied in the Milky Way on large angular scales. Nakagawa et al. (1995) found the ratio of [C II] line emission to far–infrared continuum emission ($I_{[CII]}/I_{FIR}$) to decrease towards the centre of the Galaxy and explained this by the absence of C^+ due to the soft radiation field of cool stars and self–shielding effects. Shibai et al. (1991) found that the observed diffuse [C II] line emission comes primarily from PDRs.

- The Far–Infrared Absolute Spectrophotometer (FIRAS) on the Cosmic background explorer (COBE) satellite observed for the first time nearly the entire sky. This survey was used for studies of diffuse [C II] line emission due to its large beam size (Bennett et al., 1994). They showed that the [C II] emission line is the brightest line in the far–infrared and submillimeter wavelength range (Nakagawa et al., 1998).

- The Far–Infrared Line Mapper (FILM) on the infrared telescope in space (IRTS) has a better spatial resolution than FIRAS/COBE and a higher sensitivity compared to the balloon–borne surveys (Shibai et al., 1994). The [C II] line emission data from this survey were analysed by Makiuti et al. (2002), who found that diffuse [C II] emission extends to high Galactic latitudes. This

indicates that not all of the [C II] line emission comes from young stars. As the intensity of the [C II] line emission is systematically larger on the northern side ($b > 0°$) compared to the southern side ($b < 0°$), they conclude that the Sun is displaced with respect to the galactic midplane.

- The first spatially resolved survey of the [C II] line emission in the Milky Way is the Galactic Observations of the Terahertz C+ (GOT C+) survey of the *Herschel* open time key program. Langer et al. (2014b) combined the GOT C+ data at $b = 0°$ with the low angular resolution BICE and FILM data for further longitudes to measure the distribution of the [C II] line emission around the Galactic disc and determined the vertical scale height of the disc. They find a scale height of 73 pc, different from the scale heights of other tracers observed in the Milky Way, like H I, which has a scale height larger than 89 pc or CO, with a smaller scale height of 46.7 pc. Pineda et al. (2013) and Velusamy & Langer (2014) analysed the GOT C+ data in order to identify the regions and ISM phases where the radiation is emitted by using ancillary emission lines. According to Pineda et al. (2013) most of the [C II] line emission emerges from Galactocentric distances between 4 kpc and 11 kpc. Concerning the ISM phases, they estimate that $\sim 47\%$ of the emission originates from dense PDRs, $\sim 28\%$ from CO–dark H_2 gas, $\sim 21\%$ from cold atomic gas and $\sim 4\%$ from ionised gas. However, Velusamy & Langer (2014) further investigate this issue as well as the scale height of the different phases, taking additional account of the kinematic distances, and find the [C II] line emission to correlate with the spiral arms of the Milky Way. According to their analysis 62% of the emission comes from H_2 dominated regions, 18% from atomic gas, and 21% from the WIM.

- [C II] line emission is likewise investigated in other galaxies. The edge–on galaxy NGC 891 is said to "resemble our own Galaxy both in morphology and physical properties" (Madden et al., 1994). It has recently been observed again with the *Herschel* far–infrared telescope. Hughes et al. (2015) analyse different far–infrared cooling lines, among these the [C II] emission line. They determine the [C II] scale height of NGC 891 to be around 310 pc, and therefore significantly higher than the scale height of the Milky Way.

- There are also other surveys studying the [C II] emission from external sources and galaxies.

  - The Heterodyne Instrument for the Far–Infrared (HIFI, cf. de Graauw et al., 2010) on *Herschel* is used among other things to study the ISM of PDRs (Ossenkopf et al., 2013), in Orion (Goicoechea et al., 2015) as well as recently in M33 (Mookerjea et al., 2016).
  - Observations from airplanes were done between 1971 and 1995 with the *Kuiper* Airborne Observatory. With this instrument the [C II] line emission was observed e.g. in the M42 region in Orion (Boreiko et al., 1988).
  - Observations of the [C II] line emission in the near Universe as well as in external galaxies are carried out with the German REceiver for Astron-

omy at Terahertz Frequencies (GREAT) (Heyminck et al., 2012) onboard the Stratospheric Observatory for Infrared Astronomy (SOFIA) (Young et al., 2012). Recently, [C II] observations were done of the Large and Small Magellanic Clouds (Okada et al., 2015), and of the PDR emission in NGC 2023 (Sandell et al., 2015). Extragalactic surveys were recently done for M51 and M33 with the upGREAT receiver (Risacher et al., 2015, Pineda et al. in prep.) and the Field–Imaging Far–Infrared Line–Spectrometer (FIFI–LS, cf. Klein et al., 2010).

Table 1.1: Summary of the [C II] line emission observations carried out in the Milky Way *(upper part)* and in distant galaxies *(lower part)*

Survey	Beam size [FWHM]	Velocity resolution [km s^{-1}]	References
BIRT	3.4′	143	Shibai et al. (1991)
BICE	12.4′	175	Nakagawa (1993)
FIRAS COBE	7°	~ 1000	Wright et al. (1991), Bennett et al. (1994), Fixsen et al. (1994)
FILM IRTS	8′ × 13′	750	Shibai et al. (1994), Makiuti et al. (2002)
Herschel GOT C+	12″	~ 0.1	Langer et al. (2010, 2014b)
Herschel PACS	11.5″		NGC 891, Hughes et al. (2015)
Herschel HIFI	11.1″	~ 0.1	de Graauw et al. (2010), Mookerjea et al. (2016)
KAO,		0.8	Boreiko et al. (1988)
SOFIA GREAT L2	14.1″	0.007	Young et al. (2012), Heyminck et al. (2012) Okada et al. (2015)

1.5 Simulations

Besides observing the ISM at different wavelengths, one can study its evolution by carrying out numerical simulations. Although the densities found in the ISM are almost a perfect vacuum compared to the densities of fluids on Earth, the large scales of the ISM allow for the fluid approximation to be implemented. Based on the physical laws from (magneto-)hydrodynamics one can follow the time evolution of the ISM phases; thus, a great advantage compared to observations, where we only see one time step, since the evolution processes in the ISM normally happen on large time scales.

1.5.1 Numerical simulations of the ISM

For a numerical simulation of the ISM, the following system of (magneto-)hydrodynamic (MHD) equations has to be solved. We here present the ideal MHD formulation, neglecting the terms of friction and viscosity. In that sense, the Navier-Stokes equation is given as

$$\rho\frac{\mathrm{d}\overrightarrow{v}}{\mathrm{d}t} = \rho\frac{\partial\overrightarrow{v}}{\partial t} + \rho(\overrightarrow{v}\nabla)\overrightarrow{v} = -\nabla p - \rho\nabla U_{\mathrm{grav}} + \frac{1}{c}\overrightarrow{j}\times\overrightarrow{B}. \tag{1.2}$$

Here, ρ is the gas density, $\overrightarrow{v}$ the velocity of the gas, p is the gas pressure, U_{grav} the gravitational potential, $\overrightarrow{j}$ is the current density, and $\overrightarrow{B}$ the magnetic field. Since the viscosity is not taken into account in the simulations, we don't include their contribution in Eq. (1.2). The derivative $\frac{\mathrm{d}}{\mathrm{d}t}$ stands for the Lagrangian formulation, where we follow the evolution of a particle within the fluid. The formulation via $\left(\frac{\partial}{\partial t} + \mathbf{v}\cdot\nabla\right)$ represents the Eulerian one, in which the evolution is expressed in a spatial frame. Then, there is the Poisson equation

$$\triangle U_{\mathrm{grav}} = 4\pi G\rho, \tag{1.3}$$

with the gravitational constant G. Further, the continuum equation is

$$\frac{\mathrm{d}\rho}{\mathrm{d}t} + \overrightarrow{v}\nabla\rho = \frac{\partial\rho}{\partial t} + \nabla\cdot(\rho\overrightarrow{v}) = 0, \tag{1.4}$$

in the Lagrangian and Eulerian formulation, respectively. The adiabatic energy equation is

$$\frac{p}{p_0} = \left(\frac{\rho}{\rho_0}\right)^{\gamma}, \tag{1.5}$$

with the polytropic coefficient γ. The internal energy e is expressed in a caloric equation of state

$$e = e(\rho, T), \tag{1.6}$$

that includes the exchange of the inner energy with the environment. Finally the heat transfer equation is

$$\rho \frac{\partial e}{\partial t} = \kappa \triangle T - p \bigtriangledown \overrightarrow{v} + \frac{\overrightarrow{j}^2}{\sigma} + \Gamma - \Lambda. \tag{1.7}$$

with κ as the heat diffusion coefficient, σ as the conductivity, and Γ and Λ presenting the radiative heating and cooling, respectively. To have a complete set of equations in the framework of MHD, we have further the equation for the advection of the magnetic field as

$$\frac{\partial \overrightarrow{B}}{\partial t} = \bigtriangledown \times (\overrightarrow{v} \times \overrightarrow{B}). \tag{1.8}$$

This set of equations does not include the chemical evolution of the gas, which would even further influence the hydrodynamic evolution of the fluid. This system of equations can be solved within a particle approach, or within a grid of cells (Clarke, 2016).

Smoothed Particle Hydrodynamical simulations

As shown in Equations (1.2)–(1.7), the fluid dynamics can be solved in the reference frame of a fluid unit. Within the approach of smoothed particle hydrodynamics (SPH) the fluid is described as a set of particles, for which the hydrodynamical part (HD) of the equations are solved. Therefore, SPH is a Lagrangian approach. Each particle represents a certain mass of the fluid. Thus, the limiting resolution is defined as a resolution in mass. Consequently, the spatial resolution increases automatically in regions of high particle densities. The gas density in the SPH approach is quantified as the mass within a certain area defined as the smoothing length. The smoothing length itself can be defined e.g. as the radius of a region containing a fixed number of particles. The drawback of this scheme is its order of accuracy, to which the HD equations are solved. Simulations with SPH are dissipative, which causes problems when simulating e.g. the evolution of shocks within the ISM. The SPH simulations were developed independently by Lucy (1977) and Gingold & Monaghan (1977). Today, GADGET and GANDALF (Hubber et al., 2018) are examples of an HD code based on the SPH approach.

Eulerian mesh-based approach

Similarly, the MHD Equations (1.2)–(1.7), and in addition Eq (1.8), can be solved in the Eulerian reference frame. Here, the mass of the fluid is distributed in a predefined grid, and the MHD equations are solved for every grid cell. The differential equations can be solved by a high-order Riemann solver. This provides a high accuracy, which enables simulations of this scheme to follow the evolution of shocks. However, a disadvantage of this scheme is that the angular momentum is not conserved. Further, due to the orientation of the grid there exist a preferred direction of travel, and due to the fixed size of the grid cells, the spatial resolution is constant throughout the whole simulation area and advection errors of flows occur, when fluids with large velocity gradients move across grid cells (Hopkins, 2015, Clarke,

2016). However, in a version of this approach the grid itself can be refined adaptively in regions of e.g. higher densities. This is called adaptive mesh refinement (AMR Berger & Colella, 1989), and used for example in the FLASH code (Fryxell et al., 2000, Dubey et al., 2012, 2013). The criteria for the refinement are defined by the user.

Moving mesh schemes

The advantages of the SPH scheme and the grid schemes can be combined in a moving mesh scheme, e.g. the newly developed code AREPO (Springel, 2010, 2011). Here, the fluid is calculated within an unstructured moving mesh, defined by the Voronoi tessellation of a set of discrete points. Each point represents a fluid unit that evolves in a Lagrangian-like scheme, while simultaneously each point likewise represents a grid cell, defined as the volume closest to each point. Unlike SPH, there is mass transfer between the cells in the moving mesh scheme. The points can move arbitrarily. By this, the grid deforms, without that cells overlap. If the points are fixed, the scheme behaves as an Eulerian grid. Similarly, if the grid points contract homologous, the scheme behaves as a SPH scheme. For every cell, the MHD equations are solved, using the exact Riemann solver. This enables the AREPO code to describe shocks and fluid instabilities, while on the other hand keeping the advantage of the adapted spatial resolution of an SPH code.

1.5.2 Radiative transfer simulations

With numerical simulations one can study the evolution of the ISM. Doing this allows the simulators to know at a certain time step about the physical quantities of the gas, among those e.g. temperature, density, velocity and magnetic fields. However, observers detect the radiation at different wavelengths from atoms, ions and molecules in the ISM, and use this information to infer the underlying physical quantities. Thus, the prior information simulators and observers obtain, are different (physical quantities for the simulator, and emission for the observers).

To bring the simulations closer to the language the observers use, it has to be estimated what emission is expected from the gas in the simulations. For this, the numerical simulations either need to make assumptions about the chemical composition of the gas in a post-processing step, or a chemical network can calculate the non-equilibrium chemical composition of the gas while the simulation is evolving. It follows the chemical abundances more accurately accounting for their formation, destruction, and dissociation, as well as the mixing of chemical species due to turbulence. Knowing the chemical composition at all points enables the simulators to carry out radiative transfer simulations in a post-processing step. These produce synthetic emission maps that estimate the emission expected from the simulated scenario. This is the first step on the way to the same output as observers have, and useful in the sense of analysing the characteristics of the emission. Synthetic emission maps are the basis of the analysis presented in this work.

Various radiative transfer codes were written to model the chemistry and radiation from PDRs, such as CLOUDY (Ferland et al., 2013) or KOSMA-τ (e.g. Sternberg & Dalgarno, 1989, 1995, Zielinsky et al., 2000). Other radiative transfer codes are written in a more general way, suitable to calculate the radiative transfer in a wider range of densities and temperatures, such as RADMC-3D (Dullemond, 2012) or POLARIS (Reissl et al., 2016). However, the results of all codes should agree, when the same conditions are assumed. This was tested for various codes by Röllig et al. (2007).

If one wants to compare directly the output from simulations with observations, it has to be taken into account that the simulated object has a physical distance from the observer, its emission is detected with a telescope of a certain beam size and other characteristics, and noise is influencing the observation. Taking all this into account transform synthetic emission maps into synthetic observations. A tool for taking these effects into account is the FLUXCOMPENSATOR, developed by Koepferl & Robitaille (2017).

However, since the simulations we use in this work are a small probe of the ISM, and not representing a particular region or object, we carry out synthetic emission maps at several wavelengths with RADMC-3D. This enables us to study the physical properties of the radiation emitting gas at the wavelength of the [C II] line. Thus, we investigate the underlying physics rather than compare the maps with observed maps.

1.6 Purpose of this thesis

In the context of the current state of knowledge, great hopes are placed in observations of the [C II] line emission to learn about the physical and chemical properties of molecular clouds, and star formation within them, as well as about the fraction of CO-dark H_2 gas. However, it remains difficult to determine from observations the origin of the [C II] emission, which is a crucial ingredient necessary to infer the physics of the studied object from [C II] observations. Observations are limited to the projected emission, where it is hard to conclude reliably the three dimensional structure of the objects along a line of sight. The common technique to study the properties of the gas from observations, is to use complementary observations from different tracers, and to compare the data with respect to their spatial and spectral overlap. However, as found in Clarke et al. (2018), there is no clear correlation between the spectral overlap of a line, and its three dimensional spatial position.

By analysing simulations, we have access to the three dimensional structure of the gas within a simulated molecular cloud. Thus, we can locally study the origin of the [C II] line emission, and characterize the physical properties of the [C II] emitting gas. To then make a general conclusion that can be applied by observers, we have to be clear regarding the following questions:

- What kind of object have we simulated?
- What are the ranges of physical parameters, and is there a region or scenario in the Universe that we expect to be similar to our simulation?
- Do we understand from the physics we included to carry out the simulation, why the resulting ISM has this structure and properties?

The results of post-processing synthetic emission studies have to be set into this context. In order to broaden our knowledge using numerical simulations, it is important to understand the limitations of the simulations. Numerical simulations can be of great advantage in gaining knowledge, when its limitations are clearly stated.

In this thesis I study the synthetic [C II] line emission from different simulations, aiming at understanding its distribution, and characterizing the properties of the [C II] emitting gas. Simulations of the ISM were carried out within the SILCC project (Walch et al., 2015, Girichidis et al., 2016b) and the SILCC-Zoom project (Seifried et al., 2017), studying the evolution of the gas within a piece of a galactic disc and a forming molecular cloud, respectively. The simulations include the physics describing the hydrodynamical evolution of the gas as well as its chemical evolution, by treating it with a simplified chemical model. Within the SILCC simulations we achieve a spatial resolution of $\mathrm{d}x = 3.9$ pc, whereas in the SILCC-Zoom simulations we have $\mathrm{d}x = 0.122$ pc. To set the later results from the radiative transfer into the context of the underlying simulated ISM, we introduce in Section 2 the underlying SILCC and zoom-in simulations.

From these simulations we carry out, in a post-processing step, radiative transfer simulations at the wavelength of the [C II] line emission with the radiative transfer code RADMC-3D. We aim to study the origin of the [C II] line emission, which is a local property of the gas. In order to carry out this analysis precisely, we need an optically thin tracer of the emission. The [C II] line emission can become optically thick, as found both in observations by Graf et al. (2012), Ossenkopf et al. (2013) and in our simulations (Sections 4.1.3 and 4.2.1). For carbon ions there is the isotope $^{13}C^{+}$, which emits three hyperfine structure lines; the strongest one [^{13}C II] ($F = 2 - 1$) close to the frequency of the [^{12}C II] line emission. We approximate its emission and use this optically thin [^{13}C II] line emission to study the origin of the [C II] line emission. Whenever we refer to the [^{12}C II] line emission, we refer to the opacity affected [C II] line. When refering to the [^{13}C II] line emission, we refer to the approximated [^{13}C II] line, which is the optically thin [C II] line emission. The details about the radiative transfer calculations and the assumptions made are summarized in Section 3.1.

With the SILCC simulations, representing a piece of a galactic disc, we study the large scale emission, namely the distribution of the [C II] line emission around the galactic plane in Section 5. In Section 6, we further study from which gas the [C II] line emission stems. For this, we use the SILCC simulations, as well as the zoom-in simulations, which provide a higher spatial resolution of $\mathrm{d}x = 0.122$ pc, and give insight into the emission from a single molecular cloud complex. We likewise use the zoom-in simulation to study the line profiles of the [C II] line emission, with a spectral resolution of $\mathrm{d}v = 0.1$ km s^{-1} in Section 8. We try to develop a

statistical tool for the analysis of the line profiles. Lastly, we carry out synthetic H I and ^{12}CO (1–0), ^{13}CO (1–0), C^{18}O (1–0) emission maps of the zoom-in simulations. Those complementary data are useful to study our simulated molecular clouds in a similar manner as done with observations, and will be the focus of future work.

We note, that part of this work concerning the parts of the description of the method and the analysis of MC2 was submitted to MNRAS in May 2018, accepted in September 2018, and printed in December 2018 in Franeck et al. (2018).

2

Simulations

2.1 General remarks about the SILCC simulations

The SILCC[1] (Simulating the Life Cycle of molecular Clouds, e.g. Walch et al., 2015, Girichidis et al., 2016b) simulations aim to understand the interplay of the physical processes in the interstellar medium (ISM) in a self consistent manner. They are MHD (magneto-hydrodynmaic) simulations, carried out with the adaptive mesh code FLASH 4.3 (Fryxell et al., 2000, Dubey et al., 2008). A piece of a galactic disc is simulated in a stratified box of the size of 0.5 kpc × 0.5 kpc in x- and y-direction, and ±5 kpc in z-direction. At its highest resolution level the grid cells in the simulation box have a size of 3.9 pc. In x- and y-directions, periodic boundary conditions are applied, while outflow conditions along the z-direction are considered. The SILCC simulations take include a simplified chemical network with species of hydrogen (H_2, H, H^+), carbon (CO, C^+), oxygen (O) and free electrons. Silicon is taken into account as a constant fraction over the whole simulation time, remaining singly ionized. Taking into account the chemical evolution within the gas enables us to make synthetic emission maps in a post-processing step.

To interpret the output from the simulations and its synthetic emission and to compare with real observations, it is essential to understand what is included in the simulations and what their limitations are. For this purpose we here describe shortly the setup of the SILCC simulations and its chemical network. A more detailed description of it can be found in Walch et al. (2015) and Girichidis et al. (2016b).

Initially, the gas distribution $\rho(z)$ is smooth and follows a Gaussian profile in the vertical direction z with

$$\rho(z) = \rho_0 \exp\left\{-0.5 \times \left(\frac{z}{h_z}\right)^2\right\}. \tag{2.1}$$

[1] SILCC project led by S.Walch, `https://hera.ph1.uni-koeln.de/~silcc/`

Table 2.1: List of the fractional abundances of the chemical species with respect to hydrogen. The chemical model used in the SILCC simulations follows the one of Nelson & Langer (1997) and Glover & Mac Low (2007a,b). The chemical abundances are taken from Sembach et al. (2000).

chemical species	fractional abundance
x_{He}	0.1
$x_{\mathrm{C,tot}}$	1.41×10^{-4}
$x_{\mathrm{O,tot}}$	3.16×10^{-4}
$x_{\mathrm{Si,tot}}$	1.5×10^{-5}

The scale height of the gas disc is $h_z = 30$ pc, and the density profile integrates to a total gas surface density of $\Sigma_{\mathrm{gas}} = 10\ \mathrm{M}_\odot/\mathrm{pc}^2$. This is equivalent to a midplane density of $\rho_0 = 9 \times 10^{-24}$ g cm^{-3}. The hydrogen gas in the simulations is initially warm ($T = 4\,500$ K) and atomic, but rapidly evolves away from this initial state (Walch et al., 2015). Carbon is initially assumed to be in the ionised state. Overall the initial parameters are intended to mimic conditions in the solar neighbourhood.

In a galactic disc the gravitational potential determines the distribution of the ISM components in the vertical disc structure. Stars are not directly included in the SILCC simulations, but their influence is mimicked using an external stellar gravitational potential with a vertical scale height of $z_d = 100$ pc. The stellar surface density is chosen as $\Sigma_\star = 30\ \mathrm{M}_\odot/\mathrm{pc}^2$ (Spitzer, 1942, Walch et al., 2015). This number is in line with the observation of Flynn et al. (1999), that found a stellar column density of $\sim 27\ \mathrm{M}_\odot/\mathrm{pc}^2$ from direct *Hubble Space Telescope* star counts (Romano et al., 2000). Self-gravity is likewise taken into account. The Poisson equation (Eq. (1.3)) including both processes is solved with a tree-based method (Wünsch et al., 2018).

If only gravitational forces would influence the gas, the gas would form a giant molecular cloud with increasing density with time. This is not what happens in the ISM, because gas is constantly ejected due to feedback processes. Feedback comes mainly from stars formed in the ISM and can be in the form of mechanical feedback, as stellar winds and supernova (SN) explosions, and ionizing processes by stellar radiation. The different simulations include different choices of feedback processes, as described later in detail. Additionally, evolved stars produce a diffuse interstellar radiation field (ISRF) which acts to heat the gas. All simulations include a treatment of the attenuation of the diffuse ISRF in units of the Habing field of $G_0 = 1.7$ (Habing, 1968, Draine, 2011, Walch et al., 2015), which is modelled in dense regions with the TREERAY OPTICALDEPTH module (Wünsch et al., 2018) based on the TREECOL algorithm (Clark et al., 2012). Shielding can happen due to the column densities of the total gas, dust, H_2, and CO. Including these processes, the photochemical reaction rates, radiative heating rates, and the dust temperature are calculated.

The different chemical species are treated and evolved during the simulation. The chemical model used in the SILCC simulations is based on Nelson & Langer

(1997) and Glover & Mac Low (2007a,b). The implementation within the SILCC code and further details are well described in Walch et al. (2015). The chemical model is a non-equilibrium chemical network and assumes collisional ionization equilibrium. For every chemical species, that is actively followed within the chemical network, the continuity equation

$$\frac{\partial \rho_i}{\partial t} + \overrightarrow{\nabla}(\rho_i \overrightarrow{v}) = C_i - D_i \tag{2.2}$$

has to be fulfilled (cf. Glover & Mac Low, 2007a, Walch et al., 2015). This equation describes how the density of a chemical species, ρ_i, changes with time, $\frac{\partial \rho_i}{\partial t}$, and due to the spatial movement of the gas, $\overrightarrow{\nabla}(\rho_i \overrightarrow{v})$. The change is requested to be in balance with the con- and destruction of the species. C_i and D_i are the construction and destruction terms, which depend on the density of the different chemical species, the temperature and also the shielding A_V. The code uses operator splitting, which separates the chemical terms from the advection terms. In that manner the continuity equation simplifies to

$$\frac{\partial \rho_i}{\partial t} + \overrightarrow{\nabla}(\rho_i \overrightarrow{v}) = 0, \tag{2.3}$$

and the chemical composition can be calculated with

$$\frac{\partial \rho_i}{\partial t} = C_i - D_i. \tag{2.4}$$

Equation (2.4) results in a set of coupled ordinary differential equations for all actively followed chemical species (Walch et al., 2015).

The network tracks the abundance of seven key species: H_2, H^+, H, CO, ionized carbon (C^+), O and free electrons (e^-). In addition, the amount of silicon is taken as a constant fraction within the gas, but its specific chemical evolution is not modelled. It is assumed to be always ionised. Every cell in the simulation box has a volume density that is the result of the volume density of all chemical species added together. The metallicity in the setup is set to solar metallicity and the total amount of hydrogen, carbon, oxygen and silicon in the gas are fixed. Their fractional abundances relative to hydrogen are listed in Table 2.1, and correspond to the values given in Sembach et al. (2000). Whether one of these species is in molecular, atomic or ionised form, is calculated internally by the chemical network that follows the relevant cooling and heating processes and the thermal evolution of the ISM. Carbon can be present in the form of carbon monoxide (CO) and carbon ions (e.g. C^+). The model follows the formation of CO. Via a single mechanism, C^+ and H_2 react to form CH_2^+, which in turn can either *(i)* react with O to form CO, or *(ii)* it photodissociates and return to C^+. As CH_2^+ is not explicitly followed, this formation mechanism is treated as a single step with a given efficiency. Once CO is formed, it can be destroyed by the interstellar radiation field. The chemical network only follows the explicit evolution of CO, which has to fulfil Eq. (2.4). The fraction of carbon which is not in CO is assumed to be ionized:

$$x_{\mathrm{C,ion}} = x_{\mathrm{C,tot}} - x_{\mathrm{CO}}. \tag{2.5}$$

It is worth noting that $x_{\mathrm{C,ion}}$ represents the ionized fraction of carbon, i.e., all possible ionization states.

The amount of molecular and ionized hydrogen is calculated in the model by taking into account the reaction equations given in Micic et al. (2012). The formation of ionized hydrogen is determined by collisional ionization, ionization by cosmic rays, and X-rays. Its destruction happens due to radiative recombination (Walch et al., 2015). Molecular hydrogen in turn can form within this model on the surface of dust grains. On the other hand it can get destroyed by photodissociation by the interstellar radiation field, by cosmic ray ionization and by collisional dissociation. The chemical network follows the explicit evolution of molecular and ionized hydrogen, which likewise have to fulfil Eq. (2.4). The fractions of molecular and ionized hydrogen are used to derive the fractional abundance of atomic hydrogen via

$$x_{\mathrm{H}} = 1 - 2x_{\mathrm{H_2}} - x_{\mathrm{H^+}}. \tag{2.6}$$

2.2 Simulation setups

2.2.1 SILCC-01: SILCC with fixed SNe

Supernova explosions (SNe) act as a feedback process in the ISM, which stir the gas and which influence its thermo-chemical state. The position of SNe with respect to the dense, molecular gas phase influences the evolution of the ISM dynamically and chemically (Walch et al., 2015, Girichidis et al., 2016b).

In the first setup of SILCC simulations, named as SILCC-01, the acting feedback process is due to the explosions of SNe. The simulations include Type II SNe and Type Ia Sne. Type II SNe result in nature from the core collapse in massive stars and belong to a young population. Type Ia SNe come from white dwarfs, and belong to a rather old stellar population (Tammann et al., 1994). All SNe are expected to eject a thermal energy of $E_{\mathrm{SN}} = 10^{51}$ erg into the gas within a sphere with a radius of the Sedov-Taylor radius. This radius has to be resolved with at least 4 cells. In the simulations the two types of SNe only distinguish by their vertical height, at which the explosion can occur around the midplane. Walch et al. (2015) and Girichidis et al. (2016b) studied how the multi-phase ISM evolves differently when the distribution and the rate of supernovae are changed. A set of their simulations is used in this work. Those are listed in the upper part of Table 2.2. They have the following SN rates and positions:

SN RATE: Assuming a standard Kennicutt–Schmidt relation (Schmidt, 1959, Kennicutt, 1998) and a Chabrier initial mass function (IMF Chabrier, 2001), the fiducial SNR for $\Sigma_{\mathrm{gas}} = 10\,\mathrm{M_\odot/pc^2}$ is $\mathrm{SNR} = 15\,\mathrm{Myr^{-1}}$ within the simulated volume. All runs with that SNR are denoted with *S10–KS*. The error bars on the KS rela-

tion easily allow for variations of a factor of $\sim$ 3, and we explore one run with SNR = 5 Myr^{-1}. This run is called *S10–lowSN–rand*.

SN POSITION: The position of the SNe relative to the dense gas changes how the energy feedback is distributed in the ISM and affects directly the chemical composition of the gas. For runs in which all SNe are correlated with dense gas ('*peak driving*'; run *S10–KS–peak*), the simulations results in less H_2, H^+ and e^-, but more atomic hydrogen. For uncorrelated SNe ('*random driving*'; run *S10–KS–rand* and *S10–lowSN–rand*) molecular clouds can form and survive in the simulations. An ionized, hot, volume-filling phase and a galactic fountain flow, which pushes atomic and ionized gas to large scale heights, are established. '*Mixed driving*' (run *S10–KS–mix*) refers to the case of 50% random and 50% peak driving, while runs with '*clustered driving*' consider the fact that massive stars are born in associations and clusters and therefore, the SN explosions are likely to be spatially correlated. Three runs with clustered driving are considered: In run *S10–KS–clus2* all SNe are correlated type II SNe, whereas in runs *S10–KS–clus* and *S10–KS–clus–mag* we have a small fraction of uncorrelated type Ia SNe that have a larger scale height of 325 pc. The different clustering properties do not change the ISM properties dramatically (cf. Walch et al., 2015). Most of the runs are performed without a magnetic field. Only in run *S10–KS–clus–mag* a magnetic field is included with an initial strength of $B_{\mathrm{init},x} = 3\ \mu$G. It is initialized in x-direction as

$$B_x(z) = B_{\mathrm{init},x}\left(\frac{\rho(z)}{\rho_0}\right). \tag{2.7}$$

All the simulations represent one realization of the simulation setup. They include the relevant physical processes in a self-consistent way. The chosen chemical model assumes collisional ionization equilibrium, which is fine in a setup created like the SILCC setup described above and when the feedback to the gas only results from SNe. If we imagine that the Galaxy is built out of blocks with a lateral edge of 3.9 pc, it could look like one of the simulations. However, if radiative feedback would be taken into account as well, it would be necessary to consider photo-ionization instead of collisional ionization.

The total column density maps of the SILCC-01 simulations are presented in the first seven panels of Fig. 2.1 at an evolutionary time of t = 50 Myr. Regions of dense gas are situated in the midplane of the disc, enveloped by an outflowing component. The run *S10–KS–peak* shows less dense gas in the midplane, and its outflowing gas stays more concentrated around the midplane. The runs *S10–lowSN–rand* and *S10–KS–rand* show more symmetric outflowing components compared to the runs with a clustered distribution of SNe.

We illustrate the distribution of the gas in some of the runs at t = 50 Myr as a function of the gas temperature and total gas number density in Fig 2.2. The colour-coding indicates the fraction of mass. The upper four panels depict the distribution of the gas within the SILCC-01 simulations for the runs *S10–KS–rand*, *S10–KS–peak*, *S10–KS–mix*, and *S10–KS–clus*. We find the distribution of the gas

to be equal for the runs with random, mixed, and clustered distributions of SNe. All of them have a minor mass fraction of gas in the range of low total gas densities ($n_{\rm tot} \leq 10^{-2}$ cm^{-3}) and high temperature ($T \geq 10^4$ K), a prominent mass fraction of gas with $10^{-2}\,{\rm cm}^{-3} \leq n_{\rm tot} \leq 10^{0}\,{\rm cm}^{-3}$ and $T \sim 10^4$ K, and further gas at $n_{\rm tot} \geq 10$ cm^{-3} and $T \leq 100$ K. In contrast to that, the gas in run *S10–KS–peak* has number densities of $n_{\rm tot} \leq 100$ cm^{-3}, giving a hint to the fact, that no molecular gas has formed, in line with the findings of Walch et al. (2015).

It is also worth noting some of the important limitations of the current simulations. While there are no other simulations like the ones presented here in terms of size and resolution and in terms of physical and chemical processes included, they still lack a proper interpretation of:

- self-consistent star formation, which is taken into account as the formation of sink particles in other simulations, and which would reduce the densest parts in the molecular clouds.
- other feedback processes caused by the stars formed within the ISM, like their winds and their radiation field. Therefore we miss the formation of ionized gas (H II regions) around stars.
- the influence of galactic shear, which dynamical affects the gas in galactic discs.
- the evolution of gas on scales smaller than 3.9 pc. Therefore the minimum size of molecular clouds found in the simulations is limited.

The inclusion of other feedback processes may affect the chemistry and therefore requires to review the chemical processes in order to maintain a self consistent picture. Some of the above mentioned limitations are taken into account in new simulation runs described in Sec. 2.2.2 and 2.2.3.

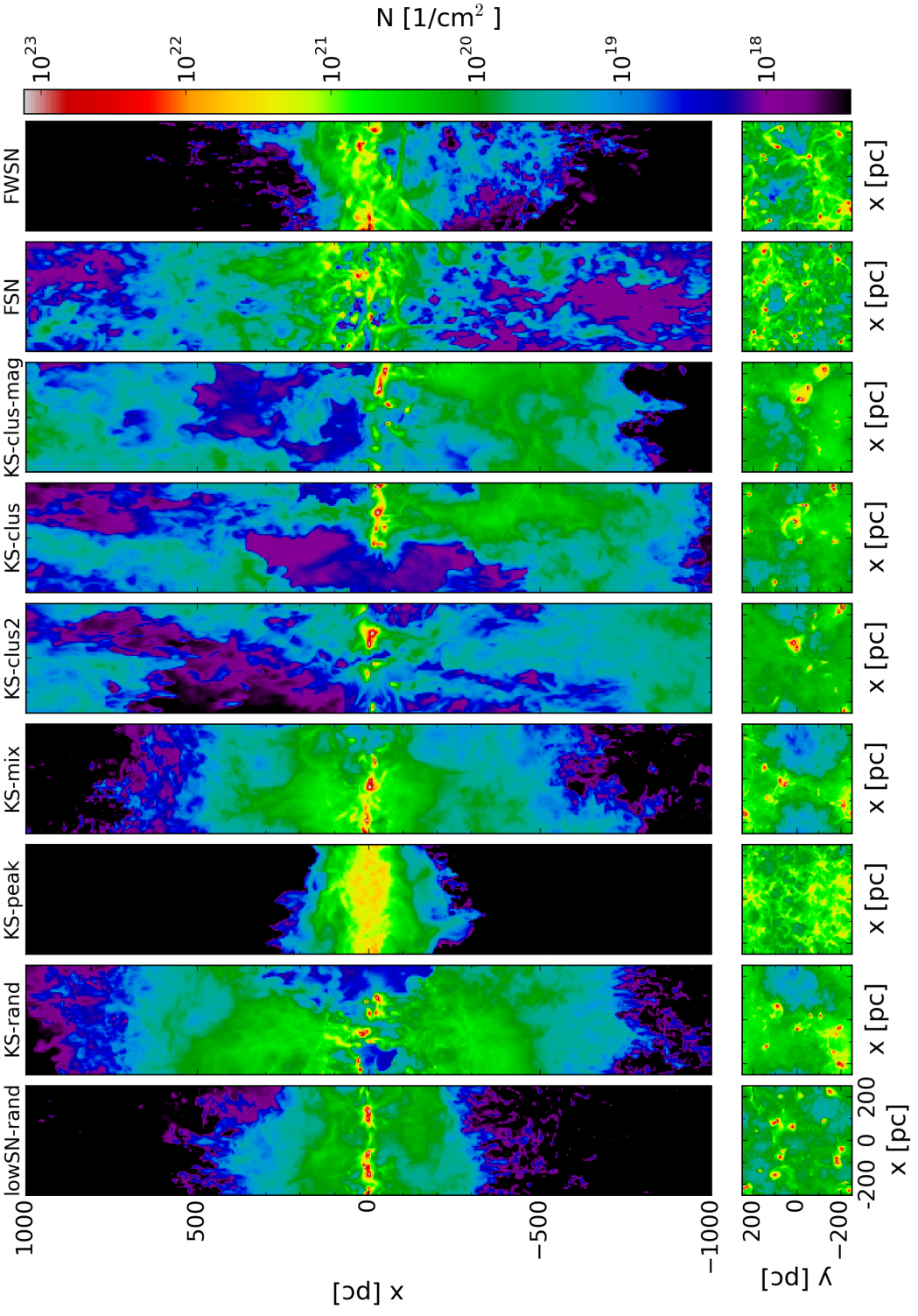

Figure 2.1: Column density maps of the total gas in the SILCC-01 and SILCC-02 simulations. The different panels show the maps for *S10–lowSN–rand*, *S10–KS–rand*, *S10–KS–peak*, *S10–KS–mix*, *S10–KS–clus2*, *S10–KS–clus*, and *S10–KS–clus–mag* at t = 50 Myr, as indicated over the panels, (cf. Walch et al., 2015, Girichidis et al., 2016b) as seen edge-on (top) and face-on (bottom), and for *FSN* and *FWSN* at t = 70 Myr (Peters et al., 2017).

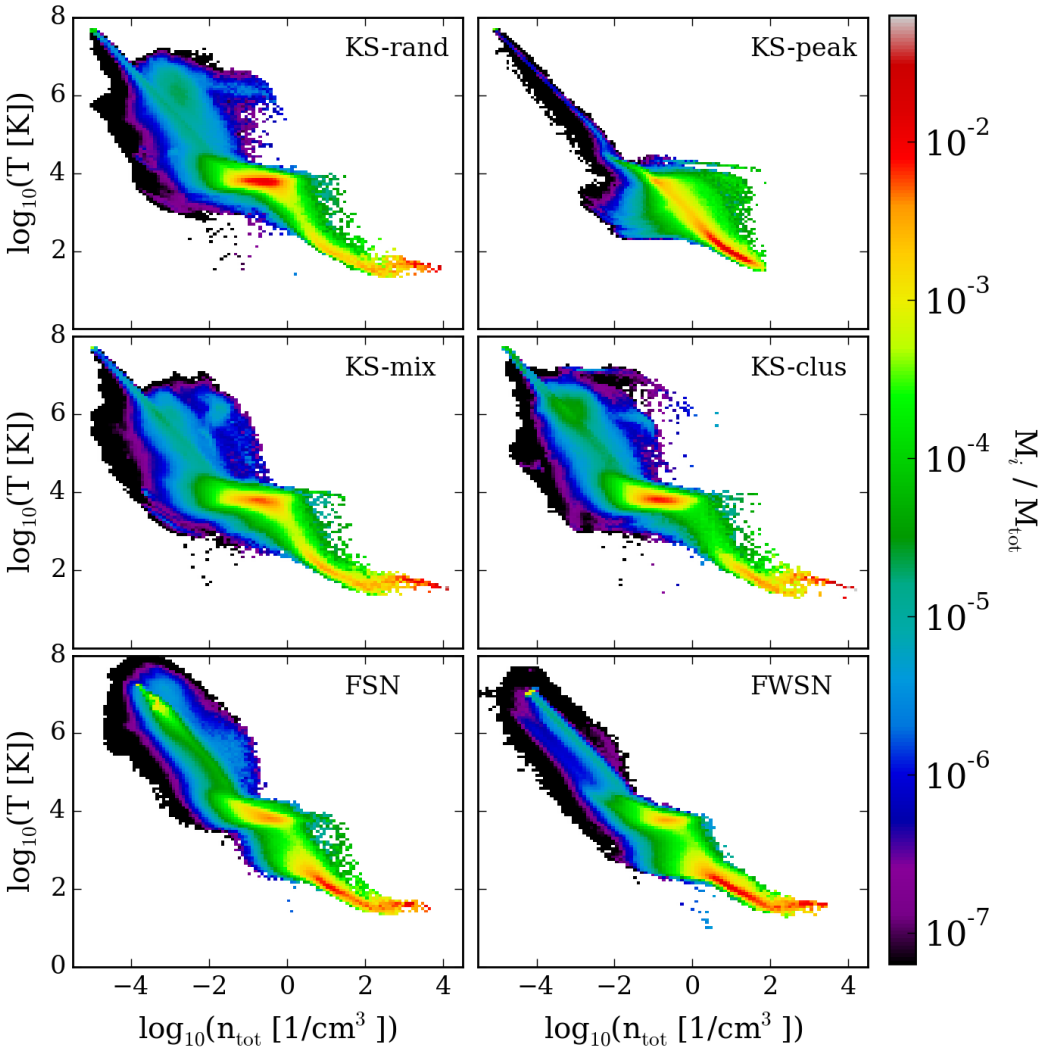

Figure 2.2: Mass weighted two-dimensional histogram showing the gas distribution for some runs in the SILCC simulation, as indicated in the panels. The distribution is presented as a function of the total gas number density and the kinetic gas temperature. The colour-coding indicates the fraction of mass in each simulation. The gas distribution for the SILCC-01 simulations are similar, except for *S10–KS–peak*. The panels in the bottom row show the distribution of the gas for the SILCC-02 simulations. Here we recover in general the distribution from most of the SILCC-01 simulations. The larger the SNR, the larger is the fraction of the gas component at low densities and high temperatures (see Table 2.2).

Table 2.2: List of the analysed SILCC simulations and their initial conditions. SN stands for supernova, G_0 is the scaling for the background UV field following the notation of Habing et al. (1968).

setup	Name	SN rate [Myr^{-1}]	G_0 [Habing field]	SN driving	additional parameters
SILCC-01	*S10–lowSN–rand*	5	0.56	random	
	S10–KS–rand	15	1.70	random	
	S10–KS–peak	15	1.70	peaked	
	S10–KS–mix	15	1.70	mixed	
	S10–KS–clus2	15	1.70	clustered	SNe of type II
	S10–KS–clus	15	1.70	clustered	SNe of type Ia and II
	S10–KS–clus–mag	15	1.70	clustered	SNe of type Ia and II $B_{\rm init} = 3\,\mu$G
SILCC-02	*FSN*	36.0		self-consistent	SNe
	FWSN	3.5		self-consistent	SNe and stellar winds

2.2.2 SILCC-02: Simulations with sink particles

Gatto et al. (2017) and Peters et al. (2017) studied the influence of different stellar feedback processes on the ISM using a SILCC setup. We will call their simulations SILCC-02 in this work. The model is described in Gatto et al. (2017), whereas the simulations are analysed in Peters et al. (2017). They include self-consistent star formation using sink particles in their simulations (Federrath et al., 2010). Their setup differs in the following points from the one described above:

Initially, until an evolutionary time of 30 Myr, turbulent motions are driven in the disc of the ISM. By this Peters et al. (2017) create a complex density structure. Sink particles, which model the formation of stars, start to form after 30 Myr, when the turbulent motions are switched off. Until this time step all their simulations evolve identical. The initial turbulent motions result in a larger vertical distribution of molecular clouds at later time steps. This can be seen in the total gas column density maps, presented for the simulations in the last two panels of Fig. 2.1.

Sink particles represent a cluster of stars instead of individual ones (Federrath et al., 2010). FLASH 4 provides a sink particle unit that is used for the simulations (see Federrath et al., 2010, Gatto et al., 2017, for more details). Whenever the density of one cell becomes larger than the threshold of $\rho_{\rm thr} = 2\times10^{-20}$ g cm^{-3}, one sink particle is formed. Following the description of Federrath et al. (2010), further sink particles are formed when all cells within the accretion radius, $r_{\rm acc}$, are at the highest refinement level, a cell represents a local gravitational potential minimum, the gas within $r_{\rm acc}$ is Jeans unstable, or in a converging flow, or gravitationally bound (Gatto et al., 2017). Gas within the accretion radius of $r_{\rm acc} = 4.5 \times \Delta x = 4.5 \times 3.9\,{\rm pc} = 17.58$ pc and with densities higher than $\rho_{\rm thr}$ is considered to be gravitationally bound to the sink particle and to collapse towards it. Once the mass of the sink particle grows to 120 M$_\odot$, individual stars are formed by randomly choosing a mass of the star following the Salpeter initial mass function (IMF, Salpeter, 1955). This mass can be in the range of 9 to 120 M$_\odot$. New stars are considered to form until the mass of the sink particle is reached.

Stellar feedback from the stars formed within the sink particles affects the evolution of the ISM. This stellar feedback is included in the code following the Geneva stellar evolution track of the individual stars formed within the sink particle (Ekström et al., 2012). The stellar winds are taken into account optionally in the simulations. SNe explosions are no longer considered with a fixed rate and position in the simulation, but occur at the end of the life times of massive stars in a self-consistent way. The simulations we analyse for comparison are listed in the lower part of Table 2.2. The run *FSN* includes only the feedback of SNe, *FWSN* takes in addition stellar winds into account. The SNRs listed in Table 2.2 are calculated as an average over the time between the first SN explosion ($t \sim 36$ Myr) until the end of the simulation ($t \sim 70$ Myr). Since the feedback process sets in later (at $t \sim 30$ Myr) compared to the SILCC-01 simulations, we also analyse here the SILCC-02 simulation at a later evolutionary time, and chose snapshots at $t = 70$ Myr. The column density maps of *FSN* and *FWSN* in the last two columns of Fig. 2.1 show this later

time step.

The distribution of the gas in the runs *FSN* and *FWSN* as a function of total gas number density and kinetic gas temperature are presented in the lower panels of Fig. 2.2. As for most of the SILCC-01 simulations, we find a small mass fraction of the gas mass to be in the range of low number densities ($n_{\rm tot} \leq 10^{-2}$ cm^{-3}), and high gas temperatures ($T \geq 10^4$ K). As the SNR in *FSN* is larger compared to the other simulations (SNR = 36 Myr^{-1}, see Table 2.2), the fraction of gas in this dilute phase is likewise larger for *FSN*. Furthermore, both SILCC-02 simulations show the gas phase with $10^{-2}\,{\rm cm}^{-3} \leq n_{\rm tot} \leq 10^{0}\,{\rm cm}^{-3}$ and $T \sim 10^4$ K, and further a prominent gas mass fraction at $n_{\rm tot} \geq 10$ cm^{-3} and $T \leq 100$ K, as we found for most of the SILCC-01 simulations. However, the maximum gas number densities in the SILCC-02 simulations are ∼5000 cm^{-3} and ∼3000 cm^{-3} for *FSN* and *FWSN*, respectively, and thus smaller compared to e.g. *S10–KS–rand*, where the maximum is ∼9100 cm^{-3}. This is due to the formation of sink particles, which let the dense gas to be converted into sink particles.

2.2.3 Zoom in simulations

Seifried et al. (2017) aim to study the formation of single molecular clouds in more detail within the SILCC-Zoom project. This part is described already in the paper Franeck et al. (2018), which was submitted to MNRAS in May 2018. For this project, they allow the resolution to increase within a certain area of the SILCC box, while keeping the whole simulation box around the simulation. We call this procedure "zoom-in". Keeping the embedding ISM during the process is necessary, since large scale flows are likely to influence the turbulent motions within a molecular cloud. In order to follow the evolution of the molecular cloud from the beginning on, the time at which the zoom-in procedure starts is chosen at a time step at which the density within the considered region is below a few times 10 cm^{-3}. This is the case at $t_0 = 11.9$ Myr. After starting the zoom-in procedure the explosions of the SNe in the simulation are turned off, so that the evolution of the molecular cloud is not further influenced by SN explosions. The initial SN driving ensures that the molecular cloud forms out of a three-phase ISM. The evolution of the simulation is then followed by another 1.5 Myr, in which the resolution is increased stepwise, while at least 200 time steps have to pass before the next resolution level is started (Seifried et al., 2017). For setting up the next resolution level the values of the old grid and the new grid are linearly interpolated to get a smooth transition to the next refinement level. The refinement was started at the level L5 with a cell size of 3.9 pc, and ended at the level L10 with the cell size of 0.122 pc. After reaching the refinement level L10, the simulation is continued at this resolution. The different levels and the resulting cell sizes are summarized in Table 4.3. A detailed description of the whole refinement process can be found in Seifried et al. (2017).

Seifried et al. (2017) simulate the evolution of two molecular clouds within the

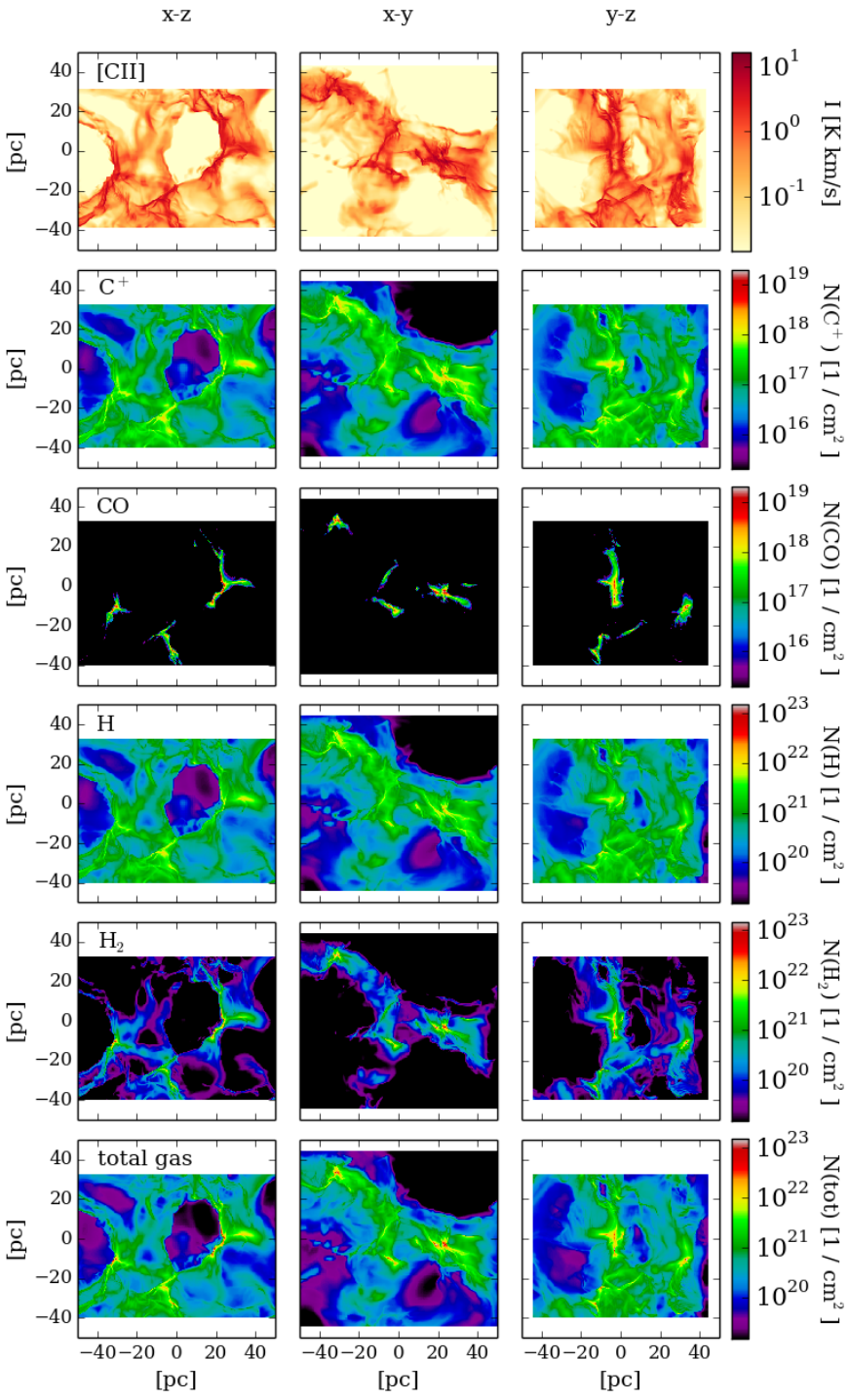

Figure 2.3: Synthetic [^{12}C II] line emission maps and column densities of the total gas and the chemical components for MC2 at $t_{\rm tot}$ = 13.9 Myr for different projections, as indicated above the panels (see Table 2.3). The synthetic [^{12}C II] emission maps are shown in the first row for a better comparison. In the following rows we present the column densities for C^+, CO, H, H_2, and the total gas column density. C^+ and H are present in large parts of the cloud, and only reduced in regions, where CO and H_2 forms. If a drop in the C^+ column density occurs, the [^{12}C II] line emission drops likewise, as it is the case for the centre in the *yz*-projection.

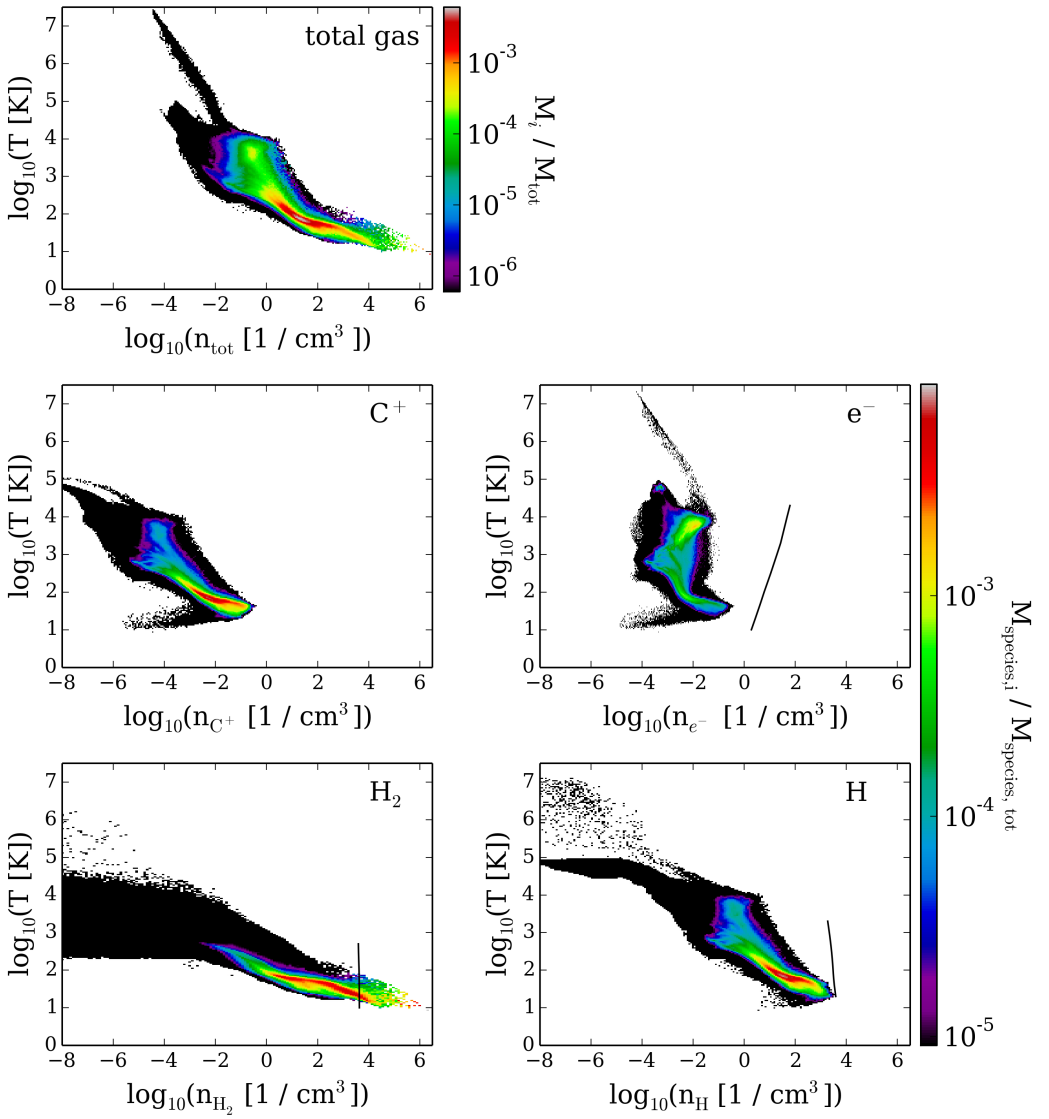

Figure 2.4: Mass-weighted two-dimensional histogram as a function of the kinetic gas temperature T, and the number density. The upper left panel shows the parameter space of the total gas for the total number density, while the four lower panels show the C^+, electron, H_2, and H distributions as a function of their number densities, respectively. The colour-coding indicates the fraction of mass for each presented species. The black lines indicate the critical densities (see Eq. 3.10) as a function of the temperature for each collisional partner. For all collisional partners but H_2, the number densities are below the critical number density. We therefore expect the C^+ ions to be subthermally excited for all gas not dominated by H_2 (see discussion in the end of Section 3.3.2).

Table 2.3: List of the zoom-in simulations by Seifried et al. (2017), their table 1, which were taken for the analysis in this work. It is complemented by the run MMC3, which is a molecular cloud in a simulation including magnetic fields.

run	centre [pc]	volume [pc^3]
MC1	(157, 125, 0)	$87.5 \times 87.5 \times 77$
MC2	(45, 196, 0)	$104 \times 88 \times 71$
MMC3	(-84, 100, 0)	$130 \times 110 \times 110$

run *S10–KS–mix*. We call these simulations "MC1" and "MC2". The centres of the zoom-in region as well as their sizes are summarized in Table 2.3. In general, we carry out the studies presented in this work for the zoom-in simulations on the example of MC2 at an evolutionary time of $t_{\rm tot} = t_0 + 2.0\,{\rm Myr} = 13.9\,{\rm Myr}$. This cloud has a mass-weighted mean velocity dispersion of 4 km s^{-1}, defined for gas with number densities between 30 cm^{-3} and 300 cm^{-3}. In addition, one molecular cloud MMC3 is studied in a setup of a magnetized ISM. In this setup, the magnetic field is initialized in the x-direction of the simulation with a strength of $B_{{\rm init},x} = 3\ \mu{\rm G}$, and scales in the z-direction with the density (see Eq. 2.7). The centre and size of this cloud is likewise listed in Table 2.3.

Figure 2.3 presents the column density maps of the zoom-in simulation MC2 at $t_{\rm tot} = 13.9$ Myr for different projections, as indicated over the panels. Although we carry out the radiative transfer simulations later in Chapter 3, we keep them here in the top panels for a better comparison. The second to sixth rows show the C^+, CO, H, H_2, and the total gas column density of MC2. C^+ is distributed within most parts of the cloud, and only reduced in regions of dense gas (for $N_{\rm tot} \gtrsim 10^{23}$ cm^{-3}), where it is converted to CO. CO needs a high visual extinction to form, and therefore is present only in the dense cores of the cloud. For the hydrogen species we find H_2 likewise in the dense regions of the cloud, but extended over a slightly wider range than CO. Atomic hydrogen forms the envelope of the molecular cloud.

We show the distribution of the gas as a function of the total gas number density and the gas kinetic temperature for MC2 at $t_{\rm tot} = 13.9$ Myr in the upper left panel of Fig. 2.4. MC2 represents a fraction of the SILCC-01 simulation *S10–KS–mix*. Its distribution of the gas was shown in Fig. 2.2 in the middle left panel. We find the distribution of the gas phases to be changed in MC2 compared to the total simulation box. In MC2 there is less gas in the warm, dilute phase. Further, also the gas phase prominent in *S10–KS–mix* with $10^{-2}\,{\rm cm}^{-3} \leq n_{\rm tot} \leq 10^{0}\,{\rm cm}^{-3}$ and $T \sim 10^4$ K has almost disappeared. Instead, a large fraction of the gas in MC2 has densities $n_{\rm tot} \gtrsim 1$ cm^{-3} and $T \lesssim 10^3$ K. Further, the range of gas densities covered in MC2 expanded to $n_{\rm tot} \sim 10^6$ cm^{-3}. The less pronounced phase of warm, dilute gas is a consequence of the turned off SNe within the zoom-ins. The in general higher gas densities are reached due to the contraction of the molecular cloud, and the resolution on smaller scales. The dense parts represent the cores in star-forming regions. Since the zoom-in simulations do not include sink particles and no stellar feedback, they represent an ISM just before the onset of star formation.

The lower four panels of Fig. 2.4 show the distribution of the chemical species as a function of the number density of the species and the gas temperature to give a general idea of the chemical composition of the gas. In Section 3.3.2 we describe the assumptions done for obtaining the number densities. The black lines indicate the critical densities for the collisional partners of C^+ (see Eq. 3.10, Section 3.1). We encourage you to read the next Section, especially Section 3.3.2, for more details.

3

Radiative transfer simulations

This Chapter introduces the method used to calculate the radiative transfer simulations. Note, that part of the content is also included in the paper submitted to MNRAS in May 2018, and printed in December 2018 in Franeck et al. (2018).

3.1 Basic concepts on radiative transfer

Radiation from components of the gas in the ISM can occur due to rotational and vibrational transitions in molecules, as well as electron transitions in ions, atoms or molecules. All of them can be described with the two level model of an upper and lower state. A very good description of these processes can be found in Rybicki & Lightman (1979). This section is based on their descriptions.

The following emission and absorption processes are responsible for the emission and its intensity that we observe:

- Spontaneous emission: light can be emitted by a spontaneous transition from an electron, atom or molecule from an excited energy state u to a lower energy state l. The probability that this transition takes place is described by the Einstein coefficient A_{ul}.
- Absorption: emitted photons can be absorbed by other particles along the line of sight. The Einstein B_{lu} coefficient is used to describe this process with

$$B_{lu}\bar{J}, \tag{3.1}$$

where $\bar{J}$ is the integrated radiation field with $\bar{J} = \int J_\nu \phi(\nu) d\nu$ and $\phi(\nu)$ is the profile function of the emission. The frequency is indicated with ν.

- Stimulated emission: photons of a radiative background field can stimulate the transition of an electron into a lower level. This is described with

$$B_{ul}\bar{J}, \tag{3.2}$$

  with the Einstein coefficient B_{ul}. This process is treated as a negative absorption process in the mathematical description.

The Einstein coefficients satisfy the relations

$$A_{ul} = \frac{2h\nu^3}{c^2} B_{ul} \tag{3.3}$$

and

$$g_l B_{lu} = g_u B_{ul} \tag{3.4}$$

with g_l and g_u as the statistical weights for the lower and the upper state, respectively. c is the speed of light, h the Planck constant, and ν the frequency of the transition. Assuming that each electron, atom or molecule contributes an energy of $h\nu$ over a solid angle of 4π, the spontaneous emission can be expressed as

$$j_\nu = \frac{h\nu}{4\pi} n_u A_{ul} \phi(\nu) \tag{3.5}$$

with n_u as the number density of particles in the upper level. The absorption coefficient consists of the part of the absorption and the stimulated emission, counted as negative absorption:

$$\alpha_\nu = \frac{h\nu}{4\pi} \phi(\nu)(n_l B_{lu} - n_u B_{ul}) \tag{3.6}$$

with n_l as the number density of ions in the lower state.

The intensity at a certain frequency I_ν along a line of sight s is the result from the emission and the absorption processes and can be described with the radiative transfer equation

$$\frac{dI_\nu}{ds} = j_\nu - \alpha_\nu I_\nu. \tag{3.7}$$

Inserting the coefficients for emission and absorption yields to

$$\frac{dI_\nu}{ds} = \frac{h\nu}{4\pi} n_u A_{ul} \phi(\nu) - \frac{h\nu}{4\pi}(n_l B_{lu} - n_u B_{ul})\phi(\nu) I_\nu. \tag{3.8}$$

The result of the radiative transfer equation depends on the numbers of particles in the lower and upper state, the so-called level population. Under the assumption of local thermal equilibrium (LTE), the level population follows the relation

$$\frac{n_l}{n_u} = \frac{g_l}{g_u} \exp\left(\frac{h\nu}{kT_{\mathrm{ex}}}\right). \tag{3.9}$$

If this is fulfilled, the excitation temperature T_{ex} is equal to the kinetic temperature T_{kin} of the gas, since collisions dominate the process of the level population.

If Eq. (3.9) is not fulfilled, the radiative transfer takes place in non-local thermal equilibrium. The collisions between the particles are not sufficient to have an excitation temperature equal to the kinetic temperature. Therefore, the level population is dominated by the effects of radiation, and the effect of collisions has to be considered separately for each collisional partner. This happens in less dense regions of the gas. One can distinguish the regions dominated by LTE by the density of the gas. In gas with a density below a critical density $n_{\rm crit}$, the radiative transfer is dominated by radiation, while above $n_{\rm crit}$ the collisions are sufficient so that $T_{\rm ex} = T_{\rm kin}$ (Tielens & Hollenbach, 1985, Draine, 2011). The critical density is defined as

$$n_{\rm crit} = \frac{A_{ul}}{R_{\rm ul}^{\rm cp}}, \tag{3.10}$$

with A_{ul} as the Einstein coefficient of the transition, and $R_{\rm ul}^{\rm cp}$ as the de-excitation coefficient of the collision. Since $R_{\rm ul}^{\rm cp}$ differs for each collisional partner and as a function of temperature, each collisional partner has its own critical density $n_{\rm crit}$.

3.2 Transition in carbon ions

The carbon ion has two isotopes, namely $^{12}C^+$ and $^{13}C^+$, with a standard isotopic ratio of $^{12}C^+/^{13}C^+ = 67$ (Wakelam & Herbst, 2008). Both ions have transition lines that can be observed in the ISM. The $^{12}C^+$ is seen by its fine structure transition [^{12}C II]. For $^{13}C^+$ the fine structure transition line splits into three hyperfine structure transition lines (see Fig. 3.1). We describe here shortly the radiative transitions in the C^+ ions. The explanation presented here can be complemented with more details in Haken & Wolf (2003) and Draine (2011). We use quantum numbers to describe the state of an atom or ion.

3.2.1 Fine structure transition of $^{12}C^+$

The coupling of the spin of electrons and the orbital angular momentum in atoms or ions lead to a splitting of the energy levels. A transition between those states is what we name as a fine structure transition. The spin **s** of an individual electron can be described by the quantum number s, and the orbital angular momentum **l** with the quantum number l. The resulting total spin angular momentum for the whole atom or ion is $\mathbf{S} = \Sigma \mathbf{s}_i$, with the corresponding quantum number S, and for the total angular momentum we obtain $\mathbf{L} = \Sigma \mathbf{l}_i$ and L. For describing the total electronic angular momentum one uses

$$\mathbf{J} = \mathbf{L} + \mathbf{S}. \tag{3.11}$$

The coupling between L and S is what is known as fine structure splitting. The quantum number J can have values between $J = L - S$ and $J = L + S$. The status of

Table 3.1: Frequencies of the [^{12}C II] fine structure and [^{13}C II] hyperfine structure lines for the transition $^2P_{3/2} \rightarrow {}^2P_{1/2}$. The fourth column lists the relative intensities of the hyperfine structure lines, and the fifth the spectral difference from the [^{12}C II] line emission.

line	$F - F'$	ν [GHz]	rel. Int.	$\Delta v(\nu_{[^{12}\mathrm{CII}]} - \nu_{[^{13}\mathrm{CII}],x})$ [km s^{-1}]
[^{12}C II]		1900.537	1	
[^{13}C II]	2 – 1	1900.466	0.625	11.2
[^{13}C II]	1 – 0	1900.950	0.250	-65.2
[^{13}C II]	1 – 1	1900.136	0.125	63.2

the particle is described in the notation by

$$^{2S+1}L_J. \tag{3.12}$$

The electron configuration of a carbon ion can be described by the configuration of Helium and three additional electrons: $1s^2 2s^2 2p^1$ (Draine, 2011). Thus, there are three valence electrons. Two of the electrons are in s-shell, and one is left on the p-shell. For the fine structure transition the one electron in the p-shell is important. The orbital angular momentum of the ion is $L = 1$ (P-state). The spin of the electron is $S = 1/2$, and therefore, the total angular momentum J can have two possible values, namely 1/2 and 3/2, with the statistical weights $g_l = 2$ and $g_u = 4$, respectively. The splitting of the energy levels is illustrated in Fig. 3.1. The transition between the two J-states for the level $n = 2$ is what we observe as the fine structure transition in C^+:

$$^2\mathrm{P}_{3/2} \rightarrow {}^2\mathrm{P}_{1/2} \tag{3.13}$$

This transition takes place at $\nu_{[^{12}\mathrm{CII}]} = 1900.5$ GHz ($\lambda_{[^{12}\mathrm{CII}]} = 157.741\ \mu$m) and is named [^{12}C II] line emission. The Einstein coefficient for this transition is $A_{ul} = 2.3 \times 10^{-6}$ s^{-1} (Mendoza, 1983, Wiese & Fuhr, 2007).

3.2.2 Hyperfine structure transition of $^{13}C^+$

The atomic nucleus of the isotope $^{13}C^+$ has one more neutron in the nucleus compared to $^{12}C^+$. Therefore, nuclear spin described by the mechanical angular momentum quantum number I is no longer $I = 0$ as it was the case for $^{12}C^+$, but has the value $I = 1/2$. The electrons in the ion generate a magnetic field at the nucleus, which interacts with the spin of the nucleus. Therefore, the angular momenta of the electrons and the nucleus are coupled. This can be expressed with the total angular momentum $\mathbf{F}$ as

$$\mathbf{F} = \mathbf{I} + \mathbf{J}, \tag{3.14}$$

and the corresponding quantum number F can have the values ranging from $F = J - I$ until $J + I$. As illustrated in Fig. 3.1, the upper level of $J = 3/2$ splits into

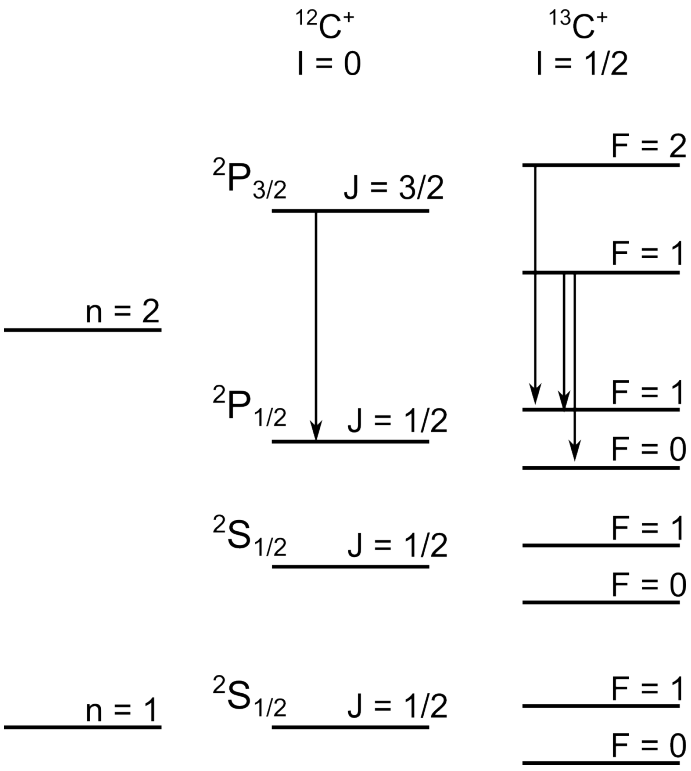

Figure 3.1: Energy scheme of the C^+ ion, showing the fine structure splitting of the levels in $^{12}C^+$, and a further hyperfine structure splitting in $^{13}C^+$. Hyperfine splitting occurs, if the nuclear spin is $I \neq 0$.

two hyperfine levels for $^{13}C^+$, in which F can be $F = 1$ or $F = 2$. The lower level with $J = 1/2$ splits into the hyperfine levels with $F = 0$ and $F = 1$. The transitions between the hyperfine structure levels in $^{13}C^+$ as well as their relative intensities (Ossenkopf et al., 2013) are summarized in Table 3.1. We take the isotopic ratio of 67 (Wakelam & Herbst, 2008) and the relative intensity of the [^{13}C II] ($F = 2 - 1$) line into account to mimic the number density of $^{13}C^+$ by scaling down the number density of $^{12}C^+$ as

$$\begin{aligned} n_{^{13}C^+} &= n_{^{12}C^+} \cdot \frac{0.625}{67} \\ &\approx n_{^{12}C^+} \frac{1}{107}. \end{aligned} \tag{3.15}$$

3.3 Radiative transfer with RADMC-3D

3.3.1 Implementation and assumption in RADMC-3D

We post-process the simulations described in Section 2 using the radiative transfer code RADMC-3D (Dullemond et al., 2012) [1] (version 0.35 and version 0.40). A 2D version of the code is described in Dullemond & Dominik (2004).

RADMC-3D uses the notation of van der Tak et al. (2007) to calculate internally the emission and absorption coefficients, and assumes that the profile functions for the emission and absorption are equal (complete redistribution). For the profile function ϕ a co-moving profile function $\tilde{\phi}$ around the line center frequency ν_{ul} is inserted, as

$$\tilde{\phi}_{ul} = \frac{c}{a_{\rm tot}\nu_{ul}\sqrt{\pi}} \exp\left\{-\frac{c^2(\nu-\nu_{ul})^2}{a_{\rm tot}^2\nu_{ul}^2}\right\}. \tag{3.16}$$

In this notation $a_{\rm tot}$ is the total linewidth. It is composed out of a thermal contribution $a_{\rm therm} = \sqrt{\frac{2k_{\rm B}T}{\mu m_{\rm H}}}$ and a turbulent linewidth $a_{\rm turb}$, so that

$$a_{\rm tot} = \sqrt{a_{\rm therm}^2 + a_{\rm turb}^2}. \tag{3.17}$$

T denotes the kinetic temperature, k_B the Boltzmann constant and $m_{\rm H}$ is the mass of the hydrogen atom. μ is the molecular weight of the emitting particle, which we set to $\mu = 12$ for the C^+ ion.

For solving the radiative transfer equation with its emission and absorption coefficients, the fractional level population for the upper and lower level (x_u and x_l) has to be calculated. Multiplying them with the number density of the carbon ions, gives the number densities of C^+ in the upper and lower state, as $n_u = x_u n_{C^+}$ and $n_l = x_l n_{C^+}$, which is used in the Equations (3.5) and (3.6). We consider the level population of C^+ not to be in local thermal equilibrium, as a large fraction of the gas is present as dilute medium. The level population under this conditions is calculated with the large velocity gradient approximation (LVG, Sobolev, 1957, Ossenkopf, 1997, Shetty et al., 2011a), which is also known as the Sobolev approximation. In that approximation the absolute value of the velocity gradient $|\nabla \mathrm{v}|$ is used to calculate an optical depth. In the local formulation of van der Tak et al. (2007) this can be written as

$$\tau_{ul}^{\rm LVG} = \frac{ch}{4\pi}\frac{n_{C^+}}{1.064|\nabla \mathrm{v}|}\left(x_l B_{lu} - x_u B_{ul}\right). \tag{3.18}$$

The optical depth τ_{ul} is used to calculate an escape probability β_{ul}. RADMC-3D calculates the escape probability as

$$\beta_{ul} = \frac{1-e^{-\tau_{ul}}}{\tau_{ul}}, \tag{3.19}$$

[1] http://www.ita.uni-heidelberg.de/~dullemond/software/radmc-3d/

(Sobolev, 1957, van der Tak et al., 2007). This is an assumption for a different geometry, but, however, used in RADMC-3D. For a further discussion we refer to Ossenkopf (1997). With β_{ul} the line integrated mean intensity is calculated as

$$J_{ul} = (1 - \beta_{ul}) S_{ul} + \beta_{ul} J_{ul}^{\mathrm{bg}}, \tag{3.20}$$

where S_{ul} is the source function as

$$S_{ul} = \frac{j_\nu}{\alpha_\nu}, \tag{3.21}$$

and J_{ul}^{bg} denotes the background radiation field at the rest frequency. We neglect the background radiation field J_{ul}^{bg} in our RADMC-3D calculations, since at the frequency of the [C II] line emission the continuum background radiation is low (Draine, 2011), and further, in observations the continuum background is subtracted.

For calculating the level population of C^+, we need further the collisional rates for C^+ with its collisional partners. The de-excitation rates are tabulated in the Leiden Atomic and Molecular Database (LAMDA, Schöier et al., 2005), and we extrapolate them to higher temperatures with the fits by Goldsmith et al. (2012), as described later. The de-excitation rates $R_{\mathrm{ul}}^{\mathrm{cp}}$ are used to calculate the rate coefficient C_{ul} per C^+ ion as

$$C_{ul} = \sum_{\mathrm{cp}} n_{\mathrm{cp}} R_{\mathrm{ul}}^{\mathrm{cp}}, \tag{3.22}$$

where n_{cp} is the number density for each collisional partner. From that the excitation rate for the upward transition C_{lu} is calculated as

$$C_{lu} = C_{ul} \frac{g_u}{g_l} e^{-\frac{\Delta E}{k_B T}}, \tag{3.23}$$

where g_u and g_l are the statistical weights, and k_B is the Boltzmann constant.

The level population is then obtained by solving the statistical equilibrium, for which the Einstein coefficients A_{ul}, B_{ul} and B_{lu} as well as the collisional rates C_{ul} and C_{lu} are needed. For the fine structure transition of the C^+ ion with the two levels u and l this can be written as

$$-\left[x_u A_{ul} \beta_{ul} + (x_u B_{ul} - x_l B_{lu}) \beta_{ul} J_{ul}^{\mathrm{bg}}\right] + [x_l C_{lu} - x_u C_{ul}] = 0. \tag{3.24}$$

The escape probability β_{ul} changes with the level population, so that the Equations (3.19) and (3.24) have to be solved iteratively.

Within the RADMC-3D simulations it might be that the co-moving line width becomes narrower than the Doppler shift. In those cases it can happen that some of the velocity channels do not contribute to the emission. This is a numerical artefact called Doppler-jump, and does not occur in nature. RADMC-3D provides a Doppler-catching method (Pontoppidan et al., 2009), that ensures a smooth behaviour of the emission in neighbouring velocity channels (see Shetty et al., 2011a,b). We use this module for our RADMC-3D calculations.

3.3.2 Input parameters for RADMC-3D

RADMC-3D needs as input parameters the kinetic temperature, the velocity of the gas, the number density of C^+ and its collisional partners as well as the collisional data for C^+ and the microturbulence for every cell to solve the radiative transfer equation. From the SILCC simulations and the zoom-in simulations we can directly get the gas velocity and the temperature. For the other parameters we need to make some assumptions that we describe now.

Number densities

Within the SILCC simulations the mass fractions $i_{\rm species}$ of the hydrogen species and the carbon species are calculated. They are normalized in a way that the sum over all mass fractions is 1. The fractional abundances $x_{\rm species}$ mentioned above and the mass fractions $i_{\rm species}$ are related by

$$x_{\rm species} = i_{\rm species}/\mu_{\rm species}, \tag{3.25}$$

whereas $\mu_{\rm species}$ is the molecular weight of the certain species. The chemical network takes into account hydrogen species (H_2, H, H^+), carbon species (CO, C^+), and further oxygen and silicate as a constant fraction. In addition, the gas of the ISM consist also of helium. Its evolution is not followed by the SILCC simulations, and therefore also not included in the mass fractions of $i_{\rm species}$, but for the post-processing simulations the number densities have to be normalized to account for the fraction of helium. The number densities are therefore correctly calculated by

$$n_{\rm species} = i_{\rm species}\rho/(\mu_{\rm species}{\rm au})/a, \tag{3.26}$$

where ρ is the density of the gas, au is the atomic weight of 1.66×10^{-24} g and a is the normalization factor given by

$$a = (1. + x_{\rm He}\mu_{\rm He} + x_{\rm C}\mu_{\rm C} + x_{\rm O}\mu_{\rm O}) \approx 1.4 \tag{3.27}$$

with the fractional abundances $x_{\rm He}$, $x_{\rm C}$, $x_{\rm O}$ for helium, carbon and oxygen as listed in Table 2.1 and their specific weights $\mu_{\rm He} = 4$, $\mu_{\rm C} = 12$ and $\mu_{\rm O} = 16$.

To obtain the number densities we use for the RADMC-3D simulations, we make further assumptions:

$n_{\rm C^+}$: In the simplified chemical model all ionized carbon is accounted to be C^+, and higher ionization states are not considered. However, in gas warmer than $T \sim 20\,000$ K carbon can be in higher ionization states. We assume that the gas is in collisional ionization equilibrium (CIE) for temperatures higher than $T > 20\,000$ K, and multiply the number density of C^+ with an ionization correction factor (ICF), according to Sutherland & Dopita (1993, fig. 3 therein). For temperatures $T > 200\,000$ K, all carbon is in higher ionization states and therefore $n_{\rm C^+}$ is set to zero. The number densities of singly ionized carbon from the SILCC simulation *S10–KS–rand* after 50 Myr before and after post-processing are shown in Fig 3.2.

$n_{\rm H}$: For the atomic hydrogen we can take the number densities directly from the simulations.

$n_{\rm H_2}$: The number density of molecular hydrogen we likewise get from the simulations. However, for the collisional partners of C^+ we distinguish between ortho-H_2 and para-H_2, which differ in their nuclear spin states. For ortho-H_2, the spins of the two nuclei are parallel, so that $I = 1$, whereas for para-H_2, the spins are antiparallel and $I = 0$. At high temperatures and densities many different rotational levels are populated, and the equilibrium ortho-to-para ratio is 3:1, according to the statistical weights ($g_I = 2I + 1$). At low temperatures ($T \leq 155$ K), only the $J = 0$ and $J = 1$ levels are populated. In this case, the ortho-to-para ratio is given by Rachford et al. (2009)

$$\frac{n(\text{ortho–}H_2)}{n(\text{para–}H_2)} = 9 \cdot e^{-171\,\text{K}/T_{\rm rot}}, \tag{3.28}$$

with $T_{\rm rot}$ as the rotational temperature in K. For our calculations we set $T_{\rm rot} = T_{\rm kin}$. However, the collisional rates for ortho-and para-H_2 are similar and distinguishing between these two collisional partners has only a negligible influence on the [C II] line emission. Therefore, also the rough estimate for the temperatures is sufficient for our purpose.

n_e: The gas in the simulations is assumed to be electrically neutral. This implies that the number density of free electrons is balances by the total number density of ions. In the chemical model ions are included as H^+ and C^+, and we expect them to dominate the scale of interest in our simulations. Spoken in abundances, there is in general more H^+ in the simulations than C^+. However, in cold gas the abundance of H^+ is low, and there C^+ provides most of the free electrons. With these considerations we calculate the number density of electrons as

$$n_e = n_{\rm H^+} + n_{\rm C^+}. \tag{3.29}$$

We come back to Fig. 2.4, which shows in the lower four panels the distribution of C^+, electrons, H_2, and H for the zoom-in simulation MC2. The last three ones are the collisional partners of C^+. The black lines indicate the temperature dependent critical number density for each collisional partner, as defined in Eq. (3.10). We find the number densities of electrons and H to be lower than $n_{\rm crit}$, while the number density of H_2 can be larger than $n_{\rm crit}$. Thus, we expect the C^+ ions to be subthermally excited for all gas not dominated by molecular hydrogen.

Collisional rates

For the assumed collisional partners of ortho-H_2, para-H_2, H and e^- for C^+ (Goldsmith et al., 2012), Leiden Atomic and Molecular Database (LAMDA, Schöier et al., 2005) lists the de-excitation rates for $R_{\rm ul}^{\rm o\text{-}H_2}$ and $R_{\rm ul}^{\rm p\text{-}H_2}$ (Wiesenfeld & Goldsmith, 2014), $R_{\rm ul}^{\rm H}$ (Barinovs et al., 2005) and $R_{\rm ul}^{e^-}$ (Wilson & Bell, 2002). Since the temperatures in the simulations can exceed the temperatures listed in LAMDA,

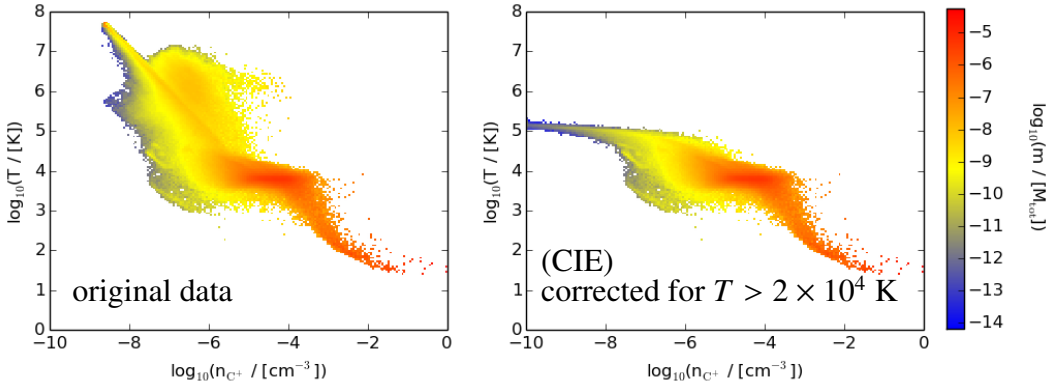

Figure 3.2: Mass distribution of C^+ ions, obtained directly from the SILCC simulation *S10–KS–rand* at $t = 50$ Myr (left) and corrected for the effects of collisional ionization at $T > 20\,000$ K, as detailed in Section 3.3.2 (right). Above $T > 10^5$ K most of the carbon is expected to be in higher ionization states.

we use the extrapolations by Goldsmith et al. (2012). In Fig. 3.3 we present the de-excitation rates including the extrapolation to higher temperatures. In the following, we describe our extrapolations based on Goldsmith et al. (2012):

R(H): The Leiden database lists the collisional rates for atomic hydrogen by Barinovs et al. (2005) for temperatures up to $T_{\rm kin} \leq 2\,000$ K. The data for temperatures within 20 K $\leq T_{\rm kin} \leq 2\,000$ K were fitted by Goldsmith et al. (2012) that found the relation between the coefficients and the kinetic temperature as

$$R_{\rm ul}({\rm H}) = 7.6 \times 10^{-10} \left(\frac{T_{\rm kin}}{100\,{\rm K}} \right)^{0.14} {\rm cm^3 s^{-1}}. \tag{3.30}$$

To extrapolate the de-excitation rates to temperatures $T > 2\,000$ K, we use this relationship.

$R(H_2)$: The Leiden database lists the de-excitation rate coefficients for molecular hydrogen by Wiesenfeld & Goldsmith (2014) up to temperatures of $T_{\rm kin} \leq 500$ K, distinguished for ortho- and para-H_2. For higher temperatures there is no good fit for the coefficients of the two spin states of hydrogen. However, we do expect the effect of collisions with molecular hydrogen to be negligible for $T_{\rm kin} \geq 500$ K, as the amount of H_2 in gas with these temperatures is very low in the simulations ($\sim 0.1\%$ of the total H_2 mass in the zoom-in simulations). We therefore assume in gas with $T_{\rm kin} \geq 500$ K that the collisional rate coefficients for ortho- and para-H_2 have the same values as for $T_{\rm kin} = 500$ K.

$R(e^-)$: For electrons the Leiden database lists the rate coefficients by Wilson & Bell (2002) for temperatures $T_{\rm kin} \leq 20\,000$ K. Goldsmith et al. (2012) find the following fit to the data,

$$R_{ul}(e^-) = 8.7 \times 10^{-8} \left(\frac{T_{\rm e}}{2000\,{\rm K}} \right)^{-0.37} {\rm cm^3 s^{-1}}, \tag{3.31}$$

that we use to extrapolate the rates to higher temperatures. For our purpose, we replace the electron temperature T_e with the kinetic temperature $T_{\rm kin}$.

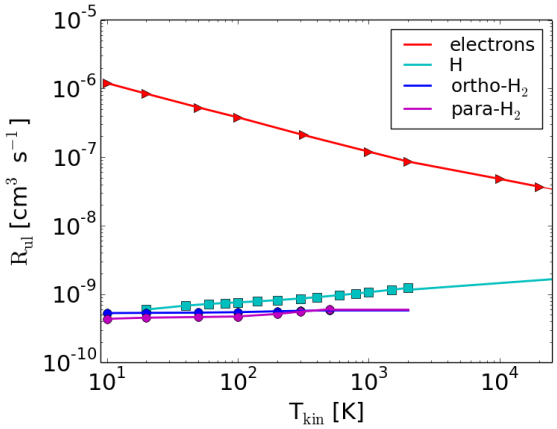

Figure 3.3: Summary of the collisional de-excitation rates for the different collisional partners of C^+ as a function of the kinetic temperature T_{kin}. The rates for the electrons, atomic hydrogen and ortho- and para-molecular hydrogen (red triangles, green squares and blue and magenta circles, respectively) are taken from the Leiden database (Schöier et al., 2005). To cover the full temperature range present in the simulations, we interpolate these database rates and extrapolate them towards higher temperatures. For both ortho- and para-H_2 we take the last value of the de-excitation coefficients given in the database at $T = 500$ K for higher temperatures.

Table 3.2: List of the spectral and spatial resolution, dv and dx, respectively, used in the different simulations.

Simulation	velocity range [km s^{-1}]	number of channels	dv [km s^{-1}]	dx [pc]
SILCC-01	±70	145	0.97	3.9
SILCC-02	±70	145	0.97	3.9
zoom-in simulations	±20	401	0.10	0.122

Microturbulence

If not stated differently, we set the microturbulence in the simulations similar to the kinetic turbulence, so that $a_{\rm turb} = a_{\rm therm}$. We test how the synthetic [C II] emission maps change, when $a_{\rm turb}$ is set to $a_{\rm turb} = x \times a_{\rm therm}$, while we vary x between 0 and 10. This we test with the SILCC-01 setup (Section 4.1.2). A further way of introducing a microturbulence is given by the work of Larson (1981). According to his work, eq. (20) therein, the microturbulence can be estimated by the length of interest L, as

$$\frac{a_{\rm turb}}{\rm km\,s^{-1}} = 1.1 \times \left(\frac{L}{\rm pc} \right)^{0.38} . \tag{3.32}$$

We use for L the size of the gird cell from the AMR grid, and test the influence of this microturbulence to the synthetic [^{12}C II] emission maps for the zoom-in simulation MC2.

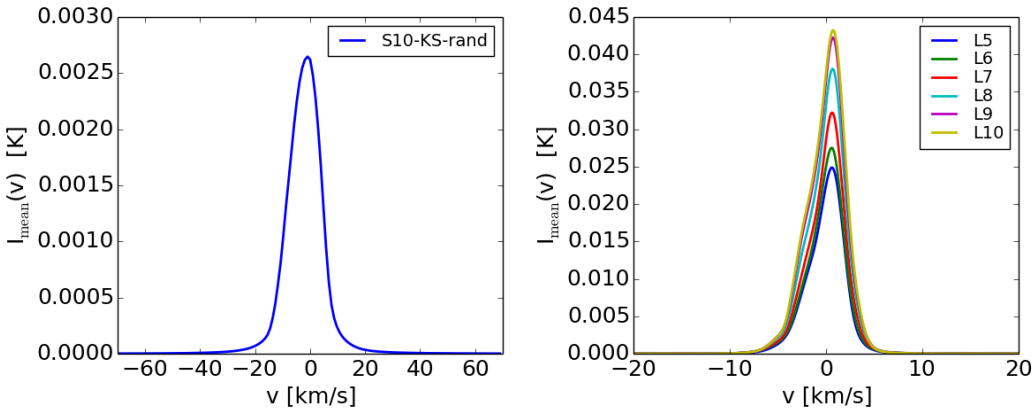

Figure 3.4: Averaged [^{12}C II] spectrum of the SILCC-01 setup at the example of the simulation *S10–KS–rand* (left) and for the zoom-in simulations at different resolutions (right). The velocity ranges are sufficient to cover the total [C II] line emission in both cases.

Resolution of the RADMC-3D simulations

The radiative transfer simulations are carried out with a grid resolution corresponding to the cell size of the highest resolution level in the used simulation, which is 3.9 pc for SILCC-01 and SILCC-02, and 0.122 pc for the zoom-ins (see Table 3.2). The code solves the radiative transfer equation for each pixel by integrating the intensity of the emission I_ν at a given frequency ν along each given line of sight.

For the spectral resolution we chose a velocity range of ±70 km s^{-1} for SICC-01 and SILCC-02 with 145 equally distributed channels, and of ±20 km s^{-1} for the zoom-ins, with 401 channels. Thus, we obtain spectral resolutions of dv = 0.97 km s^{-1} and dv = 0.10 km s^{-1} for the SILCC-01 and SILCC-02 and for the zoom-in simulations, respectively. Figure 3.4 shows the averaged [C II] spectra for an example of the SILCC-01 simulation setup (left panel) and the zoom-in simulation (right panel). This proves, that the velocity range is sufficient to cover the emission.

3.3.3 Output of RADMC-3D

We carry out the radiative transfer simulations with RADMC-3Dby taking into account all collisional partners simultaneously. For every velocity channel we obtain a synthetic emission channel map in units of [erg / (s sr Hz cm^2)]. These intensities can be converted into intensities in [K] (temperatures) using the Planck function in the Rayleigh-Jeans limit ($h\nu \ll k_B T$), which is

$$B_\nu(T) = \frac{2k_B T}{\lambda^2} \tag{3.33}$$

with the Boltzmann constant k_B. Rearranging to T, that we will call now $I_{\rm lp}$ [K], gives the connection between the intensity in [K] and [erg / (s sr Hz cm^2)], the

former called B_ν, by

$$\left(\frac{I_{\rm lp}}{\rm K}\right) = \left(\frac{\lambda}{\rm cm}\right)^2 \left(\frac{\rm erg\ K^{-1}}{2k_B}\right)\left(\frac{I_{\rm lp}}{\rm erg/(s\ Hz\ sr\ cm^2)}\right) \tag{3.34}$$

Throughout this work, $I_{\rm lp}$ denotes the intensity as as a function of the velocity channel, forming the line profile. Since it is more common for observers to express intensities in Kelvin, we will use both notations for the intensities in this work. From the line profiles, which is the intensity along the chosen velocity range, the integrated intensity I can be calculated, as well as the centroid of the line (first moment, $\bar{v}$) and the width of the line (second moment, σ).

Calculating the integrated intensity

To obtain from the synthetic emission channel cubes an integrated intensity I, we either integrate the individual intensity $I_{\rm lp}$ over the frequency, resulting in maps of units of [erg / (s sr cm^2)],

$$\left(\frac{I}{\rm erg/(s\ sr\ cm^2)}\right) = \int \left(\frac{I_{\rm lp}}{\rm erg/(s\ Hz\ sr\ cm^2)}\right)\frac{{\rm d}\nu}{\rm Hz} \tag{3.35}$$

or over the velocity, resulting in maps with units of [K km s^{-1}]

$$\left(\frac{I}{\rm K\ km\ s^{-1}}\right) = \int \left(\frac{I_{\rm lp}}{\rm K}\right)\frac{{\rm dv}}{\rm km\ s^{-1}}. \tag{3.36}$$

A simplified formula is given by Goldsmith et al. (2012) for directly converting the units of the [C II] integrated intensities via

$$\left(\frac{I}{\rm K\ km\ s^{-1}}\right) = 1.43 \cdot 10^5 \cdot \left(\frac{I}{\rm erg/(s\ sr\ cm^2)}\right). \tag{3.37}$$

The conversion between the intensity units [erg / (s sr cm^2)] and [K km s^{-1}] is not linear, because equally distributed velocity bins are not equally distributed in frequency. If two colour bars are plotted for the integrated intensity, the colour-coding gives the integrated intensity in units of [erg / (s sr cm^2)], and the second colour bar in units of [K km s^{-1}] aims for guiding the eye.

The integrated intensity over the whole map can be used to calculate the luminosity. For this we express the size of a pixel p in steradians $p_{\rm sr}$ with

$$p_{\rm sr} = \left(\tan^{-1}\left(\frac{p}{d}\right)\right)^2, \tag{3.38}$$

where we chose an arbitrary distance d, and insert both in the same unit, for which we chose [cm]. Taking into account the conversion of the units of the integrated intensity in [erg / (s sr cm^2)] to Joule by the factor 10^{-7}, we use the following relation to calculate the luminosity in [W]:

$$\left(\frac{L}{\rm W}\right) = 4\pi\left(\frac{d}{\rm cm}\right)^2 \left(\frac{I_{\rm tot}}{\rm erg/(s\ sr\ cm^2)}\right)\left(\frac{p_{\rm sr}}{\rm sr}\right) \times 10^{-7} \tag{3.39}$$

where $I_{\rm tot}$ denotes the sum of the integrated intensity over all pixels in the map.

Calculating the centroid of the line profile

For obtaining the centroid $\bar{v}_{lp}$ of the line in units of [km s^{-1}], we use the line profile in units of [K]. We derive it by

$$\left(\frac{\bar{v}_{lp}}{\mathrm{km\ s^{-1}}}\right) = \int \left(\frac{I_{lp}}{\mathrm{K}} \frac{v}{\mathrm{km\ s^{-1}}} \frac{dv}{\mathrm{km\ s^{-1}}}\right) \cdot \frac{\mathrm{K\ km\ s^{-1}}}{I} \tag{3.40}$$

Calculating the width of the line profile

Likewise for calculating the width σ_{lp} in units of [km s^{-1}] of the line profiles, we use the line profile in units of [K]. Here, we calculate

$$\left(\frac{\sigma_{lp}}{\mathrm{km\ s^{-1}}}\right) = \left(\int \frac{I_{lp}}{\mathrm{K}} \left(\frac{v - \bar{v}}{\mathrm{km\ s^{-1}}}\right)^2 \frac{dv}{\mathrm{km\ s^{-1}}} \cdot \frac{\mathrm{K\ km\ s^{-1}}}{I}\right)^{1/2} \tag{3.41}$$

3.4 Synthetic [C II] emission maps

We calculate the synthetic [^{12}C II] and [^{13}C II] line emission maps with the assumptions described above. Before analysing the [C II] line emission, we here present the synthetic [^{12}C II] emission maps for the SILCC-01, SILCC-02, and zoom-in simulation.

In Fig. 3.5 we show the synthetic [^{12}C II] emission maps of the simulations with a fixed supernova rate in the first seven columns. The total luminosities of the synthetic [^{12}C II] and [^{13}C II] line emission maps, as well as the peak integrated intensities in each map are summarized in Table 3.3. As pointed out by Walch et al. (2015) and Girichidis et al. (2016b) the chemical evolution and the behaviour of the different gas phases in the SILCC simulations is influenced by the position of SN explosions with respect to the dense gas. We have therefore produced [^{12}C II] synthetic emission maps for the seven different simulations listed in the upper part of Table 2.2, using the $t = 50$ Myr snapshot in each case. We see in most synthetic emission maps a narrow, intense component around the galactic midplane and a fainter extended component. The exception is run *S10–KS–peak* (third column in Fig. 3.5), which has no extended component and a less intense midplane signal. In this run, the SN explode in local density peaks. As a result, they, on the one hand, locally destroy dense molecular clouds and, on the other hand, are subject to efficient radiative cooling. Consequently they do not manage to drive a galactic fountain flow. Instead most gas remains close to the midplane as filamentary, atomic gas (Walch et al., 2015) resulting in a weaker but broader [^{12}C II] signal.

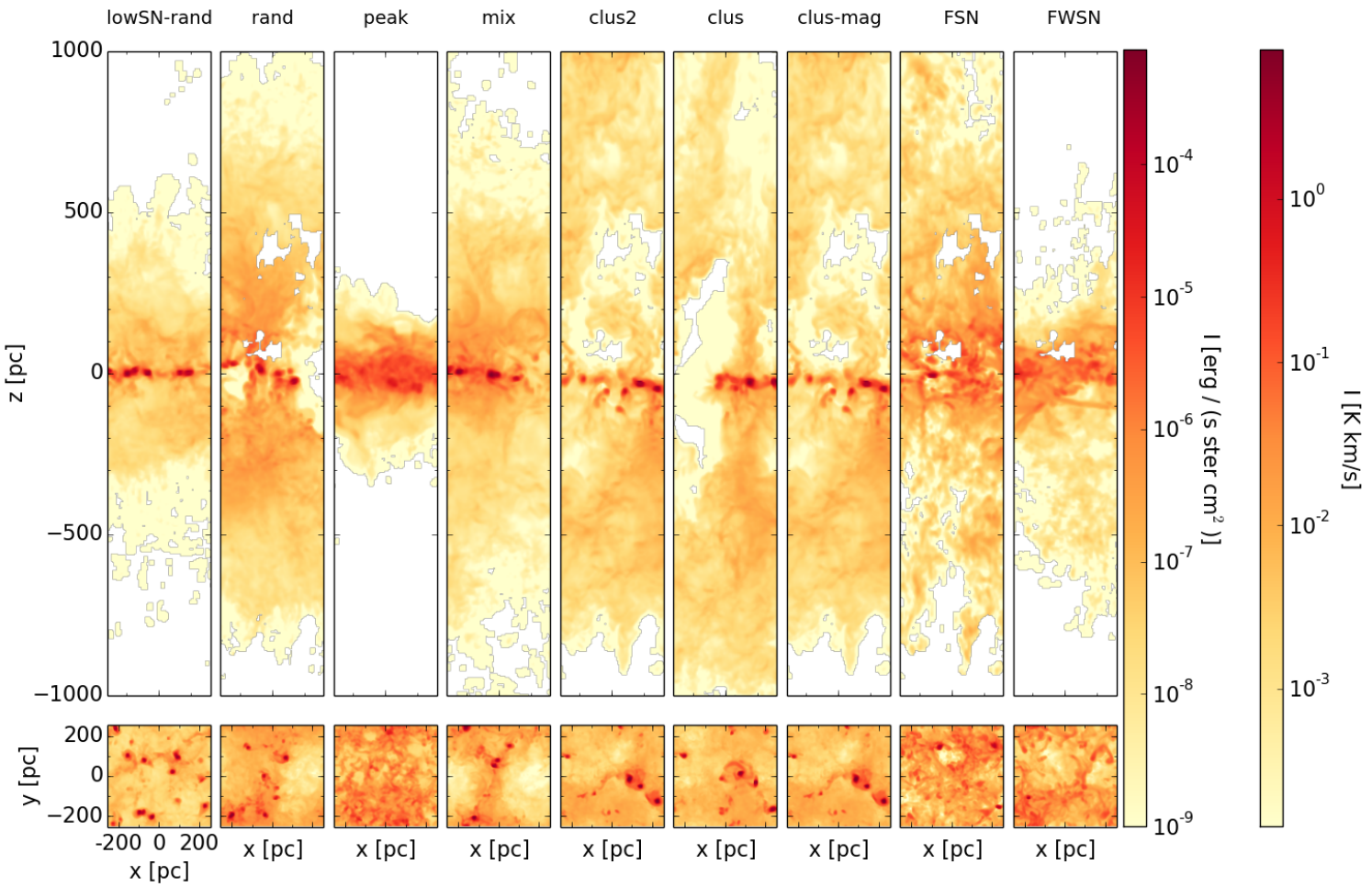

Figure 3.5: [^{12}C II] synthetic emission maps of the simulations *(from left to right) S10–lowSN–rand*, *S10–KS–rand*, *S10–KS–peak*, *S10–KS–mix*, *S10–KS–clus2*, *S10–KS–clus*, and *S10–KS–clus–mag* at $t = 50$ Myr (cf. Walch et al., 2015, Girichidis et al., 2016b) as seen edge-on (*top*) and face-on (*bottom*). The last two columns show the emission maps of the simulations *FSN* and *FWSN* at $t = 70$ Myr (Peters et al., 2017). The [C II] line emission shows a strong signal around the midplane for most of the simulations, which follows the distribution of dense clouds. Extended, outflowing gas is visible as faint [^{12}C II] line emission at larger scale heights.

Table 3.3: List of the peak intensities and luminosities of the synthetic emission maps of the [^{12}C II] and the [^{13}C II] line, calculated for the SILCC-01 (upper part) and SILCC-02 (lower part) simulations, as listed in Table 2.2.

Run	[^{12}C II]		[^{13}C II]	
	$I_{\rm peak}$ [K km s^{-1}]	$L_{\rm tot}$ $\times 10^3$ [L$_\odot$]	$I_{\rm peak}$ [K km s^{-1}]	$L_{\rm tot}$ [L$_\odot$]
S10–lowSN–rand	114	22.9	4.5	582
S10–KS–rand	114	17.2	4.9	307
S10–KS–peak	4	7.6	0.04	76
S10–KS–mix	164	27.1	6.1	505
S10–KS–clus2	204	35.1	7.8	704
S10–KS–clus	189	26.3	6.2	506
S10–KS–clus–mag	123	16.8	8.6	521
FSN	56	11.5	0.5	100
FWSN	74	7.7	1.1	79

We show the integrated [^{12}C II] intensity maps for the three projections of the zoom-in simulation MC2 at $t_{\rm tot}$ = 13.9 Myr in Fig. 3.6. The peak integrated intensities and luminosities for the three projections are summarized in Table 3.4. We additionally carried out the synthetic [^{13}C II] emission maps, and present their peak integrated intensities and luminosities likewise in Table 3.4. The overall structure of the emission map follows the distribution of the gas, as it was presented in Fig. 2.3. In regions with high column densities ($N \geq 10^{23}$ cm^{-2}) gas can have high densities along the line of sight. There, carbon is converted to CO, and no longer present as C$^+$. A well visible example of this scenario can be seen in the centre of the map in *yz*-projection. The synthetic [^{12}C II] line emission maps show in this position with high CO abundance a drop in the [^{12}C II] line.

The integrated intensities presented in the synthetic [^{12}C II] emission maps are shown on logarithmic scale in Fig. 3.6 to make the faint emission visible. However, in observations we expect an integrated [^{12}C II] intensity of $I_{[^{12}\rm CII]} \geq 0.5$ K km s^{-1} to be detectable. This assumed detection limit is in line with the 3σ detection limits of Velusamy & Langer (2014) and Croxall et al. (2012). In the work of Croxall et al. (2012), the [^{12}C II] line emission is studied from nearby spiral galaxies, detected with the PACS instrument on board of the *Herschel* satellite. They report a 3σ detection limit of $\sim 0.04\times10^{-7}$ W m^{-2} sr^{-1}, corresponding to $\sim 4\times10^{-6}$ erg s^{-1} sr^{-1} cm^{-2}, or 0.57 K km s^{-1} in temperature units. Better sensitivities can be achieved, if one or a few pointings are observed in [^{12}C II] , but for extended maps a detection limit of 0.5 K km s^{-1} is reasonable. To illustrate, which part of the synthetic [^{12}C II] line emission would be visible assuming this detection limit, we show in Fig. 3.7 the same emission maps as in Fig. 3.6, but plotting this time the integrated intensities on linear scale. The contours indicate the assumed detection limit. We find about 21, 16, and 27% of the total field of the maps to be above the assumed detection limit in each projection, respectively. The luminosity taken from only the observable area recovers ~80% of the total luminosity along each line of sight.

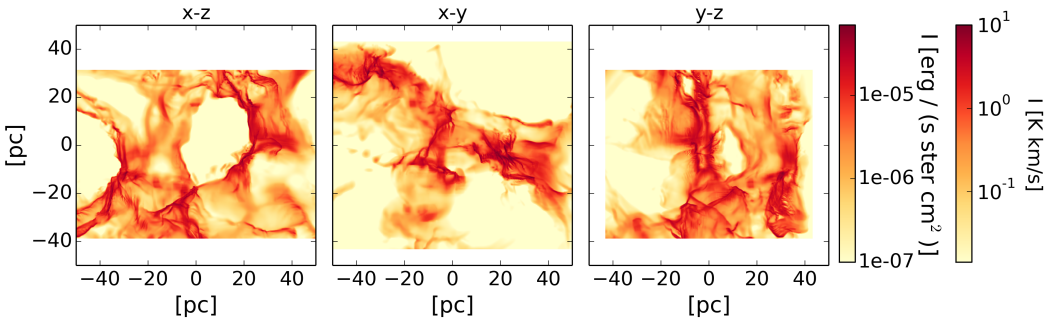

Figure 3.6: Synthetic [^{12}C II] emission maps of the zoom-in simulation MC2 for different projections. The colour map indicates the integrated intensity in [erg / (s sr cm^2)], the colour bar for the integrated intensity in [K km s^{-1}] is for guiding the eye.

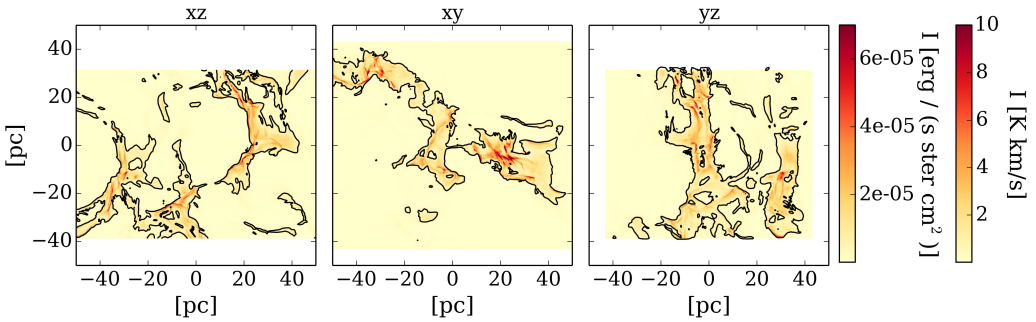

Figure 3.7: Same as Fig. 3.6, but this time showing the integrated [^{12}C II] intensity on linear scale. The contours mark the regions, in which $I_{[^{12}\mathrm{CII}]} \geq 0.5$ K km s^{-1} is fulfilled. These parts are expected to be observable. We find about 21, 16, and 27% of the total map for the three projections, respectively, to be detectable.

Table 3.4: Same as Table 3.3, but for the zoom-in simulation MC2 for all three projections.

Projection	[^{12}C II]		[^{13}C II]	
	I_{peak} [K km s^{-1}]	L_{tot} $\times 10^3$ [$L_\odot$]	I_{peak} [K km s^{-1}]	L_{tot} [$L_\odot$]
xz	10.56	652.30	0.21	6.52
xy	16.41	622.95	0.36	6.52
yz	13.44	676.73	0.29	6.52

4

Testing the simulations

As described in Section 3.3, we calculate the [C II] line emission not in the local thermal equilibrium and chose the LVG approximation for the calculation. At high densities, the result is equal as in LTE conditions. Further, we assume the line width induced by the microturbulence to be the same as the thermal line width (see Section 3.3). Both assumptions will influence our result. To what extend this happens, we analyse here on the example of the simulation *S10-KS-rand* at $t = 50$ Myr from the SILCC-01 setup. As a further test, we calculate whether the [^{12}C II] line emission becomes optically thick within the SILCC simulations.

Based on the findings from the tests in the SILCC simulations, we start testing the zoom-in simulation MC2 with respect to its optical depth. Since the zoom-in simulation exist for different spatial resolutions, we continue by testing the convergence between the resolution levels. After this, the spectral resolution is tested, and as a last test we investigate whether different escape length probabilities in the LVG method influence our results. Note, that the test done for MC2 are part of the paper submitted to MNRAS in May 2018 (Franeck et al., 2018).

Finally, we test the influence of the resolution on our result on the example of a spherical molecular cloud, simulated with the FLASH code and the same chemical network as used for the SILCC and the zoom-in simulations. As done in the other simulations, we calculate the synthetic [^{12}C II] emission maps of this test setup, and study the abundance of the chemical species as a function of the radius of the cloud. By this, we investigate the influence of an enhanced density in the cloud to the result.

Table 4.1: Peak intensity and the luminosity of the integrated [^{12}C II] synthetic emission maps for the simulation *S10-KS-rand* at $t = 50$ Myr calculated within different modes. The modes are given as the lines_mode variable in the RADMC-3D input file. In the upper part of this table the non-LTE modes are listed. The lines_mode = 3 indicates the LVG mode with an escape probability lengthscale $L_{\max}$. The lines_mode = 4 presents the optically thin approach. In the lower part of the table the values for the LTE calculation (lines_mode = 1) are presented.

lines_mode	$I_{\rm peak}$		$L_{\rm tot}$	
	[erg / (s sr cm^2)]	[K km s^{-1}]	[W]	[$L_\odot$]
3, $L_{\max} = \infty$	8.08×10^{-4}	113.6	6.43×10^{30}	1.68×10^4
3, $L_{\max} = 10$ pc	8.22×10^{-4}	116.9	6.56×10^{30}	1.71×10^4
3, $L_{\max} = 500$ pc	8.22×10^{-4}	116.9	6.57×10^{30}	1.72×10^4
4	3.59×10^{-4}	51.6	3.30×10^{30}	8.70×10^3
1 (LTE)	1.807×10^{-3}	256.9	3.49×10^{32}	9.10×10^5

4.1 Test with the SILCC setup

4.1.1 Modes for the calculations in RADMC-3D

RADMC-3D offers different ways to calculate the radiative transfer in the non-local thermal equilibrium. One can choose between the different modes by setting the parameter "lines_mode". On the example of the simulation *S10-KS-rand* at $t = 50$ Myr we want to show here the differences of the modes in RADMC-3D. For completeness, we will also carry out one calculation in the local thermal equilibrium (LTE). The synthetic [^{12}C II] emission maps carried out with a non-LTE and a LTE calculation are presented in Fig. 4.1 in the left panels of the two groups of panels. Figure 4.2 shows the averaged vertical profiles of the emission maps for the different modes.

Non-LTE calculation with LVG approximation

There is the option to calculate the [C II] line emission assuming non-LTE by combining the large velocity gradient approximation (LVG) with a finite escape probability lengthscale in lines_mode = 3, as it was described in Section 3.3. The optical depth τ is calculated with the velocity gradient ($\tau_{ul}^{\rm LVG}$, see Eq. (3.18)). If a velocity field is not given in the simulation, or the velocity gradient becomes too small, RADMC-3D offers the possibility to specify an escape probability lengthscale $L_{\max}$. With that the optical depth can be calculated as

$$\tau_{ul}^{\rm L} = \frac{ch}{4\pi} \frac{n_{\rm C^+} L_{\max}}{\sqrt{\pi} a_{\rm tot}} \left(x_l B_{lu} - x_u B_{ul}\right), \tag{4.1}$$

where c is the speed of light, h the Planck constant, $n_{\rm C^+}$ the number density of C^+, $a_{\rm tot}$ the total line width, x_l and x_u the fractional level population of the lower and upper levels, and B_{lu} and B_{ul} the Einstein coefficients. If no escape probability length

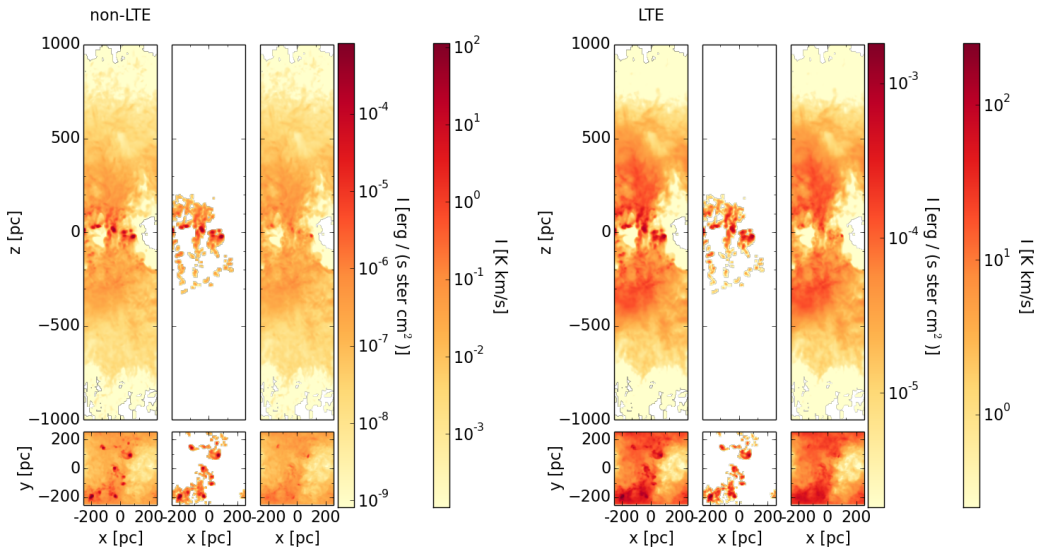

Figure 4.1: Synthetic [^{12}C II] emission maps of the simulation *S10-KS-rand* at $t = 50$ Myr, calculated in the non-LTE (left) and in the LTE mode (right). The first plot in each panel shows the synthetic emission map for the whole simulation, in the middle is the map for gas with $T < 300$ K, and on the right side is the map for gas with $T > 300$ K. Microturbulence is taken into account for both cases as $a_{\rm turb} = a_{\rm therm}$.

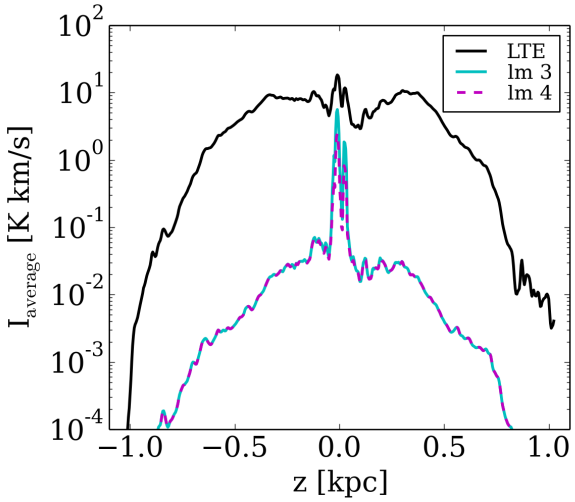

Figure 4.2: Intensity profiles of the synthetic [^{12}C II] line emission maps for the simulation *S10–KS–rand* at $t = 50$ Myr calculated with different modes in RADMC-3D. Assuming a local thermal equilibrium yields to the highest intensity values. In case of non-LTE all results are identical in the dilute gas and the peak intensity drops. For the LVG approximation (lines_mode = 3), the level population in dense regions converges to the LTE case. Therefore, the [^{12}C II] emission from the dense regions is enhanced.

is specified, then $L_{\rm max} = \infty$ and there is no escape probability. If $L_{\rm max}$ is specified, RADMC-3D calculates both $\tau_{ul}^{\rm LVG}$ and $\tau_{ul}^{\rm L}$ and takes the minimum of them for the radiative transfer calculation. It is recommended to chose a lengthscale $L_{\rm max}$ comparable to the structures of interest in the simulation box. An educated guess is the size of the molecular cloud itself, or the size of the simulation box.

We chose escape probability lengthscales $L_{\rm max}$ of 10 pc and 500 pc, converted into centimetres in the input file, and we set by accident $L_{\rm max} = 10$ cm in one calculation. In Table 4.1 we list the luminosities of the synthetic emission maps and the peak intensities for the different lengthscales assumed. Setting $L_{\rm max}$ to a reasonable value, results in similar peak intensities and luminosities for [^{12}C II] as for $L_{\rm max} = \infty$. When setting $L_{\rm max}$ to the small and unreasonable value of $L_{\rm max} = 10$ cm, the peak intensity and luminosity is reduced, and takes the same values as for the optically thin case, as discussed below.

The synthetic emission map for this calculation is shown in the third column of the left panel of Fig. 4.1. The vertical profile of this calculation assuming an infinite escape probability lengthscale is presented as the cyan line in Fig. 4.2.

Non-LTE calculation with the optically thin approach

RADMC-3D provides the option that non-local thermal equilibrium can be calculated in the optically thin approach (lines_mode = 4). In this case the level population of the carbon ion is calculated assuming that all emitted line radiation escapes and is not reabsorbed. However, the ray tracing calculation itself is done in the normal non-LTE manner, without the optically thin approach. In this mode the [^{12}C II] synthetic emission maps of the simulation *S10–KS–rand* at $t = 50$ Myr show the same intensities as the one done in lines_mode = 3 with the unreasonable finite escape probability lengthscale of $L_{\rm max} = 10$ cm. The values of the peak intensity, as well as the luminosity are listed in Table 4.1. In Fig. 4.2 the vertical emission profile of this calculation is shown as the magenta dashed line. In the regions with dilute gas, the synthetic emission maps calculated with lines_mode = 3 ($L_{\rm max} = \infty$) and lines_mode = 4 are the same, since there the emission is optically thin, so that the level population in both cases are equal. However, in the dense regions within the midplane the intensities are smaller compared to the LVG case, since in the optically thin approach the level population is assumed to be everywhere optically thin.

LTE calculation

In the analysis of observational studies of the [^{12}C II] line emission LTE is assumed in various cases (e.g. Okada et al., 2015). In the scenario of LTE, the level population of the carbon ions follow Eq. (3.9), and $T_{\rm ex} = T_{\rm kin}$. The [^{12}C II] line intensity is therefore larger in general as in the case of a non-LTE and should give an upper limit of the values. By setting lines_mode = 1 in RADMC-3D, one can calculate the radiative transfer in LTE. We use this for the same simulation *S10-KS-rand* at $t = 50$ Myr, plotting the resulting synthetic emission map in the first column of the right panel in Fig. 4.1 and the vertical averaged profile as black solid line in

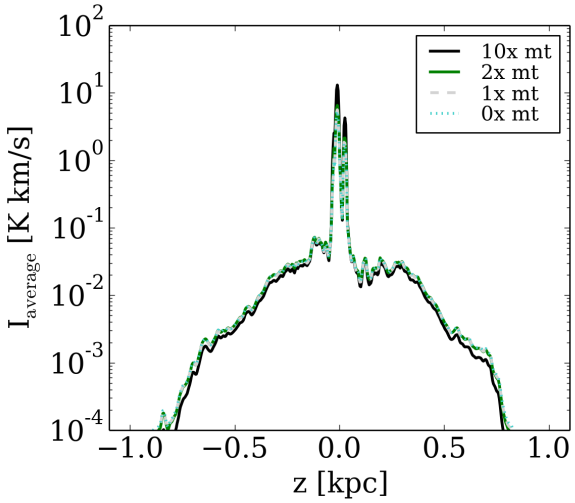

Figure 4.3: Vertical profiles of the [^{12}C II] line emission maps for the simulation *S10–KS–rand* at t = 50 Myr, calculated in non-LTE with lines_mode = 3 and $L_{max} = \infty$. Microturbulences are varied between no microturbulence and 10 times of the value chosen in this work. There are only slight variations between the emission profiles calculated with the different microturbulences.

Table 4.2: List of the peak intensities and luminosities in the synthetic [^{12}C II] emission maps for *S10–KS–rand* at t = 50 Myr, assuming different microturbulences. The calculations were done in non-LTE (with lines_mode = 3 and $L_{max} = \infty$).

microturbulence ×	I_{peak} [erg / (s sr cm^2)]	[K km s^{-1}]	L_{tot} [W]	[$L_\odot$]
0×	8.08×10^{-4}	114.8	6.11×10^{30}	1.60×10^4
1×	8.08×10^{-4}	113.6	6.43×10^{30}	1.68×10^4
2×	8.59×10^{-4}	122.1	7.36×10^{30}	1.92×10^4
10×	15.58×10^{-4}	6.68	12.35×10^{30}	3.22×10^4

Fig. 4.2. The intensities are overall larger in this scenario, especially the emission of the dilute gas beyond the midplane. There is also dilute gas in the midplane, so that the peak intensities in the LTE mode are higher compared to the calculation in the LVG calculation. Since the file from the LAMDA data base for the fine level of C^+ contains only the two levels $^2P_{1/2}$ and $^2P_{3/2}$, the upper level is overpopulated in regions with very high temperatures. The peak intensity, as well as the luminosity of the map in LTE is listed in Table 4.1.

4.1.2 Variation of the microturbulence

The assumed level of microturbulence might influence the results. To test this effect, we make calculations in which we vary the value of the microturbulence for the simulation *S10–KS–rand* at t = 50 Myr, calculated in non-LTE with lines_mode = 3 and $L_{max} = \infty$. We scale the microturbulence to values between 0× and 10× the

microturbulence that we included as described in Section 3.3. The vertical averaged profiles of the maps are shown in Fig. 4.3. Overall, the synthetic emission maps do not change much. Table 4.2 lists the peak intensities of the synthetic emission maps $I_{\rm max}$, and their luminosities $L_{\rm tot}$. The peak intensity of the synthetic emission maps increases when the microturbulence becomes larger, e.g. it almost doubles from the case of including no microturbulence to the case with 10 times the microturbulence, since a larger line width results in a higher integrated intensity. Consequently, the luminosities of the maps behave in the same manner.

4.1.3 Optical depth within the SILCC setup

In the analysis of this work we will not assume local thermal equilibrium, nor assume that the majority of the gas is optically thin. The code RADMC-3D offers the possibility to calculate, whether the emission becomes optically thick ($\tau \geq 1$) for a velocity channel along each line of sight. We calculate for all velocity channels whether the emission becomes optically thick, and then add up the number of optically thick velocity channels. Multiplying the number of channels with the spectral resolution results in a velocity range Δv. Figure 4.5 shows for the SILCC-01 simulations at $t = 50$ Myr and the SILCC-02 simulations at $t = 70$ Myr, over which velocity space the [C II] line emission is optically thick. Gas in the midplane, where it is dense, becomes optically thick. However, the majority of the volume contains optically thin gas. We further indicate the area of the simulation, that we assume to be observable ($I_{[^{12}\rm CII]} \geq 0.5$ K km s^{-1}, see Section 3.4), with black contours in Fig. 4.5. A great part of the observable area is optically thick for most of the simulations. In simulations with more dispersed gas, that evolves in our examples either by the explosions of SNe in dense gas (*S10–KS–peak*), or by the initially driven turbulence and the additional low SNR (*FSN*), the area with lines of sight of optically thick [^{12}C II] emission is smaller.

In Fig. 4.4 we present the histogram of the fraction of pixels as a function of the column density of the total gas $N_{\rm tot}$. We further distinguish between lines of sight with optically thin and thick emission. As seen in Fig. 4.5, only a small fraction of lines of sight is optically thick. Whether the line is optically thick does not strictly depend on the column density. Instead, we find lines of sight optically thick in [^{12}C II] for $N_{\rm tot} < 10^{19}$ cm^{-2}, where the majority of the lines of sight is optically thin. However, due to the limited spatial resolution, carbon remains as C^+ in the SILCC setup, so that at high column densities $N_{\rm tot} \geq 10^{22}$ cm^{-2} all lines of sight become optically thick in the [^{12}C II] line.

We test further, whether the [^{13}C II] line becomes optically thick within the SILCC-01 and SILCC-02 setups, and find the [^{13}C II] line emission to be optically thin everywhere.

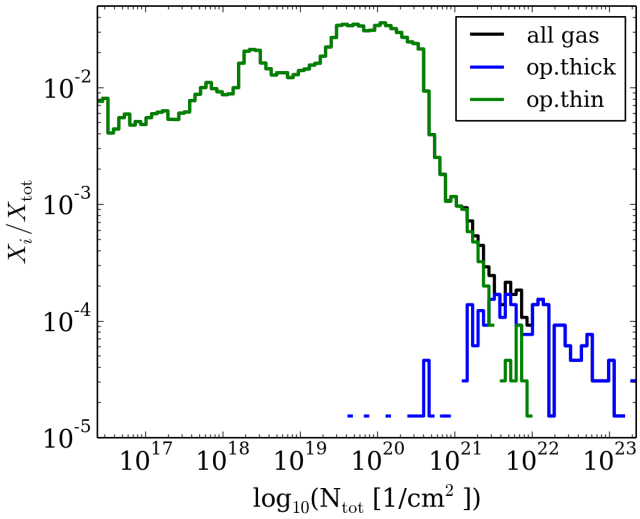

Figure 4.4: Histogram of the amount of optically thin and thick pixels as a function of the column density of the total gas $N_{\rm tot}$ for the SILCC simulation *S10–KS–rand*. The histogram is done for the edge-on projection of the gas. Lines of sight with column densities of $N_{\rm tot} \geq 10^{22}$ cm^{-2} are optically thick in the [^{12}C II] line emission.

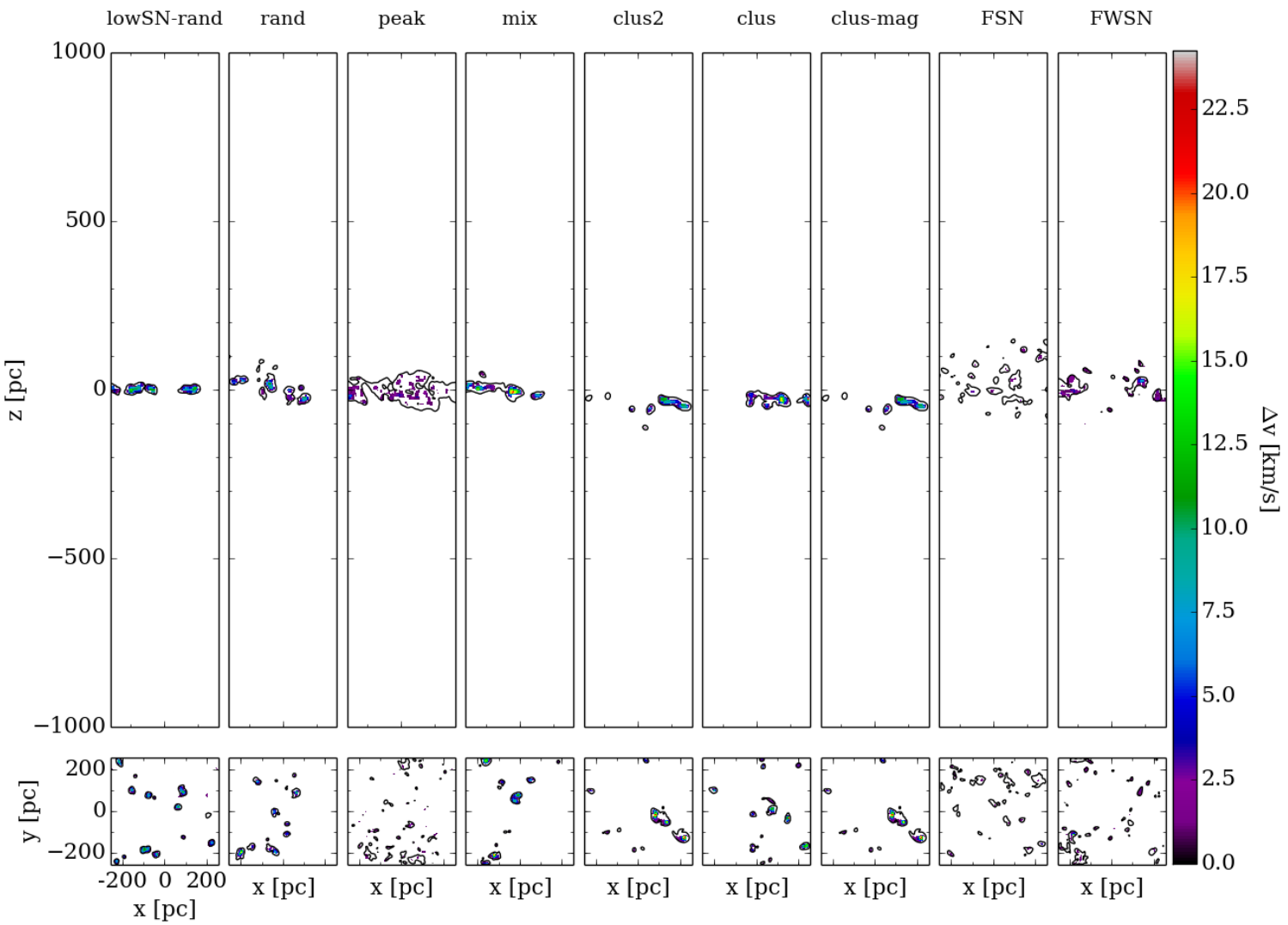

Figure 4.5: Maps of the the SILCC-01 and SILCC-02 setups, showing where the [^{12}C II] line emission becomes optically thick. The colours indicate over which range in velocity the emission is optically thick along the lines of sights. The different panels show the maps for *(from left to right)* *S10–lowSN–rand*, *S10–KS–rand*, *S10–KS–peak*, *S10–KS–mix*, *S10–KS–clus2*, *S10–KS–clus*, and *S10–KS–clus–mag* at $t = 50$ Myr (cf. Walch et al., 2015, Girichidis et al., 2016b) as seen edge-on (*top*) and face-on (*bottom*), and for *FSN* and *FWSN* at $t = 70$ Myr (Peters et al., 2017). The contours indicate the regions with $I_{[^{12}\mathrm{CII}]} \geq 0.5$ K km s^{-1}, which are assumed to be observable (see Section 3.4).

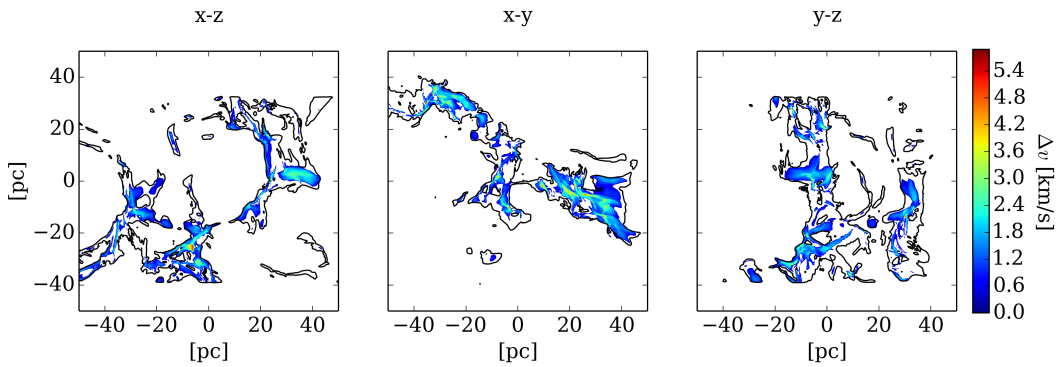

Figure 4.6: Maps, showing where the [^{12}C II] emission line becomes optically thick along the different projections for MC2, L10. We colour-coded the width in velocity space, over which the emission is optically thick. The observable area ($I_{[^{12}\mathrm{CII}]} \geq 0.5$ K km s^{-1}) is marked with contours. For the *xz*, *xy* and *yz* projection, we find 39%, 34% and 47% of the observable area ot be optically thick.

4.2 Tests with the zoom-in simulation MC2

Since we find the [^{12}C II] line emission to be optically thick in the SILCC setups, we test for the zoom-in simulation MC2 first the optical depth for the [^{12}C II] line, and the [^{13}C II] line. Thereafter we investigate whether the synthetic [^{12}C II] and [^{13}C II] line emission maps are spatially and spectrally converged. Finally, we investigate the influence of a different microturbulence, following the approach of Larson (1981), and the influence of an escape velocity lengthscale on our results. Note, that the tests presented in this Section are part of the paper submitted to MNRAS in May 2018 (Franeck et al., 2018).

4.2.1 Optical depth within MC2

We investigate, whether the [^{12}C II] line emission becomes optically thick ($\tau \geq 1$) for the zoom-in simulation MC2. In Fig. 4.6 we show the simulation of MC2 at a resolution level of L10 from the different projections , the colours showing the velocity range, Δv, over which the emission becomes optically thick. The contours indicate in which areas the [^{12}C II] line emission is larger than $I_{[^{12}\mathrm{CII}]} \geq 0.5$ K km s^{-1}. We find about 10% of the area to be optically thick in all projections. This optically thick area accounts for 45%, 54% and 40% of the total luminosity in the *xz*, *xy* and *yz* projections, respectively. The observable region with $I_{[^{12}\mathrm{CII}]} \geq 0.5$ K km s^{-1} takes about 21%, 16% and 27% of the total area of the map in the *xz*, *xy* and *yz* projection, respectively, and accounts for about 80% of the total luminosity. About 39%, 34% and 47% of the observable area is optically thick in the [^{12}C II] line emission in the three (*xz*, *xy* and *yz*) projections.

Figure 4.7 shows a histogram indicating the fraction of pixels as a function of the total gas column density N_{tot}. The bin size is chosen as $\Delta(N_{\mathrm{tot}}\,[\mathrm{cm}^{-2}]) = 0.05$.

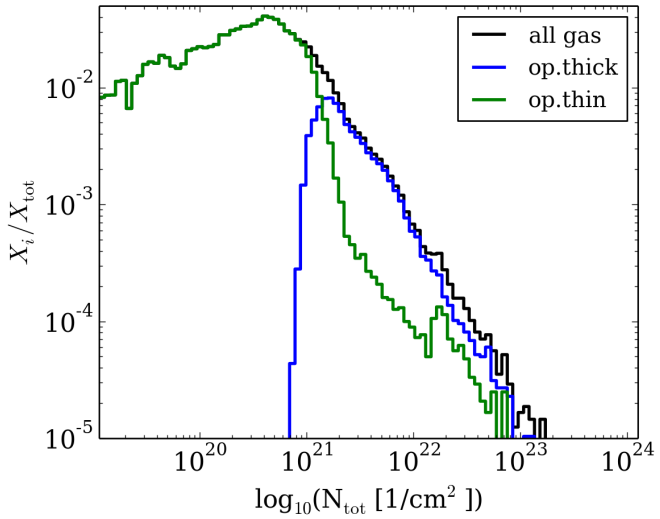

Figure 4.7: Histogram as a function of total gas column density, showing over which range the [^{12}C II] line emission is optically thin (green) and thick (blue). Around $N_{\rm tot} \sim 10^{21}$ cm^{-2} the [^{12}C II] line emission becomes optically thick.

We find that for column densities around $N_{\rm tot} \sim 10^{21}$ cm^{-2} the [^{12}C II] line emission becomes optically thick. This is in agreement with the value given in Tielens (2005) in their table 2.7, where they state that the [^{12}C II] line emission reaches a line-averaged optical depth of unity at an H column density of $\sim 10^{21}$ cm^{-2}.

We also test the [^{13}C II] line emission concerning the optical depth and find it to be optically thin everywhere for MC2 at L10. Thus, we can compare the level population between the [^{12}C II] and the [^{13}C II] line emission and do this by calculating the excitation temperature $T_{\rm ex}$ of the lines, defined in Eq.(3.9). This can be rearranged to

$$T_{\rm ex} = \frac{-h\nu_{ul}}{k} \cdot \left[\ln\left(\frac{x_u}{x_l} \frac{g_l}{g_u} \right) \right]^{-1} . \tag{4.2}$$

In Fig. 4.8 we show $T_{\rm ex}$ for [^{12}C II] and [^{13}C II] as a function of the kinetic temperature $T_{\rm kin}$ in the left and the right panel, respectively. The colour-coding indicates the fraction of the total emission. Whenever $T_{\rm kin} = T_{\rm ex}$ the excitation is in local thermal equilibrium. This is the case for low $T_{\rm kin}$, with $T_{\rm kin} \leq 30$ K. The [C II] line emission comes mostly from gas with temperatures around $T_{\rm kin} \approx 50$ K. For this value of $T_{\rm kin}$, the excitation temperature drops towards $T_{\rm ex} \sim 20$ K. Thus, the emission is dominated by subthermal emission. The optical depth further influences the excitation temperature $T_{\rm ex}$, as a comparison of $T_{\rm ex}$ for the optically thick [^{12}C II] and optically thin [^{13}C II] line emission shows (Fig. 4.9). Due to the optical depth in the [^{12}C II] line emission, the [^{12}C II] line emission is radiatively excited. This increases $T_{\rm ex}$ for [^{12}C II] compared to [^{13}C II]. In the range of 10 K and 35 K of the optically thin $T_{\rm ex}$, the optically thick $T_{\rm ex}$ is enhanced by up to 10 K.

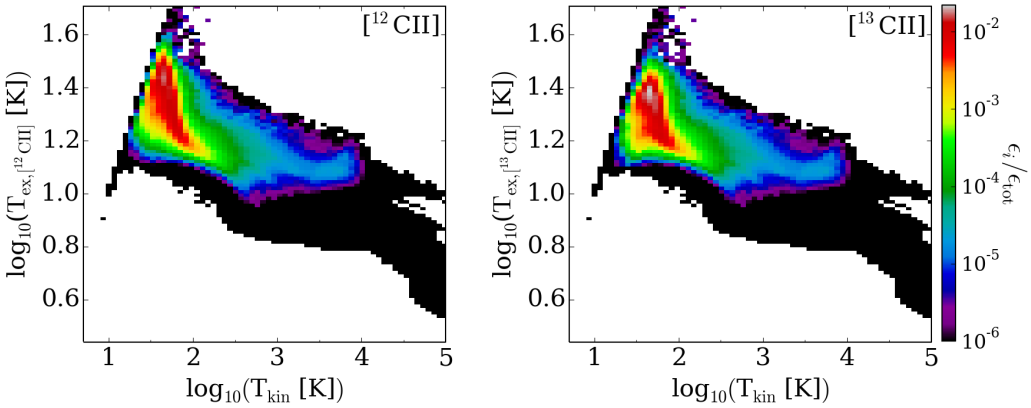

Figure 4.8: Histograms showing the distribution between the kinetic gas temperature $T_{\rm kin}$ and the excitation temperature $T_{\rm ex}$ for the opacity affected [^{12}C II] line emission (left) and the optically thin [^{13}C II] line emission (right). The colour-coding indicates the fraction of emission with respect to the total emission $\epsilon_i/\epsilon_{\rm tot}$ in the gas. The straight upper left boundary of the populated area is the identity $T_{\rm kin} = T_{\rm ex}$, in which the LTE conditions are fulfilled.

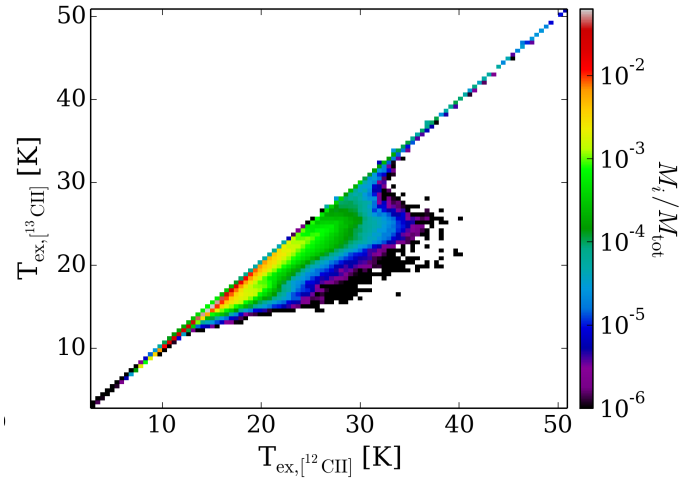

Figure 4.9: Two-dimensional histograms of the distribution of the excitation temperature $T_{\rm ex}$ for the opacity affected [^{12}C II] line emission (x-axis) and the optically thin [^{13}C II] line emission (y-axis). The colour-coding indicates the fraction of mass in the distribution.

Table 4.3: Summary of the zoom-in simulation MC2 at different spatial resolutions. The first column lists the names used for the simulations in Seifried et al. (2017), the second the names after their resolution level, used in this work. In the third column, the spatial resolution is given. We further list for the xz-projection of the maps the maximum integrated intensities and the total luminosities; both for the opacity affected [C II] line emission and the optically thin case ([^{13}C II]).

Run name in S17	resolution level	dx	[^{12}C II], opac. aff.		[^{13}C II], opt. thin	
			$I_{\rm peak}$	$L_{\rm tot}$	$I_{\rm peak}$	$L_{\rm tot}$
		[pc]	[K km s^{-1}]	[L$_\odot$]	[K km s^{-1}]	[L$_\odot$]
MC2_dx-3.9	L5	3.9	1.36	353	0.01	3.00
MC2_tau-0.0_dx-2.0	L6	2	1.90	390	0.02	3.45
MC2_tau-0.5_dx-1.0	L7	1	3.60	459	0.04	4.23
MC2_tau-1.0_dx-0.5	L8	0.5	5.82	555	0.06	5.30
MC2_tau-1.25_dx-0.24	L9	0.25	10.30	628	0.12	6.14
MC2_tau-1.5_dx-0.12	L10	0.122	10.56	652	0.21	6.52

4.2.2 Spatial convergence of the synthetic emission maps

We calculate synthetic [C II] emission maps for the opacity affected [C II] line emission (named [^{12}C II] hereafter) and the optically thin [C II] line emission (corresponding to the [^{13}C II] and therefore named [^{13}C II] hereafter) at different spatial resolutions. The maps are calculated from the snapshot at an evolutionary time of $t_{\rm tot}$ = 13.9 Myr. For the radiative transfer calculations, we assume the emission to be not in local thermal equilibrium, and use the LVG approximation in RADMC-3D (lines_mode = 3, $L_{\rm max} = \infty$). We chose a spectral resolution dv = 0.1 km s^{-1}. We here investigate, whether the emission maps are converged. The synthetic emission maps for the [^{12}C II] and [^{13}C II] line emission are presented in Figs. 4.10 and 4.11, respectively. The crosses in the maps mark the positions with the maximum integrated intensities. The spatial resolutions, the peak integrated intensities and the luminosities are listed in Table 4.3. For the [^{12}C II] line emission maps we find that the position of the peak integrated intensity varies with the resolution level, and is only in the same region from level L9 to L10. With each refinement level, the mass is redistributed along the line of sight, so that the density profile becomes more distinct. Therefore, regions that were optically thin before, can become optically thick at higher resolutions. For the optically thin [^{13}C II] line emission the positions of the peak integrated intensities are similar from the resolution level L6 on. Here, the emission is not dominated by optically depth effects. However, for all resolution levels, the structures within the molecular cloud maintain their general morphology both for the [^{12}C II] and the [^{13}C II] line emission maps.

We investigate, whether the synthetic emission maps are converged as a total. For that, we first compare the luminosity integrated over the whole maps. In Figs. 4.12 and 4.13 we show in the left panels the luminosities at each resolution level. Note, that the best refinement level L10 with a spatial resolution of dx = 0.122 pc is on the left hand side of the x-axis of each plot. We find different luminosities for the different projections (xz, xy and yz) in the [^{12}C II] line emission,

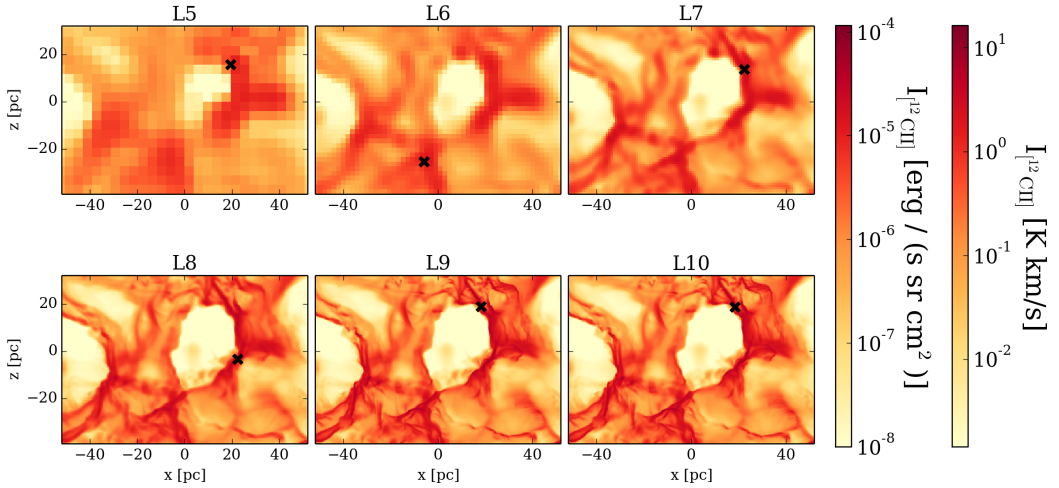

Figure 4.10: Opacity affected [^{12}C II] line emission maps of the zoom-in simulations in the xz-projection. The panels show the maps at different resolutions (see Table 4.3). The crosses mark the position with the maximum integrated intensity. Due to varying optical depths, the position changes from the refinement level L5 to L9.

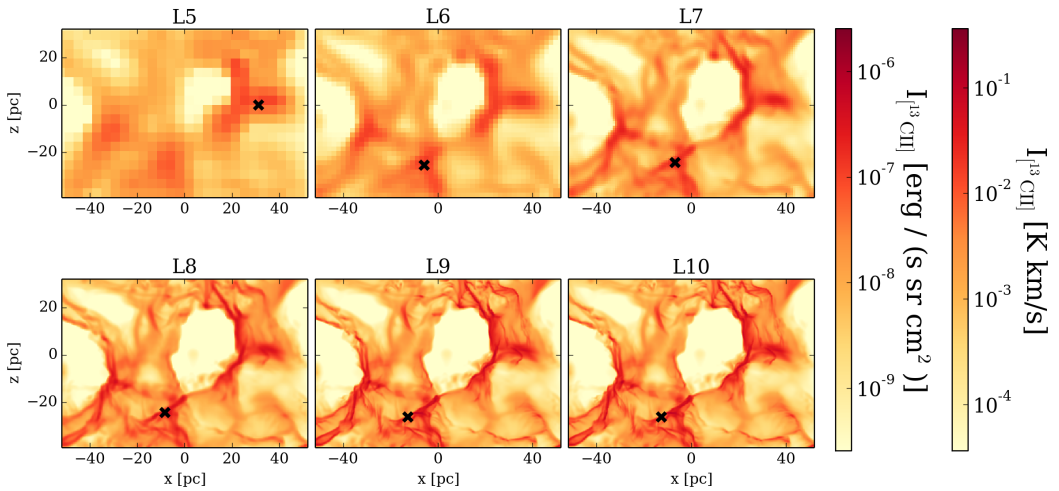

Figure 4.11: As Fig. 4.10, here the optically thin [^{13}C II] line emission maps are presented. Here, the positions with the maximum integrated intensity (crosses) remain in the same area from L6 on.

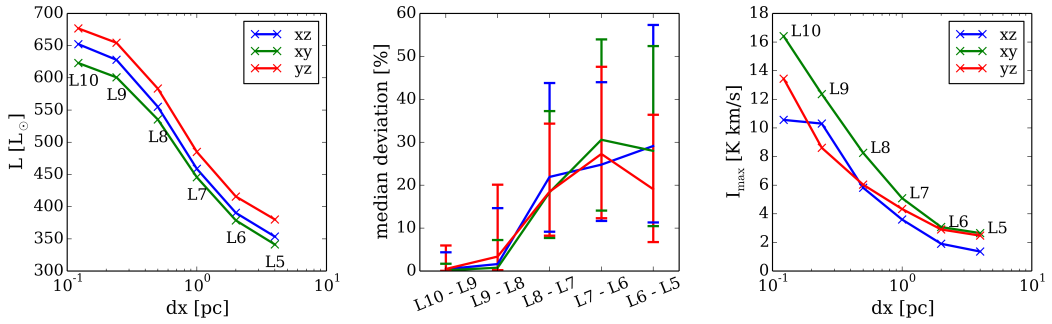

Figure 4.12: Convergence study of the [^{12}C II] emission maps, analysed with the luminosity (left) for different resolution levels (see Table 4.3) and all three projections (colour-coded). The middle panel presents the median of the deviation between the synthetic emission maps of two adjacent resolution levels. As error bars, the interquartile ranges are used. Between the maps of the resolution level L9 and L10 the median of the deviation is $< 0.5\%$. We further show the peak integrated intensity at each resolution level (right), which is not converged.

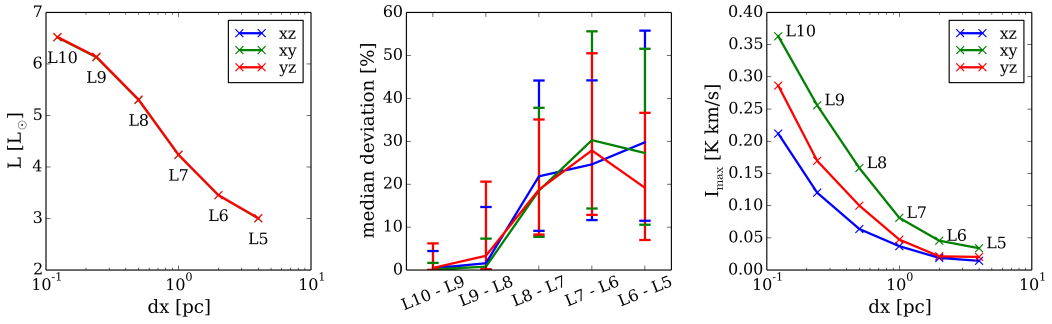

Figure 4.13: As Fig. 4.12, this time for the [^{13}C II] (optically thin [C II]) line emission. All projections have identical luminosities, so that they fall on to one curve (left).

but the same luminosities along all projections for the [^{13}C II] line emission. This is again caused by the optical depth effects. We further find the luminosity to grow with the resolution level for both the [^{12}C II] and the [^{13}C II] line emission. However, the difference between two adjacent resolution levels becomes smaller with higher spatial resolution. We test this more systematically by comparing the maps of two adjacent resolution levels Lx and L(x + 1) pixel by pixel. For this, we first reduce the amount of pixels for the higher resolution level L(x + 1) to the amount of pixel at the lower resolution level Lx, by averaging the values of the four pixels p_i^{x+1} to one value. We then calculate the deviation of the value of the averaged pixel with the value of the pixel at the lower resolution level p^x by

$$\Delta = \left(p^x - \frac{1}{4} \sum_{i=1}^{4} p_i^{x+1} \right) \cdot \frac{100\%}{p^x}. \tag{4.3}$$

We calculate Δ for every pixel in the lower resolved map Lx and determine the median of the absolute values of the distribution of Δ. The median is the value, for that 50% of all values of the distribution are included. In the middle panels of Figs. 4.12 and 4.13 we plot the median deviation for the maps at different spatial resolutions, as indicated on the x-axis. The errorbars indicate the interquartile range of the distribution, where 25% and 75% of the values are included. We find that the median deviation decreases when comparing maps of higher resolution levels. This is in line with the findings of the luminosity over the whole map, where we likewise found the difference between two adjacent resolution levels to decrease with higher spatial resolution. For L9 and L10 we find the maps to converge within 0.5%, as the median deviation indicates.

In the right panels of Figs. 4.12 and 4.13 we plot the peak integrated intensity values for all projections at each refinement level. Those values are not converged. The redistribution of the mass along a line of sight has a great influence on the individual integrated intensities within the maps.

As a further test for the convergence of the maps we calculate the distribution of pixels at different spatial refinement levels. This distribution is a histogram, normalized to the total amount of pixels in the map, and corresponds to a probability distribution function (PDF). We bin the data according to the integrated intensity in logarithmically equally distributed bins with bin size of $\Delta \log_{10}(I\,[\mathrm{K\,km\,s^{-1}}]) = 0.05$. In Fig. 4.14 we show the histograms for the integrated [^{12}C II] and [^{13}C II] emission maps in the left and right panel, respectively. With higher resolution level, the covered range in integrated intensities increases, which is in line with the analysis presented in the right panel of Figs. 4.12 and 4.13. However, from the resolution level L9 on, the overall distribution of the intensities remains similar.

4.2.3 Spectral convergence of the synthetic emission maps

We test, which spectral resolution is needed to capture the integrated intensity in the maps. In the maps shown above, we took 401 equally distributed channels

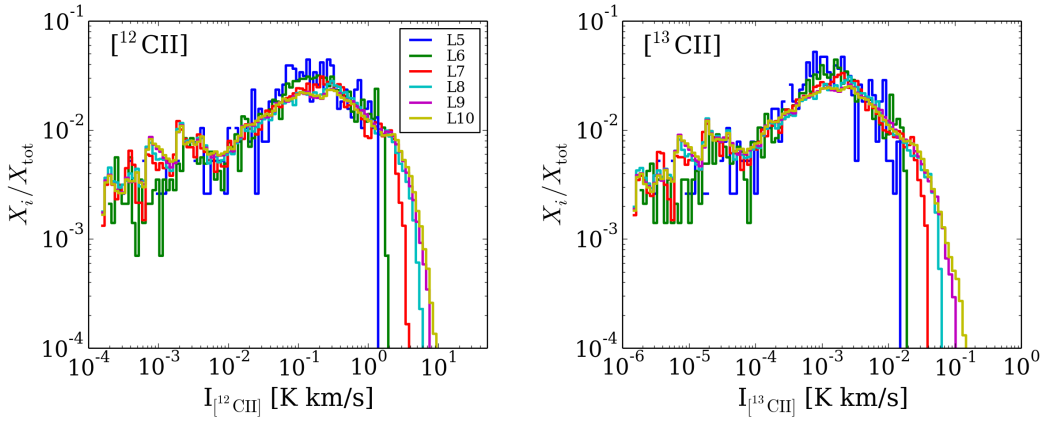

Figure 4.14: Histograms of the integrated intensities of the [^{12}C II] (opacity affected [C II]) and the [^{13}C II] (optically thin [C II]) line emission (left and right panel, respectively). The different resolutions are colour-coded, and on the y-axis fraction of pixels is indicated as $X_i/X_{\rm tot}$. From the resolution level L9 on, the histograms converge.

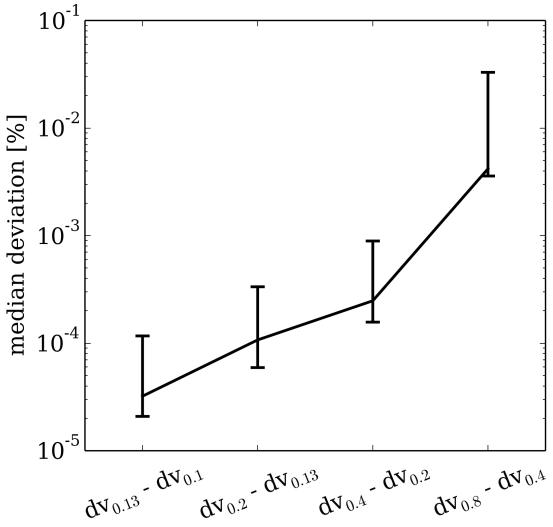

Figure 4.15: Median deviation for the integrated [^{12}C II] line emission maps at different spectral resolutions, as indicated on the x-axis.

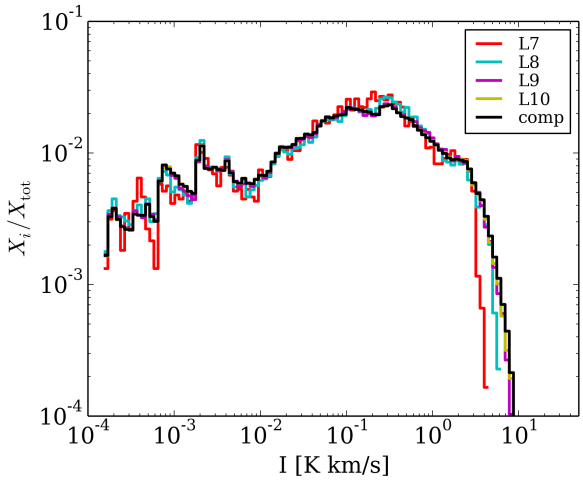

Figure 4.16: Histograms of the integrated intensities for the synthetic [^{12}C II] emission maps at different resolutions. We assume here a microturbulence according to Larson (1981). On the y-axis, we show which fraction of the pixels $X_i/X_{\rm tot}$ is present in the integrated intensity bins. For comparison, we plot the distribution for the [^{12}C II] map, in which we assumed a thermal microturbulence as black line. The influence of the emission maps by the different approaches for $a_{\rm turb}$ are negligible. Likewise, the convergence among the resolution levels is not affected.

in velocity space within the velocity range of $\Delta v = \pm 20$ km s^{-1} around the rest frequency. This results to a spectral resolution of dv = 0.1 km s^{-1}. Now, we reduce the number of channels from 401 to 301, 201, 101 and 51, corresponding to dv = 0.1, 0.13, 0.2, 0.4, 0.8 km s^{-1}, respectively. We compare the maps in a similar manner as done for the spatial resolution, by calculating the deviation between the value of a pixel $p^{{\rm dv}_x}$ with the value of the pixel at the same position in a map with a higher spectral resolution $p^{{\rm dv}_{(x+1)}}$. The deviation for each pixel is calculated as

$$\Delta_{\rm v} = (p^{{\rm dv}_x} - p^{{\rm dv}_{(x+1)}}) \cdot \frac{100\%}{p^{{\rm dv}_x}}. \tag{4.4}$$

We then calculate the median of all deviations to estimate the differences between the maps. In Fig. 4.15 we plot the median deviation at different spectral resolutions. The error bars indicate the interquartile range, for that 25% and 75% of the deviation values are included. For all chosen spectral resolutions the deviation is small ($< 0.1\%$), and the median deviation between the maps with dv = 0.2 km s^{-1} and 0.1 km s^{-1} is beyond 0.001%. Therefore, a spectral resolution of dv = 0.2 km s^{-1} is likewise sufficient when carrying out synthetic emission maps.

4.2.4 Testing a microturbulence according to Larson

As mentioned in Section 3.3.2, the total linewidth $a_{\rm tot}$ is composed of a thermal line width $a_{\rm therm}$, and a turbulent part $a_{\rm turb}$ (see Eq. (3.17)). If not indicated differently, we set $a_{\rm turb} = a_{\rm therm}$. In Section 4.1.2 we tested the influence of scaling up the microturbulence on the synthetic [^{12}C II] emission maps of the SILCC simulations.

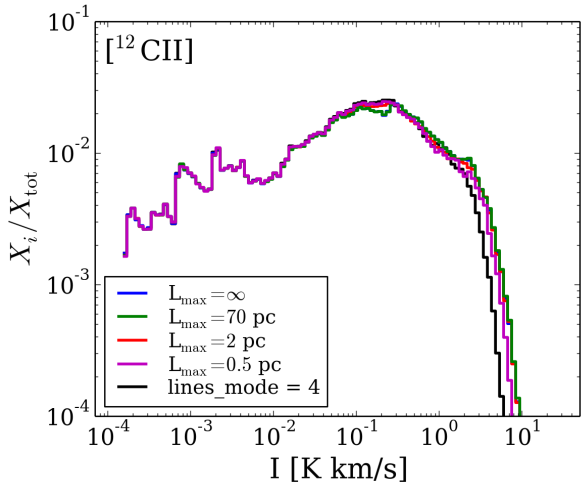

Figure 4.17: Histograms of the integrated intensities for the synthetic [^{12}C II] line emission maps, calculated with the LVG approximation with different escape length probabilities $L_{\rm max}$ (lines_mode = 3), and for the optical thin approximation (lines_mode = 4). The histograms show the distribution of the pixels in the maos, where $X_i/X_{\rm tot}$ denotes the fraction of pixels in every intensity bin. In general, we use $L_{\rm max} = \infty$ in this work. Specifying $L_{\rm max}$ has only a small influence on the synthetic emission maps.

Now, following Larson (1981, eq. (20) therein and Eq. (3.32) in this work), we calculate the turbulent linewidth as $a_{\rm turb} = 1.1 \times L^{0.38}$, and test, whether this influences the synthetic emission maps. We study this with [^{12}C II] synthetic emission maps at different resolution levels. In Fig. 4.16 we show the distribution of the integrated intensity for different resolutions. The data is binned in logarithmic bins of the integrated intensity with sizes of $\Delta\log_{10}(I\,[\mathrm{K\,km\,s^{-1}}]) = 0.05$. As comparison, we also plot the distribution of the intensities for the L10 [^{12}C II] map with $a_{\rm turb} = a_{\rm therm}$ (solid black line). From the histogram we find only negligible differences between the two microturbulence approaches. The synthetic emission maps with Larson's microturbulence converge as well from the refinement level L9 on.

4.2.5 Testing escape probability lengths $L_{\rm max}$

As described in Section 4.1.1, there are different ways of calculating the synthetic emission maps within the LVG approximation by setting an escape probability lengthscale $L_{\rm max}$. In Section 4.1.1 we tested some values for $L_{\rm max}$ within the SILCC-01 setup. Here, we test the influence of $L_{\rm max}$ on the zoom-in simulations. In the synthetic emission maps shown before, we do not specify $L_{\rm max}$, and hence, $L_{\rm max} = \infty$. We test values of $L_{\rm max} = 70$ pc, corresponding to the size of the simulation box, and of $L_{\rm max} = 2$ pc and 0.5 pc, corresponding to the sizes of the structures within the molecular cloud. In Fig. 4.17 we show the distribution of the integrated intensities, calculated for the [^{12}C II] line emission in the xz-projection of the cloud, where we set the bin sizes to $\Delta\log_{10}(I\,[\mathrm{K\,km\,s^{-1}}]) = 0.05$. We find the histograms for the maps with escape probability lengthscales of $L_{\rm max} = \infty$ and $L_{\rm max} = 70$ pc to be close to each other. The deviations become larger for $L_{\rm max} = 2$ pc and $L_{\rm max} = 0.5$ pc. As fur-

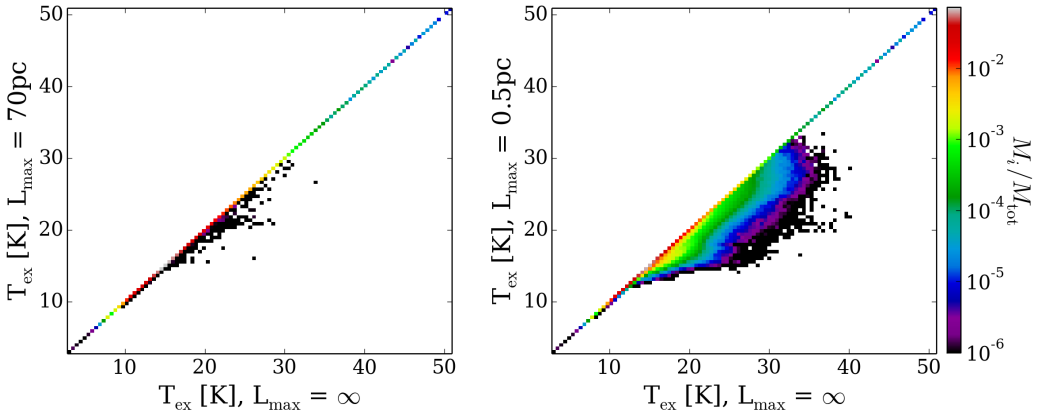

Figure 4.18: Two-dimensional histograms of the excitation temperatures $T_{\rm ex}$ for the calculations with $L_{\rm max} = \infty$ versus $L_{\rm max} = 70$ pc (left) and $L_{\rm max} = \infty$ versus $L_{\rm max} = 0.5$ pc (right). The colour-coding indicates the fraction of mass within the distribution.

ther comparison we show the histogram of the map calculated within the optically thin approach (lines_mode = 4) as black line. The smaller the value set for $L_{\rm max}$, the closer becomes the histogram to the one for the optically thin approach.

We further compare the excitation temperatures $T_{\rm ex}$ of the simulations calculated with the LVG approximation with an escape probability length of $L_{\rm max} = \infty$ versus $L_{\rm max} = 70$ pc and $L_{\rm max} = \infty$ versus $L_{\rm max} = 0.5$ pc in Fig. 4.18 in the left and right panel, respectively. We show the comparison as two-dimensional histograms (PDFs), where the fraction of mass within the distribution is colour-coded. For the comparison of $L_{\rm max} = \infty$ and $L_{\rm max} = 70$ pc in the left panel, we find very similar excitation temperatures, and only small deviations between $T_{\rm ex} \sim 20$ K and ~35 K. In the right panel, where we compare $T_{\rm ex}$ for $L_{\rm max} = \infty$ and $L_{\rm max} = 0.5$ pc, the deviations are larger. Here, for low intensities, $T_{\rm ex}$ is similar to the optically thin [^{13}C II] line emission. For higher intensities, $T_{\rm ex}$ takes intermediate values between the opacity affected [^{12}C II] line emission, and the optically thin [^{13}C II] line emission.

4.3 Setup of a molecular cloud

4.3.1 Molecular cloud inspired from the SILCC simulations

We test the influence of the resolution on the RADMC-3D calculations with a simple setup simulating a molecular cloud with FLASH. The box has an extension of 64 pc in each direction, the molecular cloud is assumed as spherical with a radius of 20 pc. Within the molecular cloud we set the density of the gas to $\rho_{\rm MC} = 2.5 \cdot 10^{-22}$ g cm^{-3}, and to $\rho_{\rm A} = 1.5 \cdot 10^{-24}$ g cm^{-3} in the ambient medium. Assuming a mean molec-

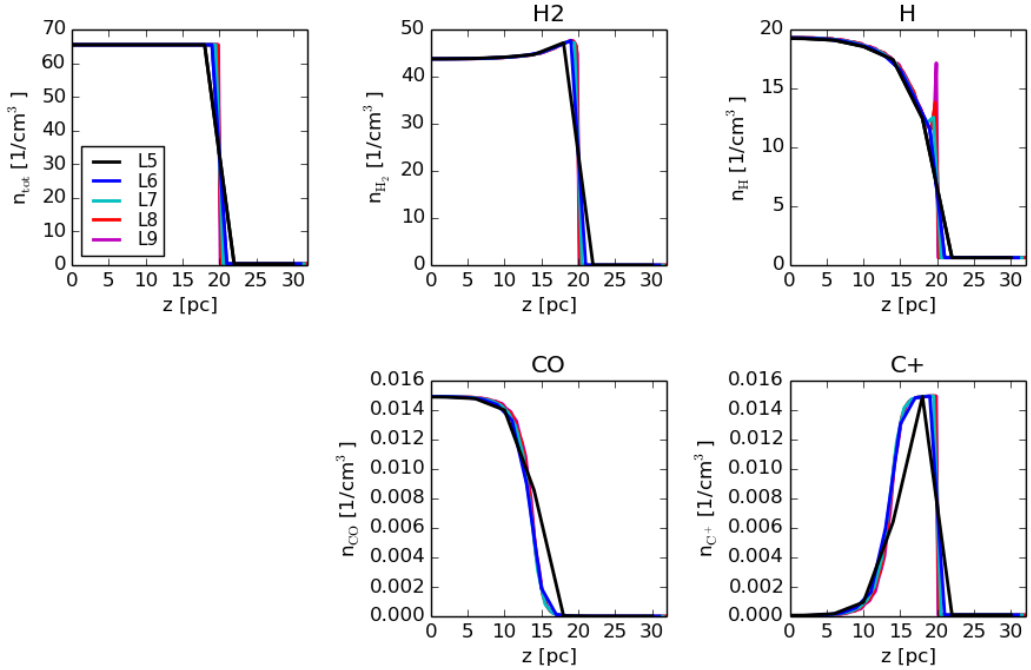

Figure 4.19: Number density along a line of sight towards the centre of the molecular cloud, which is at $z = 0$ pc, for the total gas (upper left panel) and the different chemical species, as indicated over the panels. The colours represent the different resolutions (see Table 3.2).

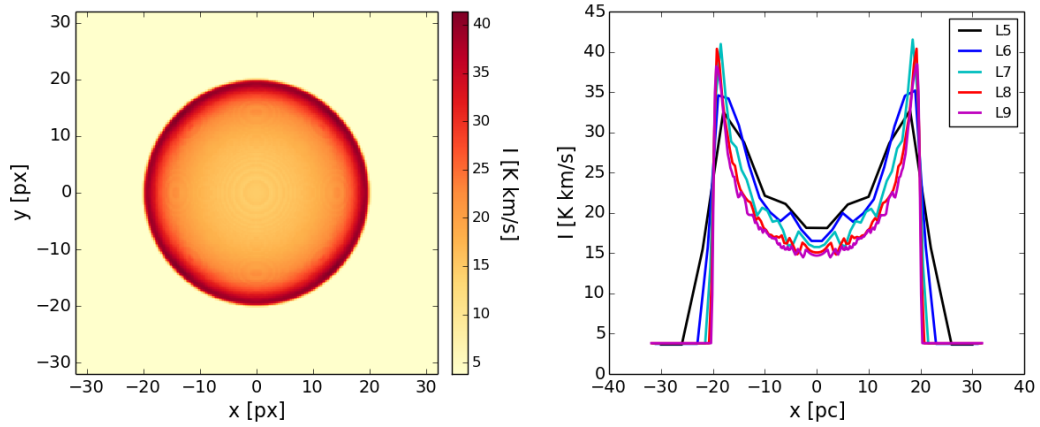

Figure 4.20: Synthetic [^{12}C II] emission map for the simulation of the test setup of a spherical molecular cloud Test-01-L9 (left), and the profile of the integrated [^{12}C II] line intensity through the centre of the molecular cloud at $y = 0$ for different resolution levels (right, see Table 3.2). The maximum integrated intensity saturates from Test-01-L7 on.

Table 4.4: List of the resolution levels (1st column) used for the simulation of a molecular cloud in a test setup. The simulation box has an extent of 64 pc in each direction. With the resolution level the amount of pixels in each direction increases. The resulting pixel size is listed in the 2nd column. The 3rd column lists the peak intensity of the synthetic [^{12}C II] emission map in [K km s^{-1}] and the 4th column the luminosity over the whole simulation box.

resolution level	dx [pc]	$I_{\rm peak}$ [K km s^{-1}]	$L_{\rm tot}$ $\times 10^3$ [$L_\odot$]
Test-01-L5	4	34.86	2.86
Test-01-L6	2	42.02	2.70
Test-01-L7	1	43.49	9.09
Test-01-L8	0.5	43.24	9.30
Test-01-L9	0.25	41.36	8.94

ular weight of $\mu = 2.3$, this corresponds to number densities of $n_{\rm MC} = 65$ cm^{-3} and $n_{\rm A} = 0.39$ cm^{-3}. These values are inspired by the molecular clouds formed in the simulation of the SILCC-01 setup. We assume pressure equilibrium and chose $p = 6.235 \cdot 10^{-13}$ erg K^{-1}. Consequently the temperature is almost constant within the molecular cloud with $T_{\rm MC} = 25$ K and in the ambient medium with $T_{\rm A} = 3.3 \cdot 10^3$ K. As in the SILCC setup, the molecular cloud is illuminated by the external stellar radiation field of $1.7\,G_0$. Therefore, photon dominated regions (PDRs) can form in the outer boundary region of the cloud.

We aim to test the resolution of the chemical evolution in the gas and therefore don't take the hydrodynamics into account. As in the SILCC simulations, hydrogen is initially present as atomic hydrogen, and carbon as ionized carbon. The chemical evolution of the gas is calculated with the simplified chemical network by Nelson & Langer (1997) and Glover & Mac Low (2007a,b). With increasing resolution level the amount of pixels in each direction doubles. In Table 4.4 we list the resolution levels and the corresponding pixel size for our setup. For distinguishing these simulations from the zoom-in simulations, we call them here "Test-01-Lx", whereas the "x" refers to the same resolution level as in the zoom-in simulations. For the simulation Test-01-L5 the pixels have a size of 4 pc. This corresponds to the resolution in the SILCC-01 and SILCC-02 simulations. We analyse the simulation of the molecular cloud after an evolutionary time of 25 Myr. In Fig. 4.19 we show the number densities of the total gas and of the chemical species along one line of sight towards the centre of the cloud. The colour-coding represents the different resolution levels. As we built the model, the number density of the total gas is constant within the molecular cloud, and likewise in the surrounding medium. The chemical species change according to the radiation field they experience. The atomic hydrogen has its largest number densities within the molecular cloud. At low resolutions (Test-01-L5 and Test-01-L6) $n_{\rm H}$ decreases towards the edge of the cloud. However, from the resolution level Test-01-L7 on, we find a thin layer between the molecular cloud and the ambient medium to evolve. With larger resolution (Test-01-L7, Test-01-L8, Test-01-L9) $n_{\rm H}$ increases in this layer. Thus, as a result of the ISRF, a PDR has formed at the boundary of the molecular cloud. For the carbon species

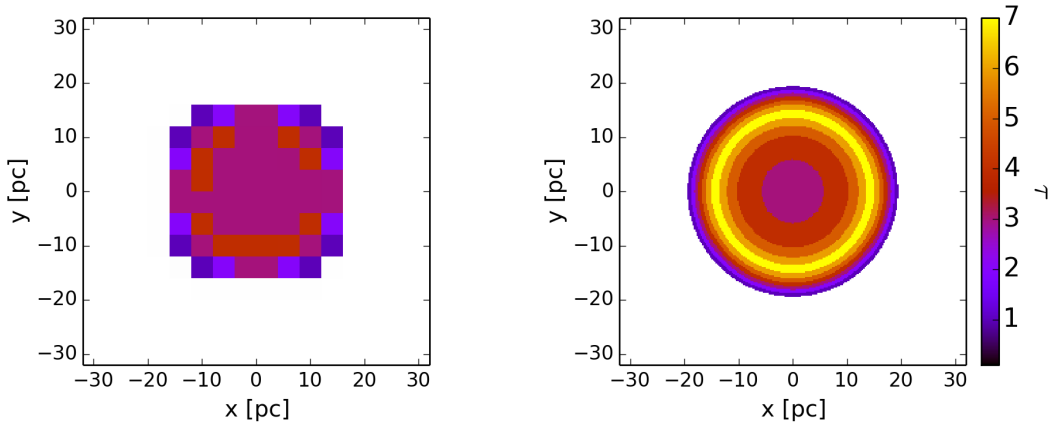

Figure 4.21: Maps showing the optical depth τ for the [^{12}C II] line emission of the test setup of the molecular cloud Test-01-L5 (left) and Test-01-L9 (right). With higher spatial resolution the optical depth is increased. The optical depth increases in rings, whereas close to the edge of the cloud τ remains still small.

we find CO to be present in the molecular cloud itself, and its number density $n_{\rm CO}$ decreasing towards the edge of the molecular cloud. As $n_{\rm CO}$ sinks, $n_{\rm C^+}$ raises. C^+ forms a thick layer (~10 pc) at the edge of the cloud. The number densities for CO and C^+ are similar along the line of sight from level L7 on.

We carry out radiative transfer simulations for the test setup, using RADMC-3D, and assuming, that the emission is not in local thermal equilibrium. We use the LVG approximation, and no escape length probability ($L_{\rm max} = \infty$, lines_mode = 3, see Section 3.3). Figure 4.20 shows in the left panel the synthetic [^{12}C II] line emission map for the test setup of the molecular cloud Test-01-L9. In the right panel, we show the integrated intensity as a profile through the midplane of the cloud at different resolution levels (colour-coded). The integrated [^{12}C II] line emission has for all resolution levels its maximum at the edge of the cloud, while the maximum for Test-01-L7 is the largest among the resolution levels. For higher resolution levels, the maximum intensity at the edge decreases again. Table 4.4 lists in the third and fourth column the integrated peak intensities and the luminosities over the whole synthetic emission maps of the molecular clouds. There are small variations of the intensity along one ring of the molecular cloud. A reason for this is the spherical geometry of the cloud within the Cartesian, square grid. Therefore, the values listed in Table 4.4 are slightly higher than the maximum values presented in the profiles in Fig. 4.20. For Test-01-L8 and Test-01-L9 the peak intensity remains very close to the value of Test-01-L7, but decrease slightly due to optical depth effects, since part of the emission is absorbed on the way through the cloud, before it can reach the observer. The luminosity increases with the resolution from Test-01-L5 to Test-01-L7. Thereafter, the luminosity only changes slightly, but decreases again, in line with the peak intensities and the optical depth effects.

We test the optical depth in the molecular cloud in the test setup by calculating with RADMC-3D which regions in the projection have a τ between 1 and 8. We find for all test setups $\tau < 8$, and the maximum τ to increase with the resolution level. In

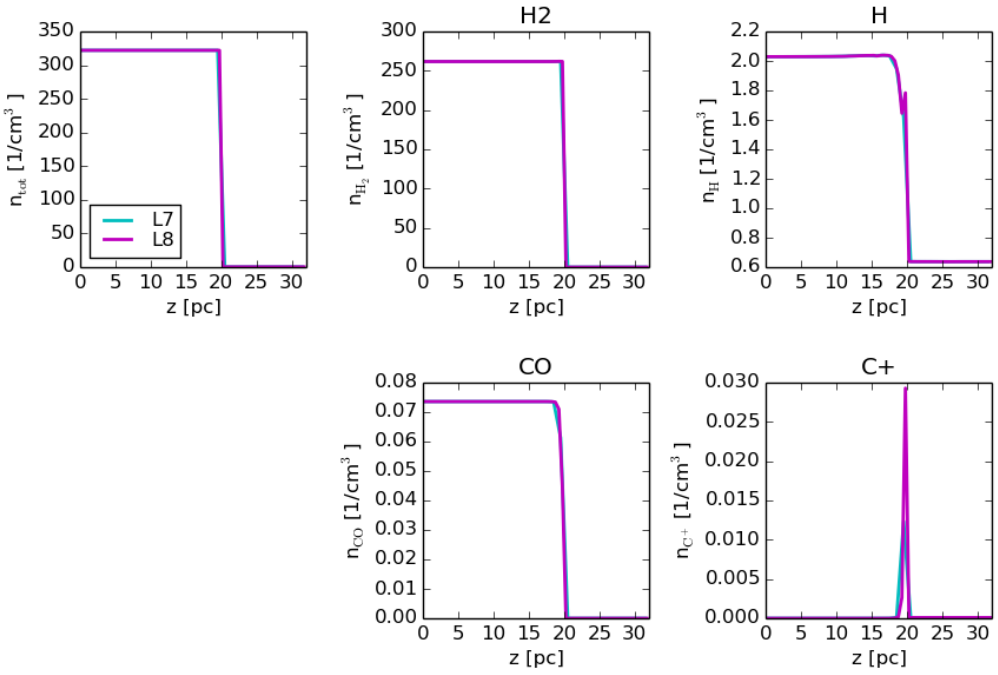

Figure 4.22: Same as Fig. 4.19, but for a higher density of the molecular cloud. The colours represent the different resolutions (see Table 3.2).

Fig. 4.21 we show the optical depth τ for the molecular cloud Test-01-L5 (left) and Test-01-L9 (right). Due to the projection of the number density to a column density, the regions with larger optical depth form within rings at the edge of the cloud. The closer one gets to the edge of the cloud, the smaller is the optical depth, since there is less gas along the line of sight. Thus, although the layer containing a high number density of C^+ has a thickness about 10 pc, the integrated [^{12}C II] intensity peaks at the edge of the cloud, where the abundance of C^+ is high, but the optical depth of the emission is still small.

Molecular clouds at a resolution level as Test-01-L5 with a diameter of 40 pc are represented in the simulations with 10 pixels in each direction. From the test setup we see, that PDRs can form within the code for spatial resolutions of d$x \leq 1$ pc (Test-01-L7). In the SILCC-01 and SILCC-02 setup they are not resolved and a molecular cloud with a diameter of 40 pc is represented in the simulations with 10 pixels in each direction. By this, we underestimate the maximum intensity and the luminosity.

4.3.2 Molecular cloud at higher densities

We further aimed to compare the RADMC-3D output with a PDR code, and discussed to take KOSMA-τ (e.g. Sternberg & Dalgarno, 1989, 1995, Zielinsky et al., 2000). The code KOSMA-τ is a one dimensional PDR code and can be used to calculate

Table 4.5: Same as Table 4.4, but for the test setup of a molecular cloud at higher densities (see text).

resolution level	dx [pc]	$I_{\rm peak}$ [K km s^{-1}]	$L_{\rm tot}$ $\times 10^3$ [$L_\odot$]
Test-02-L7	1	23.02	5.56
Test-02-L8	0.5	49.78	8.11

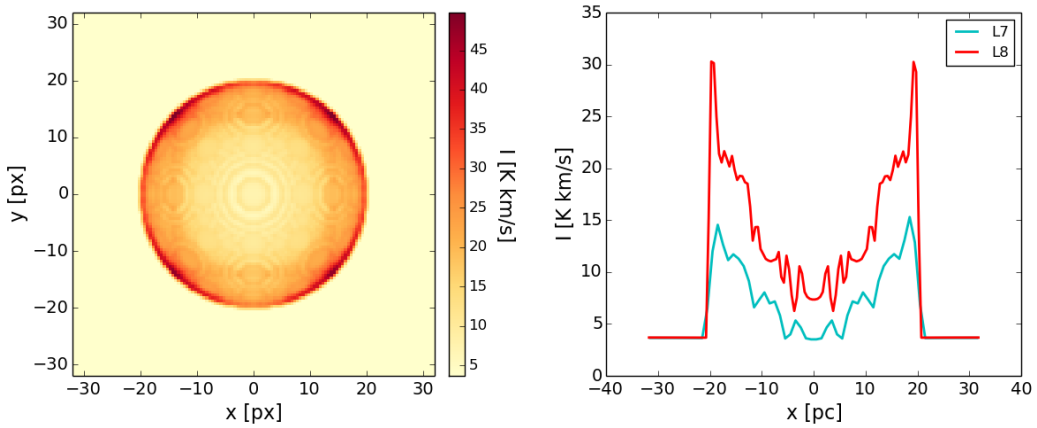

Figure 4.23: Same as Fig. 4.20, but for the test setup of the molecular cloud at higher density. The left panel shows the synthetic [C II] emission map at the resolution level L8.

PDRs of molecular clouds. Since it cannot be used in the density range we have in our simulations, a direct comparison is not possible. However, we can test with our setup what happens, if we increase the density of the molecular cloud. We do this and increase the density in the molecular cloud to $\rho_{\rm MC} = 1.23 \cdot 10^{-21}$ g cm^{-3}, while maintaining the density in the ambient medium at $\rho_{\rm A} = 1.5 \cdot 10^{-24}$ g cm^{-3}. As a pressure we chose $p = 2.045 \cdot 10^{-12}$ erg K^{-1}. We calculate the molecular cloud with the higher density for the resolution levels L7 and L8, while we name them "Test-02-Lx" to distinguish them from the zoom-in simulations (see Table 4.22). In Fig. 4.22 the number densities along one line of sight through the centre of the cloud is shown. We find qualitatively the same behaviour as in the molecular cloud with the lower density (Fig 4.19), as atomic hydrogen forms within a thin layer at the edge of the cloud. There is also a layer of ionized carbon at the edge of the cloud. However, in the the environment with the higher density, the layer with C^+ is thinner (~2 pc).

In Fig. 4.23 we present in the left panel the integrated [^{12}C II] intensity map of the test setup of the molecular cloud Test-02-L8. The right panel shows the cut through the integrated intensity map for Test-02-L7 and Test-02-L8. As can be seen in the plots, the integrated peak [C II] intensity is increased in this setup compared to the one with lower density (see Section 4.3.1). In Table 4.5 we list the peak intensities and the luminosities over the maps, as done for the setup with the lower densities in Table 4.4. In this setup the change in the integrated peak [^{12}C II] intensity between Test-02-L7 and Test-02-L8 is larger than the change in the setup with

the lower density. The luminosities over the maps are comparable to the luminosities in the setup with lower density.

From this test we see, that PDRs are forming due to the ISRF on the outer boundaries of molecular clouds. With higher volume density the formed PDR becomes thinner. We expect the same behaviour when increasing the ISRF. The thinner the PDR, the higher resolution is required to resolve it. If a PDR is unresolved, the luminosity of the total cloud is lower compared to a simulation with resolved PDR.

4.4 Discussion

We analysed the influence of different assumptions for the RADMC-3D calculations on the resulting [^{12}C II] emission maps. Since the gas is dilute, and most of the number densities of the chemical species are beyond the critical number density (see Section 2.2.3), we expect large parts of the gas to be not in local thermal equilibrium. The exception is gas dominated by molecular hydrogen, where the number densities of n_{H_2} can exceed the critical density. Thus, we conclude to calculate the synthetic [^{12}C II] and [^{13}C II] emission maps with the LVG method, corresponding to lines_mode = 3, and not assuming an escape length probability. In this mode, the optical depth is taken into account, when calculating the level population. Further, in regions with high number densities, the result converges to LTE conditions.

Nevertheless, we tested the different modes, and found the synthetic [C II] emission maps to be only slightly influences by the choice of the mode. We further tested the influence of the assumed microturbulence in the simulation. We scaled the assumed micorturbulence by a factor between 0 and 10, and in addition tested a microturbulence according to Larson (1981). We found that the different microturbulences change slightly the peak integrated intensity, but the overall synthetic emission maps remained the same under all conditions. Thus, we conclude that the assumptions done for the microturbulence does not change the results of the work.

We found thee synthetic [^{12}C II] emission maps to become optically thick in both the SILCC simulations and the zoom-in simulation MC2. In MC2, about ~40% of the observable area is optically thick in [^{12}C II]. In observations, the [^{12}C II] line emission is likewise found to be optically thick in regions of dense gas (Graf et al., 2012, Ossenkopf et al., 2013). The observational conclusion of the optically thick [^{12}C II] line emission is based on observations of the [^{13}C II] line emission at the same positions. For our analysis we therefore construct both [^{12}C II] and [^{13}C II] ($F = 2 - 1$) synthetic emission maps. For studying the [C II] emissivity properties of the cloud we use the [^{13}C II] line emission, since this line remains optically thin for both the SILCC setups and for MC2.

For the zoom-in simulation MC2 we tested the spatial and spectral resolution of the maps, and found that the synthetic [^{12}C II] and [^{13}C II] emission maps are about

to converge within 0.5% for the spatial resolution of $dx \leq 0.2$ pc (L9). The median deviation between the tested spectral resolutions of $0.1\,\mathrm{km/s} \leq dv \leq 0.8\,\mathrm{km/s}$ are below 0.1%. Thus, we conclude that a spectral resolution of $dv = 0.2\,\mathrm{km\,s^{-1}}$ would be sufficient for the analyses presented in this work. In case we chose this lower spectral resolution, we stated this in the beginning of the Chapter.

As a last test setup we investigated how a synthetic [^{12}C II] emission map looks like for a spherical molecular cloud at different spatial resolution, and with different densities. We find a PDR to form at the boundary of the cloud. The width becomes smaller with increasing density, since the radiation can penetrate less deep into the cloud. Thus, we expect the width of the PDR to become wider, if the radiation field is increased. If the PDR is not resolved, the luminosity of the total cloud is smaller, since the contribution from the PDR is missing. This is the case for the SILCC simulations, with their spatial resolution of $dx = 3.9$ pc. However, for the zoom-in simulations we might resolve the PDRs caused by the ISRF.

5

Distribution of the [C II] emission

The SILCC setups are created in a stratified box representing a small part of a galactic plane. Therefore we can further study the synthetic [C II] line emission on larger scales, analyse how it is distributed around the midplane and how the distribution changes with time. In this Section, we will first introduce the methods used by observers to quantify the distribution of the emission around a galactic midplane, and thereafter apply them to our synthetic emission maps. Note, that an example of the analysis of the distribution of the [C II] emission around the galactic plane was already presented in the conference contribution by Franeck et al. (2015).

5.1 Theory

5.1.1 Scale height via Gaussian fitting

In a locally isothermal and self-gravitating disc the vertical density distribution (along the z-direction) can be described by a sech^2 function (Spitzer, 1942, van der Kruit & Searle, 1981a,b, Banerjee & Jog, 2007),

$$\rho(z) = \rho_0 \, \mathrm{sech}^2\left(\frac{z}{z_0}\right). \tag{5.1}$$

The scale height z_0 depends on the velocity dispersion $\langle\sigma_z^2\rangle^{1/2}$ of the considered component (van der Kruit & Searle, 1981b) according to

$$z_0 = \frac{\langle\sigma_z^2\rangle^{1/2}}{(2\pi G\rho_0)^{1/2}}. \tag{5.2}$$

Here, G denotes the gravitational constant, and ρ_0 the density within the midplane. Likewise, the distribution of light in discs of spiral galaxies can be characterised by a sech^2 function. A model using this function for the description of observations was developed and tested on NGC 891 by van der Kruit & Searle (1981a,b). However, in the analysis of observations the vertical distribution of the emission is often fitted by a Gaussian instead of a sech^2 function as done by Langer et al. (2014a), who studied the vertical distribution of the [C II] line emission in the Milky Way. The authors fitted the [C II] emission with

$$f(z) = f(z_{\rm shift}) \exp\left\{-0.5 \times \left(\frac{z - z_{\rm shift}}{z_0}\right)^2\right\}. \tag{5.3}$$

Their scale height z_0 is related to the full width at half maximum of the peak by

$$\mathrm{FWHM} = 2(2\ln(2))^{0.5} z_0 \approx 2.35 \cdot z_0. \tag{5.4}$$

The offset of the peak is taken into account by $z_{\rm shift}$ (Langer et al., 2014a).

5.1.2 Scale height via Variance

When studying in observations the distribution of the emission around the midplane, the assumption of a Gaussian distribution is not necessarily fulfilled. One example is the [C I](1 − 0) line emission at $\nu = 492$ GHz of carbon atoms on local scales in the Milky Way, which was studied in the PhD thesis of Glück (2016). His studies and a later comparison with our simulations are presented in Section 5.4.1. Since the distribution of the emission is no longer Gaussian, one needs a different method for quantifying its width.

We calculate the variance of the [C II] intensity distribution and use it as a measure of the scale height. In the case of a Gaussian distribution the square root of the variance corresponds to the same scale height z_0 as defined in Eq. (5.3) in Section 5.1.1. The variance Var is given by

$$\mathrm{Var} = \frac{\int I(z)(z - \bar{z})^2 dz}{\int I(z) dz}, \tag{5.5}$$

where the mean value $\bar{z}$ is calculated as

$$\bar{z} = \frac{\int I(z) z dz}{\int I(z) dz}. \tag{5.6}$$

Since our emission profile is discrete, we replace the integral with a sum over all z. The step size is dz = 4 pc, which corresponds to the size of one cell in the simulation, given by the spatial resolution in these simulations. Measuring the distribution of the emission with the variance has the advantage that the faint emission is taken into account. Since the faint emission is in most of the boxes asymmetric, it cannot be fitted by a Gaussian, and is therefore hard to consider. The variance provides us a measure of the outflowing gas traced by the [C II] line emission.

Table 5.1: Peak intensities and luminosities of the synthetic [^{12}C II] line emission maps for the run *S10–KS–rand* at different times. The maximum average intensities I_0 for the vertical profiles of the simulation at different time steps (Fig. 5.2) are listed in the fourth column.

	[^{12}C II]		
time	$I_{\rm peak}$	$L_{\rm tot}$	I_0
[Myr]	[K km s^{-1}]	$\times 10^3$ [L$_\odot$]	[K km s^{-1}]
30	36	13.19	3.33
50	114	17.16	5.61
70	181	16.68	7.44
90	133	11.26	4.02

5.2 Analysis

5.2.1 Analysis of S10-KS-rand

We study the distribution of the emission in more detail using the run *S10-KS-rand*. The synthetic [C II] emission maps of this run at time steps between 30 and 90 Myr are shown in Fig. 5.1. As in Fig. 3.5 the second colour bar provides an impression of the intensity in K km s^{-1}, as the velocity integrated and the frequency integrated maps do not scale linearly. At all evolutionary states there is strong [C II] line emission from the region in and around the disc midplane, where, according to the analysis of Walch et al. (2015; section 4.1 and fig. 4 therein), the molecular clouds are located. These are clearly visible in the face-on [C II] synthetic emission maps. At larger distances from the midplane there is fainter [C II] line emission that expands with time, tracing the gas outflowing from the midplane (see Walch et al., 2015, Girichidis et al., 2016b).

In order to study the distribution of the emission around the midplane we calculate the vertically averaged and normalized emission profiles of the synthetic emission maps. For the maps of the simulation *S10–KS–rand* shown in Fig. 5.1 the corresponding profiles are presented in Fig. 5.2. We calculate the average intensity at every height z by averaging the integrated intensity for a given z-position along the x-direction in the synthetic emission maps. For each time step, we compute the maximum of the averaged intensity, I_0, which we use for normalisation. The values for I_0 are given in the upper part of Table 5.1.

Connection to the density and temperature

In Franeck et al. (2015), we presented an example of the analysis of the scale height of the synthetic [C II] emission map and the corresponding intensity profile for the simulation *S10–KS–rand* at $t = 50$ Myr. Here we expand upon this preliminary analysis. In Fig. 5.3 we show the [C II] intensity profile of the simulation *S10–KS–rand* at $t = 50$ Myr for gas in several different temperature regimes. The black line shows

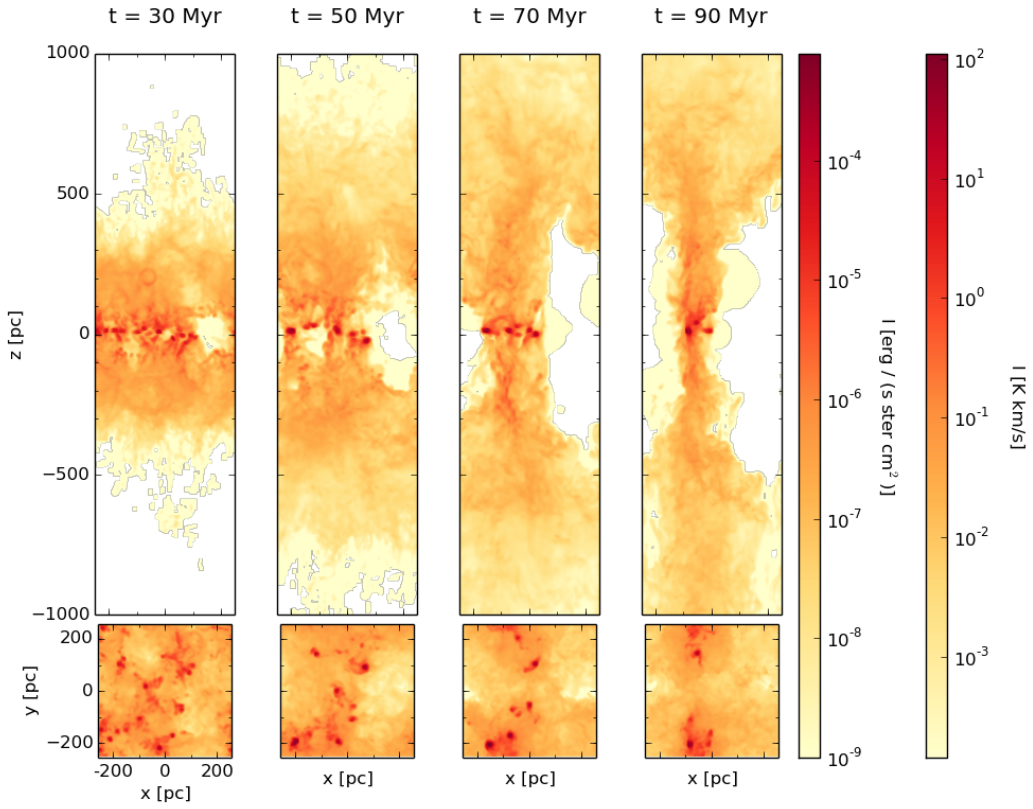

Figure 5.1: Synthetic [C II] emission maps of the simulation *S10–KS–rand* at evolutionary times of $t = 30$, 50, 70 and 90 Myr, as indicated above the panels. The synthetic emission maps are shown from an edge-on view (top panels) and a face-on view (bottom panels). Strong [C II] line emission is visible in and around the midplane from molecular clouds at all evolutionary stages. The faint emission from outflowing gas below and above the midplane expands with time.

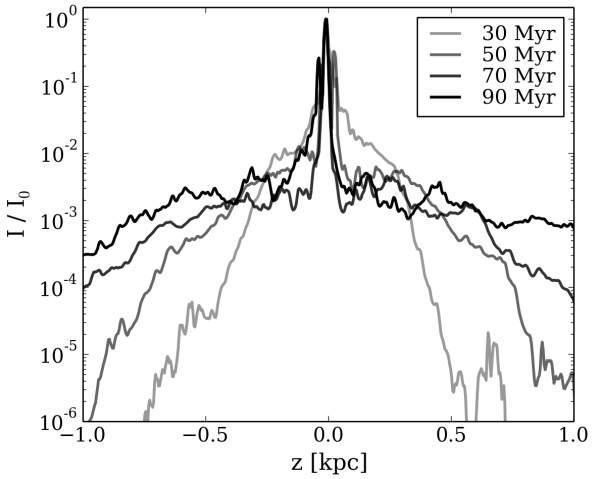

Figure 5.2: Vertical averaged profiles of the normalised integrated [C II] intensity I/I_0 for the run *S10–KS–rand* presented in Fig. 5.1 at different time steps. I_0 is the maximum of the averaged intensity at each time and is listed in Table 5.1. With increasing time the faint emission expands.

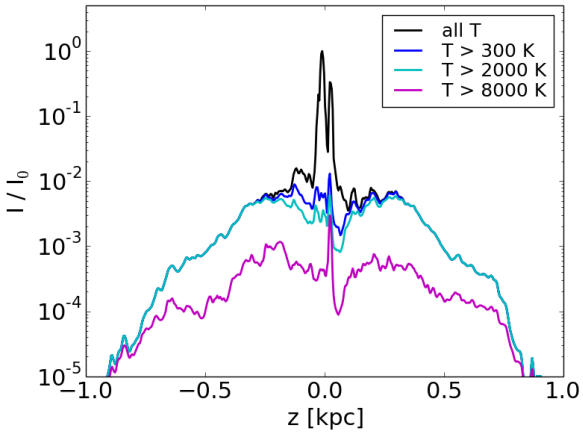

Figure 5.3: Normalised intensity profiles of the simulation *S10–KS–rand* at $t = 50$ Myr for four different temperature cuts. The three components found in the total [C II] intensity profiles originate from gas at different temperatures.

the total profile, while the blue, cyan, and magenta lines show the contributions from gas with temperatures greater than 300, 2 000, and 8 000 K, respectively. A narrow component *(a)* around the midplane stems from cold gas below temperatures of 300 K. This component is surrounded by warmer gas with lower density, corresponding to component *(b)*. At high temperatures we find a faint but vertically extended component *(c)*.

This pattern is found at all time steps in this simulation (cf. Fig. 5.2), so that we in general can distinguish between three different components:

- component *(a)*: one or several narrow intensity peaks caused by the molecular clouds near the disc midplane
- component *(b)*: a broader but less intense component around the midplane
- component *(c)*: an extended, very faint component, whose width increases with time due to the outflowing gas.

In Fig. 5.4 we compare in the left panel the total [C II] intensity profile to the averaged vertical column density profiles of the different chemical species. Since CO is only formed in very dense and cold regions, $x_{\mathrm{C,ion}} \approx x_{\mathrm{C,tot}}$ for most parts of the simulation and thus, C^+ is present as a constant fraction in the gas. Therefore, the vertical C^+ density profile is similar to the total density profile. In the right panel of Fig. 5.4 we over-plot the [C II] intensity profile (orange line) and the C^+ column density profile (black line). Both show similar features in the inner and outer regions. In the outer regions of the profile ($|z| \gtrsim 0.5$ kpc) the vertical [C II] line profile follows the averaged column density profile. In the inner region, the [C II] line emission is larger due to stimulated emission of [C II]caused by the presence of the collisional partners.

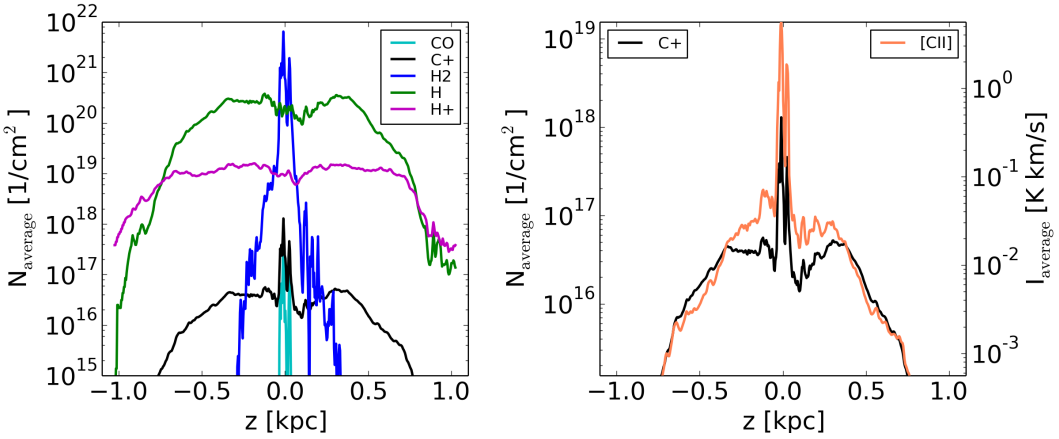

Figure 5.4: Vertical profiles of the averaged column densities of the followed chemical species for run *S10–KS–rand* at $t = 50$ Myr (left panel). In the right panel, the vertical [C II] line emission profile (orange) is compared with the column density profile of C^+ (black).

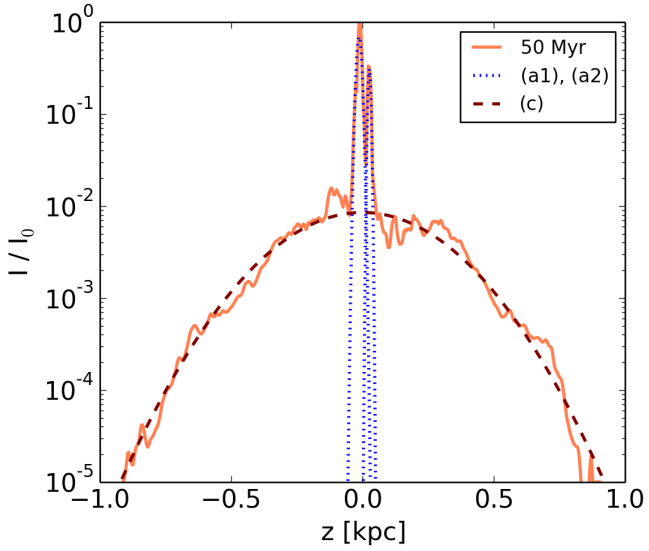

Figure 5.5: Fit of the components *(a)* and *(c)* to the normalised vertical [C II] intensity profile. There are two narrow components *(a1)* and *(a2)* around the midplane fitted separately. The scale heights of the Gaussians of the components are $z_{a1} = 5 \pm 0.5$ pc, $z_{a2} = 9 \pm 1$ pc and $z_c = 250 \pm^{57}_{10}$ pc.

Quantifying the distribution

The vertical intensity profiles of *S10–KS–rand* are not describable by a single Gaussian function, but the individual components are. We therefore fit Gaussians to every single component in order to quantify the distribution. As fitting routine we use the progam MAGIX (Möller et al., 2013). We fit the logarithm of our data. MAGIX has the advantage that different swarm and fit algorithms, which are already implemented, can be combined in order to find a good set of fitting parameters. We first look for good initial parameters with the bees swarm algorithm before fitting the profiles with the Levenberg–Marquardt algorithm.

In addition, MAGIX also provides error estimates for the fits. For this purpose, the standard deviation of the average value at each point in the profile is taken into account. The two narrow components *(a)* have each the fitting parameters f_a (amplitude), z_a (scale height) and $z_{\mathrm{shift,\,a}}$, and component *(c)* is fitted with f_c, z_c centred around $z_{\mathrm{shift,\,c}} = 0$. The sum of these components describes the total intensity profile.

$$f_{\mathrm{fit}}(z) = a_1 \cdot e^{-0.5\cdot\left(\frac{z-z_{\mathrm{shift,\,a1}}}{z_{a1}}\right)^2} + a_2 \cdot e^{-0.5\cdot\left(\frac{z-z_{\mathrm{shift,\,a2}}}{z_{a2}}\right)^2} + c \cdot e^{-0.5\cdot\left(\frac{z}{z_c}\right)^2} \tag{5.7}$$

The intermediate component *(b)* is not considered in the fitting routine, since its contribution from gas at $100\,\mathrm{K} < T < 2\,000\,\mathrm{K}$ is weak and asymmetric, and therefore negligible. In Fig. 5.5 we over-plot the fitted components to the vertical intensity profile. At $t = 50$ Myr we derive the following scale heights: $z_{a1} = 5 \pm 0.5$ pc, $z_{a2} = 9 \pm 1$ pc, and $z_c = 250^{+57}_{-10}$ pc. The scale heights z_{a1} and z_{a2} are very narrow and in the order of magnitude of the resolution of the simulation (3.9 pc). The corresponding FWHM of these scale heights z_{a1} and z_{a2} are ∼12 pc and ∼21 pc (see Eq. (5.4)), and thus represented by 3 to 5 grid cells.

5.2.2 Analysis of SILCC with fixed SNe

The vertical emission profiles of all the simulations with fixed SNe are shown in the first two rows of Fig. 5.6. The corresponding synthetic emission maps were presented earlier in Fig. 3.5. The vertical profiles are in general not Gaussian. The runs with random and mixed driving are more symmetric than runs with clustered driving, which show a more asymmetric outflow structure. Only for the run with randomly distributed SNe the single components in the profiles are similar to Gaussians. Run *S10–lowSN–rand* has a lower SN rate, resulting in a more narrow [C II] profile than the other simulations (see upper left panels of Fig. 5.6).

Due to the complex structure of the vertical emission profile in general we quantify the distribution by calculating their scale height with the variance, as described in Section 5.1.2. The square root of the variance corresponds to the scale height z_0, as defined in Eq. (5.3). We carry out this analysis for several time steps of each simulation, and thus, studying the evolution of the scale height. In Fig. 5.7 we show the

Table 5.2: Same as Table 5.1, but for the SILCC-01 (upper part) and SILCC-02 (lower part) simulations at $t = 50$ Myr.

	[^{12}C II]		
Run	$I_{\rm peak}$	$L_{\rm tot}$	I_0
[Myr]	[K km s^{-1}]	$\times 10^3$ [L$_\odot$]	[K km s^{-1}]
S10–lowSN–rand	36	4.5	13.40
S10–KS–rand	114	17.2	5.61
S10–KS–peak	4	7.6	0.83
S10–KS–mix	164	27.1	10.83
S10–KS–clus	204	35.1	20.13
S10–KS–clus2	189	26.3	10.18
S10–KS–clus–mag	123	16.8	5.53
FSN	56	11.5	2.91
FWSN	74	7.7	2.03

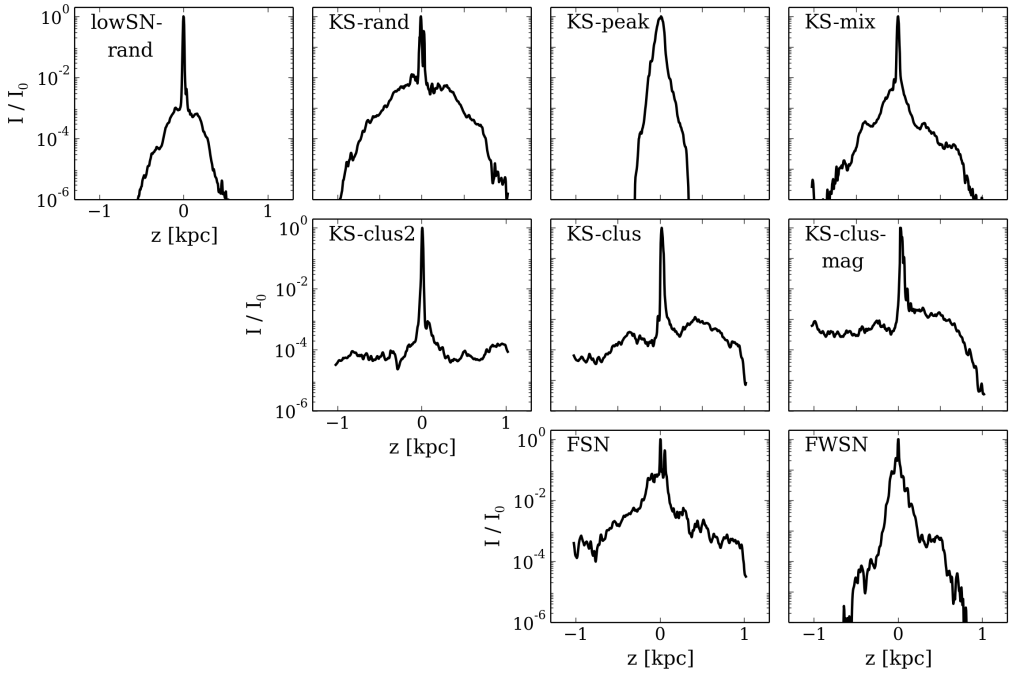

Figure 5.6: Vertical profiles of the normalised average intensity I/I_0 of the [C II] synthetic emission maps for the same runs as shown in Fig. 3.5. The corresponding values of I_0 are listed in Table 5.2. The first two rows show the profiles for the SILCC-01 simulations. The two profiles in the bottom row are from the SILCC-02 simulations with sink particles. An intense contribution from a narrow region around the disc midplane is found in all simulations but *S10–KS–peak* (see third panel in the first row). Simulations with a clustered and mixed distribution of the SNe show an asymmetric profile.

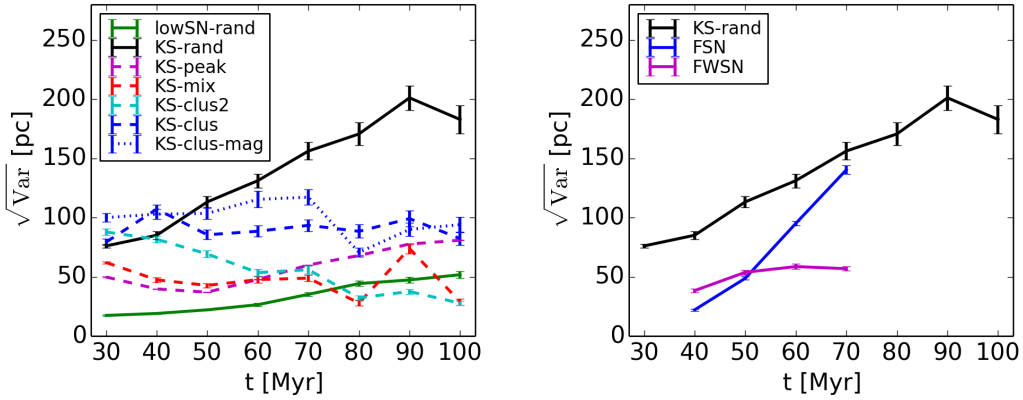

Figure 5.7: Evolution of the scale height for the SILCC-01 (left) and SILCC-02 (right) simulations, where the scale height is determined from the square root of the variance (cf. Eq. 5.5). For comparison, the evolution for run *S10–KS–rand* is also shown in the right panel.

results for the simulations with fixed SNe (SILCC-01) in the left panel. The errors are calculated with error propagation using the standard deviation of the mean intensity at each z position. The scale height obtained by this method increases when the peak of the [C II] emission near the midplane is less pronounced and/or if the peak becomes broader. For *S10–KS–rand* (black line) the vertical extent of the envelope component *(c)* increases with time while the central peak intensity changes only little. Therefore the scale height increases from ~70 pc at early times to ~200 pc at late times. For comparison, the [C II] scale height of the Milky Way measured by Langer et al. (2014a) is 73 pc.

The other SILCC-01 simulations, which include different SN driving schemes, do not show such a clear trend of $\sqrt{\mathrm{Var}}$ as a function of time. Their evolution of the scale height is rather flat, while some runs show high variability (e.g. *S10–KS–mix*, which has the highest molecular hydrogen fraction) or even a decrease (e.g. *S10–KS–clus2* which has quite strong outflows and blows away most of the disc before ~70 Myr). On average the scale heights range between ~50 pc and ~120 pc for runs with a Kennicutt–Schmidt SN rate. The run with a lower SN rate also gives a smaller scale height of $\lesssim$50 pc. Overall, the evolution of the scale heights show similar trends as Girichidis et al. (2016b) found for the vertical heights enclosing 60% of the mass in the simulations (cf. section 5 and fig. 8 therein).

5.2.3 Analysis of SILCC with sink particles

The vertical emission profiles of the simulations with sink particles are shown in Fig. 5.6 in the last row. They have a less extended outflowing component due to their reduced SNR, which is asymmetric around the midplane. In the right panel of Fig 5.7 the evolution of the scale heights of the simulations with self-consistent feedback and, for comparison of *S10–KS–rand*, are presented. The maximum val-

Table 5.3: Summary of the chosen distances and the resulting spatial resolutions for the convolution of the synthetic maps with a Gaussian beam of $\theta_{\rm FWHM} = 11.5''$. The corresponding values of $z_{0,\rm min}$ as calculated using Eq. (5.4) are listed in the third column. We expect a scale height of $3 \times z_{0,\rm min}$ to be reliably measured by such observations.

Distance [Mpc]	$\theta_{\rm FWHM}$ [pc]	$z_{0,\rm min}$ [pc]
0.5	28	11.9
1.0	56	23.8
2.5	139	59.1
5.0	279	118.4

ues of the averaged vertical profiles I_0 are listed in the lower part of Table 5.2. For *FSN* the scale height increases rapidly with time due to the high SNR. Since the SN explosions set in at later times compared to *S10–KS–rand*, the increase of the scale height starts at later times. The lower SNR in *FWSN* causes a smaller increase in the scale height, since the outflowing gas component is smaller.

5.3 Convolution with a Gaussian beam

So far, the [C II] synthetic emission maps that we have been analysing are idealised in the sense that the only factor limiting their resolution is the resolution of the underlying hydrodynamical simulation. In reality, the finite angular resolution of our observations will often be a much bigger limitation on the physical scales than the simulation's resolution. To investigate the impact of finite angular resolution on the vertical profiles derived from our synthetic emission maps, we have explored what happens when we convolve the maps with a Gaussian beam. We keep the angular size of the beam fixed at $\theta_{\rm FWHM} = 11.5''$, corresponding to the *Herschel* PACS beam size at the frequency of the [C II] line (Hughes et al., 2015), and consider the effect of placing our simulated galaxy at several different arbitrary distances: $d = 0.5, 1.0, 2.5$ and 5.0 Mpc. These distances are still smaller than the ones of the Milky Way like galaxies NGC 891 with d $\sim$ 10 Mpc (Karachentsev et al., 2004, Mouhcine et al., 2010) or NGC 1232 with d $\sim$ 22 Mpc (Nasonova et al., 2011), but give a basic impression of the emission seen from some distance observed with an instrument. As we increase the distance to the galaxy, the spatial resolution of our beam decreases proportionately. Table 5.3 lists the spatial resolution of the beam in the four cases we examine, as well as the corresponding scale height, $z_{0,\rm min}$, which is related to the FWHM as described in Eq. (5.4). We expect that an observation can measure scale heights of $3 \times z_{0,\rm min}$ reliably.

Figure 5.8 shows the convolved synthetic [C II] emission maps that we obtain from run *S10–KS–rand* at $t = 50$ Myr for our four different distances, corresponding to different values of $\theta_{\rm FWHM}$ in physical units. The corresponding vertical profiles are shown in Fig. 5.9. With decreasing spatial resolution, the signal from the

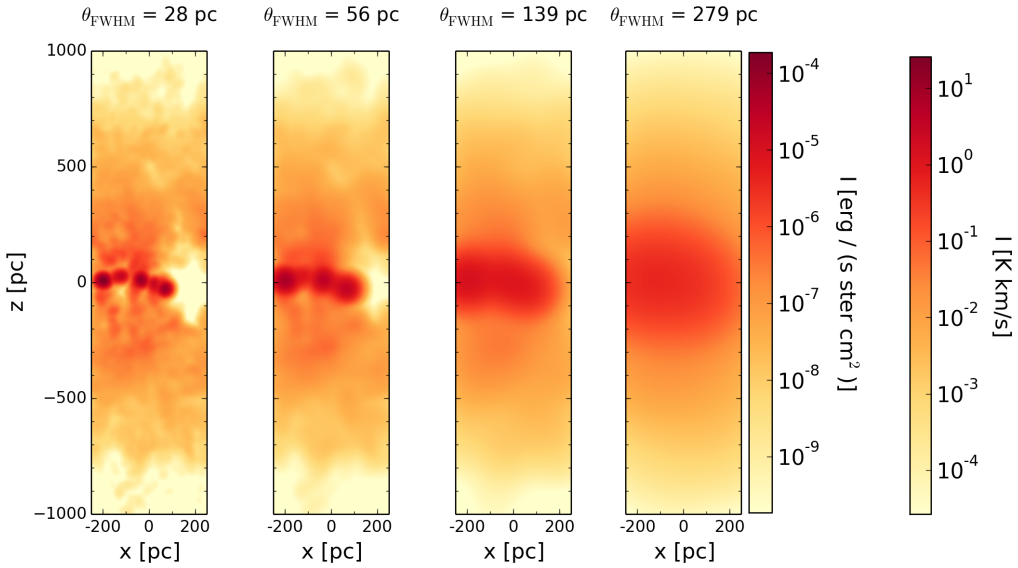

Figure 5.8: Synthetic [C II] emission maps based on run *S10–KS–rand* at $t = 50$ Myr and convolved with a Gaussian beam of size $\theta_{\rm FWHM} = 11.5''$ for several different distances (from left to right) $d = 0.5$, 1.0, 2.5, and 5.0 Mpc. The resulting spatial resolutions are indicated above the figures.

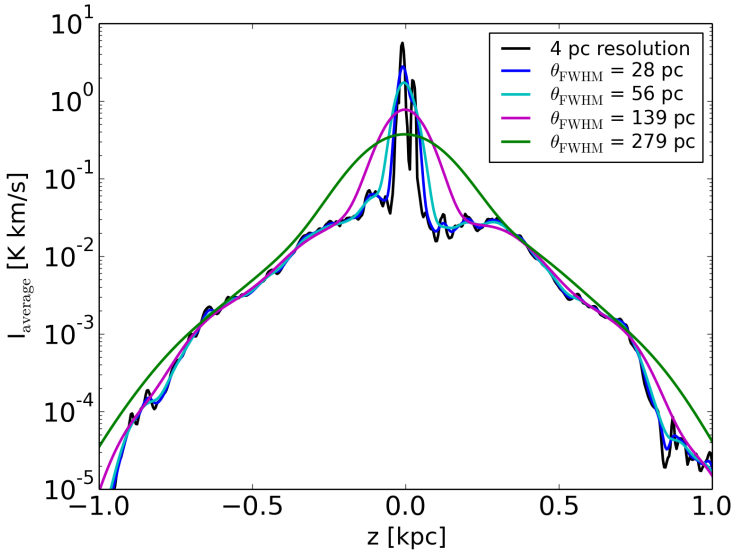

Figure 5.9: Vertical profiles of the convolved synthetic emission maps shown in Fig. 5.8. The maps were done for the run *S10–KS–rand* at $t = 50$ Myr, and convolved for different spatial resolutions, as indicated with the physical size of $\theta_{\rm FWHM}$ (see text). The narrow peak around the midplane is smeared out with larger spatial resolution.

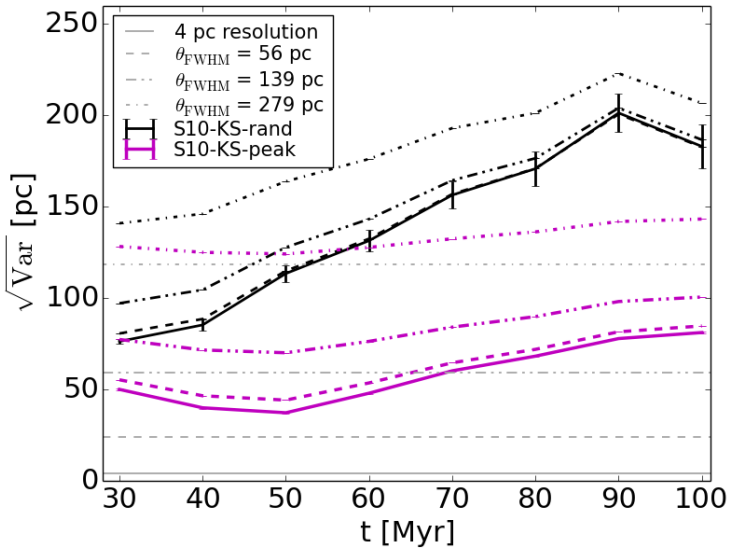

Figure 5.10: Evolution of the scale height for the simulations *S10–KS–rand* (black lines) and *S10–KS–peak* (magenta lines) as determined by applying the variance method to the convolved synthetic emission maps with different spatial resolution. The grey horizontal lines indicate the minimum scale height $z_{0,\mathrm{min}}$ corresponding to the resolution (cf. Table 5.3). The individual scale heights increase with larger spatial resolution, but the overall evolution follows the same trend for low and high resolutions.

narrow, dominant intensity peak near the midplane is smeared out. Furthermore, the difference in intensity of the peak and the surrounding emission decreases as substructures in the extended disc and halo are steadily washed out. Nevertheless, the peak intensity of the convolved map with a spatial resolution of $\theta_{\mathrm{FWHM}} = 279$ pc is $I_{\mathrm{peak}} = 0.56$ K, corresponding to $\sim 3.90 \times 10^{-6}$ erg/(s ster cm^2), which is still above the assumed detection limit of 0.5 K km s^{-1} (see Section 3.4).

We compute the scale height of these profiles with the variance method described in Section 5.1.2. The results are presented in Fig. 5.10 for two examples, run *S10–KS–rand* (black lines) and run *S10–KS–peak* (magenta lines). The different spatial resolutions are indicated by different line styles. In addition, the grey horizontal lines show the minimum scale height for each resolution $z_{0,\mathrm{min}}$. We clearly see that the scale heights in the convolved maps are systematically larger than the real scale height. With increasing θ_{FWHM} physical size this effect becomes worse. Using the coarsest beam, the scale height for run *S10–KS–rand* would be overestimated up to $\sim 40\%$. For run *S10–KS–peak*, beam smearing severely dominates the result and the scale height is overestimated by a factor of 2 ($\sim 100\%$). As we assume that observations could resolve reliably a scale height of $3 \times z_{0,\mathrm{min}}$, we find in Fig. 5.10 all convolved scale height to be unresolved, which is in accordance with the fact, that the convolved scale heights are artificially enlarged.

5.4 Discussion

5.4.1 Comparison with observations

The profiles of the synthetic [C II] emission maps from the SILCC-01 and SILCC-02 simulations show in general a complex structure. In all simulations there is faint [C II] line emission surrounding the signal from the midplane, where the molecular clouds are situated. This faint emission is in line with observations in the Milky Way by Makiuti et al. (2002). They suggest that this faint emission stems from the WIM. The faint emission in the SILCC simulations stems dominantly from WNM, but due to the absence of photoionization feedback in the SILCC simulations, the gas surrounding the midplane remains largely atomic (Walch et al., 2015). When including photoionization feedback, we expect the gas to become ionized due to ionizing photons escaping from the midplane (see e.g. Barnes et al., 2014).

In general, the profiles we find are not describable by one single Gaussian. Only the vertical profile of the simulation *S10–KS–rand* at $t = 50$ Myr can be represented by the composition of several Gaussians, taking into account the contributions from the cold, molecular gas, and the faint broad contribution from the warm gas surrounding the midplane. We found scale heights of $z_{a1} = 5 \pm 0.5$ pc, $z_{a2} = 9 \pm 1$ pc, and $z_c = 250^{+57}_{-10}$ pc. The fact that our vertical emission profiles show a complex shape seems to stand in contrast to the results from observations: Langer et al. (2014a) analysed FILM, BICE and GOT C+ data and estimated the vertical distribution of the [C II] emission in the Milky Way by combining the GOT C+ survey at $b = 0°$ ($\theta_{\mathrm{FWHM}} = 12''$) with BICE for other latitudes ($\theta_{\mathrm{FWHM}} = 12.4'$) . By averaging the data over the whole galactic plane with all its varying physical conditions they obtain one vertical profile. For this profile, they find a [C II] scale height of 73 pc for the Milky Way, by fitting it with one Gaussian and using the definition of the scale height z_0 as presented in Eq. (5.3). This is wider than our narrow components of $z_{a1} = 5 \pm 0.5$ pc and $z_{a2} = 9 \pm 1$ pc. Velusamy & Langer (2014) analysed the z distribution of the different gas components visible in [C II] in the Milky Way separately. They distinguished between dense H_2 gas (coming from regions where they also detected CO), diffuse CO–faint H_2 gas and diffuse H I or WIM (where no CO is detected). Velusamy & Langer (2014) find scale heights of ~55 pc, 86 pc and 139 pc, respectively, for these three phases. Our scale heights z_{a1} and z_{a2} from the peak around the midplane are smaller than the scale heights Velusamy & Langer (2014) found for the different components, whereas their scale height for the WIM is smaller compared to z_c.

Possible reasons for the differences between our simulations and the observations are *(i)* that the observations are averaged over entire galaxies, and hence over regions with a range of different physical conditions. Our simulations are designed to reproduce the behaviour of one small part of the ISM, and will not necessarily do a good job of predicting the behaviour of the [C II] emission in regions such as the Galactic centre or the outer parts of the Galactic disc. In this context, it is interesting

to note that Shibai et al. (1991) found in their study of the Milky Way a narrow peak in the [C II] line emission signal at the position of the W43 molecular cloud complex, demonstrating that there is at least some observational support for the idea that molecular clouds can cause a sharp, intense and localized signal. The assumption of a Gaussian shaped vertical intensity profile might therefore only be valid when averaged over much larger regions than those considered in our simulations. Langer et al. (2014a) also provide the results of Sanders et al. (1984) for the scale height of the ^{12}CO emission in the Milky Way. They find a scale height of $z_0 = 46.7$ pc for CO, not much smaller than their scale height for [C II]. Rice et al. (2016) indicate that the molecular clouds in the Milky Way can be displaced from the galactic plane up to 100 pc. However, since in our simulation the molecular clouds are not seen in superposition on the vertical axis, we have a small scale height of the molecular gas, and find that the vertical distribution of the [C II] emission from the midplane follows this trend. *(ii)* There are indications that the Milky Way is warped in the outer disc (Burton & te Lintel Hekkert, 1986, Momany et al., 2006). Seen from edge on, the positions of the molecular clouds are therefore distributed over a larger vertical height resulting in larger scale heights. The scale heights Langer et al. (2014a) measure is therefore an upper limit of the vertical distribution of the emission. As we do not model the full disc, our simulations cannot account for this effect. *(iii)* Furthermore, the observations discussed above have a limited spatial resolution. Convolving the synthetic emission maps to larger spatial resolutions shows that the emission from the narrow peak smears out over a larger region. This likewise causes an increase of the inferred scale height. Note further that the viewing angle of the study by Langer et al. (2014a) due to our position inside the Milky Way might influence their result and enlarge the scale height. *(iv)* Finally, there are several caveats regarding missing or simplified physics in our simulations that might potentially impact our results on the [C II] scale height.

Within the SILCC project we do not provide simulations of a whole galaxy, but compute the evolution of the ISM in a local surrounding of 0.5 kpc $\times$ 0.5 kpc. However, to compare our simulations with observations, we need observational studies of the *local* vertical distribution of the emission around the midplane of a galaxy. Using the velocity information of a signal it is possible to disentangle the kinematic distance of the source towards the sun and the Galactic Center (see Burton et al., 2013, Glück, 2017), and thus, estimate the position within the galactic disc. Knowing the distance of the source allows to convert the longitudinal coordinate b to a physical distance z [pc] from the midplane. Glück (2017) followed such a procedure in his work when analysing CO and [C I] emission in the fourth quadrant of the Milky Way at galactic latitudes between $-2^\circ < b < 2^\circ$ (b–strips) at eight different galactic longitudes (l = 306.0°, 315.6°, 323.1°, 300.0°, 336.4°, 342.5°, 348.0°, 354.0°). For his model he used the Galactic rotation curve of Brand & Blitz (1993). He calculates the kinematic distances for each source and bins adjacent sources into boxes (see Glück, 2017, section 6.4.2, fig. 6.17 therein). From these boxes he carries out averaged emission profiles, which provide such a local surrounding we are looking for. Keep in mind that he studies CO emission lines and [C I] emission, but however, this is a starting point.

The emission profiles of the local boxes are shown in fig. 6.18 of Glück (2017).

The profiles of the CO emission lines and the [C I] emission do not vary much. It is striking that none of the profiles show a single Gaussian vertical distribution. Instead, these profiles consist of the contributions from various sources distributed around the galactic midplane. The median position z_c follows the warp of the galactic plane (see Glück, 2017, section 6.4.3, fig. 6.19 therein). The scale height of a single peak is $z_0 \approx 10$ pc, which is in good agreement with the scale height we found for the emission of the cold, molecular gas in the Galactic plane of the SILCC simulations. In order to quantify the distribution of the emission around the galactic plane, he calculates the square root of the variance, as we did likewise in Section 5.1.2. The scale heights he find for [C I] and the CO observations are between $25\,\mathrm{pc} \lesssim z_0 \lesssim 50\,\mathrm{pc}$ and increase by a root function with increasing distance of the box towards the Galactic Center (see Glück, 2017, fig. 6.19, and tables 6.5 and 6.6 therein).

In order to compare our [C II] scale heights with observations we need such local observations of the [C II] from the Milky Way. Observations with GREAT and upGREAT onboard SOFIA for some of the b–strips already studied in CO and [C I] by Glück (2017) could be an option. This might be part of future work.

5.4.2 Influences on the simulations

In the SILCC simulations we find in most simulations a thin disc that does not fit with the observations when averaging over the whole Milky Way. In addition to the issues discussed above, concerning the point that most of the observational studies have averaged the data over a large range in the Milky Way, the setup of the simulation also differs from the system found in nature. These can be caused by the included physical mechanisms, or by the simplifications assumed for the simulation.

We found the discs of the SILCC-02 to be broader than for the SILCC-01 simulations. This is caused by the initially driven turbulence, which is necessary to create a complex density structure for the self-consistent formation of stars. Thus, the turbulent motion is one aspect to influence the thickness of the disc.

Although the formation of sink particles is included self-consistently in the SILCC-02 simulations, none of the simulations account for radiative feedback. Such a feedback would ionize the gas on large scale, and thus, might increase the contribution of the [C II] line emission at higher altitudes, since collisions with electrons are more efficient than with atomic hydrogen to excite carbon ions. Thus, photoionization feedback might enhance the emission from the surrounding gas, but might not change the overall structure of the profiles. Further, the photoionization feedback would cause the formation of dense PDRs, or H II regions around stars. According to Pineda et al. (2014), roughly 50% of the [C II] line emission stems from dense PDRs or H II regions. Thus, our simulations only account for the other 50% of the emission, associated with the cold molecular and atomic gas phase. The interstellar radiation field (ISRF) yields to the formation of PDRs on the outer surfaces of the molecular clouds in the simulations. However, we miss the

formation of substructures of molecular clouds and their PDRs on scales smaller than 4 pc. This limit is set by the spatial resolution in the SILCC simulations. Concerning PDRS, this effect becomes larger for larger ISRF. For an ISRF of $G_0 = 1.7$, we expect the effect of substructures from PDRs to be small (Andree-Labsch et al., 2017). Molecular clouds with sizes smaller than 4 pc, are likely to be distributed on larger vertical scale around the thin midplane (Stark & Lee, 2005). Thus, we expect a larger scale height in simulations, that are able to resolve them.

The implementation of the SNe changes the distribution of the gas phase, as shown in Walch et al. (2015), Girichidis et al. (2016b). In the SILCC-01 simulations, a constant SNR is assumed, and thus, the simulated ISM is unable to self-regulate (Girichidis et al., 2016b). As a result, massive molecular clouds form within these simulations with an artificially long lifetime. The explosions of SNe in the simulations with randomly, clustered, or mixed distributed SNe are unable to destroy the massive clouds. Only the peak driven SN implementation does this, but this simulation fails to produce the hot gas, and thus, is not a good model for the real ISM (Walch et al., 2015). In the SILCC-02 simulations the formation of stars, and by this the explosions of SNe is implemented self-regularly. These simulations have molecular clouds distributed on larger scales around the galactic midplane. Including the feedback of stellar winds then reduces the formation of stars, thus the SNR is smaller, and the outflowing gas and the scale height of the disc is likewise reduced.

Cosmic rays (CR) as a further feedback process, can likewise influence the scale height of the disc. In the SILCC simulations, they are not taken directly into account. Girichidis et al. (2016a) study the influence of CR on the evolution of the ISM. They carry out a set of MHD simulations, in which the SNe inject purely thermal energy, purely CR or both thermal energy and CRs. CRs in general can escape the dense gas regions of star formation and thus, they generate a stable vertical pressure gradient (Girichidis et al., 2016a). Therefore the vertical structure of the disc is influenced. The gas from the midplane is pushed away and an extended atmosphere is formed. The heights of 90% enclosed mass increase from ∼30 pc (purely thermal energy simulation) to ∼1500 pc (purely CR) and ∼300 pc (both thermal energy and CR injection). Girichidis et al. (2016a) show that the density distribution they obtain from the simulations with CRs are in agreement with the expected vertical gas density distribution by Dickey & Lockman (1990).

Magnetic fields on the other hand are found to leave the vertical structure of the disc unaffected (Hill et al., 2012b,a). This is in agreement with our simulation *S10–KS–clus–mag*, which likewise show the thin disc from the molecular clouds in the midplane. Only the emission from the surrounding gas might be a bit higher ($\sim 10^{-4}$ to 10^{-3} of the vertically averaged, and normalized intensity profile, see Fig. 5.6) compared to the surrounding emission in the other simulations ($\lesssim 10^{-4}$).

Finally, the simplified chemical model in connection with the limited spatial resolution of 4 pc might influence the result found here. Glover & Clark (2012) benchmarked the model by Nelson & Langer (1997) against various other CO for-

mation models of varying degrees of sophistication and showed that it predicts an earlier transition (at lower density and A_V) from C^+ to CO than is found in more sophisticated models. However, since the molecular clouds in the disc midplane can be be small, as we found scale heights of the [C II] line emission originating from them around ~5 pc, there are only small regions in the simulation in which C^+ is converted to CO. Since hydrogen needs less shielding compared to carbon to be transformed in its molecular state, C^+ coexist with H_2 in those molecular clouds, producing the strong signal from the midplane.

6

Origin of the [C II] line emission

In nature the [C II] emission line can be produced in several different phases of the ISM, namely *(i)* regions of warm gas with ionized hydrogen (H II regions), *(ii)* dense PDRs surrounding bright O and B stars, *(iii)* diffuse molecular gas and *(iv)* in warm or cool atomic gas (WNM and CNM, respectively; see e.g. Velusamy & Langer, 2014). In our simulations we do not account for the radiative feedback of individual stars formed during the evolution of the ISM. Therefore, only PDRs formed due to the interstellar radiation field (ISRF) on the outer surfaces of molecular clouds are included. Especially in the SILCC-01 and SILCC-02 simulations we miss substructures of the gas, since the spatial resolution in those simulations is 4 pc. The substructures are better resolved with the zoom-in simulations, where the spatial resolution is 0.122 pc. Despite these limitations, we can usefully explore the contribution made by the WNM, CNM and the diffuse molecular phase.

We aim to study the origin of the [C II] line emission from the ISM in the zoom-in simulations. As we found in Sections 4.1.3 and 4.2.1, the [^{12}C II] line simulations are affected by optical depth effects. With the origin of the emission we study a local property of the gas, and therefore need an optically thin tracer. The optically thin [C II] line emission, corresponding to the [^{13}C II] line, is suitable for this purpose, since it originates from the same regions as the opacity affected [^{12}C II] line emission. We know from the simulations the physical properties of every grid cell, and take selectively only cells below or above a certain limiting value. With this selection of cells, we calculate a synthetic emission map and estimate the luminosity over the whole map with Eq. (3.39). Since we use an optically thin tracer, we can build up the total luminosity of the synthetic emission map by increasing (decreasing) the limiting value of the parameter. The results are then presented in a cumulative plot. For classifying the parameter range from which the [C II] emission originates, we record the parameter values at which 25%, 50% and 75% of the total luminosity are reached. The difference between the parameter characterizing 25%

and 75% of the total luminosity is called interquartile range. The parameter value for which 50% of the total luminosity is reached, is called median.

We proceed in the described manner, analysing the origin of the emission with respect to the kinetic temperature of the gas T and its total number density n, as well as with respect to the fractional amount of molecular hydrogen x_{H_2} and the visual extinction A_V. The radiation field G and the visual extinction A_V are connected by

$$G = G_0 \times e^{-2.5 A_V} \tag{6.1}$$

with the Habing field $G_0 = 1.7$ and the shielding factor of dust as $e^{-2.5 A_V}$. The Habing field gives the strength of the radiation field with 1.6×10^{-3} erg cm^{-2} s^{-1} (Habing, 1968).

We first investigate the origin of the [C II] line emission for the SILCC-01 simulations, having a fixed SNR. Here, we use the run *S10–KS–rand* at $t = 50$ Myr for a detailed study. Thereafter, we present the same analysis for the SILCC-02 simulations with sink particles, and investigate more details on the example of run *FWSN*. Last, we show the results for zoom-in simulation MC2. Note, that the method used in the whole Section and the results concerning the analysis of MC2 were submitted to be published in MNRAS in May 2018 (Franeck et al., 2018). Further, large parts of the discussion were also partly subject in the mentioned publication.

6.1 Simulations with a fixed SNR

6.1.1 Temperature dependence

We carry out a series of radiative transfer calculations, each of which only takes into account the contribution from cells below a limiting temperature T_i, as $T < T_i$. We increase T_i from 10 K to 10^5 K. The resulting cumulative plot for run *S10–KS–rand* at $t = 50$ Myr is shown in the upper left panel of Fig. 6.1. The upper right panel shows the result as the derivative of the cumulative plot. As mentioned above, we here use the [^{13}C II] line emission to carry out this analysis. At an evolutionary time of $t = 50$ Myr the different mass fractions (e.g. of ionized, atomic, and molecular hydrogen) have converged in this simulation (see Walch et al., 2015, section 4.3, especially fig. 10 therein for details). We find most of the [C II] line emission (~90%) to originate from cool gas ($T < 100$ K), while there is a small contribution (~4%) from gas with temperatures between 100 K and 10^3 K, and for $T \geq 10^3$ K (~6%). About 50% of the emission comes from gas with temperatures between 38 K and 56 K, indicating that the [C II] line emission is correlated with the molecular gas phase (see Table 6.1). We consider several different snapshots located between $t = 48$ Myr and $t = 52$ Myr in order to quantify how much this distribution vary from snapshot to snapshot. In practice, we find that the changes are very small: the

Table 6.1: Summary of the parameter space of the [C II] emitting gas, analysed for the optically thin [^{13}C II] line emission for the SILCC-01 and SILCC-02 simulations. We give the values of $T_{\rm kin}$, n, the fractional abundance of H_2 (x_{H_2}), and the visual extinction (A_V) at which 25%, 50% (median) and 75% of the total luminosity are reached.

[^{13}C II]	run	$L/L_{\rm tot}$		
		$\geq 25\%$	$\geq 50\%$	$\geq 75\%$
$T_{\rm kin}$	S10–lowSN–rand	36 K	43 K	50 K
	S10–KS–rand	38 K	45 K	56 K
	S10–KS–peak	81 K	138 K	472 K
	S10–KS–mix	38 K	47 K	57 K
	S10–KS–clus2	42 K	48 K	58 K
	S10–KS–clus	40 K	46 K	57 K
	S10–KS–clus–mag	41 K	47 K	57 K
	FSN	47 K	84 K	280 K
	FWSN	42 K	70 K	156 K
n	S10–lowSN–rand	1118 cm^{-3}	2428 cm^{-3}	4921 cm^{-3}
	S10–KS–rand	741 cm^{-3}	1944 cm^{-3}	4001 cm^{-3}
	S10–KS–peak	4 cm^{-3}	9 cm^{-3}	19 cm^{-3}
	S10–KS–mix	1073 cm^{-3}	2347 cm^{-3}	6214 cm^{-3}
	S10–KS–clus2	1304 cm^{-3}	3000 cm^{-3}	5998 cm^{-3}
	S10–KS–clus	1091 cm^{-3}	3306 cm^{-3}	7260 cm^{-3}
	S10–KS–clus–mag	1453 cm^{-3}	3687 cm^{-3}	7042 cm^{-3}
	FSN	6 cm^{-3}	38 cm^{-3}	362 cm^{-3}
	FWSN	7 cm^{-3}	32 cm^{-3}	905 cm^{-3}
x_{H_2}	S10–lowSN–rand	0.488	0.492	0.496
	S10–KS–rand	0.487	0.491	0.496
	S10–KS–peak	0.008	0.026	0.054
	S10–KS–mix	0.485	0.490	0.495
	S10–KS–clus2	0.488	0.492	0.496
	S10–KS–clus	0.488	0.492	0.496
	S10–KS–clus–mag	0.488	0.492	0.496
	FSN	0.02	0.12	0.35
	FWSN	0.13	0.36	0.49
A_V	S10–KS–rand	4.52	10.31	16.45
	FSN	0.26	0.73	2.83
	FWSN	0.35	0.79	5.70

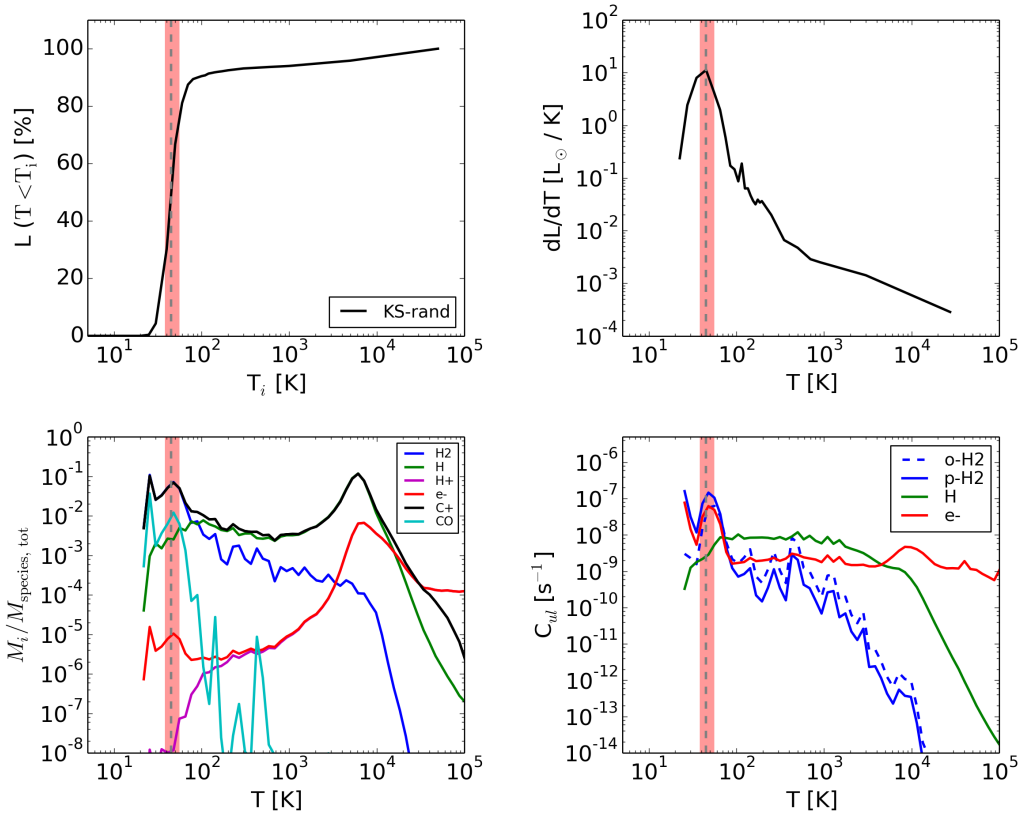

Figure 6.1: *Upper row, left:* Plot of the [^{13}C II] line luminosity originating from gas with $T \leq T_i$ in the simulation *S10–KS–rand* at $t = 50$ Myr. The interquartile range and the median of the distribution are marked with the red shaded area and the grey, dashed line (see Table 6.1). *Upper row, right:* The slope of the cumulative luminosity distribution, obtained by the derivative of the luminosity with respect to the temperature. *Bottom row, left:* Chemical composition of the gas, presented as the mass-weighted temperature distribution of the included species. All hydrogen- (carbon-) containing species are normalized to the total hydrogen (carbon) mass, and the electrons to the amount of possibly available free electrons (see text). In the temperature range from which 50% of the luminosity originates, all collisional partner coexist; however, H_2 dominates. *Bottom row, right:* Mass-weighted excitation coefficients for every species (Eq. (3.22)) as a function of the temperature. Collisions with para-H_2 and electrons contribute most to the [C II] emission in the characterized temperature range.

standard derivation in the fraction of emission produced by $T < T_i$ is less than 2% for most values of T_i, which is smaller than the width of the line in Fig. 6.1.

In the bottom left panel of Fig. 6.1 we show the chemical composition of the gas as a function of the temperature. The y-axis indicates the fraction of mass of the chemical species, where all hydrogen species are normalized to the total amount of hydrogen ($M_{\mathrm{H,\,tot}} = M_{\mathrm{H_2}} + M_{\mathrm{H}} + M_{\mathrm{H^+}}$, with $M_{\mathrm{H_2}}$, M_{H} and $M_{\mathrm{H^+}}$ as the total H_2, H and H^+ masses within the simulation box) and all carbon species are normalized to the total amount of carbon ($M_{\mathrm{C,\,tot}} = M_{\mathrm{CO}} + M_{\mathrm{C^+}}$). The electrons are normalized to the mass of electrons, that could potentially be free electrons, as $M_{\mathrm{e,\,tot}} = m_e \cdot (2n_{\mathrm{H_2}} + n_{\mathrm{H}} + n_{\mathrm{H^+}} + n_{\mathrm{CO}} + n_{\mathrm{C^+}}) \cdot d\mathrm{V}$. The data are binned on logarithmic scales according to its temperature, with bin sizes of $\Delta\log_{10}(T\,[\mathrm{K}]) = 0.07$. As in the upper row, the red shaded area marks the region of the interquartile range characterizing the temperature of the [C II] emitting gas. For temperatures below 100 K H_2 is the most abundant hydrogen species in the gas. Since it coexist with C^+, it causes the dominant fraction of the [C II] line emission. The bottom right panel of Fig. 6.1 shows the mass weighted excitation rates for each species, calculated with Eq. (3.22). In the gas with temperatures between 38 and 56 K, collisions with para-H_2 and electrons dominate the excitation of C^+.

We repeat the same analysis as presented in the upper left panel of Fig. 6.1 for all simulations listed in Table 2.2. The results for the simulations with a fixed SNR at $t = 50$ Myr are shown in the upper left panel of Fig. 6.2. In the temperature values at which 25%, 50%, and 75% of the total [^{13}C II] luminosity are reached, are summarized in Table 6.1. All the simulations, except run *S10–KS–peak*, show the [C II] line emission to originate from a similar temperature range ($36\,\mathrm{K} \leq T \leq 58\,\mathrm{K}$). For the run *S10–KS–peak*, the SNe explode in the dense gas regions, and thus, the amount of molecular gas in this run is much smaller. The peak driving run shows a smooth and more shallow increase with T_i, so that the gas emitting the [C II] line has temperatures between $81\,\mathrm{K} \leq T \leq 472\,\mathrm{K}$.

6.1.2 Density dependence

As done for the temperature, we investigate the number densities, n, of the gas from which the [C II] line emission originates. This time, we select gas above a certain limiting number density, n_i, so that $n > n_i$. We likewise carry out this analysis with the [^{13}C II] line. Figure 6.3 shows in the upper row the result as a function of the number density for the simulation *S10–KS–rand* at $t = 50$ Myr. The left panel shows the cumulative distribution of the [^{13}C II] luminosity, and the middle panel its slope. The interquartile range is marked with the red shaded area, whose parameter values are listed in Table 6.1. For this simulation, we find the [C II] line emission to originate from gas with number densities between 741 cm^{-3} and 4001 cm^{-3}. The chemical composition as a function of the number density is shown in the right panel of Fig. 6.3, where we chose equally distributed bins in logarithmic space with

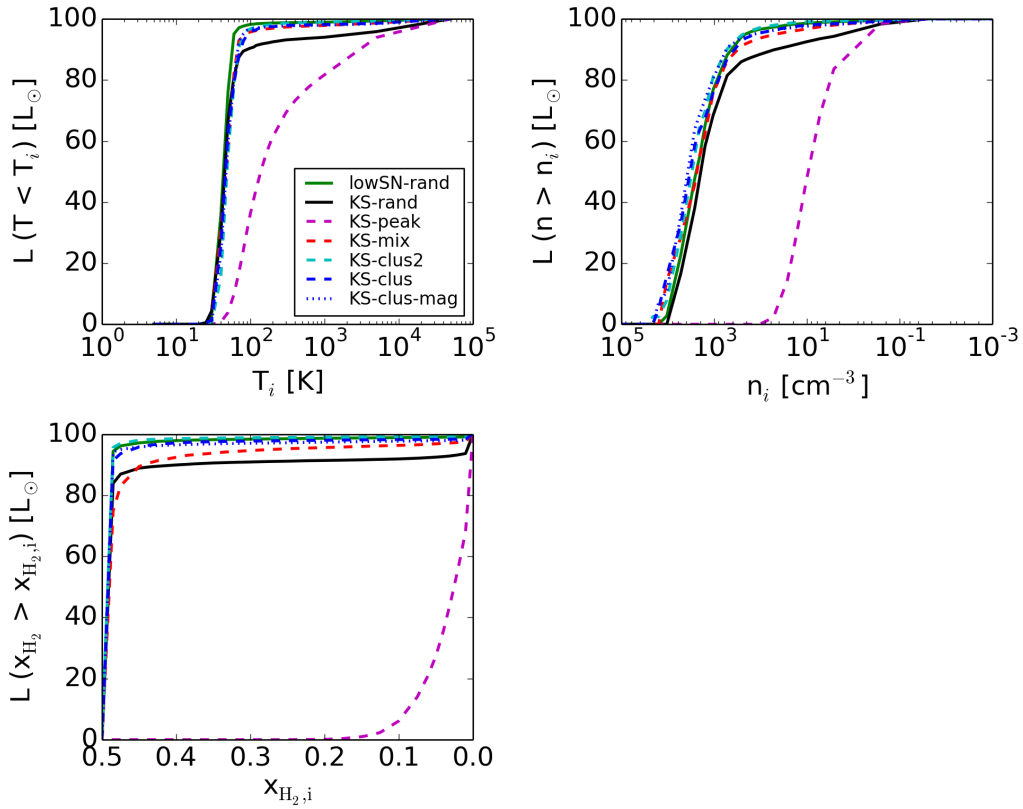

Figure 6.2: Cumulative plots, showing the origin of the [C II] line emission for the SILCC-01 simulations (see Table 2.2) The origin is studied with the optically thin [^{13}C II] line emission as a function of the gas temperature (upper left), number density of the gas (upper right) and fraction of molecular hydrogen $x_{\mathrm{H_2}}$ (bottom left). The parameter values, at which 25%, 50% and 75% of the total luminosity are reached, are summarized in Table 6.1.

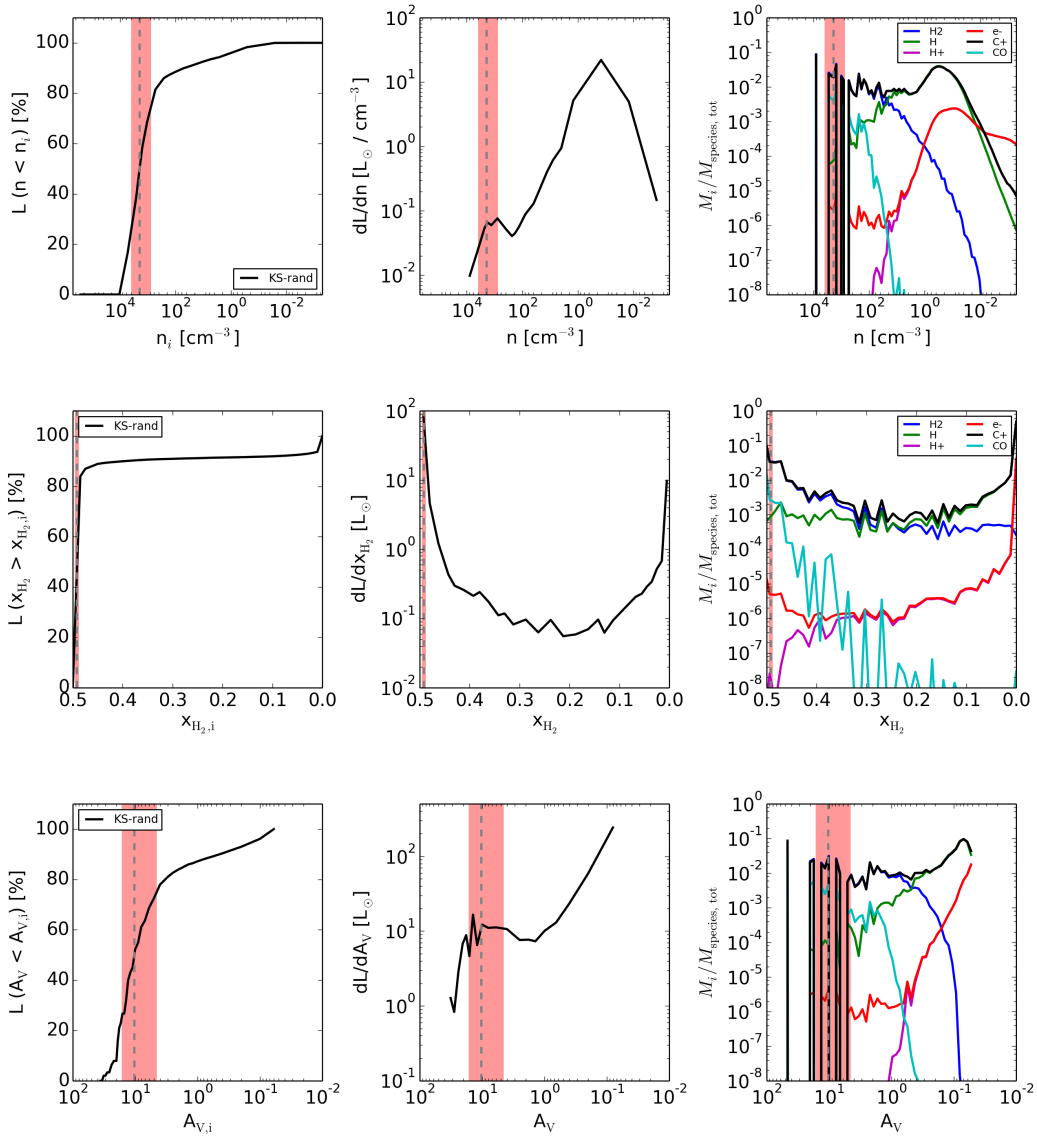

Figure 6.3: Origin analysed for the SILCC-01 simulation *S10–KS–rand* at $t = 50$ Myr as a function of the number density n (upper row), the fraction of molecular hydrogen $x_{\mathrm{H_2}}$ (middle row), and the visual extinction $\mathrm{A_V}$. The left panels show the cumulative luminosity distribution, the middle panels the slope of this distribution, and the right panels the chemical composition of the gas. The red shaded area indicates the interquartile range, characterizing the parameter space of the physical properties, from which the [C II] line emission originates. The values are listed in Table 6.1. The x-axes of all plots are arranged such that the dense gas appears on the left hand side of the plot.

bin sizes of $\Delta\log_{10}(n\,[\mathrm{cm}^{-3}]) = 0.09$. In the range of number densities of the [C II] emitting gas, H_2 is the most abundant species of hydrogen, and thus, contributing most to the [C II] line luminosity. This is in line with the results we found for the chemical composition of the gas as a function of the temperature.

The results for the other SILCC-01 simulations are presented in the upper right panel of Fig. 6.2. As for the analysis with respect for the temperatures, we find the range in the number densities of the [C II] emitting gas to be similar for all runs, except *S10–KS–peak*. In the first mentioned, the [C II] line emission stems from gas with $740\,\mathrm{cm}^{-3} \leq n \leq 7300\,\mathrm{cm}^{-3}$, whereas in *S10–KS–peak* the range in number densities is smaller, between $4\,\mathrm{cm}^{-3} \leq n \leq 19\,\mathrm{cm}^{-3}$. This is caused by the different distribution of the ISM phases in this simulation (see Walch et al., 2015).

6.1.3 Molecular hydrogen dependence

As described in Section 2.1, the fraction of molecular hydrogen x_{H_2}, ionized hydrogen x_{H^+} and atomic hydrogen x_{H} are calculated internally by the chemical network (see Eq. (2.6)). If all hydrogen in a cell is H_2, the fraction of molecular hydrogen is $x_{\mathrm{H}_2} = 0.5$. In order to investigate the correlation of the [C II] line emission with the molecular gas, we select cells of the simulation with respect to their x_{H_2} values, so that they fulfil $x_{\mathrm{H}_2} > x_{\mathrm{H}_2,i}$. In Fig. 6.3 we show in the middle row the results for the run *S10–KS–rand* at $t = 50$ Myr. We find 90% of the [^{13}C II] luminosity to stem from gas that mainly consists of molecular hydrogen ($x_{\mathrm{H}_2} \sim 0.49$). A second contribution (~6%) of the emission originates from gas with $x_{\mathrm{H}_2} \sim 0.1$, which is therefore not molecular, but presumably atomic gas. This can be confirmed by the chemical composition of the gas, shown in the middle right panel of Fig. 6.3. The mass weighted species distribution is binned with respect to x_{H_2} in equally linear distributed bins of sizes of $\Delta x_{\mathrm{H}_2} = 0.02$. Molecular hydrogen dominates the gas for $x_{\mathrm{H}_2} \geq 0.25$, and thereafter atomic hydrogen is the dominating hydrogen species. The amount of electrons is also high in this regime, although the gas is still atomic due to its low ionization degree. The result we find here for the analysis with respect to x_{H_2} is in agreement with the result with respect to the temperature presented in Section 6.1.1, where we found the same fraction of the luminosity to originate from the cold gas phase (~90% of L_{tot} from $T \sim 43$ K) and the dilute warm phase (~6% of L_{tot} from $T \geq 10^3$ K).

The bottom left panel of Fig. 6.2 shows the cumulative [C II] luminosity distribution for all other SILCC-01 simulations. Similar to the other studies, we find all but the run *S10–KS–peak* to originate from gas with similar fractions of molecular hydrogen, around $x_{\mathrm{H}_2} \sim 0.49$. For the run *S10–KS–peak* the formation of molecular gas is limited due to the impact of the SN explosions taking place in the molecular clouds itself. Therefore, the [C II] line emission stems from the atomic gas phase, with $0.008 \leq x_{\mathrm{H}_2} \leq 0.054$ (see Table 6.1).

6.1.4 Visual extinction dependence

One way to identify diffuse molecular hydrogen is to make use of the visual extinction. Following this definition, gas with roughly $0.5 \leq A_V \leq 2$ is counted as diffuse molecular gas. The visual extinction A_V is calculated within our version of the FLASH simulations, using the TREERAY / OPTICALDEPTH module (Wünsch et al., 2018). Note, that in our definition the visual extinction corresponds to a local weighted average along different lines of sight, whereas in observations it is calculated for one line of sight. We distinguish the contribution from cells with $A_V < A_{V,i}$. The results for the simulation *S10–KS–rand* at $t = 50$ Myr are shown in the bottom row of Fig. 6.3, and values for A_V characterizing where 25%, 50% and 75% of the total [C II] luminosity are originating, are summarized in Table 6.1. In line with the analyses done above, we find the [C II] emitting gas to have visual extinctions in the range of $4.5 \leq A_V \leq 16.5$. Gas, classified as diffuse molecular gas with $0.5 \leq A_V \leq 2$ contributes with ∼5% to the total [C II] luminosity.

6.2 Simulations with sink particles

In the last two columns of Fig. 3.5 we present the synthetic [^{12}C II] emission maps of the simulations with the sink particles at an evolutionary time of $t = 70$ Myr. We chose the different time step compared to the other simulations to give enough time for the simulation to evolve including the sink particles. The [^{12}C II] and [^{13}C II] luminosities and peak intensities of the synthetic emission maps are summarized in Table 3.3. The signal around the midplane is distributed on larger scales due to the initial turbulence, as described in Section 2.2.2. Stellar winds suppress the formation of massive stars and therefore, the SNR in the simulation *FWSN* is smaller and the outflowing component is less extended compared to the simulations with only SN feedback (see Table 2.2).

As done for the SILCC-01 simulations, we analyse the origin of the SILCC-02 simulations with the [^{13}C II] line emission. We likewise carry out this study with respect to the gas temperature, the total gas number density, the fraction of molecular hydrogen, and the visual extinction. We present the results for the run *FWSN* in more detail, and then compare with the results of the run *FSN*.

6.2.1 Temperature dependence

First, we analyse the temperature of the [C II] emitting gas by selecting only cells up to a certain limiting temperature T_i, so that they fulfil $T < T_i$. We present the result for the run *FWSN* $t = 70$ Myr in Fig. 6.4. The upper left panel of Fig. 6.4 shows the

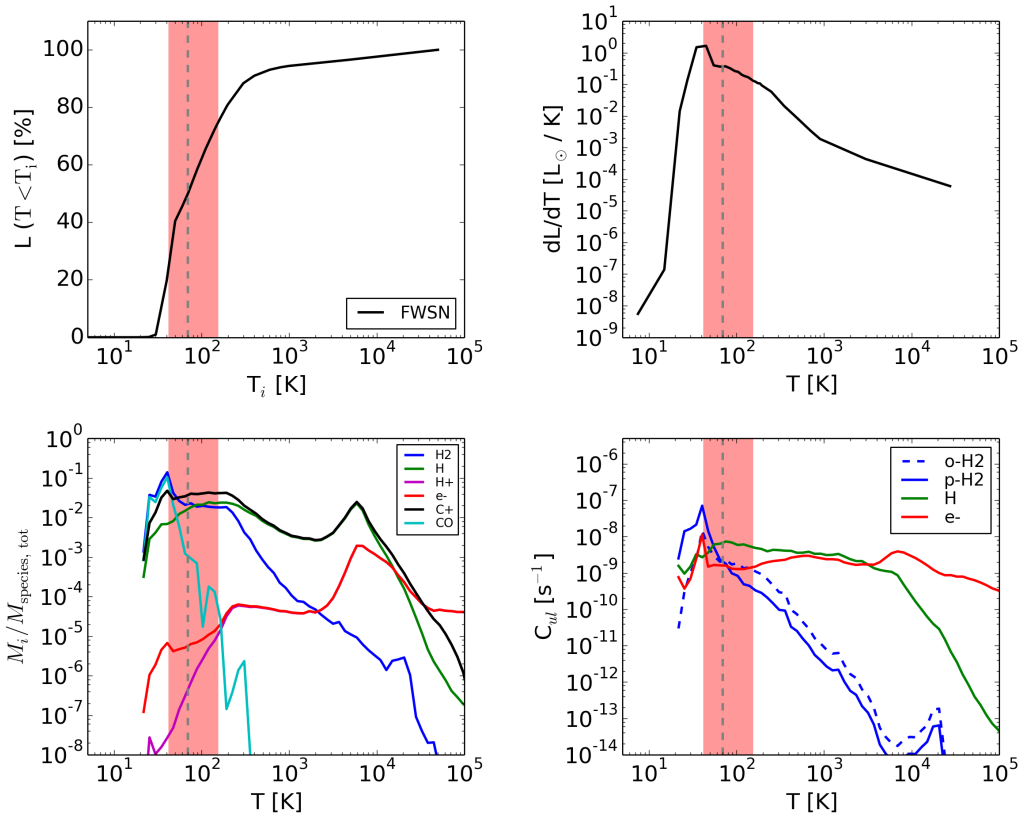

Figure 6.4: Same as Fig 6.1, but for the simulation *FWSN* at $t = 70$ Myr. Compared to *S10–KS–rand* the chemical composition of the gas is different (see bottom left panel). Similar to *S10–KS–rand*, around $T \sim 80$ K the transition between H_2 and H takes place, but in contrast carbon is dominantly present as CO for $T \leq 45$ K. Thus, the interquartile range of temperatures for the [C II] emitting gas starts at slightly higher temperatures, and expands to higher temperature values compared to *S10–KS–rand*. Also the contribution to the excitation (bottom right panel) is dominated by collisions with H_2 for lower, and with H for higher temperatures.

cumulative luminosity distribution as a function of the temperature, and the upper right panel the corresponding slope of this distribution. We find that gas within a wider temperature range ($42\,\mathrm{K} \leq T \leq 156\,\mathrm{K}$) compared to the SILCC-01 simulations produces 50% of the [C II] luminosity, as characterized by the interquartile range. The corresponding values are summarized in Table 6.1. The lower left panel of Fig. 6.4 shows the chemical composition of the gas as a function of the temperature. The y-axis indicates the mass fraction of hydrogen species with respect to the total hydrogen mass, the mass fraction of carbon containing species to the total carbon containing mass, and the fraction of free electrons with respect to the potentially free electrons in the simulation. For more details, we refer to the description presented in Section 6.1.1. The transition between H_2 to H takes place in both the simulation *S10–KS–rand* (Fig. 6.1) and *FWSN* (Fig. 6.4) at a temperature $T \sim 80$ K. However, C^+ is the dominant carbon species at low temperatures in *S10–KS–rand*, whereas in *FWSN* carbon is mainly present as CO in gas with $T \leq 45$ K. Therefore, the fraction of the [C II] emission originating from this cold gas phase is smaller in *FWSN* compared to *S10–KS–rand*, and gas at higher temperatures, containing atomic hydrogen, also contributes an important part to the [C II] line emission. In the bottom right panel of Fig. 6.4 we present the excitation coefficient for each collisional partner, and find para-H_2 to be the dominant collisional partner for gas at $T \leq 55$ K, followed by ortho-H_2 and electrons. For $T \geq 55$ K, the contribution from collisions with H play a major role.

We carry out the analysis studying the origin of the [C II] emitting gas as a function of temperature likewise for the simulation *FSN*, using the [^{13}C II] line emission. The cumulative luminosity distribution is shown in the upper left panel of Fig. 6.5. Both runs, *FSN* and *FWSN*, show similar cumulative distributions, especially for $T \leq 300$ K. For *FSN* the total [^{13}C II] (and [^{12}C II]) luminosity is larger. When not normalizing the plots (not shown here), it becomes clear that for *FSN* there is a additional contribution to the [C II] line emission from gas with $T \geq 300$ K. Thus, when normalizing the distributions, the one for *FSN* appears compressed. This causes a larger interquartile temperature range towards higher temperatures, so that 50% of the [C II] emission originate from gas with $47\,\mathrm{K} \leq T \leq 280\,\mathrm{K}$ (see Table 6.1).

6.2.2 Density dependence

We investigate the range of number densities of the [C II] emitting gas in a similar manner as above, and show the resulting cumulative [C II] luminosity plot for *FWSN* at $t = 70$ Myr in the upper row of Fig. 6.6. In contrast to the other cumulative luminosity distributions, the one for *FWSN* is bimodal, meaning that two distinct contributions building the total luminosity. The first contributions stems from gas with number densities of $n \geq 100\ \mathrm{cm}^{-3}$, while the second from gas with $0.1\,\mathrm{cm}^{-3} \leq n \leq 100\,\mathrm{cm}^{-3}$. The fact that we find the gas to be split into two separate phases in density could be caused by the feedback of winds within this particular simulation. Characterizing the number densities in the way as done above, gives only a rough orientation of the range of number densities. However, if we simply

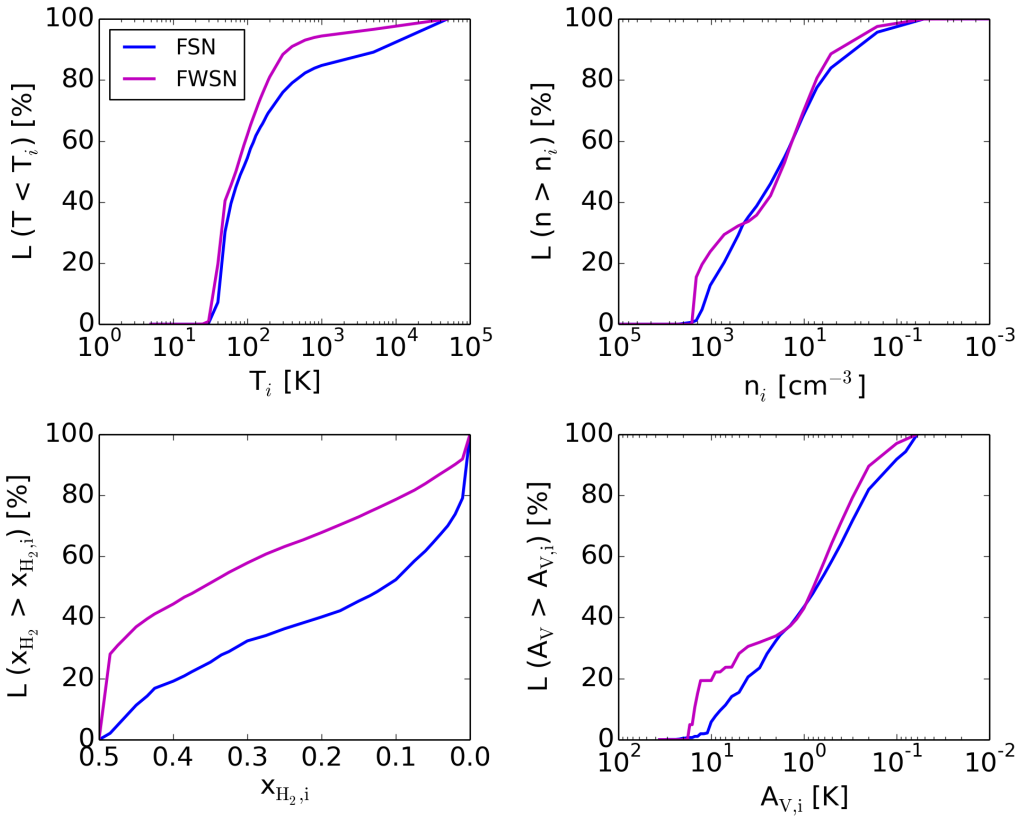

Figure 6.5: Same as Fig. 6.2, for the SILCC-02 simulations *FSN* and *FWSN* at an evolutionary time of $t = 70$ Myr. In addition to Fig. 6.2, the origin is likewise studied as a function of the visual extinction A_V (bottom right panel).

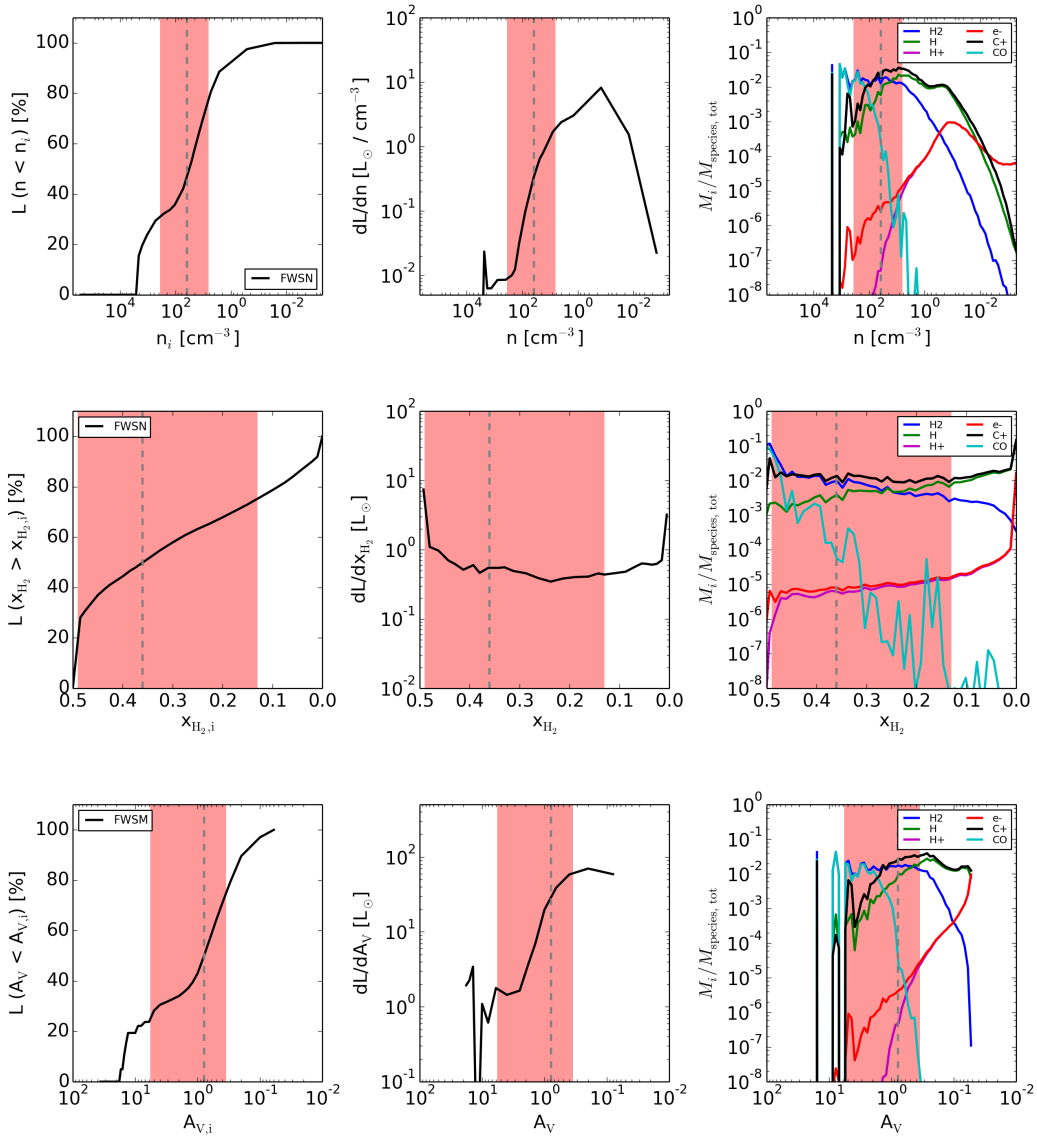

Figure 6.6: Same as Fig. 6.3, but for the simulation *FWSN* at $t = 70$ Myr.

apply this method, we find the number density range of the gas contributing to the [C II] line emission to be much smaller ($7\,\mathrm{cm}^{-3} \leq n \leq 905\,\mathrm{cm}^{-3}$) compared to the number density range found in the SICC-01 simulations. This is caused by the simulation setup: The SILCC-02 discussed now include the formation of sink particles (see Section 2.2). Thus, the gas at high number densities is converted into the sink particles and does no longer contribute to the [C II] line emission. Therefore, the number density range we find for *FWSN* is smaller. The chemical composition of the gas as function of the number density is presented in the upper right panel of Fig. 6.6. We find that for $n \leq 140\ \mathrm{cm}^{-3}$ carbon is dominantly present as CO, and the transition between H_2 and H takes place at $n \sim 17\ \mathrm{cm}^{-3}$. Thus, we find again H_2 and H to contribute to the [C II] line emission.

For the run *FSN* at $t = 70$ Myr we find the cumulative [C II] luminosity distribution to be similar to the one of *FWSN*, bot not having the bimodal shape (see upper right panel of Fig. 6.5). However, gas with higher number densities ($n \geq 300\ \mathrm{cm}^{-3}$) contribute to a larger part to the [C II] line emission in the run *FWSN* compared to run *FSN*. This could be the result of the stellar winds as a feedback process to the gas in the ISM. The number densities, at which 25%, 50% and 75% of the total luminosity are reached, are summarized in Table 6.1.

6.2.3 Molecular hydrogen dependence

We study the correlation between the [C II] emitting gas and the fraction of molecular hydrogen likewise for the SILCC-02 simulations, taking into account only gas fulfilling $x_{\mathrm{H}_2} > x_{\mathrm{H}_2,i}$. In the middle row of Fig. 6.6 we show the cumulative [C II] luminosity plot as well as its derivation and the chemical composition of the gas as a function of x_{H_2} for the run *FWSN* at $t = 70$ Myr. We find gas with fractional abundances between 0.13 and 0.49 to contribute with 50% to the [C II] luminosity (see Table 6.1). Thus, between 26% and 98% of the hydrogen mass are in the form of H_2. This reflects the fact that both gas with chemical compositions dominated by H_2 and H contribute to the [C II] luminosity. Gas, dominated by molecular hydrogen ($x_{\mathrm{H}_2} \geq 0.25$, so that 50% of the hydrogen mass is in form of H_2), contributes to 63% to the [C II] luminosity.

In the bottom left panel of Fig. 6.5 we show the comparison of the luminosity distribution between the run *FSN* and *FWSN*. For *FSN* gas with slightly lower fractions of molecular hydrogen ($0.02 \leq x_{\mathrm{H}_2} \leq 0.35$) contributes to the [C II] luminosity, presenting gas, in which between 4% and 70% of the hydrogen mass is in form of H_2. Thus, the fraction of [C II] luminosity associated with the molecular gas ($x_{\mathrm{H}_2} \geq 0.25$) is smaller with 36%, and a larger fraction stems from the atomic gas phase.

6.2.4 Visual extinction dependence

As a last parameter we study the dependence on the visual extinction A_V in the gas. We note again that the definition of A_V calculated within FLASH refers to the local weighted average along different lines of sight (see Section 6.1.4). The bottom row in Fig. 6.6 shows the result for the run *FWSN* at $t = 70$ Myr. As discussed for the number density dependency, also this cumulative plot is bimodal, having a contribution from gas with $A_V \geq 4$, and from gas between $0.1 \leq A_V \leq 4$. Thus, characterizing the contribution by its interquartile range only gives a rough estimate, for which we find that gas with a visual extinction between 0.35 and 5.70 contribute to 50% to the total [C II] luminosity, as listed in Table 6.1. At $A_V \geq 1.7$ the carbon in the gas is dominantly CO, and the transition from H_2 to H takes place at $A_V \sim 0.45$. Thus, we find again that both H_2 and H contribute to the [C II] line emission. Defining the diffuse molecular gas as those with $0.5 \leq A_V \leq 2$, we find that ~30% of the [C II] luminosity stems from this gas phase.

The comparison to the run *FSN* at $t = 70$ Myr is presented in the bottom right panel of Fig. 6.5. We find a slightly smaller range of visual extinctions of the [C II] emitting gas in *FSN* ($0.26 \leq A_V \leq 2.83$, see Table 6.1) compared to *FWSN*. About ~25% of the [C II] luminosity originates in *FSN* from the diffuse molecular gas, slightly less than for *FWSN*. This is in agreement with the results of the analysis with respect to the number density n, the fractional H_2 abundance x_{H_2} and the temperature T. From this we can conclude that a larger fraction of [C II] in run *FSN* is emitted by gas at higher temperature, lower number density, containing less H_2, and thus, being likewise less shielded.

"Momo starrte Meister Hora fassunglos an. Leise fragte sie: 'Und was ist das für eine Krankheit?'
'Am Anfang merkt man noch nicht viel davon. Man hat eines Tages keine Lust mehr, irgend etwas zu tun. Nichts interessiert einen, man ödet sich. Aber diese Unlust verschwindet nicht wieder, sondern sie bleibt und nimmt langsam immer mehr zu. Sie wird schlimmer von Tag zu Tag, von Woche zu Woche. Man fühlt sich immer mißmutiger, immer leerer im Inneren, immer unzufriedener mit sich und der Welt. Dann hört nach und nach dieses Gefühl auf, und man fühlt gar nichts mehr. Man wird ganz gleichgültig und grau, die ganze Welt kommt einem fremd vor und geht einen nichts mehr an. Es gibt keinen Zorn mehr und keine Begeisterung, man kann sich nicht mehr freuen und nicht mehr trauern, man verlernt das Lachen und das Weinen. Dann ist es kalt geworden in einem, und man kann nichts und niemand mehr lieb haben. Wenn es einmal soweit gekommen ist, dann ist die Krankheit unheilbar. Es gibt keine Rückkehr mehr. Man hastet mit leerem, grauem Gesicht umher, man ist genauso geworden wie die grauen Herren selbst. Ja, dann ist man einer der ihren. Diese Krankheit heißt: Die tödliche Langeweile.'
Momo überlief ein Schauder.
'Und wenn du ihnen nicht die Zeit aller Menschen gibst', fragte sie, 'dann machen sie, daß alle Menschen so werden wie sie?'
'Ja', antwortete Meiser Hora, 'damit wollen sie mich erpressen'. Er stand auf und wandte sich ab.

Table 6.2: Parameter space of the gas, emitting the [C II] line emission, studied with the optically thin tracer of [^{13}C II]. The table lists the interquartile range and the median values of the cumulative plots, in which the origin of the emission is analysed concerning the kinetic temperature $T_{\rm kin}$, the number density of the gas n, the elemental fraction of molecular hydrogen $x_{\rm H_2}$, and the visual extinction $A_{\rm V}$ (see Figs. 6.7 and 6.8). The analyses are done for by considering all pixels in the maps ("total"), and only the assumed observable range, fulfilling $I_{[^{12}{\rm CII}]} \geq 0.5$ K km s^{-1} ("observable").

[^{13}C II]	taken pixels	$L/L_{\rm tot}$ $\geq 25\%$	$\geq 50\%$	$\geq 75\%$
$T_{\rm kin}$	total	43 K	52 K	64 K
	observable	41 K	48 K	57 K
n	total	53 cm^{-3}	166 cm^{-3}	438 cm^{-3}
	observable	103 cm^{-3}	247 cm^{-3}	524 cm^{-3}
$x_{\rm H_2}$	total	0.08	0.14	0.22
	observable	0.11	0.17	0.23
$A_{\rm V}$	total	0.50	0.68	0.91
	observable	0.60	0.76	0.96

'Ich habe bis jetzt darauf gewartet, daß die Menschen selbst sich von diesen Plagegeistern befreien würden. Sie hätten es gekonnt, denn sie selbst haben ihnen ja auch zum Dasein verholfen. Aber nun kann ich nicht länger warten. Ich muß etwas tun. Aber ich kann es nicht allein.'
Er blickte Momo an. 'Willst Du mir helfen?' " (Ende, 1973, chapter 19 therein)

6.3 Zoom-in simulations

As done for the SILCC-01 and SILCC-02 simulations, we analyse the origin of the [C II] line emission for the zoom-in simulation MC2. This simulation provides a better spatial resolution of dx = 0.122 pc (see Section 2.2.3). We take a snapshot at an evolutionary time of t = 13.9 Myr. Here, we carry out all studies by *(i)* taking into account all pixels of the map, and *(ii)* by taking only those pixels, that are assumed to be observable with $I_{[^{12}{\rm CII}]} \geq 0.5$ K km s^{-1} (see Section 3.4). Note that these results were submitted to MNRAS in May 2018 (Franeck et al., 2018).

6.3.1 Temperature dependence

We analyse the temperature dependence of the [C II] emitting gas for the zoom-in simulation MC2 at a resolution level of L10 (see Table 4.3). In Fig. 6.7 we show in the upper left panel the resulting cumulative plot for the optically thin [^{13}C II] line emission. The solid line represents the result, if the whole map is taken into account, and the dashed line, when only the observable part ($I_{[^{12}{\rm CII}]} \geq 0.5$ K km s^{-1})

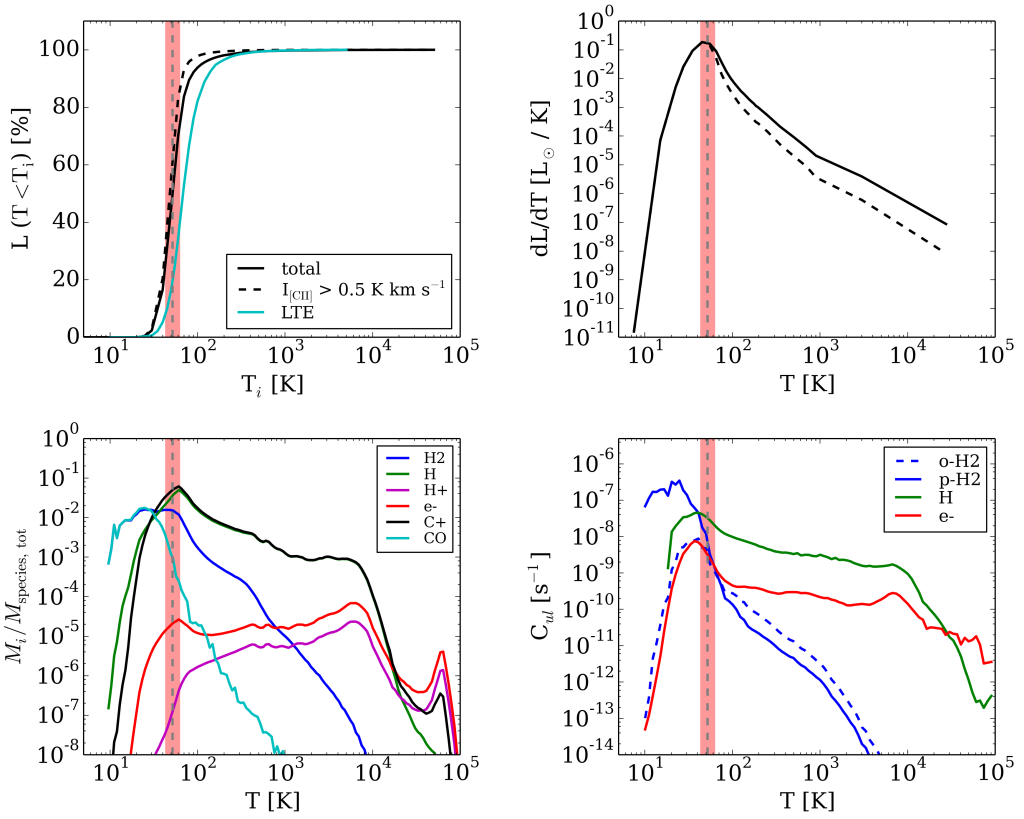

Figure 6.7: Same as Fig. 6.1, but for the zoom-in simulation MC2 at an evolutionary time of $t = 13.9$ Myr. The solid lines in the panels in the upper row present the results for the analysis of the total map, and the dashed lines if only those pixels above the assumed observational detection limit ($I_{[^{12}\mathrm{CII}]} \geq 0.5$ K km s^{-1}) were taken into account. As comparison, we estimate the luminosity, if all C^+ ions were in LTE (upper left plot, cyan line). The lower panels show the chemical composition of the gas (left) and the excitation coefficient (right) for each collisional partner. In the temperature range, from which the [C II] line emission originates, the excitation coefficient C_{ul} for H is larger than the ones from the other collisional partners.

is considered. There is only a small difference between these analyses, since 80% of the total luminosity originates from the observable region. This is in line with Goldsmith et al. (2012), who characterize the [^{12}C II] line emission as "effectively optically thin". We find almost all emission to originate from temperatures between 20 and 100 K. In Table 6.2 we summarize the median and the interquartile range of the cumulative plot. These values indicate, at which values 25%, 50% (median) and 75% of the total luminosity is reached. According to this, the [C II] line emission originates from gas with temperatures between 43 and 64 K, with a median of 52 K. The red shaded area in the plot marks the interquartile range, estimated for the analysis taking all values into account. In the upper right panel of Fig. 6.7 we show the deviation of the cumulative plot, indicating again the temperature regions, from that the [C II] line emission originates. If the analysis is done only with the observable region of the map, the contributions from gas at higher temperature $T > 100$ K is partially missed.

As discussed above, it is assumed that the [C II] line emission is not in a local thermal equilibrium. However, we further compare our result with a LTE prediction. This is shown in the cumulative plot (upper left panel in Fig. 6.7) as the cyan line. For this, we assume that the luminosity under LTE conditions is proportional to

$$L_{\mathrm{LTE}} \propto h\nu A_{ul} n_{\mathrm{C}^+} \frac{g_u}{g_l} \frac{1}{Z(T)} e^{-\frac{h\nu_{ul}}{k_B T}}, \tag{6.2}$$

with h as the Planck constant, ν as the frequency of the line, A_{ul} as its Einstein coefficient, g_u and g_l as the statistical weights of the fine structure levels, k_B as the Boltzman constant, and T as the kinetic temperature. $Z(T)$ denotes the partition function, calculated as

$$Z(T) = 1 + \frac{g_u}{g_l} e^{-\frac{h\nu_{ul}}{k_B T}}. \tag{6.3}$$

In regions with high densities, LTE conditions would be obtained. We find that the curves of our simulations in the cumulative plot are below the cyan curve of the LTE prediction. This indicates, that most of the [C II] line emission is subthermal. This is in agreement with the number densities we have in the simulation box, that are to a great part beyond the critical density. The gas is both subthermally excited, and the emission is likewise subthermally. We therefore obtain the [C II] line emission from temperatures lower than it would be expected from the LTE prediction. This result is in agreement with Goldsmith et al. (2012), who discussed, that a large part of the [C II] line emission in the galaxy stems from thin, subthermally excited gas.

The lower left panel of Fig. 6.7 shows the chemical composition of the gas as a function of the temperature. As described in Section 6.1.1, the y-axis indicates which fraction of the total hydrogen mass is in H_2, H, and H^+, which fraction of the total carbon-containing species is in CO and C^+, and which fraction of electrons is present as free electrons, with respect to the possibly free electrons in the simulation. For the temperature binning, we use equally distributed bins in logarithmic space with sizes of $\Delta\log_{10}(T\,[\mathrm{K}]) = 0.32$. The red shaded area marks the temperature range from that the [C II] line originates. Almost for the entire temperature range the fraction of mass of C^+ is aligned with the fraction of mass with atomic

H. About 73% of the the total C^+ mass is present in gas with temperatures in the range of 20 and 100 K. Since the mass fraction of C^+ and H have their peaks in this temperature range, it is evident that also the [C II] line emission originates from these temperatures. The bottom right panel of Fig. 6.7 shows the mass weighted excitation rates for each species, calculated with Eq. (3.22). At low temperatures, $T < 40$ K, the excitation coefficient for para-H_2 is the dominating contribution. However, above 40 K the contribution of atomic hydrogen to the excitation rate coefficient dominates.

6.3.2 Density dependence

We estimate the total gas number density of the [C II] line emitting gas by selecting only gas above a limiting number density, $n > n_i$, so that the cold, dense gas remains on the left hand side of the resulting plot. We present the result of this analysis in the upper row of Fig. 6.8, considering the total map (solid line) and the observable regions (dashed line). We used the optically thin tracer of [^{13}C II] for this study. The upper left panel shows the cumulative plot of the analysis, the middle panel the derivative of the cumulative plot, and the red shaded area marks the region, where 25, 50 and 75% of the total luminosity are reached. We find the [C II] line emission to originate from gas with number densities between 53 cm^{-3} and 438 cm^{-3} (see Table 6.2). The right panel shows the mass fraction for the different chemical species, where the mass of the species is normalized to the total mass of hydrogen, carbon or the mass of the potentially free electrons in the simulation box (further descriptions in Sec. 6.3.1). We chose bins, equally distributed in logarithmic space with bin sizes of $\Delta\log_{10}(n\,[\mathrm{cm}^{-3}]) = 0.05$. The mass fractions of C^+ and H align from number densities below 1.2×10^3 cm^{-3}, which includes the range of number densities of the interquartile range, where the [C II] line emission stems from.

6.3.3 Molecular gas dependence

We study further the fraction of molecular hydrogen in the [C II] emitting gas for MC2, again with the optically thin tracer [^{13}C II]. In the middle row of Fig. 6.8 we show in the left panel the cumulative plot for the analysis, and in the middle panel the derivative of the cumulative plot. Note, that we present the result in a way, that on the left side of the x-axis the high values of $x_{\mathrm{H_2},i}$ are plotted. $x_{\mathrm{H_2}} = 0.5$ is the largest value the fractional abundance of molecular hydrogen can have. For cells with $x_{\mathrm{H_2}} = 0.5$ all hydrogen is in molecular form. The [C II] line emission starts to increase at $x_{\mathrm{H_2,i}} \sim 0.4$. Here 80% of the hydrogen is in molecular form. However, only 20% of the emission stems from gas dominated by H_2 with $x_{\mathrm{H_2,i}} \gtrsim 0.23$ (~47% of hydrogen in its molecular form). The median of the cumulative plot is at $x_{\mathrm{H_2}} = 0.14$ (see Table 6.2). Thus 50% of the emission comes from gas in which less than 28% of hydrogen is in molecular form. From that we confirm that the gas associated with the [C II] line emission is mostly atomic. The middle right panel of Fig. 6.8

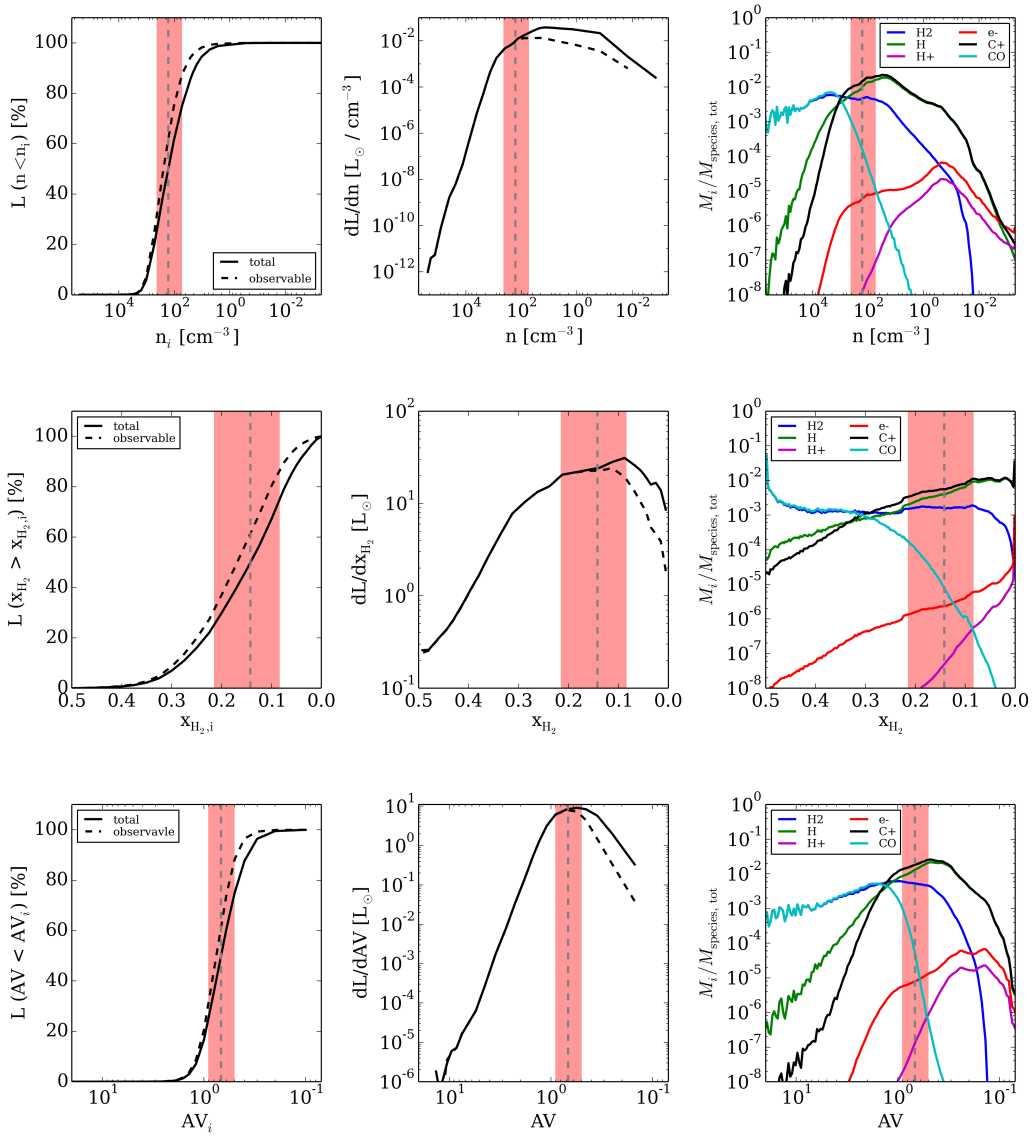

Figure 6.8: Same as Fig. 6.3, calculated for the zoom-in simulation MC2 at an evolutionary time of $t = 13.9$ Myr. The solid lines in the panels in the upper row present the results for the analysis of the total map, and the dashed lines if only those pixels above the assumed observational detection limit ($I_{[^{12}\mathrm{CII}]} \geq 0.5$ K km s^{-1}) were taken into account.

Table 6.3: Same as Table 6.2, but analysed for the opacity affected [^{12}C II] line emission. The values, characterizing where 50% of the emission originates, are similar to the ones resulting from the analysis with the [^{13}C II] line emission. Note, that the results of the [^{12}C II] line emission are only listed here for sake of completeness, since they are affected by the opacity of the line.

[^{12}C II]	taken pixels	$L/L_{\rm tot}$ $\geq 25\%$	$\geq 50\%$	$\geq 75\%$
$T_{\rm kin}$	total	44 K	53 K	65 K
	observable	40 K	47 K	55 K
n	total	62 cm^{-3}	193 cm^{-3}	490 cm^{-3}
	observable	131 cm^{-3}	292 cm^{-3}	610 cm^{-3}
$x_{\rm H_2}$	total	0.08	0.13	0.20
	observable	0.11	0.16	0.22
A_V	total	0.48	0.64	0.84
	observable	0.57	0.72	0.90

shows the chemical composition of the gas, binned within equally logarithmic bins of the size of $\Delta x_{\rm H_2} = 0.02$. The mass fraction of C^+ becomes larger than the fraction of CO around $x_{\rm H_2} \lesssim 0.3$. Thus, its transition happens only slightly deeper in cloud compared to the transition from H to H_2, which takes place at $x_{\rm H_2} = 0.25$.

6.3.4 Visual extinction dependence

In the lower row of Fig. 6.8 we show the visual extinction of the [C II] emitting gas, where we plot the cumulative luminosity plot in the left, and its derivative in the middle panel, respectively. The [C II] line emission originates from gas with a visual extinction below $A_V < 2$. The interquartile range indicates a parameter range for A_V between 0.5 and 0.91 (see Table 6.2). As for the other studies, the results are similar when taking all pixels in the map, or only the region, that is assumed to be observable. Since the dilute gas is expected to be not bright in emission, we do not cover all gas at low visual extinction, if we only take the observable part into account. Following the definition of diffuse molecular gas to have visual extinctions between $0.5 \leq A_V \leq 2$, we find 75% of the total [C II] luminosity to originate from gas with visual extinctions in this range.

6.3.5 Origin of the emission, analysed with an optically thick tracer

In the analysis above we have studied the parameter space of the [C II] line emitting gas by using the optically thin [^{13}C II] line emission. This is valid, since the [^{12}C II] and [^{13}C II] line emission originate from the same regions in the gas, and it is necessary, since the [^{12}C II] line emission is affected by the opacity. Here we prove that

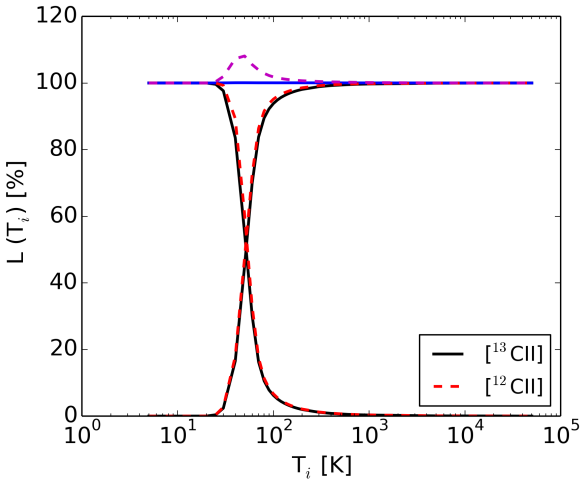

Figure 6.9: Comparison of the results of the analysis concerning the origin of the [C II] line emission for the optically thin [^{13}C II] line emission (solid lines) and the opacity affected [^{12}C II] line emission (dashed lines). Summing the luminosity from gas above and below the limiting temperature T_i results to the total luminosity for the optically thin [^{13}C II] line emission, but overestimates the luminosity for the opacity affected [^{12}C II] line emission.

the [^{13}C II] and [^{12}C II] line emission behave similar at the example of the study concerning the origin of the emission as a function of the temperature. For this purpose we show in Fig. 6.9 how much of the [^{13}C II] (black, solid lines) and [^{12}C II] (red, dashed lines) line emission originates for $T < T_i$ and $T > T_i$. For an optically thin tracer the emission for $T < T_i$ and $T > T_i$ add up to the total emission for every T_i. This is the case for the [^{13}C II] line emission, for which we plot the sum over both lines with the blue, solid line. We repeat the same analysis for the [^{12}C II] line emission. Adding up the emission for $T < T_i$ and $T > T_i$ (dashed, magenta line) overestimates the total emission about 10% for T_i between 30 K and 100 K. This is caused by the optical depth of the line. Despite the overestimation of the [^{12}C II] intensity by selecting only parts of the box and thus, avoiding absorption effects, the [^{12}C II] and [^{13}C II] line emission behave similar in the analysis: The emission from C^+ stems dominantly from the dense, clumps in the cloud, that contain hydrogen dominantly in the atomic form. For sake of completeness, we summarize the values of the parameters characterizing the gas from which 25, 50, and 75% of the [C II] emission originates in Table 6.3 for all studies carried out above. Note, that these values are defective due to the absorption effects. To reach for example 50% of the emission, higher densities are required when carrying out the analysis with the [^{12}C II] line emission, since part of the [^{12}C II] emission is absorbed before it can reach the observer. The values of $T_{\rm kin}$ and $x_{\rm H_2}$, characterizing where 25% and 75% of the total [C II] line emission come from, are similar and narrow for [^{12}C II] as for the [^{13}C II] line emission. For the visual extinction A_V we obtain slightly lower values, when carrying out the analysis with [^{12}C II]. To avoid of being influenced by the optical depth effects, we take the [^{13}C II] line emission in this work for studying the origin of the [C II] line emission in general.

Table 6.4: List of the parameters characterizing the [C II] line emitting gas for MC2 at different resolutions (see Table 4.3), analysed with the [^{13}C II] line emission.

[^{13}C II]	resolution	$L/L_{\rm tot}$ ≥ 25%	≥ 50%	≥ 75%
$T_{\rm kin}$	L5	41 K	60 K	89 K
	L6	41 K	58 K	81 K
	L7	42 K	53 K	71 K
	L8	42 K	53 K	67 K
	L9	43 K	53 K	64 K
	L10	43 K	52 K	64 K
n	L5	11 cm^{-3}	29 cm^{-3}	77 cm^{-3}
	L6	14 cm^{-3}	36 cm^{-3}	91 cm^{-3}
	L7	23 cm^{-3}	60 cm^{-3}	147 cm^{-3}
	L8	35 cm^{-3}	93 cm^{-3}	225 cm^{-3}
	L9	47 cm^{-3}	137 cm^{-3}	327 cm^{-3}
	L10	53 cm^{-3}	166 cm^{-3}	438 cm^{-3}
$x_{\rm H_2}$	L5	0.05	0.10	0.16
	L6	0.05	0.10	0.16
	L7	0.06	0.11	0.18
	L8	0.07	0.12	0.19
	L9	0.08	0.13	0.20
	L10	0.08	0.14	0.22

6.3.6 Origin of the emission at different spatial resolution

Figure 6.10 shows the analysis of the origin of the [C II] line emission as a function of the gas temperature T, the number density n, and the fraction of molecular hydrogen $x_{\rm H_2}$, studied with the simulation MC2 at different resolution levels, from L5 to L10 (see Table 4.3). As done before, we use the optically thin [^{13}C II] line emission for this study. Although the total luminosity is smaller for lower resolution levels (compare also the values listed in Table 4.3), the cumulative plot as a function of the temperature shows qualitatively the same behaviour for all resolution levels. The values of T characterizing the range, from which 25, 50, and 75% of the total [C II] luminosity originate, are listed in Table 6.4. The cumulative plots as a function of the number density and the molecular hydrogen fraction show qualitatively the same behaviour, but are shifted to less dense gas at lower resolution levels. As an example, the [C II] emitting gas in L6 has lower number densities ($14\,{\rm cm^{-3}} \leq n \leq 90\,{\rm cm^{-3}}$) compared to the values found for L10 ($53\,{\rm cm^{-3}} \leq n \leq 438\,{\rm cm^{-3}}$). In line with that the fraction of molecular hydrogen in the [C II] emitting gas is slightly lower for L6 ($0.05 \leq x_{\rm H_2} \leq 0.16$) than for L10 ($0.08 \leq x_{\rm H_2} \leq 0.22$).

In Fig. 6.11 we investigate whether the median values have converged among the different resolution levels. We study this by calculating the deviation between

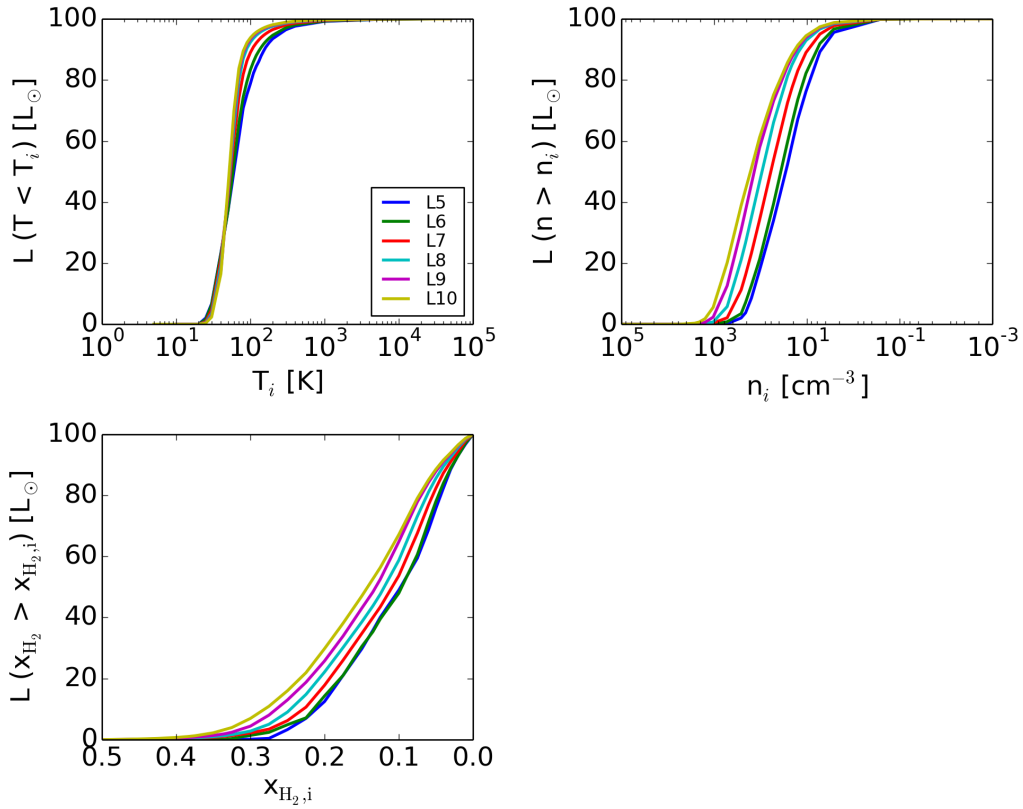

Figure 6.10: Comparison of the cumulative [C II] luminosity distributions for MC2 at L6 and L10 as a function of the gas temperature (upper right), the number density (upper left), and the fraction of molecular hydrogen (lower left).

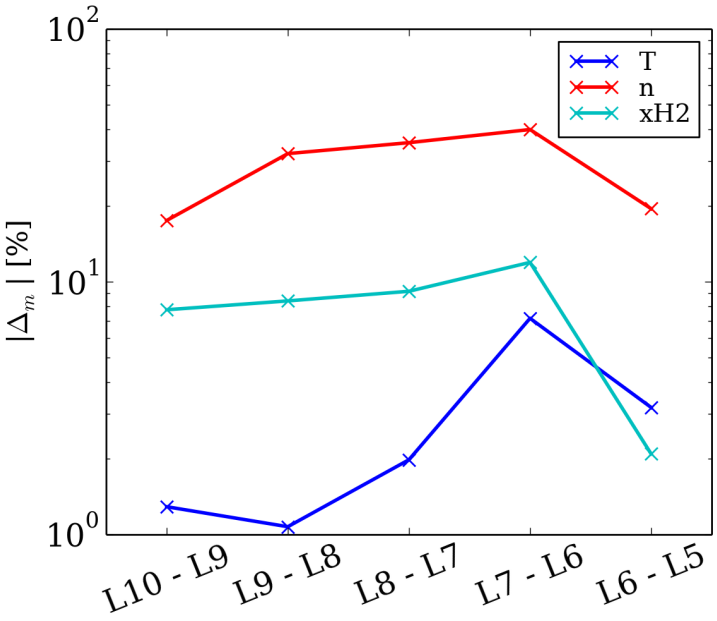

Figure 6.11: Convergence of the median values from the analysis of the origin of the [C II] line emission concerning the temperature T, total gas number density n, and molecular hydrogen fraction $x_{\mathrm{H_2}}$ (see Eq. 6.4). The x-axis indicates which resolution levels are compared for this. The temperature is the best converged parameter, while the number density and the molecular hydrogen fraction still change with the resolution level.

the median values m of two adjacent resolution levels, indicated with x and $x+1$, as

$$\Delta_{\mathrm{m}} = (m^x - m^{x+1}) \cdot \frac{100\%}{m^x}, \tag{6.4}$$

and take the absolute value of Δ_{m} as a measure. This is calculated for the median values of T, n, and $x_{\mathrm{H_2}}$. On the x-axis in Fig. 6.11 it is indicated which resolution levels are compared. We find the smallest deviations for the median values of T in the order of magnitude of 1%, while the median values of n and $x_{\mathrm{H_2}}$ are larger (∼10%). For n we find the deviation to decrease with higher resolution level, while for $x_{\mathrm{H_2}}$ the deviation remains similar from the resolution L7 on. Thus, we conclude that the temperature of the gas is converged already at a low resolution level, while the total number density of the gas and its chemical composition are still evolving.

In Fig. 6.12 we compare the chemical composition of the gas for L6 and L10 as a function of T, n, and $x_{\mathrm{H_2}}$. In line with the distributions of the cumulative [C II] luminosity for these quantities, we find the chemical composition of the gas to be similar for $T \geq 100$ K and $n \leq 10$ cm^{-3} for all species except CO (see upper row of Fig. 6.12). The dense, molecular gas is not resolved at L6, causing differences for low temperatures and high densities. Likewise, the chemical composition of the gas with respect to $x_{\mathrm{H_2}}$ shows large differences between L6 and L10, indicating that the molecular gas is not resolved at L6.

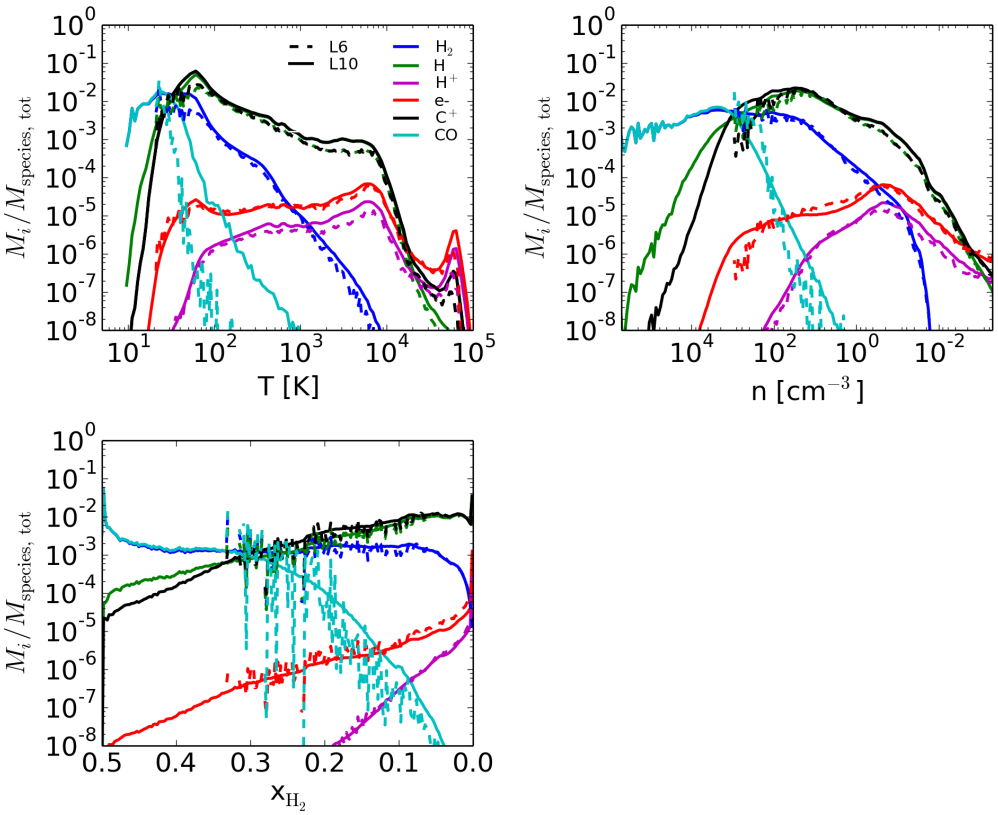

Figure 6.12: Comparison of the chemical composition of the gas in MC2 for the resolution L6 (dashed lines), and L10 (solid lines) as a function of the gas temperature (upper left), the number density (upper right), and the molecular hydrogen fraction (lower left). The best agreement is achieved between the resolution levels for the temperature.

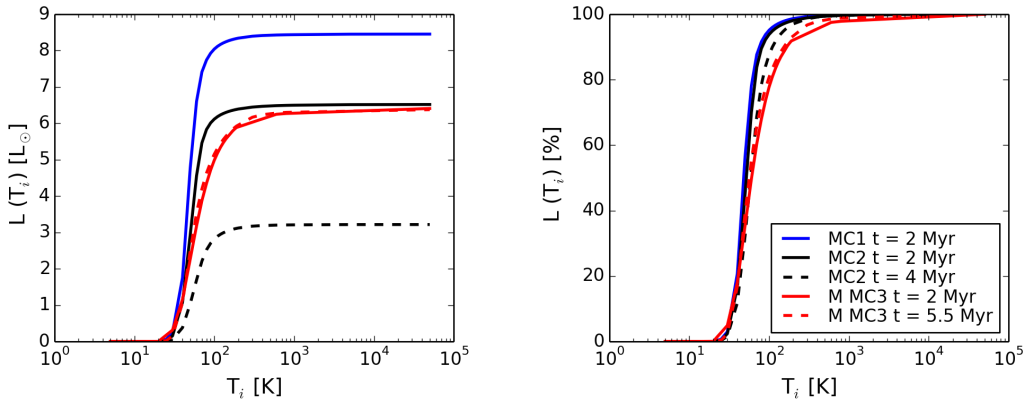

Figure 6.13: Results of the analysis studying the origin of the [C II] line emission with the optically thin [^{13}C II] line for different setups and different times. We present MC1 (blue line), MC2 (black lines) and a molecular cloud simulated including a magnetic field MMC3 (red lines). The solid lines indicate the earlier time steps (t = 2 Myr), and the dashed the later ones (t = 4 Myr or 5.5 Myr).

6.3.7 Testing different clouds and different times

To constrain the validity of the results, we study the origin of the [^{13}C II] line emission for the molecular cloud MC1, and a molecular cloud simulation including a magnetic field (MMC3) as well as different time steps. As an example calculation, we investigate the origin again as a function of the gas temperature. The resulting cumulative plots are presented in Fig. 6.13, where the left panel shows the results with their direct luminosities, and the left panel normalized to the individual maximum of the luminosity. We find for all molecular clouds and all time steps the same qualitative behaviour of the [C II] emission to stem mostly from gas with $T < 300$ K. For MC1 and MC2 the result of the analysis at t = 2 Myr is very similar (blue and black solid lines). At a later step of t = 4 Myr for MC2, the overall behaviour is still the same, but the total luminosity is dropped (black dashed line). For the molecular cloud MMC3 the slope of the cumulative plot is less steep (red lines) compared to the simulations without a magnetic field, but the qualitative behaviour is not changed. We analysed for MMC3 a snapshot at t = 2 Myr and t = 5.5 Myr, and find the results of both times to be very similar. Also their luminosities are similar. This could mean, that the chemical composition between the two times does only change slightly.

6.4 Comparison

In this chapter we investigated the physical properties of the gas emitting the [C II] line emission with respect to its kinetic temperature T, its total number density n, its fraction of molecular hydrogen x_{H_2}, and its visual extinction A_V. We carried out all analyses with the [^{13}C II] line emission, as it is not affected by opacity affects,

as shown for the zoom-in simulation MC2 in Section 6.3. The results we presented in cumulative distributions of the [C II] luminosities. We characterized the range of values for these four quantities by investigating at which value 25, 50, and 75% of the total [C II] luminosity in the cumulative plot are reached.

In general, we found that all SILCC-01 simulations with a fixed SNR, except *S10–KS–peak*, show with respect to the investigated physical properties (T, n, x_{H_2}, A_V) the same behaviour. For these runs, we found 50% of the [C II] luminosity to originate from gas with temperatures in the range of $36\,\mathrm{K} \leq T \leq 58\,\mathrm{K}$, number densities in the range of $740\,\mathrm{cm^{-3}} \leq n \leq 7300\,\mathrm{cm^{-3}}$, molecular hydrogen fractions around $x_{H_2} \sim 0.49$, and visual extinctions between $4.5 \leq A_V \leq 16.5$. In these simulations the [C II] line emission stems mainly from the cold, dense molecular gas, with H_2 and electrons being the dominant collisional partners.

In the run *S10–KS–peak* from the SILCC-01 simulations, the SNe explode in the positions of the molecular clouds. Therefore, the molecular gas is destroyed, the total [C II] luminosity drops, and also the results, characterizing the parameter space of the [C II] emitting gas, change. Here, we find the [C II] emission to stem from gas at higher temperatures ($81\,\mathrm{K} \leq T \leq 472\,\mathrm{K}$), lower number densities ($4\,\mathrm{cm^{-3}} \leq n \leq 19\,\mathrm{cm^{-3}}$) and smaller fractional abundances of the molecular hydrogen ($x_{H_2} \leq 0.05$). This indicates that the [C II] emitting gas in this simulation stems from warm, atomic gas.

We did the same analysis for simulations with sink particles (SILCC-02), in which the feedback by SNe (*FSN*) or the feedback by SN and stellar winds was considered (*FWSN*). For the chemical composition of the gas in the run *FWSN* we found carbon to be dominantly in CO for temperatures $T \leq 45$ K. This is not the case for the run *S10–KS–rand* of the SILCC-01 simulations, where C^+ is the dominant carbon species at all temperatures. As a result, 25% of the total [C II] luminosity are reached at temperatures of $T \sim 42$ K, comparable, with the values found for the SILCC-01 simulations (with $T \sim 36$ K), but the temperature at which 75% of the total [C II] luminosity is reached, is higher for the SILCC-02 simulations, with $T \sim 280$ K or 156 K for *FSN* and *FWSN*, respectively. For comparison, in the SILCC-01 simulations 75% of L_{tot} were reached at around ~58 K. Concerning the parameters of the number densities, fractional molecular hydrogen, and visual extinction of the gas, the results between SILCC-01 and SILCC-02 were very different, as we found for the SILCC-02 simulations the [C II] emitting gas to be at number densities between $6\,\mathrm{cm^{-3}} \leq n \leq 905\,\mathrm{cm^{-3}}$, present in almost the full range of fractional abundances of hydrogen ($0.02 \leq x_{H_2} \leq 0.35$ for *FSN*, and $0.13 \leq x_{H_2} \leq 0.49$ for *FWSN*), and with visual extinctions $A_V \leq 5.7$. Further, in the run *FWSN* we found a bimodal cumulative [C II] luminosity distribution. Concluding from these simulations, we found the [C II] line emission to originate partially from the molecular gas phase, and to a second part from the atomic gas phase.

Finally, we carried out the same studies for the zoom-in simulation MC2 with a spatial resolution of $dx = 0.122$ pc. We found the [C II] emitting gas to cover a narrow temperature range of $43\,\mathrm{K} \leq T \leq 64\,\mathrm{K}$, comparable to the one found for

the SILCC-01 simulations. However, for n, x_{H_2}, and A_V the parameter ranges for the [C II] emitting gas changed compared to the SILCC-01 simulations. Here, we find the gas to have number densities between $53\,\mathrm{cm}^{-3} \leq n \leq 438\,\mathrm{cm}^{-3}$, with fractional molecular abundances of $0.08 \leq x_{H_2} \leq 0.22$, and visual extinctions between $0.50 \leq A_V \leq 0.91$. This implies that the [C II] line emission is correlated with the atomic gas phase, being the assembly of the molecular clouds, and in transition to become molecular. Taking only pixels above an assumed detection limit of $I_{[^{12}CII]} \geq 0.5$ K km s^{-1} does not change the result.

To investigate, whether the results we found for MC2 are dependent on the chosen resolution level, we repeated the analysis for MC2 for the lower resolution levels (see Table 4.3). We found overall the same qualitative behaviour of the cumulative [C II] luminosity as a function of T, n, and x_{H_2}. However, at lower resolution levels the molecular gas is not resolved, and thus, the parameter range from which 50% of the [C II] luminosity stems is shifted in n and x_{H_2} towards lower densities and smaller molecular hydrogen fractions. The temperature, however, is least affected by the resolution.

Closing the loop to regarding the SILCC-01 and SILCC-02 simulations, we found that the results of the parameters, characterizing the origin of the emission depend in general on the resolution of the simulation as well as on the picked region in which the analysis is carried out. Simply reducing the resolution level of the zoom-in simulation does not reproduce the result found in SILCC-01 and SILCC-02. Among all studied parameters and simulations, we found the temperature range to be similar in all analysed studies.

6.5 Discussion

6.5.1 Comparison with observations

It is interesting to compare these results with observational efforts to determine the contribution from different ISM phases to the [C II] emission in the Milky Way. For example, Shibai et al. (1991) find that the diffuse [C II] emission observed with the Balloon-Borne Infrared Telescope (BIRT) agrees well with the observed distribution of ^{12}CO $J = 1 - 0$ emission, but not with the H I distribution in the Galaxy. They argue, based on this, that much of the observed emission must arise from the envelopes of giant molecular clouds illuminated by the interstellar radiation field, although it must be noted they require a radiation field strength $G_0 \sim 23$, roughly an order of magnitude larger than the value we adopt in our simulations. Keep in mind that the spatial resolution of the BIRT observations was $3.4'$ (see Table 1.1), which probably does not resolve the structures of the ISM on parsec scales.

More recently, Pineda et al. (2013, 2014) and Velusamy & Langer (2014) have

also attempted to estimate the amount of [C II] emission produced by molecular gas in the Galaxy, using the results of the GOT C+ survey, which provides a higher spatial resolution of 12″ (see Table 1.1). Velusamy & Langer (2014) find that around $\sim$ 62% of the observed emission must originate from diffuse and dense molecular clouds. However, some fraction of this emission must be produced by dense PDRs. Pineda et al. (2014), on the other hand, report that around 30% of Galactic [C II] emission originates from dense PDRs, 25% from CO-dark molecular gas, 25% from cold atomic hydrogen, and the remaining 20% from ionized gas. From the SILCC-01 and SILCC-02 simulations we found the [C II] line emission to originate mainly from the cold gas phase, and only a small contribution (e.g. $\sim$10% for the simulation *S10–KS–rand*) from temperature $T \geq 100$ K. In the zoom-in simulation MC2 the results only showed a contribution from the cold gas phase. This could be caused by cutting out a specific region of the simulation box. However, more generally spoken, Pineda et al. (2013, 2014), Velusamy & Langer (2014) find that a large part ($\sim$50%) of the [C II] emission originates from cold, dense gas. Since we do not include the contribution of PDRs, we only account for the contribution from the cold gas phase. Thus, the results of Pineda et al. (2013, 2014), Velusamy & Langer (2014) are qualitatively in good agreement with our results.

Further, Goldsmith et al. (2018) used [C II] observation of GREAT and upGREAT onboard SOFIA (see Table 1.1) to study the origin of the [C II] line emission. They combined these observations with H I 21 cm observations. In total four positions were studied. Assuming a fractional abundance of ionized carbon, they calculate the volume density and the external pressure of each source. Their results show, that the [C II] line emission originates from gas with number densities of $13\,\mathrm{cm}^{-3} \leq n(\mathrm{H} + \mathrm{H_2}) \leq 1903\,\mathrm{cm}^{-3}$, where between 10% and 67% of the hydrogen mass is in H_2. Further, they find the line widths of the [C II] emission lines and the H I absorption lines to be comparable. Therefore, they conclude that the [C II] line emission is associated with the atomic hydrogen. This is in line with the results of the analysis of the zoom-in simulations (see Section 6.3).

Beuther et al. (2014), or recently Bisbas et al. (2018) studied the [C II] line emission in four IRDCs. In the most quiescent regions, they could not detect [C II], whereas the [C II] emission get stronger in more actively star-forming regions. Beuther et al. (2014) finds the [C II] line emission to trace the environment around dense gas, and to be sensitive to the UV field. This is in line with the results we obtained for the zoom-in simulations. We likewise find the [C II] line emission to trace the envelope around the densest part of the molecular clouds, and being associated with atomic hydrogen. From our simulations, we further conclude that the [C II] line emission is detectable in molecular clouds even before the onset of star formation.

6.5.2 Comparison with other simulations

The origin of the [C II] line emission is likewise studied within other numerical simulations. Such a simulation was done by Smith et al. (2014), aiming to study the ISM comparable to the Milky Way. For this, the ISM is simulated within a torus, using the moving mesh code AREPO (Springel, 2010). Their simulations account for the galactic potential, but neglect the feedback from star formation, as well as self-gravity. As our simulations, they take the chemical network by Glover & Mac Low (2007a,b), Nelson & Langer (1997) into account. The [C II] properties of their simulations are studied in Glover & Smith (2016). For this, they estimate the [C II] emissivity of every cell and assume that the [C II] line emission is optically thin. This is comparable to our study, since we used the optically thin [^{13}C II] line emission for determine the physical properties of the [C II] emitting gas. Glover & Smith (2016) find in their simulation the warm neutral medium (WNM, $n \sim 0.2$ cm^{-3}, $T \sim 10^4$ K) to contribute to a small part to the [C II] line emission. Such a contribution we do not have for the zoom-in simulations, but we likewise saw in the SILCC-01, and SILCC-02 simulations. Thus, the contribution from the WNM comes from the surrounding medium, present with large volume filling factors in SILCC-01 and SILCC-02. The larger contribution to the [C II] line emission in the simulations of Glover & Smith (2016) stems from the cold, atomic and CO-dark H_2 gas, broadly distributed around $n \sim 20$ cm^{-3}, and $T \sim 100$ K. This large contribution we find likewise in our simulations. As Smith et al. (2014), Glover & Smith (2016) we do not account for the stellar feedback in the underlying 3D simulations, and therefore neither their nor our results contain the contribution from PDRs. However, we do account for self-gravity (lacking in the simulations of Smith et al. (2014)), and therefore, the gas in our simulations, especially the zoom-in simulation, can accrete to higher number densities and smaller temperatures. Further, the spatial resolution of the simulation influence the result. Therefore, we find with the zoom-in simulations 50% of the [C II] line emission to originate from $40\,\mathrm{K} \leq T \leq 65\,\mathrm{K}$ and $53\,\mathrm{cm}^{-3} \leq n \leq 438\,\mathrm{cm}^{-3}$, thus, being slightly different ranges as found by Glover & Smith (2016). Glover & Smith (2016) further discuss whether the [C II] line emission is correlated with the atomic or molecular gas. They define gas of H_2 dominated regions as gas, in which more than 50% of the hydrogen mass is in H_2. In their simulations, half of the emission from the cold gas phase is associated with H_2 dominated gas. They count this fraction of being CO-dark H_2 gas. Following the same definition, we on the other hand, find only ∼20% of the [C II] emission to originate from H_2-dominated gas in the zoom-in simulations. This difference can be caused likewise by self-gravity, which might prevent the formation of CO in the simulations of Smith et al. (2014), since the necessary shielding is not achieved.

A study, aiming to quantify numerically the origin of the [C II] line emission on a galactic scale, was presented by Accurso et al. (2017). Their setup couples the stellar spectrophotometric code STARBURST99 with the photoionization and astrochemistry codes MOCCASIN and 3D-PDR. With that they simulate entire star forming regions, so that their setup includes the feedback from stars. They assume a spherical symmetric geometry with an ionizing source in the centre of the cloud, while hydrodynamic effects, as turbulence, are neglected. Compared to our simula-

tions, they include the stellar feedback, that we do not account for, and neglect the hydrodynamics, that we focus on. Accurso et al. (2017) assume that the physical conditions found in each of their clouds represent the average physical conditions on galaxy-wide scales. They investigate, which fraction of the [C II] line emission ($f_{[\mathrm{CII}],mol}$) stems from the molecular gas phase. In their definition, gas with more than 1% of hydrogen in H_2 is molecular. They apply a Bayesian formalism and statistical weights for the clouds, and fit $f_{[\mathrm{CII}],mol}$ as a function of the density, dust mass fraction, specific star formation rate (SSFR), and metallicity. For the parameter space of the Milky Way, they find around 75% fo the [C II] line emission to be correlated with the molecular gas, according to their definition. Taking the same definition, we would have 99.8% of the [C II] line emission to be correlated with molecular gas.

7

Correlation of the [C II] line emission with the number density

The analysis presented in this Chapter is based on the zoom-in simulation MC2. Here, we study the correlation between the integrated [^{12}C II] intensities and the column densities of the gas. This is part of the paper, submitted to MNRAS in May 2018 as Franeck et al. (2018).

7.1 Direct correlation

In extragalactic studies the [^{12}C II] line emission is used to constrain the mass of the different components of a galaxy. For this, PDR models are used. As an example, in the studies of submilimetre galaxies by Swinbank et al. (2012) and starburst galaxies by Hailey-Dunsheath et al. (2010) the mass of the molecular and atomic gas was estimated by the [^{12}C II] line emission. Further studies correlate the column density with the [^{12}C II] line emission, as done by Goicoechea et al. (2015) in Orion and by Langer et al. (2014b) in the Milky Way. Both calculate the C^+ column density out of the [^{12}C II] line emission. An estimate of the correlation between the [^{12}C II] line emission and the C^+ column density was given by Goldsmith et al. (2012). Inspired by these approaches, we here investigate the correlation of the [^{12}C II] line emission with the column densities of the gas within the zoom-in simulations. We note, that the zoom-in simulations represent a molecular cloud before the onset of star formation. Thus, they do not include PDRs from individual stars. As we found in Section 6.3, the [^{12}C II] line emission originates from gas associated with atomic

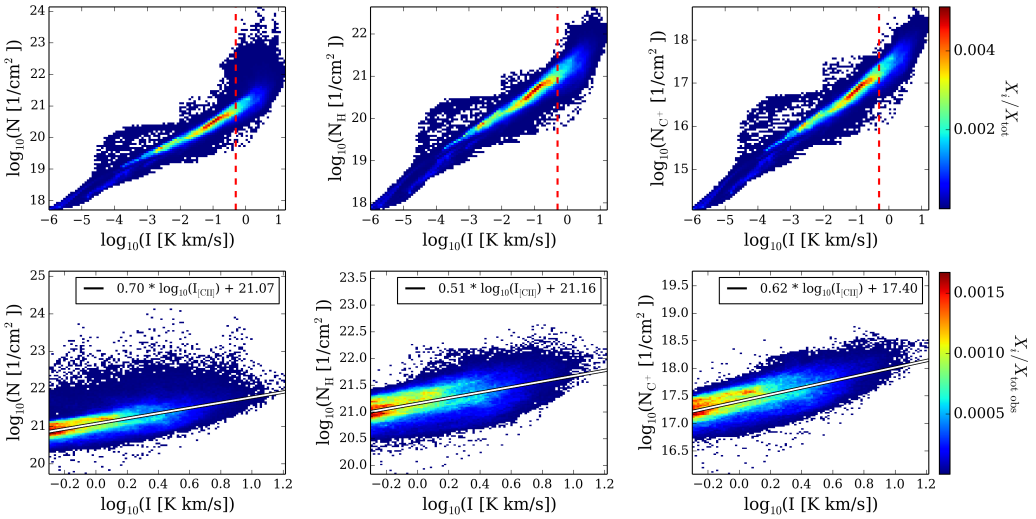

Figure 7.1: Two-dimensional histograms of the distribution of the opacity affected [^{12}C II] line intensity and several column densities, as for the total gas (left), atomic hydrogen H (middle) and carbon ions C^+ (right). In the top row we show the distributions combined for all three projections of the data in the whole map. The observable limit of $I_{[^{12}\mathrm{CII}]} \geq 0.5$ K km s^{-1} is marked with the red dashed lines. In the bottom row we show only the part of the observational data and their linear fits. The colour-coding indicates the fraction of pixels in the entire maps (X_i/X_{tot}, top row), and of the observable pixels ($X_i/X_{\mathrm{tot,\,obs}}$, bottom row).

hydrogen. Therefore, we constrain ourselves to study the correlation of the [^{12}C II] line emission with the total column density of the gas, the C^+ column density and the H column density.

In the upper row of Fig. 7.1 we present the two-dimensional histogram of the distribution between the integrated [^{12}C II] line emission and the different column densities of the gas: the total column density (left), the H column density (middle) and the C^+ column density (right). As bin sizes we use logarithmically equal distributed bins with $\Delta\log_{10}(I\,[\mathrm{K\,km\,s^{-1}}]) = 0.07$ and $\Delta\log_{10}(N_i\,[\mathrm{cm^{-2}}]) = 0.06$. In these double-logarithmic plots the integrated [^{12}C II] intensities follow a power law as a function of the column densities. However, with higher column densities the integrated [^{12}C II] line emission does not necessarily grow, and we find a steepening in the correlation. This is caused *(i)* by the optical depth of the line, and *(ii)* by the fact, that C^+ is transformed to CO in high densities, and therefore is less abundant in regions with high densities. Therefore, the scatter in the range of observable integrated [^{12}C II] intensities is larger in the correlation plot. We marked the assumed limit of $I_{[^{12}\mathrm{CII}]} = 0.5$ K km s^{-1} with the red dashed lines in the plot.

In the lower row of Fig. 7.1 we show the distribution of the integrated [^{12}C II] intensity and the column density only for the observable fraction of pixels. As bin sizes we use $\Delta\log_{10}(I\,[\mathrm{K\,km\,s^{-1}}]) = 0.02$ and $\Delta\log_{10}(N_i\,[\mathrm{cm^{-2}}]) = 0.04$. Although the scatter is large, we find a power law in all three distributions, that can be fitted

by

$$\log_{10}\left(\frac{N_{\rm tot}}{\rm cm^2}\right) = (0.702 \pm 0.002) \times \log_{10}\left(\frac{I_{[^{12}\rm CII]}}{\rm K\ km\ s^{-1}}\right) + (21.0722 \pm 0.0005), \tag{7.1}$$

$$\log_{10}\left(\frac{N_{\rm H}}{\rm cm^2}\right) = (0.514 \pm 0.001) \times \log_{10}\left(\frac{I_{[^{12}\rm CII]}}{\rm K\ km\ s^{-1}}\right) + (21.1595 \pm 0.0004), \tag{7.2}$$

$$\log_{10}\left(\frac{N_{\rm C^+}}{\rm cm^2}\right) = (0.616 \pm 0.001) \times \log_{10}\left(\frac{I_{[^{12}\rm CII]}}{\rm K\ km\ s^{-1}}\right) + (17.4008 \pm 0.0004). \tag{7.3}$$

For fitting, we used the numpy python package "polyfit", and calculate the errors Δm and Δb for the linear equation $y(x) = (m \pm \Delta m)x + (b \pm \Delta b)$ as

$$\Delta m = \sqrt{\frac{1}{(n-2)}\frac{r}{D}} \tag{7.4}$$

and

$$\Delta b = \sqrt{\frac{1}{(n-2)}\frac{r}{D}\left(\frac{D}{n} + \overline{I}^2\right)}. \tag{7.5}$$

Here, n denotes the number of data points, r is the residual, D is the variance, and $\overline{I}$ is the mean intensity of the considered data. The variance is calculated with the algebraic formula for the variance as

$$D = \sum_{i=1}^{n}(I_i)^2 - \frac{1}{n}\left(\sum_{i=1}^{n} I_i\right)^2. \tag{7.6}$$

The errors calculated in this manner correspond to the ones obtained by the Jacobian matrix.

7.2 Correlation analysed with $Y_{\rm CII}$

To create a scale invariant quantity, we define a $Y_{\rm CII}$ factor for characterizing the relation between the total column density of the gas $N_{\rm tot}$ in [cm^{-2}] and the integrated [^{12}C II] intensity I in [K km s^{-1}] as

$$Y_{\rm CII} = \frac{N_{\rm tot}}{I}. \tag{7.7}$$

If the column density $N_{\rm tot}$ would scale linearly with the integrated intensity I, the $Y_{\rm CII}$ factor would be constant. We calculate the $Y_{\rm CII}$ factor for MC2 in the xz-projection and present the map in the left panel of Fig. 7.2. Opaque colours mark

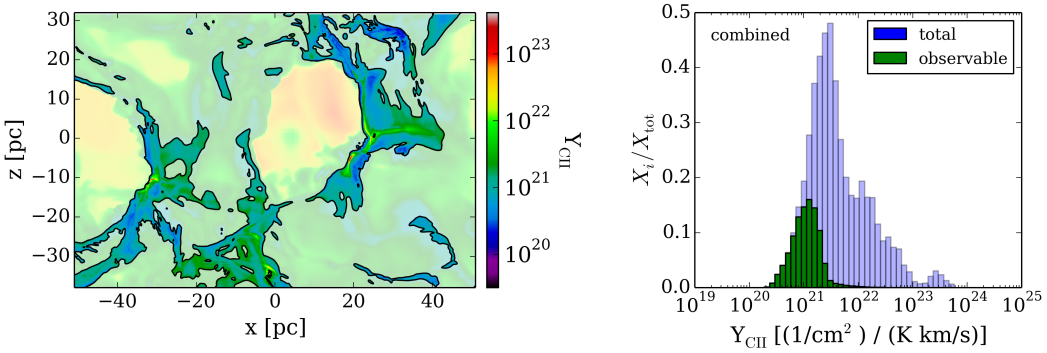

Figure 7.2: Map of the Y_{CII} values (Eq. (7.7)) in the xz-projection of MC2 at L10 (left panel). Opaquely coloured regions in the map indicate pixels that we assume to be observable ($I_{[^{12}\mathrm{CII}]} \geq 0.5$ K km s^{-1}). The histogram (right) presents the distribution of the Y_{CII} values combined for all projections considering the total map (blue) and the observable pixels (green). The fraction of pixels in every bin is indicated with X_i/X_{tot}.

Table 7.1: Summary of the values of the Y_{CII} factor, quantifying the range of Y_{CII} values, calculated for the xz-projection in MC2 at the resolution level of L10, and for the combined data of all projections for MC2 at L10. In the upper part we lost the Y_{CII} values of the assumed observable region ($I_{[^{12}\mathrm{CII}]} \geq 0.5$ K km s^{-1}), and in the lower part the values considering the whole map.

projection		Y_{CII} [cm^{-2} (K km s^{-1})$^{-1}$]			
		25%	50% (median)	75%	mean
xz	observable	7.27×10^{20}	1.09×10^{21}	1.53×10^{21}	1.37×10^{21}
combined	observable	7.48×10^{20}	1.11×10^{21}	1.59×10^{21}	1.44×10^{21}
xz	total	1.65×10^{21}	2.83×10^{21}	5.98×10^{21}	7.23×10^{21}
combined	total	1.76×10^{21}	3.21×10^{21}	9.39×10^{21}	1.49×10^{22}

those regions with integrated intensities, that we assume to be observable ($I_{[^{12}\mathrm{CII}]} \geq 0.5$ K km s^{-1}). The right panel in Fig. 7.2 shows the histogram of the Y_{CII} combined for the pixels of all three projections for MC2 at L10, where the blue part represents all pixels in the map, and the green part only the observable pixels. The bin size is set to $\Delta\log_{10}(Y_{\mathrm{CII}}\,[\mathrm{cm}^{-2}(\mathrm{K\ km\ s}^{-1})^{-1}]) = 0.08$. In general, we find that the values in Y_{CII} cover a range between 10^{20} and 10^{24} cm^{-2} (K km s^{-1})$^{-1}$. Almost all high values in Y_{CII} occur in regions with unobservable low integrated intensities. To describe the distribution of the Y_{CII} values, we determine again at which value of Y_{CII} 25, 50 and 75% of the Y_{CII} value distribution are included. The values of Y_{CII} for the whole map and the observable regions are listed in Table 7.1. For the *xz*-projection in Fig. 7.2 we find within the interquartile range (e.g. the distance between the value at which 25% and 75% of the Y_{CII} value distribution are included) Y_{CII} values of $2.83^{+3.15}_{-1.18} \times 10^{21}$ cm^{-2} (K km s^{-1})$^{-1}$ considering all pixels, and $1.09^{+0.44}_{-0.36} \times 10^{21}$ cm^{-2} (K km s^{-1})$^{-1}$ considering only the assumed observable pixels. In an unresolved study we would obtain a single value of the integrated intensity, which we estimate with the averaged integrated intensity over the whole map as $I_{\mathrm{unres}} = 0.4$ K km s^{-1}. Further, we would also only obtain one single value for the total column density, where we have the average over the whole map as $N_{\mathrm{tot,\,unres}} = 6.3 \times 10^{20}$ cm^{-2}. With these simplified values we would obtain $\mathrm{Y}_{\mathrm{CII,\,unres}} = 1.5 \times 10^{21}$ cm^{-2} (K km s^{-1})$^{-1}$. This value is lower than the resolved values listed in Table 7.1.

Eq. (7.1) can be expressed in terms of Y_{CII} as

$$\begin{aligned} &\log_{10}\left(\frac{Y_{\mathrm{CII}}}{\mathrm{cm}^{-2}(\mathrm{K\ km\ s}^{-1})^{-1}}\right) = \\ &-(0.298 \pm 0.165) \times \log_{10}\left(\frac{I_{[^{12}\mathrm{CII}]}}{\mathrm{K\ km\ s}^{-1}}\right) + (21.0722 \pm 0.0005). \end{aligned} \tag{7.8}$$

When estimating the Y_{CII} value and the total column density N_{tot} out of the [^{12}C II] intensity, it might be of advantage to use Eqs. (7.1) and (7.8) instead of a single value. As a first test of this statement, we calculate the width of the distribution of the Y_{CII} values around the fitting function of Eq. (7.8). We measure the width of the distribution in interquartile range d_{iqr}, as the difference between the value including 25% and 75% of the distribution. We find $d_{\mathrm{iqr}} = 7.5 \times 10^{20}$ cm^{-2} (K km s^{-1})$^{-1}$ for the distribution around the fitting function, which is slightly smaller than $d_{\mathrm{iqr}} = 8.4 \times 10^{20}$ cm^{-2} (K km s^{-1})$^{-1}$ as the width around the median Y_{CII} value. As a second test we calculate the deviation between the distribution of Y_{CII} values and the ones calculated with Eq. (7.8) as

$$\Delta_{Y_{\mathrm{CII}}} = |Y_{\mathrm{CII}}^{\mathrm{fit}} - Y_{\mathrm{CII}}^{\mathrm{map}}| \cdot \frac{100\%}{Y_{\mathrm{CII}}^{\mathrm{fit}}}. \tag{7.9}$$

From this, we find 25% (50%, 75%) of the pixels to deviate from the fit by $\Delta_{Y_{\mathrm{CII}}} \approx 16\%$ (33%, 54%, respectively).

As a third test we calculate the Y_{CII} values out of the [^{12}C II] intensities of the map in *xz*-projection of MC2 with Eq. (7.8) and derive from this the gas mass. In

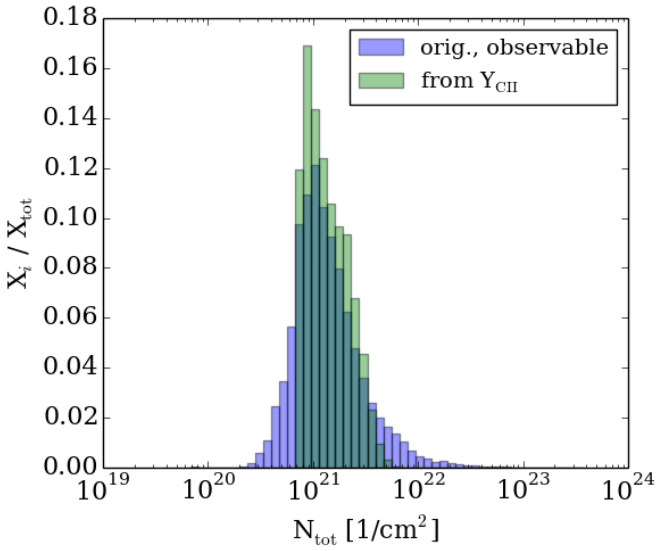

Figure 7.3: Distribution of column densities in the observed area of MC2 in the *xz*-projection (blue), and recalculated using the integrated [^{12}C II] intensity and Eq. (7.8) (green). The projected mass is underestimated by 22% to 35% when using the fitting function. This is more precise than taking a single value. The fraction of pixels is indicated with $X_i/X_{\rm tot}$.

the assumed observable part of the cloud, 70% of the total mass of the cloud are included ($m_{\rm tot} = 8.4 \times 10^4$ M$_\odot$, $m_{\rm proj} = 5.8 \times 10^4$ M$_\odot$). Calculating $Y_{\rm CII}$ from the observable part and then estimating the mass, we recover $m_{\rm cloud,\,YCII} = (4.1^{+0.405}_{-0.320}) \times 10^4$ M$_\odot$, which corresponds to 65% to 78% of $m_{\rm proj}$. We illustrate this result in Fig. 7.3, where we show the histograms of the column densities from the map of the *xz*-projection of the observable area (blue), and of the column densities calculated with the fit by Eq. (7.8) from the same area (green). The bin sizes are chosen to $\Delta\log_{10}(Y_{\rm CII}\,{\rm cm^{-2}(K\,km\,s^{-1})^{-1}}) = 0.08$. By applying the fit, we reproduce the intermediate column densities in the range of 5×10^{20} cm^{-2} to 6×10^{21} cm^{-2}, but not the lower and higher ones. For comparison, we take the single value of $Y_{\rm CII} = 1.11^{+0.48}_{-0.37} \times 10^{21}$ cm^{-2} (K km s^{-1})$^{-1}$ for recalculating the mass of the cloud, and obtain $m_{\rm cloud,\,YCII} = (11.25^{+4.85}_{-3.65}) \times 10^4$ M$_\odot$. By this, we overestimate the projected mass, as the lower limit of this value corresponds to 130% of $m_{\rm proj}$, and the upper limit to 280% of $m_{\rm proj}$. From this analysis we conclude, that $Y_{\rm CII}$ is not constant, and is estimated best with a scaling with the integrated [^{12}C II] intensity as $I^{-0.3}_{[^{12}{\rm CII}]}$ (see Eq. 7.8).

8

Line profiles

The SILCC simulations from the setup SILCC-01 and SILCC-02 have a resolution of 3.9 pc at their highest refinement level. The zoom-in simulations provide a best spatial resolution of 0.122 pc. Due to the high resolution of the zoom-ins we can also study the line profiles of [C II]. For this, we calculate the line profiles with a spectral resolution of dv = 0.1 km s^{-1}. We study the line profiles using the example of the opacity affected [^{12}C II] line emission. We investigate a method based on the work by Tauber et al. (1996) aiming to find a statistical tool for characterizing the line profiles within the zoom-in simulations. Such a method could be helpful for comparing in a more general way the simulations with the observations. In this chapter we first describe some examples of [C II] line profiles and then introduce a method for a statistical tool.

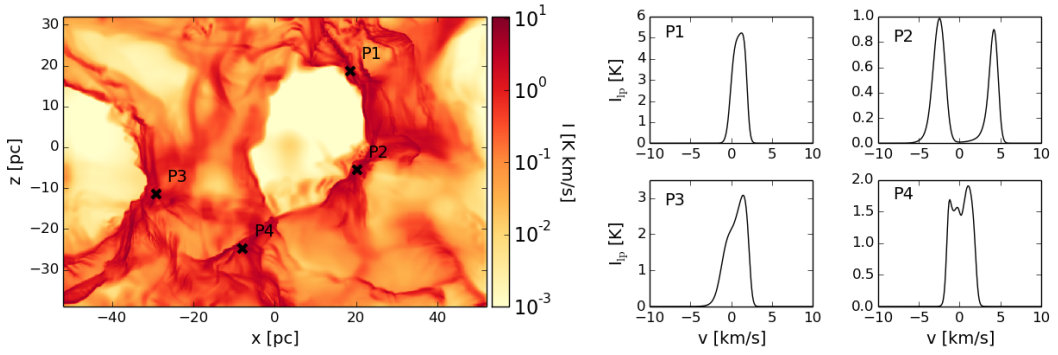

Figure 8.1: Synthetic [^{12}C II] emission map of MC2 in xz-projection (left) and some example line profiles (right) of the points marked in the map.

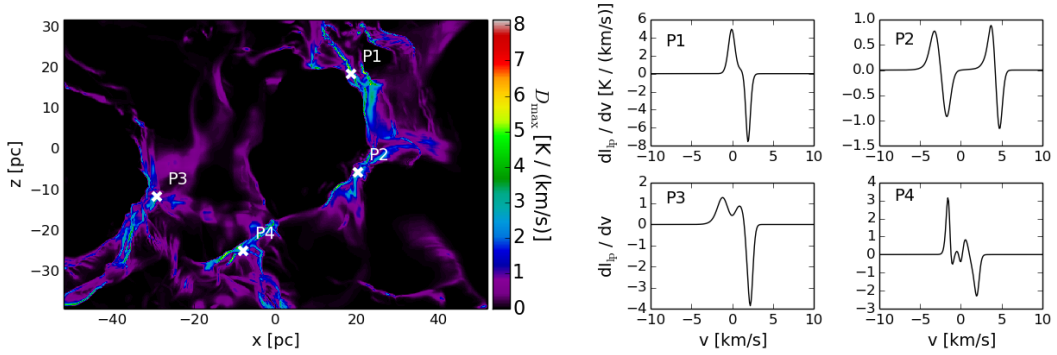

Figure 8.2: Maximum of the absolute value of the derivative of the [^{12}C II] line profiles,$D_{\max}$, shown for the map of MC2 in the xz-projection (left), and the derivatives of the line profiles P1, P2, P3 and P4 (right).

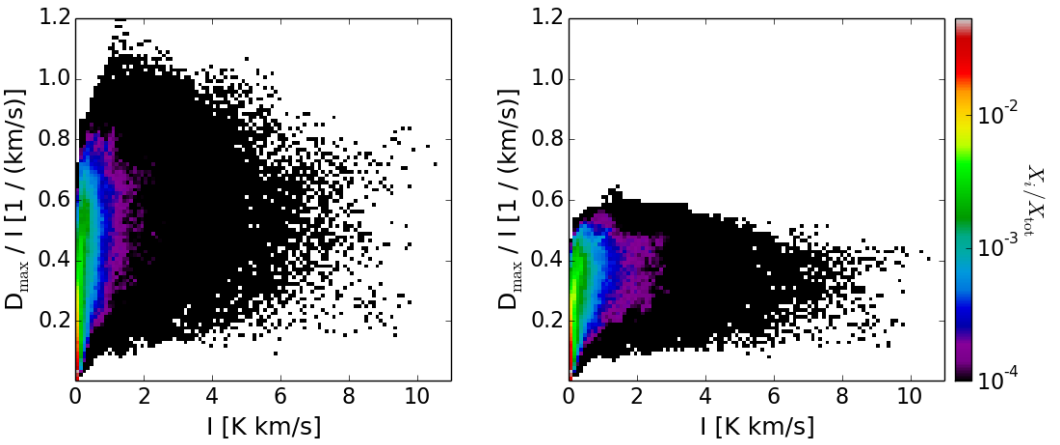

Figure 8.3: Distribution of the pixels as a function of the maximum slope normalized by the integrated [^{12}C II] intensity, $D_{\max}/I$, and the integrated [^{12}C II] intensity I for MC2 in the xz-projection, for the original data (left) and the smoothed data (right). The colour-coding indicates the fraction of pixels in each bin with respect to the total amount of pixels. The spectral resolution for the original data is $\mathrm{dv} = 0.1$ km s^{-1}, and for the smoothed data $\mathrm{dv} = 0.4$ km s^{-1}. Line profiles with a high integrated [^{12}C II] intensity are more likely to show a steeper slope, and have therefore higher values in $D_{\max}$.

8.1 Examples of line profiles

Fig. 8.1 shows the synthetic [C II] emission map in the *xz*-projection, and some example line profiles (P1, P2, P3, P4) within MC2 for the resolution level L10. Those line profiles are assumed to be observable, since their integrated intensity is well above the assumed detection limit of $I_{[^{12}\mathrm{CII}]} \geq 0.5$ K km s^{-1} (see Table 8.1). P1 is the line profile of the pixel with the maximum integrated [C II] intensity. It has one single component along the line of sight. For P2, there are two well separated components. P3 gives an example, in which the components are close together, resulting in an asymmetric profile. This profile has a sharp slope on the side of the positive velocities, and a shoulder on the other side. The example of P4 shows a complex line profile of several components, that differ much from a Gaussian. Within the discussion process of the work it was demurred whether the steep slopes seen in some of the profiles are an artefact of the simulations, or whether they also occur in observed profiles. We test this with the first derivative of the profiles, by calculating the maximum of the absolute value of the derivative D_{max} as

$$D_{\mathrm{max}} = \max\left\{\left|\frac{\mathrm{d}I_{\mathrm{lp}}}{\mathrm{dv}}\right|\right\}. \tag{8.1}$$

Fig. 8.2 shows D_{max} for MC2 in the *xz*-projection, and the derivatives of the line profiles shown in Fig. 8.1. We find that the slopes (D_{max}) of the profiles become steeper in regions with higher integrated intensities, with $D_{\mathrm{max}} \leq 8$. Since for a Gaussian line profile D_{max} scale linearly with its amplitude, we normalize D_{max} by the integrated intensity I for a general study. We show in Fig. 8.3 in the left panel the scatter plot of D_{max}/I as a function of the integrated intensity I. The values of D_{max}/I covers a range of $D_{\mathrm{max}}/I \leq 1.2$, whereas the scatter in the values decreases slightly with increasing I.

To judge, whether the values we obtain are reasonable, we compare the values of D_{max} from the simulations with observations from Beuther et al. (2014)[1]. They studied the [^{12}C II] line emission in four infrared dark clouds, and detected [^{12}C II] in three of them (G48.66, IRDC18223, IRDC18454). We take the data for G48.66 (28–45 km s^{-1}), since this data has integrated [^{12}C II] line intensities comparable to the intensities we find in our simulation MC2. The observational data provide a spectral resolution of dv = 0.08 km s^{-1} (see table 3 in Beuther et al., 2014). As this being observational data, they include noise, so that we cannot directly calculate the derivative of the line profiles. Instead, we first smooth the data with a Gaussian kernel. As a free parameter, we set the standard deviation of the Gaussian in amount of pixels s. Fig. 8.4 shows an example line profile of the data (black line), smoothed with a Gaussian kernel of two pixels ($s = 2$, red line) and five pixels ($s = 5$, blue line). For $s = 2$, the peaks of the noise are considered as part of the signal. For $s = 5$ we recover only the features of the signal and the noise is removed. By smoothing the line profiles, we reduce the spectral resolution to $\mathrm{dv}_s = s \times 0.08$ km s^{-1}, resulting in $\mathrm{dv}_{s=2} = 0.16$ km s^{-1} for $s = 2$ and $\mathrm{dv}_{s=5} = 0.40$ km s^{-1} for $s = 5$. Fig. 8.5

[1]Beuther et al. (2014) published the data at `http://cdsarc.u-strasb.fr/viz-bin/qcat?J/A+A/571/A53`

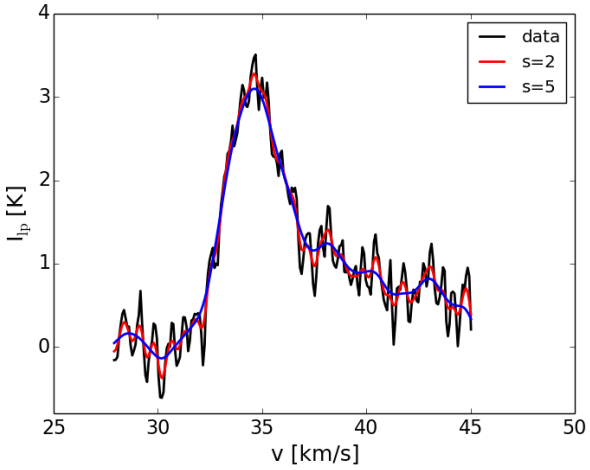

Figure 8.4: [^{12}C II] line profile from G48.66 (data from Beuther et al., 2014) as the raw data (black line) and smoothed with $s = 2$ and $s = 5$ (red and blue lines). A smoothing of $s = 5$ is sufficient to avoid taking the noise for the derivative study into account.

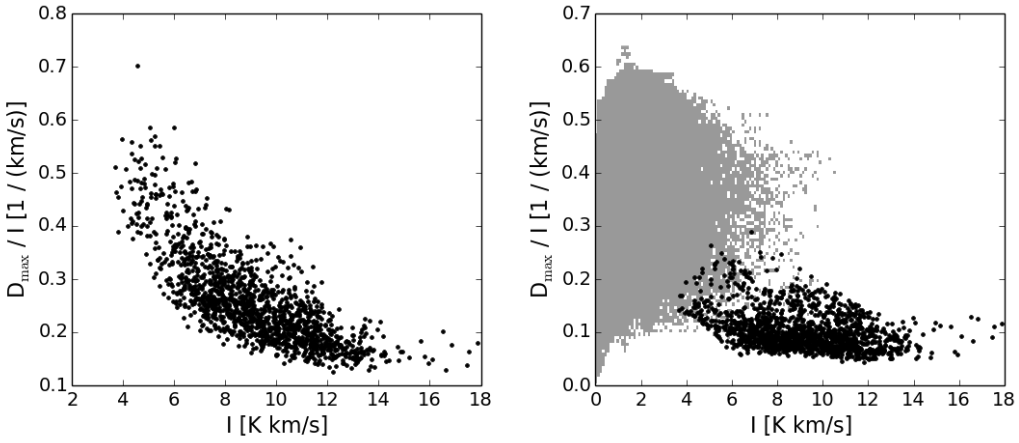

Figure 8.5: Scatter of $D_{\max}/I$ and the integrated [^{12}C II] intensity I for the infrared dark cloud G48.66 with the data from Beuther et al. (2014). The data was smoothed with the smoothing parameters $s = 2$ (left) and $s = 5$ (right). Taking a larger smoothing parameter results into smaller values for $D_{\max}$, and thus, $D_{\max}/I$ drops likewise. The grey shaded area marks the parameter range we found for MC2 at the same spectral resolution, as shown in the right panel of Fig. 8.3.

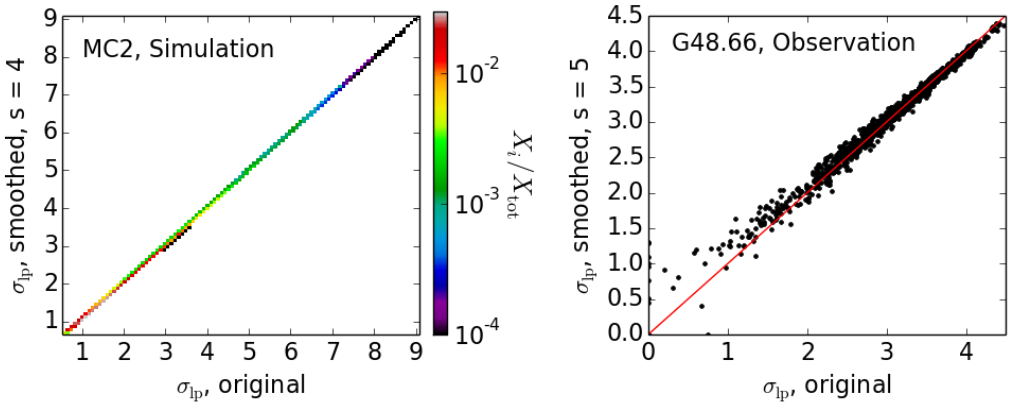

Figure 8.6: Comparison of the widths of the line profiles σ_{lp} for the original line profiles, and the smoothed ones. The left panel shows the scatter plot for the data from the simulation, and the right one for the data from the observations. The smoothing has only a minor impact on σ.

shows the scatter plots between the normalized maximum of the slope D_{max}/I and the integrated [^{12}C II] intensity I for the infrared dark cloud G48.66, whereas D_{max} is calculated after smoothing the data with $s = 2$ (left) and $s = 5$ (right). As we found for the simulation MC2, there is the tendency that with higher integrated intensities the values of D_{max} are larger. A smoothing with a higher s reduces D_{max} in general, and therefore, also the ratio D_{max}/I is reduced.

To compare the simulations with the observations, we have to bring the data to the same spectral resolution, that the observational data have after the smoothing. To obtain the spectral resolution of $dv_{s=5} = 0.40$ km s^{-1}in the simulations, we smooth the simulation data with a kernel of $s = 4$, so that $dv_{sim,s=4} = 4 \times 0.1 = 0.4$ km s^{-1}. The resulting scatter plot of the smoothed profiles is shown in the right panel of Fig. 8.3. The values of D_{max} are now smaller, up to $D_{max} \leq 4.4$, and D_{max}/I has dropped likewise to $D_{max}/I \leq 0.6$. We compare the distribution from the smoothed simulation with the smoothed observational data in Fig. 8.5, and indicate the prarmeter range of the simulation as grey shaded area in the right panel of (Fig. 8.5. We find the values for D_{max}/I to be smaller in the observations compared to the simulations. However, the range of values for D_{max}/I in the simulations is in the range of the simulations.

We additionally investigate, whether the smoothing influences the width σ_{lp} of the line profiles. The widths of the original data and the smoothed ones are compared in Fig. 8.6 for the data from the simulation (left panel) and from the observation (right panel). We find, that the smoothing does not change σ of the line profiles of the simulation data and has only a minor impact on σ for the observed data.

8.2 Tauber method

For finding a statistical tool for analysing the line profiles, we use the work of Tauber et al. (1996) as a starting point. The ansatz of his method is to compare the line profiles with a reference function. We take over this idea in this work and compare the line profile with a Gaussian profile and with a boxcar function. If a line profile consists of a single optically thin component, the shape of the profile can be described by a Gaussian. For an optically thick profile, we assume the line profile to be more similar to a boxcar function. The Gaussian we define as

$$G(\mathrm{v}) = A_{\mathrm{Gauss}} \exp\left\{-0.5 \times \left(\frac{\mathrm{v} - \overline{\mathrm{v}}}{\sigma_{\mathrm{Gauss}}}\right)^2\right\}, \tag{8.2}$$

and the boxcar function as

$$B(\mathrm{v}) = A_{\mathrm{Box}} \times \{H(\mathrm{v} - a) - H(\mathrm{v} - b)\}, \tag{8.3}$$

where, $b > a$, and with $H(\mathrm{v})$ being the Heaviside step function. For every line we calculate reference functions in a way, that the reference functions conserve the zeroth, first and second moment of the line profile (i.e., the area, the centroid and the width of the functions). For the Gaussian the first moment defines the position of the peak, the second moment is its standard deviation σ_{Gauss}. The centroid and standard deviation are taken directly from the line profile, so that $\sigma_{\mathrm{Gauss}} = \sigma_{\mathrm{lp}}$, and $\overline{\mathrm{v}}_{\mathrm{Gauss}} = \overline{\mathrm{v}}_{\mathrm{lp}}$, for calculating $G(\mathrm{v})$. The amplitude A_{Gauss} is chosen in a way, that the zeroth moment is conserved.

For the boxcar function the centroid is likewise given by the first momentum of the line profile, $\overline{\mathrm{v}}_{\mathrm{Box}} = \overline{\mathrm{v}}_{\mathrm{lp}}$. The standard deviation of the box car function, defined within the boundaries a and b is given by

$$\sigma_{\mathrm{Box}} = \int_a^b (v - \overline{\mathrm{v}})^2 d\mathrm{v}. \tag{8.4}$$

The centroid $\overline{\mathrm{v}}_{\mathrm{Box}}$ and the lower and upper limits a and b are connected via

$$\overline{\mathrm{v}}_{\mathrm{Box}} = \frac{b + a}{2}. \tag{8.5}$$

We further introduce the parametrization

$$\Delta\mathrm{v} = b - a \tag{8.6}$$

an thus, σ_{Box} can be written as

$$\sigma_{\mathrm{Box}} = \frac{1}{12}\Delta\mathrm{v}. \tag{8.7}$$

Having calculated the borders of a and b, so that $\sigma_{\mathrm{Box}} = \sigma_{\mathrm{lp}}$, the amplitude A_{Box} of the function is likewise chosen so that the area beyond the function is equal to the

Table 8.1: Values of the integrated intensity, velocity centroid $\overline{v}$ and width σ of the profiles shown in Figs. 8.1 and 8.7. The coordinates are given in pixels within the total map of 1024×1024 pixels, and in parsec, as in Figs 8.1 and 8.2. The last columns give the Tauber values.

point	coordinates		I	$\overline{v}$	σ	Tauber values	
	pixel	[pc]	[K km s^{-1}]	[km s^{-1}]	[km s^{-1}]	V_{Gauss}	V_{Box}
P1	[665, 664]	[18.68, 18.55]	10.56	0.922	0.694	0.026	0.072
P2	[467, 678]	[-5.49, 20.26]	3.155	0.144	3.319	0.493	0.630
P3	[418, 273]	[-11.47, -29.17]	8.855	0.559	1.151	0.057	0.107
P4	[309, 448]	[-24.78, -7.81]	5.97	0.20	1.09	0.069	0.060

zeroth moment.

Each line profile from the simulation is compared with the reference functions in every velocity channel. This is done by taking the difference between the value of the line profile l_i and the value of the reference function r_i for every channel map i in the following form:

$$\Delta T_R = \sqrt{\frac{1}{n}\sum_{i=0}^{n}(l_i - r_i)^2} \tag{8.8}$$

Using the quadratic mean is important especially for observers, since they need to take the noise in each channel into account.We further take for the calculation of ΔT_R only values into account within $\pm 3\sigma$ around the rest frequency. By this, we avoid to sum up zero values along the profile, when the signal is only present in a distinct velocity range. Such a summation of zero values would diminish the value of ΔT_R. The Tauber value V_R is then calculated as

$$V_R = \Delta T_R / T_R, \tag{8.9}$$

whereas T_R is the peak of the Gaussian or the Boxcar function. The index R indicates, whether the Tauber value is calculated with the Gaussian or the Boxcar function as reference function.

In Fig. 8.7 the line profiles of P1, P2, P3 and P4 are overplotted with their Gaussian and Boxcar reference functions. Only the range of 3σ, as indicated by the grey shaded area in the plots, is used for calculating the Tauber values V_{Gauss} and V_{Box}. Table 8.1 lists the characteristic values of the line profiles, as well as the Tauber values estimated by the two reference functions. For P1, the line profile is close to the shape of a Gaussian function. Therefore the Tauber value V_{Gauss} is small ($V_{\mathrm{Gauss}} = 0.026$). Since the deviation from the boxcar function is larger, also V_{Box} is larger than V_{Gauss} ($V_{\mathrm{Box}} = 0.072$). The line profile P2 consist of two components. Since only one centroid and width is calculated for the whole profile, none of the reference functions match the shape of the line profile. As a result, the Tauber values are both larger than for P1. In the third example (P3), the components of the profile build again only one peak. This makes the Tauber values in general smaller. As in P1, the shape of the profile is closer to a Gaussian, so that the Tauber value $V_{\mathrm{Gauss}} = 0.057$ is smaller than $V_{\mathrm{Box}} = 0.107$. The example of P4 shows a line profile

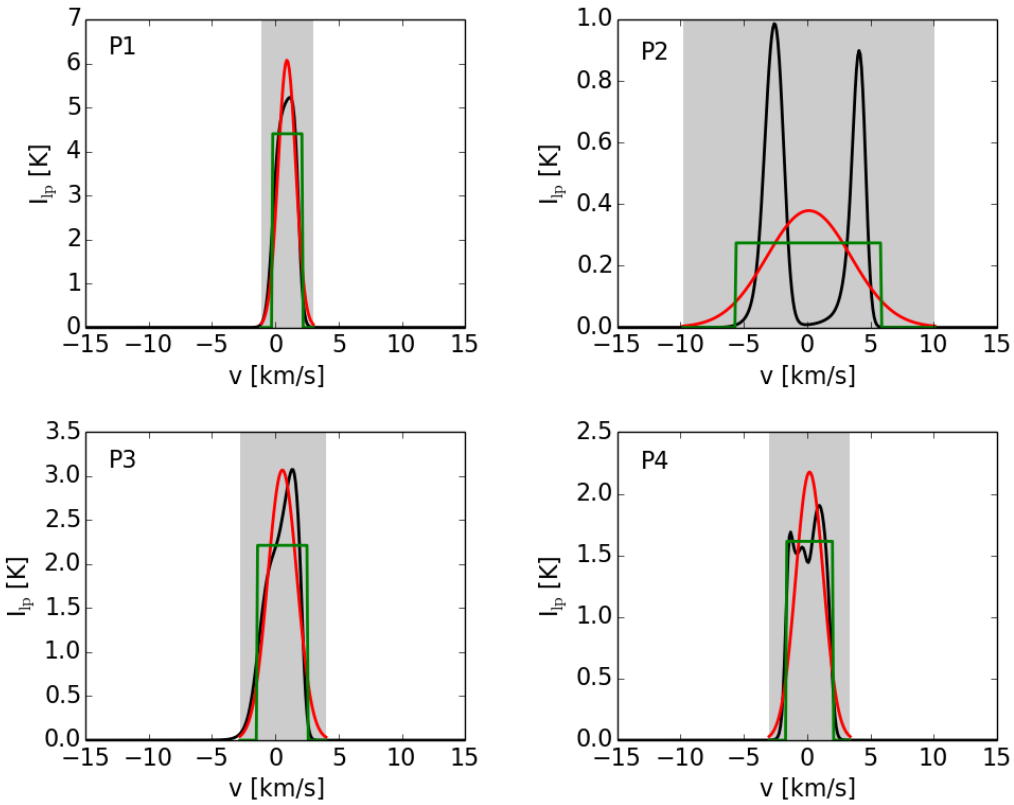

Figure 8.7: Line profiles of the examples P1 – P4, overplotted with the Gaussian and Boxcar reference functions. The reference functions have the same area, centroid and width, as the line profiles. The grey shaded area indicates the 3σ region, in which the Tauber values are calculated.

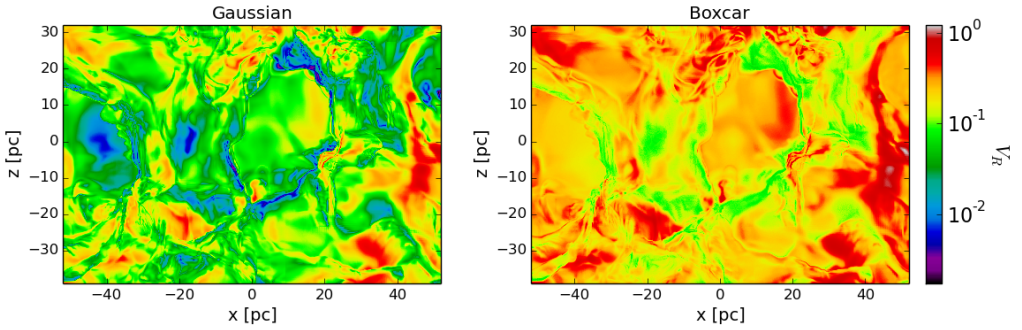

Figure 8.8: Maps of the Tauber values, calculated with a Gaussian (left) and a Boxcar function (right) as reference function. The Tauber values V_R are in general larger for $V_{\rm Box}$, since the line profiles are more similar to a Gaussian shape in general.

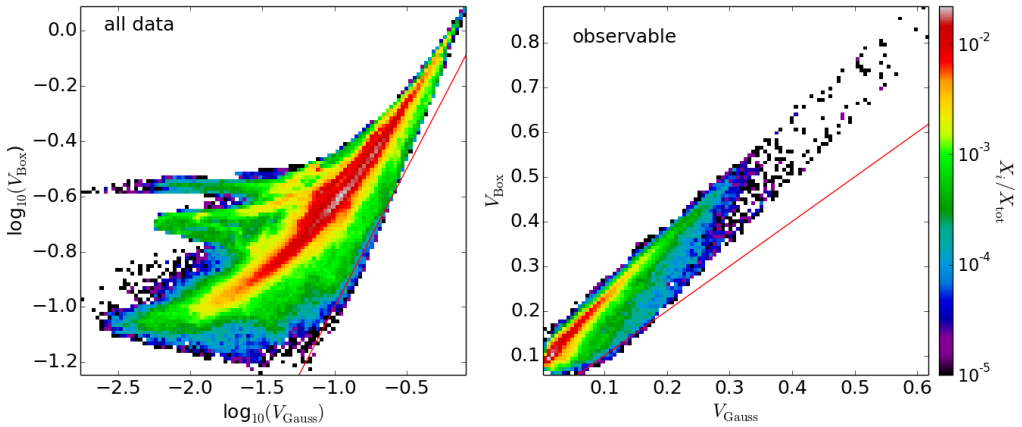

Figure 8.9: Comparison of the Tauber values calculated with the Gaussian ($V_{\rm Gauss}$, x-axis) and the Boxcar function ($V_{\rm Box}$, y-axis) as reference function. The left panel shows the scatter plot for the whole dataset, and the right panel the scatter plot, when only those pixels are taken into account, that are assumed to be observable ($I_{12[\rm CII]} \geq 0.5$ K km s^{-1}). The colour-coding indicates the fraction of pixels within the distribution. The red line denote $V_{\rm Gauss} = V_{\rm Box}$. For most of the line profiles $V_{\rm Gauss}$ is smaller than $V_{\rm Box}$.

with several components close together. Thus, the overall shape of the profile differs more from the Gaussian than from the boxcar function. Therefore, in this example $V_{\rm Box}$ is smaller than $V_{\rm Gauss}$.

Fig. 8.8 shows the map of the Tauber values calculated with the Gaussian function (left panel) and the Boxcar function (right panel). In both cases, the structures in the maps are similar compared to the structures in the integrated intensity maps (see Fig. 8.1). However, the Tauber values calculated with the Gaussian reference function cover a larger dynamical range ($0.002 \leq V_{\rm Gauss} \leq 0.813$) and are in general smaller than the Tauber values calculated with the Boxcar function ($0.057 \leq V_{\rm Box} \leq 1.223$). In Fig. 8.9 we compare in the left panel the Tauber values $V_{\rm Gauss}$ and $V_{\rm Box}$ in a scatter plot for all pixels, with bin sizes of $\Delta \log_{10}(V_{\rm Gauss}) = 0.0267$ and $\Delta \log_{10}(V_{\rm Gauss}) = 0.0133$, and in the left panel we only take pixels that we assume

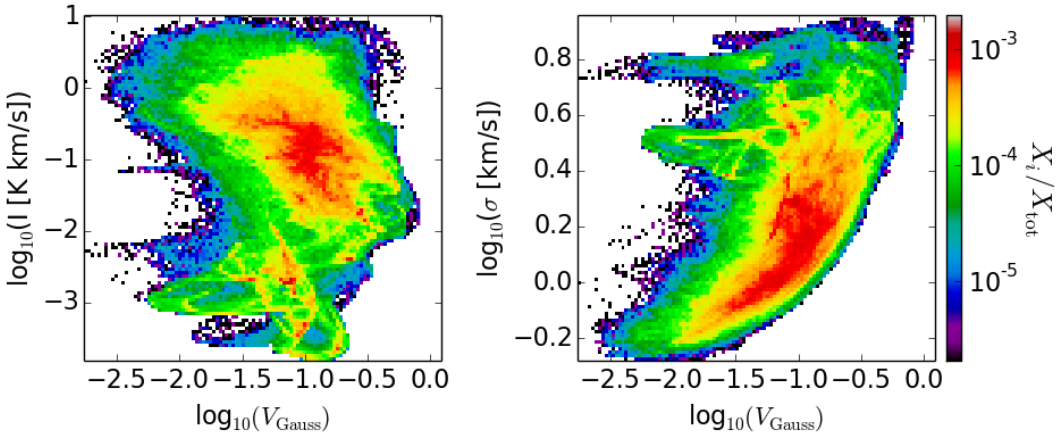

Figure 8.10: Two-dimensional histograms of the Tauber values V_{Gauss} with the integrated intensity (I, left) and the width of the distribution (σ, right). The colour-coding indicates the fraction of pixels in each bin.

to be observable ($I_{[^{12}\mathrm{CII}]} \geq 0.5$ K km s^{-1}, with bin sizes of $\Delta V_{\mathrm{Gauss}} = 0.006$ and $\Delta V_{\mathrm{Box}} = 0.008$). We find V_{Gauss} and V_{Box} to be linearly correlated. The red line indicates $V_{\mathrm{Gauss}} = V_{\mathrm{Box}}$. The plot confirms, that the values of V_{Gauss} are in general smaller than V_{Box}. This is caused by the fact that the [^{12}C II] line emission is optically thin throughout most of the cloud. We therefore use only V_{Gauss} for the further analyses.

We investigate, whether the Tauber values are correlated with the integrated intensity and the width of the profiles in Fig. 8.10 for the whole dataset. For the scatter plots we use bin sizes of $\Delta \log_{10}(V_{\mathrm{Gauss}}) = 0.027$, $\Delta \log_{10}(I\,[\mathrm{K\ km\ s^{-1}}]) = 0.048$ and $\Delta \log_{10}(\sigma\,[\mathrm{km\ s^{-1}}]) = 0.012$. There is no clear trend in the scatter plots. There might be a tendency that the Tauber values become smaller, when the integrated intensity raises, but the scatter is very high. Concerning the correlation with the width of the profile, the scatter is likewise large. However, the trend of getting higher Tauber values with larger widths is more clear. One example for this is the line profile P2, which has a width of $\sigma = 3.319$ km s^{-1}. However, this width does not represent the width of a single component, but is the result of several components along the line of sight.

Fig. 8.11 shows the same scatter plots, restricted to the lineprofiles that are assumed to be observable ($I_{[^{12}\mathrm{CII}]} \geq 0.5$ K km s^{-1}), this time on linear scale ($\Delta V_{\mathrm{Gauss}} = 0.006$, $\Delta I = 0.101$ K km s^{-1}, $\Delta\sigma = 0.033$ km s^{-1}). We likewise find the tendency that the Tauber values are more likely to be small with larger integrated intensities, and that they become larger with increasing width of the profile. This is in agreement with the example profiles (P1, P2, P3, P4). In the line profile P2, we found, that the two components in the line profile result in a large width σ, and thus the Tauber values are large.

In Fig. 8.12 we show the ratio maps between the integrated intensities and the Tauber values (upper row), and the ratio maps between the widths of the line profiles and the Tauber values (lower row). From the scatter plots (Figs. 8.10 and 8.11)

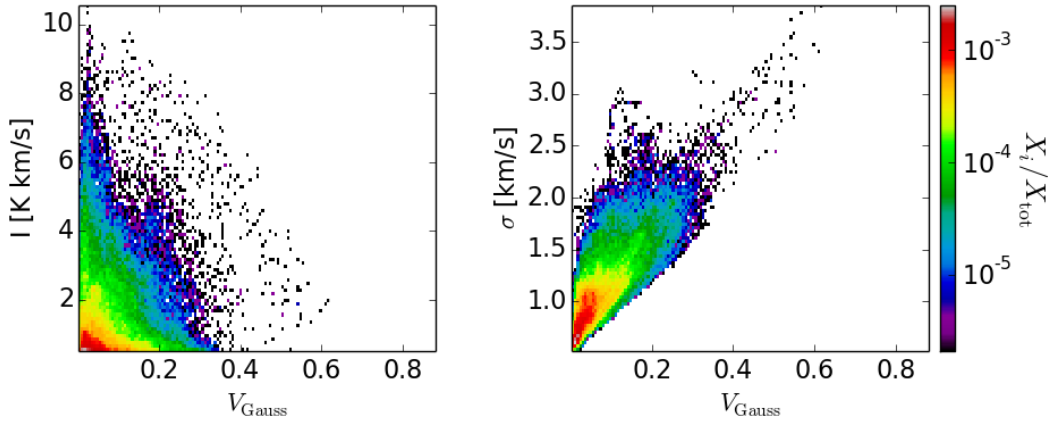

Figure 8.11: Same as Fig. 8.10, but now restricted to the pixels, that are assumed to be observable with $I_{[^{12}\rm CII]} \geq 0.5$ K km s^{-1}, and showing the correlation on linear scale.s

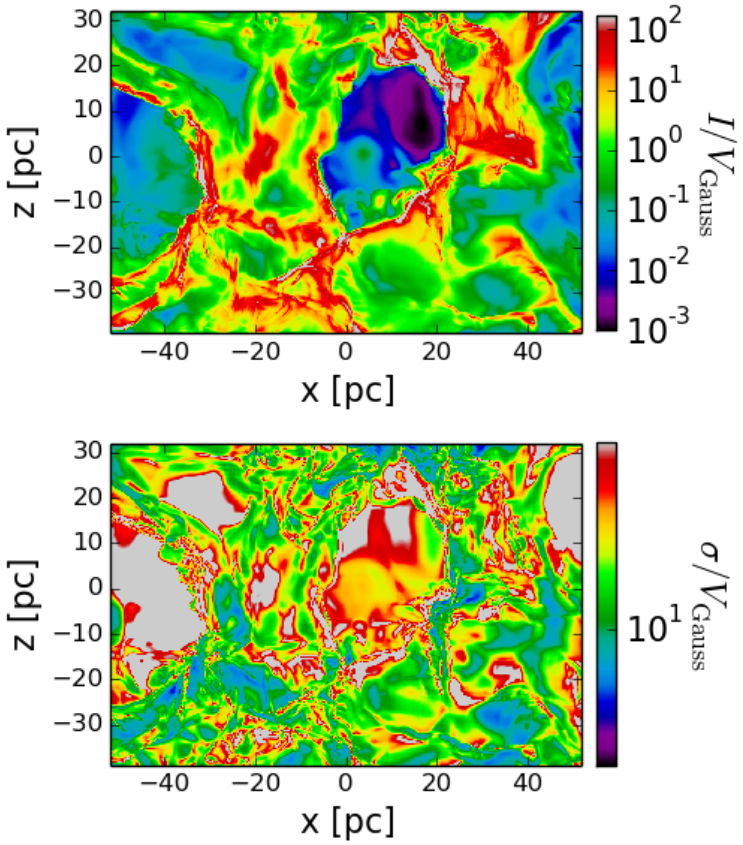

Figure 8.12: Ratio maps between the integrated intensity and the Tauber values (upper row) and the width of the profiles (σ) and the Tauber values (lower row).

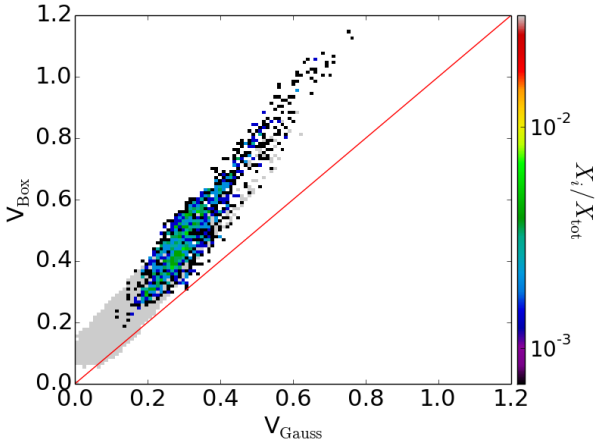

Figure 8.13: Scatter plot of the Tauber values of the observation of G48.66 calculated with a Gaussian (V_{Gauss}) and with a Boxcar function (V_{Box}) as reference function. The underlying grey distribution indicates the scatter plot for the simulation restricted to the observable pixels, shown in Fig. 8.9 in the left panel. Both, the observation and simulation cover the same parameter space. The red line represents $V_{\mathrm{Gauss}} = V_{\mathrm{Box}}$.

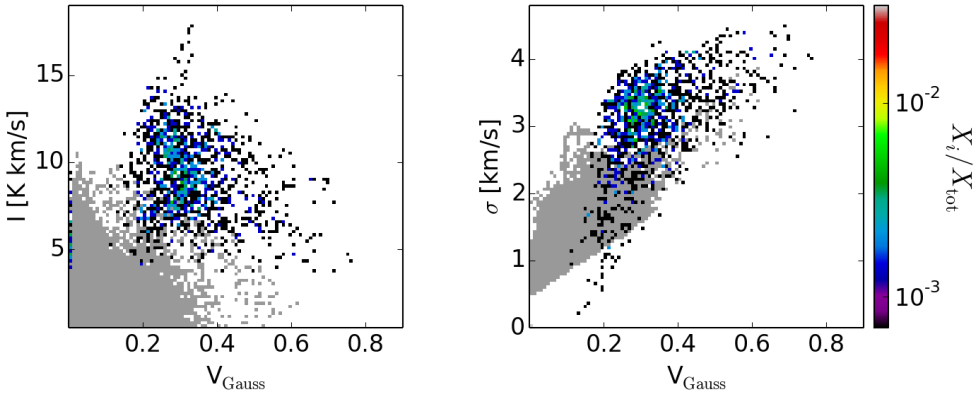

Figure 8.14: Same as Fig. 8.11, but for the observational data of G48.66. The underlying grey shaded area indicates the parameter range for the simulations shown in Fig. 8.11.

we know, that a high ratio in I/V_R can be caused by a high integrated intensity as well as by a low Tauber value. For the ratio maps between the width of the profiles (σ) and the Tauber values, we find the dynamical range of the values to be much smaller than for the I/V_R ratio maps. This is in line with the correlation of V_R and σ we found in Figs. 8.10 and 8.11 to be more clear than for V_R and I.

We further compute the Tauber values for the observational data of G48.66 from Beuther et al. (2014). We use the data without smoothing with a Gaussian kernel. In Fig. 8.13 we show the scatter plot of V_{Gauss} and V_{Box}. For comparison, the distribution of the Tauber values from the simulations is indicated as grey shaded area. As bin sizes for the distribution we use $\Delta \log_{10}(V_{\mathrm{Gauss}}) = 0.008$, $\Delta \log_{10}(V_{\mathrm{Box}}) = 0.011$ for the observational data. We find the parameter range of V_{Gauss} and V_{Box} to be similar in both the observations and simulations. However, for the simulations V_{Gauss}

and $V_{\rm Box}$ can have smaller values compared to the observations. The noise in the observations sets the lower limit of the Tauber values in the observations. As described above, the Tauber values are derived with Eqs. (8.8) and (8.9). When calculating ΔT_R with Eq. (8.8), the difference between the line profile and the reference function is calculated with the quadratic mean. If the line profile would be a Gaussian with noise, ΔT_R gives the noise level as the result, and thus, it sets the lower limit of the Tauber value, weighted by the amplitude. Beuther et al. (2014) report a 1σ noise level of 0.31 K for the observation of G48.66 (see table 3 in Beuther et al., 2014). The Tauber values we find to be larger than $V_R > 0.1$.

In Fig. 8.14 we plot the scatter plot between the integrated intensity I and the width of the profiles σ for the observational data of G48.66. We only have a comparable parameter space in the intensities and the width of the profiles but not the same, and thus, the distributions shown in Fig. 8.14 differ. The bin sizes in the distribution for the observational data are $\Delta V_{\rm Gauss} = 0.008$, $\Delta V_{\rm Box} = 0.011$, $\Delta I = 0.142$ K km s^{-1}, $\Delta\sigma = 0.045$ km s^{-1}.

8.3 Line profiles at different resolution levels

We analyse, whether the line profiles are converged, when going to higher resolution levels, on the example profile of the maximum pixel in L8. In the resolution level L9, there are four pixels replacing the one pixel from level L8. Going even one level higher (L10), the pixel splits into 16 pixels (lines of sight). In Figs. 8.15 and 8.16 we show the pixels at the resolution levels L9 and L10. In all of these profiles we find the two components, from which the one at negative velocities is more pronounced. To test the convergence, we take the average of the profiles from the resolution levels L9 and L10, and compare them with the profile at L8 in Fig. 8.17. The overall shape of the profile is rebuild; however, the intensities along the line profiles are not. The peaks in the averaged L9 and L10 spectra are narrower, and the one at negative velocities has a higher intensity. Further, the averaged line profiles for L9 and L10 are more similar to each other than to the profile of L8. Due to the higher resolution level, the mass along a line of sight, resulting in one pixel in the integrated intensity map, is redistributed, so that the gas can become more dense at a smaller spatial scale. This results on the other hand to regions with lower density along the line of sight. As a result, the peaks are more distinct and the intensities can become larger. Note further, that the pixels with the maximum integrated intensity are situated at a different position for L9 and L10, compared to L8 . Also this is a result of the better refined mass along a line of sight in the simulations. These findings are in line with the convergence study of the integrated intensity maps, discussed in Section 4.2.2.

As done with the line profiles at the resolution level L10 in Fig. 8.3, we investigate the slope of the line profiles with $D_{\rm max}$ and normalize it with the integrated intensity I. The scatter plot between $D_{\rm max}/I$ and the integrated intensities I is shown in Fig. 8.18 for the levels L5, L7 and L9. The colour-coding indicates the fraction

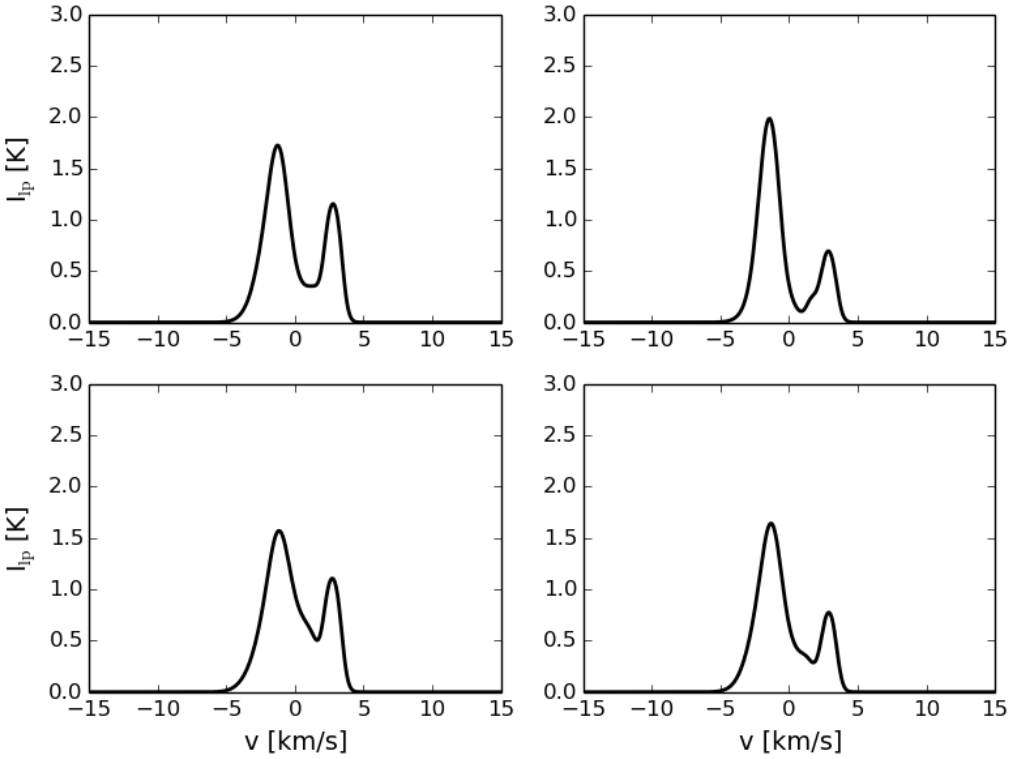

Figure 8.15: Resolved line profile of the maximum pixel in L8 (Fig. 8.17, blue line), showing the four line profiles at the same position in L9. The intensity on the y-axis in [K] is shown as a function of the velocity in [km s^{-1}] on the x-axis in all panels.

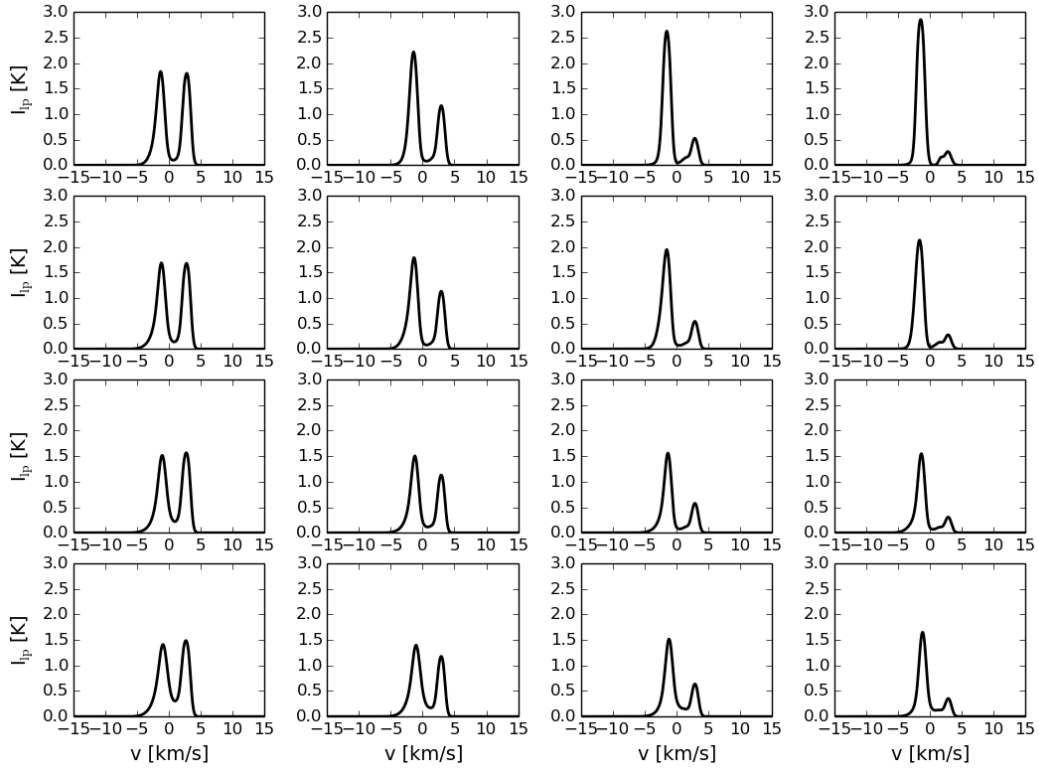

Figure 8.16: Same as Fig. 8.15, but resolved for the resolution level L10.

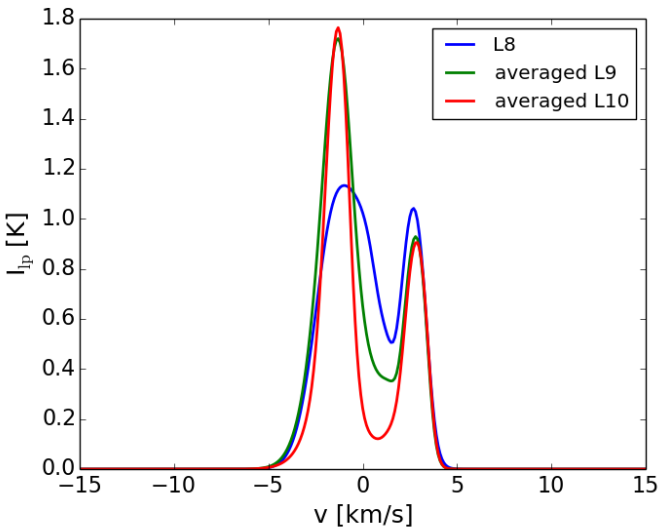

Figure 8.17: Averaged line profile for L9 (Fig. 8.15, green line) and for L10 (Fig. 8.16, red line), compared with the line profile of the same position from the resolution level L8 (maximum pixel). The averaged line profiles are more distinct than the line profile in L8.

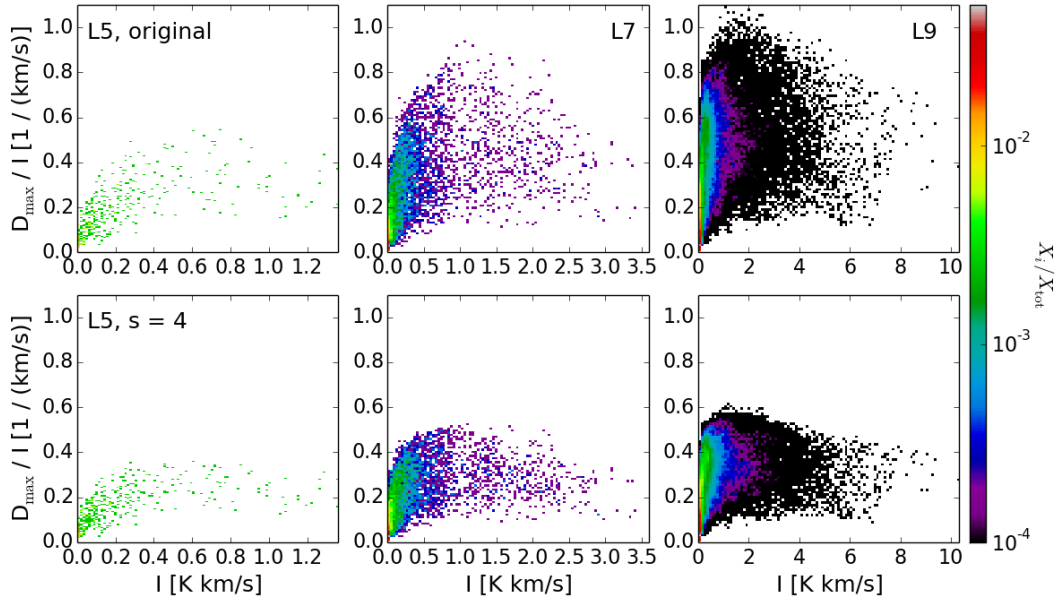

Figure 8.18: Scatter plot of the integrated intensities for the line profiles at different resolution levels (L5, L7 and L9 in the left, middle and right panels, respectively) as a function of the maximum value of the derivative ($D_{\max}$). The upper row shows the data directly from the simulation, with a spectral resolution of $\mathrm{dv} = 0.1$ km s^{-1}. With smaller spatial refinement the range of $D_{\max}$ increases. When smoothing the data to a spectral resolution of $\mathrm{dv} = 0.4$ km s^{-1} ($s = 4$, bottom row), $D_{\max}$ is likewise reduced. The colour-coding indicates the fraction of pixels. The normalization is done by the total amount of pixels for each resolution level.

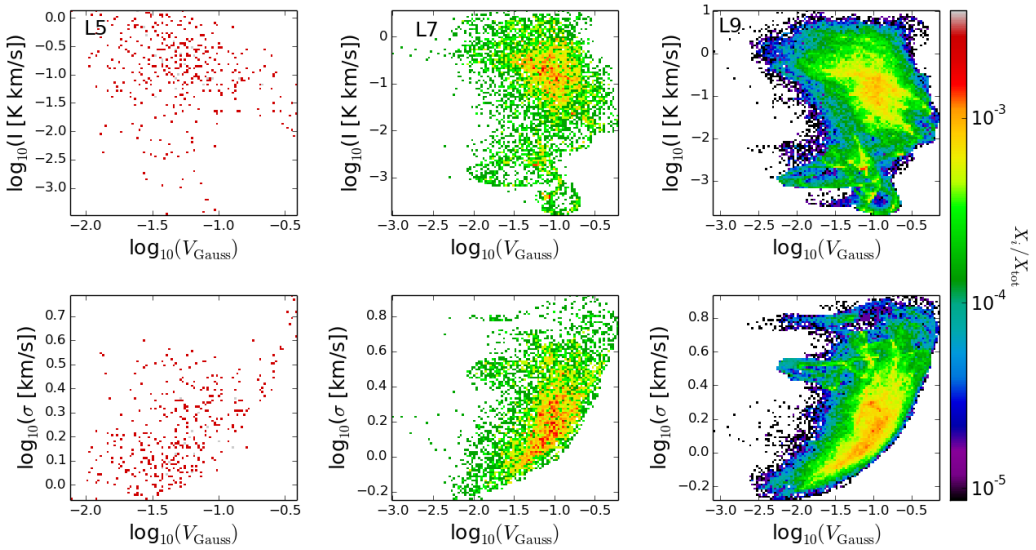

Figure 8.19: Scatter plots of the Tauber values V_{Gauss} and the integrated intensity I (upper row) and the width of the profiles σ (lower row) for the resolution levels L5 (left), L7 (middle) and L9 (right). The colour-coding indicates the fraction of pixels in every bin. The scatter plots are similar at all resolution levels.

of pixels, normalized to the total amount of pixel at each resolution level. The upper row shows the scatter, when all data is taken into account. D_{max} covers a smaller range of values for lower resolution levels, as for L5 it is $D_{\mathrm{max}} \leq 0.5$ and for L9 it is $D_{\mathrm{max}} \leq 6$, although the fraction of pixels with the larger values of D_{max} is in general small, as the colour-coding in the scatter plots indicates. Likewise, the range of values of the ratio D_{max}/I increases with the resolution level from 0.6 for L5 to 1.1 for L9. We reduce the spectral resolution in the line profiles by smoothing the profiles with a Gaussian kernel (with a standard deviation of $s = 4$, where s gives the number of pixels). By this, we obtain a spectral resolution of $\mathrm{dv} = 4 \times 0.1$ km s^{-1} = 0.4 km s^{-1}. As can be seen in the lower row of Fig. 8.18, the values of D_{max}/I are reduced, as it was the case for L10 (see Section 8.1).

We further investigate, whether the distribution of the pixels as a function of Tauber values and the integrated intensities (I, Fig. 8.19, upper row) and the width of the line profiles (σ, Fig. 8.19, lower row) changes with the resolution level. We here only show the scatter plot as a function of V_{Gauss}, and bin the data logarithmically in 100 bins with sizes of $\Delta \log_{10}(V_{\mathrm{Gauss}}) = 0.017, 0.028, 0.030$, $\Delta \log_{10}(I\,[\mathrm{K\ km\ s^{-1}}]) = 0.036, 0.043, 0.048$ and $\Delta \log_{10}(\sigma\,[\mathrm{km\ s^{-1}}]) = 0.009, 0.012, 0.012$ for the resolution levels L5, L7 and L9, respectively. We find the same range of Tauber values at all resolution levels. However, the range of values in the integrated intensity I increases with higher resolution level. The scatter plots in Fig. 8.19 indicate, that there is no clear correlation between V_{Gauss} and I, and there is a weak chance to find a lower Tauber value at high intensities. Also for the scatter plots of V_{Gauss} and σ in Fig. 8.19 (lower row), we find that the scatter plots do not change with the resolu-

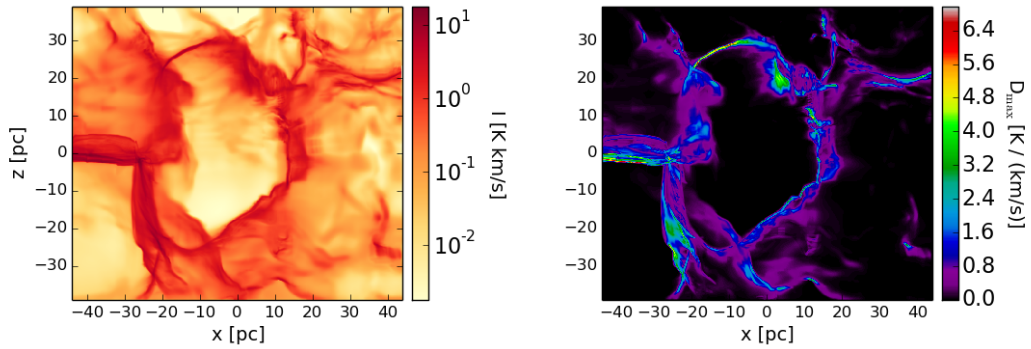

Figure 8.20: Map of the integrated [^{12}C II] intensity (left panel) and the maximum of the absolute value of derivative of the line profiles $D_{\max}$ (right panel). In regions with larger integrated intensities, the values of $D_{\max}$ are likewise larger.

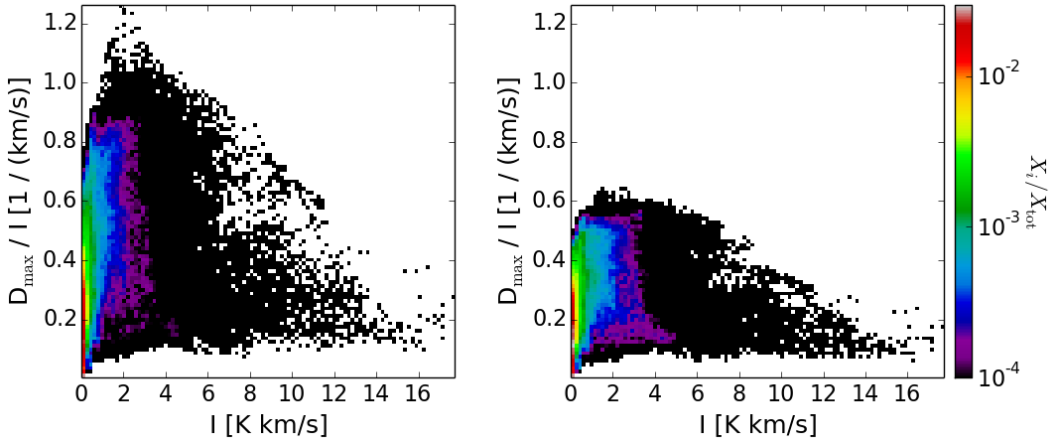

Figure 8.21: Similar to Fig. 8.3, but for the molecular cloud MC1, at the resolution level of L10. The values for $D_{\max}$, and thus $D_{\max}/I$, are comparable to MC2, but the range of integrated [^{12}C II] intensities is larger for MC1 compared to MC2.

tion level. The values of σ cover a comparable range at all resolution levels. The weak correlation indicating that it is more likely to have a high Tauber value when σ is large, is fulfilled at all resolution levels.

8.4 Line profiles for the zoom-in molecular cloud MC1

So far we investigated the line profiles for the molecular cloud MC2 in the zoom-in simulation. We now study, whether the statistics from the line profiles are different between MC2 and MC1. In Fig. 8.20 we show the [^{12}C II] synthetic emission map of MC1 at L10 in the xz-projection (left panel) and the map of $D_{\max}$ in the same projection. As we found for MC2, we likewise find here large values for $D_{\max}$ in regions with a large [^{12}C II] integrated intensity. The scatter plot of $D_{\max}/I$ and

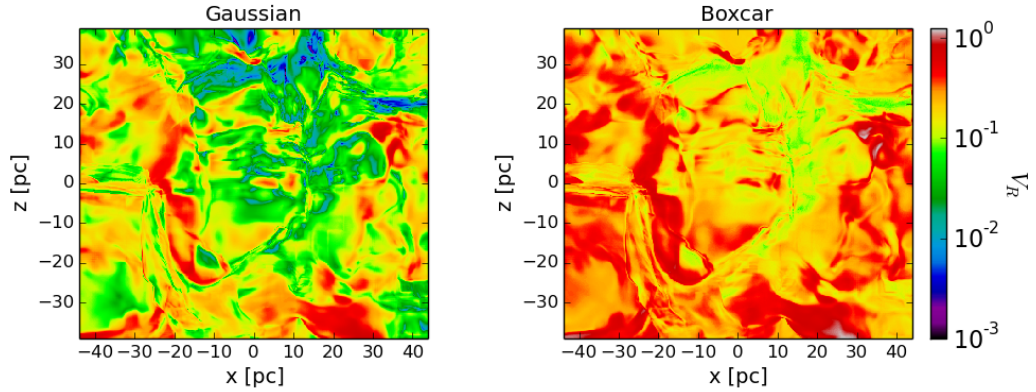

Figure 8.22: Similar to Fig. 8.8, but for the molecular cloud MC1, at the resolution level of L10. As for MC2, V_{Gauss} can have smaller values than V_{Box}, indicating that the line profiles are more similar to a Gaussian.

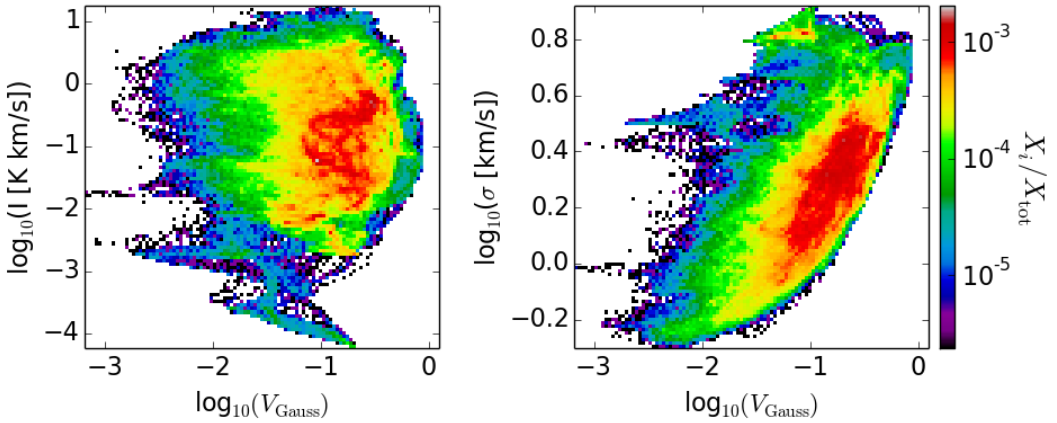

Figure 8.23: Similar to Fig. 8.10, but for the molecular cloud MC1, at the resolution level of L10. The distribution of the Tauber values V_{Gauss} and V_{Box} with the integrated [^{12}C II] intensity I and the width of the line profiles σ are similar to MC2.

the integrated [^{12}C II] intensity I is shown in Fig. 8.21. The left panel presents the scatter of the data directly from the simulations, where we calculated the line profiles with a spectral resolution of dv = 0.1 km s^{-1}. The range in D_{max} for MC1 is comparable to the one in MC2, but the integrated [^{12}C II] line emission can become larger in some pixels. This is caused by the different density distribution of the gas in MC1 and MC2. To study this in more detail, will be part of future work. In the right panel of Fig. 8.21 we first smoothed the line profiles with a Gaussian kernel of 4 pixels to a spectral resolution of dv = 0.4 km s^{-1} before calculating D_{max}. By this, we reduce D_{max}, as it was the case for MC2, and the ratio D_{max}/I decreases. The ranges of D_{max}/I for both the original and the smoothed data is comparable with the ranges of these cases found in MC2, in both cases. With larger integrated intensity the ratio D_{max}/I likewise decreases.

We calculate the Tauber values of the line profiles of MC1 at the resolution level of L10, and present them in Fig. 8.22, both calculated with a Gaussian (V_{Gauss}, left) and with a Boxcar function as reference function (V_{Box}, right). As we found

for MC2, the dynamical range of $V_{\rm Box}$ is smaller than for $V_{\rm Gauss}$, in a way that $V_{\rm Gauss}$ covers a range towards smaller values, indicating, that the differences of some line profiles with a Gaussian are small and thus, the profiles are predominantly from optical thin emission. In Fig. 8.23 we show the scatter plots of the Tauber values with the integrated [^{12}C II] intensity I and the width of the line profiles σ, with bin sizes of $\Delta \log_{10}(V_{\rm Gauss}) = 0.031$, $\Delta \log_{10}(I\ [\mathrm{K\ km\ s^{-1}}]) = 0.055$ and $\Delta \log_{10}(\sigma\ [\mathrm{km\ s^{-1}}]) = 0.012$. Also these distributions are similar to MC2 (Fig. 8.10) in a sense that there is no clear correlation. However, the distributions are not the same. These differences could be caused by the different internal structures of MC2 and MC1. We will study this in more detail in future work.

8.5 Discussion

In this Chapter we analysed the line profiles of the [^{12}C II] line emission, and started with comparing the general shape of the line profiles with observations. We discussed, whether the simulated profiles have steeper slopes than found in observed line profiles. To test this, we calculated the maximum of the absolute value of the derivative $D_{\rm max}$, and used the ratio of $D_{\rm max}$ with the integrated intensity I ($D_{\rm max}/I$) as a measure of this. Smoothed to the same spectral resolution, we compared the distribution of $D_{\rm max}/I$ as a function of I for the simulated and observed data, for which we took the [^{12}C II] line observations in G48.66 (28 – 45 km s^{-1}) by Beuther et al. (2014). We chose this data, since it has comparable integrated [^{12}C II] intensities as we find the simulations. We found $D_{\rm max}/I$ to be lower in the observed data than in the simulated one. This means, that the line profiles of the simulated data have indeed steeper slopes compared to the observations. One reason for this could be the process of observation, where the beam size and noise affect the line profile. We stress that we here analysed the synthetic emission maps, and suggest to study this issue in future work with synthetic observations.

We have studied the line profiles of the simulations in a statistical way, aiming of characterizing the line profiles. For this, we compared the line profiles with a reference function, that we chose to be Gaussian or a Boxcar function. As a Gaussian, it represents a line profile of an optically thin line, whereas the line profile is expected to be similar to a Boxcar function in the optically thick limit. We calculated the difference between the reference function and the line profile as the quadratic mean, and weight it with the amplitude of the reference function. The resulting value we call "Tauber value" ($V_{\rm Gauss}$, $V_{\rm Box}$, respectively).

We found the Tauber values at all resolution levels of MC2 to cover the same range of values. Further, we plotted the distribution of the Tauber values with the integrated [^{12}C II] intensity, and the width σ of the line profiles. We could not find a clear trend within these distributions. As a tendency, the Tauber values are larger for line profiles with large widths σ. This is, because those line profiles often contain several components, but only one width for the whole line profile is calculated.

Thus, the difference between the one reference function and the line profile is large, resulting in a high Tauber value.

To test, whether the findings for MC2 are also valid for other simulations, we analysed in the same manner the molecular cloud MC1 at an refinement level of L10. The results of the analysis confirm the findings from the analysis of MC2.

Further, we tested the method with observational data by Beuther et al. (2014). However, the minimum Tauber values found from observational data are larger compared to the minimum in the simulations. This is caused by the noise in the observational data. The quadratic mean for an ideal Gaussian noisy line profile is given as the noise level of the line. For the Tauber value, this noise level is weighted by the amplitude of the reference function.

The Tauber values estimated from the observed line profiles matches the range of Tauber values from the simulations. For the distribution of the Tauber values against the integrated [^{12}C II] intensity and the width of the line profiles, we find the distributions to differ compared to the ones in the simulations, since the range in intensity and width does not match perfectly the simulation data.

9

Complementary synthetic emission maps

For studying the ISM in observations, to learn about their physical properties and the gas dynamics, observations are carried out at several wavelengths. Information of the physical properties can be obtained by intensity ratios, and dynamics can be studied for example when analysing and comparing the line profiles at different wavelengths. So far, we have analysed the synthetic [C II] line emission in our simulations, which is the focus of this work. However, with RADMC-3D we can carry out synthetic emission maps at further wavelengths. In the context of molecular clouds and the results concerning the origin of the [C II] line emission, it might be interesting to study further the emission lines of atomic hydrogen and carbon monoxide. We here introduce the synthetic emission maps for the H I 21 cm line and the ^{12}CO $(1-0)$, ^{13}CO $(1-0)$, and C^{18}O $(1-0)$ lines (see Table 9.1). With that we aim to give a first impression of the simulations at these wavelengths and intent to set a good basis for future work in this field.

We first describe the assumptions done for calculating the synthetic H I and CO emission maps. We then present the H I emission maps for the SILCC setup on the example of the run *S10-KS-rand* at $t = 50$ Myr, and for the zoom-in simulation MC2. For the synthetic CO emission maps we restrict ourselves to the zoom-in simulation MC2, since its spatial resolution of $\mathrm{d}x = 0.122$ pc is sufficient to follow the formation of CO.

Table 9.1: List of the frequencies for the complementary data in H I, and the ^{12}CO (1 – 0), ^{13}CO (1 – 0), and C^{18}O (1 – 0) emission lines. The data are taken from Gould (1994) and LAMDA (Schöier et al., 2005, Yang et al., 2010).

line	transition	ν
H I	$F = 1 - 0$	1420.4 MHz
^{12}CO	$J = 1 - 0$	115.27 GHz
^{13}CO	$J = 1 - 0$	110.20 GHz
C^{18}O	$J = 1 - 0$	109.78 GHz

9.1 H I emission line

9.1.1 Hyperfine structure transition atomic carbon

With RADMC-3D we calculate the H I 21 cm emission line from the atomic hydrogen. This line occurs from the hyperfine transition in H, due to the interaction between the spin of the electron and the spin of the nucleus. The angular momentum resulting from the coupling of the angular momentum of the electron and the nucleus can be expressed with **F** and the quantum number F (similar to the hyperfine structure transition in C^+, as described in Section 3.2.2). In atomic hydrogen the spin of the nucleus is $I = 1/2$, and the total electron angular momentum is $J = L + S = 0 + 1/2 = 1/2$. Thus, since the quantum number F can have values between $J - I$ and $J + I$, it can be $F = 0$ and $F = 1$. A transition of $F = 1 - 0$ results in the emission of a H I line at $\lambda_{\rm HI} = 21$ cm ($\nu_{\rm HI} = 1420.4$ MHz, see Table 9.1). The Einstein coefficient of the H I line is $A_{ul} = 2.8843 \times 10^{-15}$ s^{-1} (Gould, 1994), so that a transition of this kind takes place every $\tau = 1/A_{ul} = 3.5 \times 10^{15}$ s. This corresponds to around 11 million years. However, since the amount of atomic hydrogen is large in the ISM, the line can be observed, which was done for the first time by Ewen & Purcell (1951). From theory, it was first predicted by van de Hulst (1945).

9.1.2 Level population in H I

The level population of the H I line is in general not in the local thermal equilibrium, since the collisions are not sufficient enough to thermalize the line (Liszt, 2001, Bihr et al., 2015). The excitation temperature at which the transition happens, is no longer the kinetic temperature $T_{\rm kin}$, but by a spin temperature $T_{\rm spin}$, which determines the level population by

$$\frac{n_u}{n_l} = \frac{g_u}{g_l} \frac{1}{k_B T_{\rm spin}} \exp^{-h\nu_{\rm HI}} = 3 \exp^{-T_{\rm HI}/T_{\rm spin}}, \tag{9.1}$$

with $T_{\rm HI} = E_{ul}/k_B = 0.068$ K (Furlanetto et al., 2006). The spin temperature is determined by collisions with other particles, the scattering processes with UV

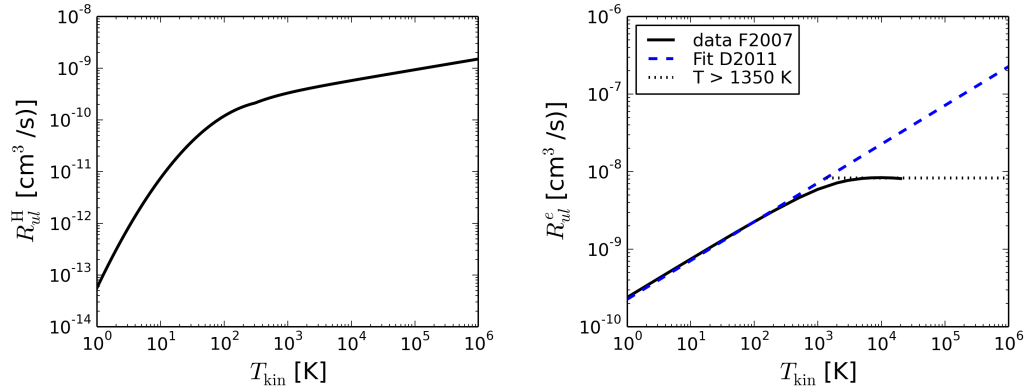

Figure 9.1: De-excitation coefficients for H-H collisions (R^{H}_{ul}, left) and H-e^- collisions (R^{e}_{ul}, right). For R^{H}_{ul} we take the description from Kim et al. (2014), (see Eq. (9.4)). For R^{e}_{ul}, the data for the de-excitation coefficients is listed in Furlanetto & Furlanetto (2007) (black line), and fitted for temperatures $T < 500$ K by Draine (2011). We use the fit by Draine (2011) for $T_{\mathrm{kin}} \leq 1350$ K, and set $R^{e}_{ul} = 8.3 \times 10^{-9}$ cm^{-3}s^{-1} for higher temperatures (black dotted line).

photons (Wouthuysen-Field effect), and scattering processes with the cosmic microwave background (Furlanetto & Furlanetto, 2007). We describe here shortly the influences, and refer to Liszt (2001), Furlanetto et al. (2006) and Kim et al. (2014) for more details.

Collisions

Collisions with other hydrogen atoms and electrons influence the spin temperature (Liszt, 2001, Furlanetto & Furlanetto, 2007, Kim et al., 2014). Collisions with protons are negligible, since electrons are under all conditions more abundant than protons (Liszt, 2001). A factor y_c for the collisions can be defined as

$$y_c \equiv \frac{T_{\mathrm{HI}}}{T_{\mathrm{kin}}} \frac{C^c_{ul}}{A_{ul}} \tag{9.2}$$

with the rate coefficient

$$C^c_{ul} = n_{\mathrm{H}} R^{\mathrm{H}}_{ul} + n_e R^{e}_{ul}, \tag{9.3}$$

while n_{H} and n_e are the number densities of atomic hydrogen and electrons, and R^{H}_{ul} and R^{e}_{ul} are the de-excitation rates, respectively. As done by Draine (2011) and Kim et al. (2014), we take the de-excitation rates for atomic hydrogen from Allison & Dalgarno (1969) and Zygelman (2005), with

$$R^{\mathrm{H}}_{ul} = \begin{cases} 1.19 \times 10^{-10} T_2^{0.74-0.20 \ln T_2}\ \mathrm{cm^3 s^{-1}} & \text{for } 20\,\mathrm{K} < T_{\mathrm{kin}} < 300\,\mathrm{K} \\ 2.24 \times 10^{-10} T_2^{0.207} e^{-0.876/T_2}\ \mathrm{cm^3 s^{-1}} & \text{for } 300\,\mathrm{K} < T_{\mathrm{kin}} < 10^3\,\mathrm{K} \end{cases} \tag{9.4}$$

with $T_2 = T_{\mathrm{kin}}/100$. We present these de-excitation rates as a function of the temperature T_{kin} in the left panel of Fig. 9.1. For electrons, we take the de-exciation rates as listed by Furlanetto & Furlanetto (2007) in table 1 and fig. 3 therein. Draine (2011) (eq. (17.14) therein) fitted the data in the range of $1 \leq T_{\mathrm{kin}} \leq 500$ K by

$$R^{e}_{ul} = 2.26 \times 10^{-9} T_2^{0.5}\ \mathrm{cm^3 s^{-1}}, \tag{9.5}$$

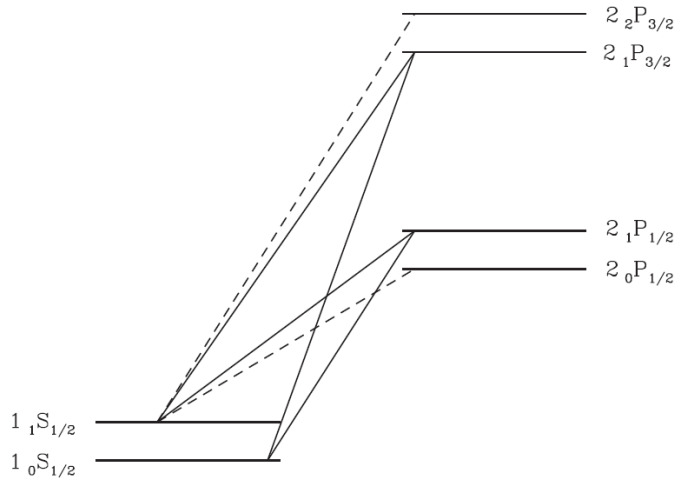

Figure 9.2: Sketch by Pritchard & Furlanetto (2006, fig. 1 therein) of the hydrogen hyperfine structure levels in atomic hydrogen, and the excited states, due to the absorption of a Lyα photon. By absorbing the Lyα photon, the H atom can be excited to a P-state . When relaxing back to the S-state, the atom can have both $F = 0$ and $F = 1$ at the end of the process, and thus a mixing of the level population in the both hyperfine structure levels happens. The transitions of causing this effect are indicated as black lines in the sketch. The dashed lines indicate other transitions, not relevant here.

with $T_2 = T_{\rm kin}/100$. We take this relation until $T_{\rm kin} \leq 1350$ K, and set thereafter R^e_{ul} to a constant, as $R^e_{ul}(T \geq 1350\,{\rm K}) = R^e_{ul}(T = 1350\,{\rm K}) = 8.3 \times 10^{-9}$ cm^{-3}s^{-1}. The electron de-excitation coefficients are presented in the right panel of Fig. 9.1.

Wouthuysen-Field effect

Scattering with UV photons influences the spin temperature (Wouthuysen-Field effect, Wouthuysen, 1952, Field, 1959, Furlanetto et al., 2006). This effect names the process, in which a Lyα photon is absorbed by atomic hydrogen and with that the total azimuthal quantum number (L) changes from the S-state ($L = 0$) to the P-state ($L = 1$). The hydrogen atom relaxes to the S-state by spontaneously re-emitting a photon, but it can end up in both, the $F = 0$ and $F = 1$ state. Therefore, the Wouthuysen-Field effect results in a mixing of the hyperfine spin states. This is important in the dilute gas, and weak in the neutral gas. In Fig. 9.2 we show a sketch of this process, as presented by Pritchard & Furlanetto (2006) in their fig. 1, and Furlanetto et al. (2006) in their fig. 3. Here the black lines indicate the transitions between the S and the P levels, that cause the hyperfine spin state mixing. Following Kim et al. (2014) a factor y_α for the Wouthuysen-Field effect is given by

$$y_\alpha = 5.9 \times 10^{11} \frac{n_\alpha}{T_\alpha T^{0.5}_{\rm kin}}, \tag{9.6}$$

with $n_\alpha = 10^{-6}$ cm^{-3} as the number density of Lyα photons near the Lyα line centre, and T_α as the temperature determined by the spectrum near Lyα (Liszt, 2001, Kim et al., 2014). Assuming the spectrum to be similar in first approximation to a Planck curve, one can set $T_\alpha = T_{\rm kin}$ (Field, 1959, Kim et al., 2014).

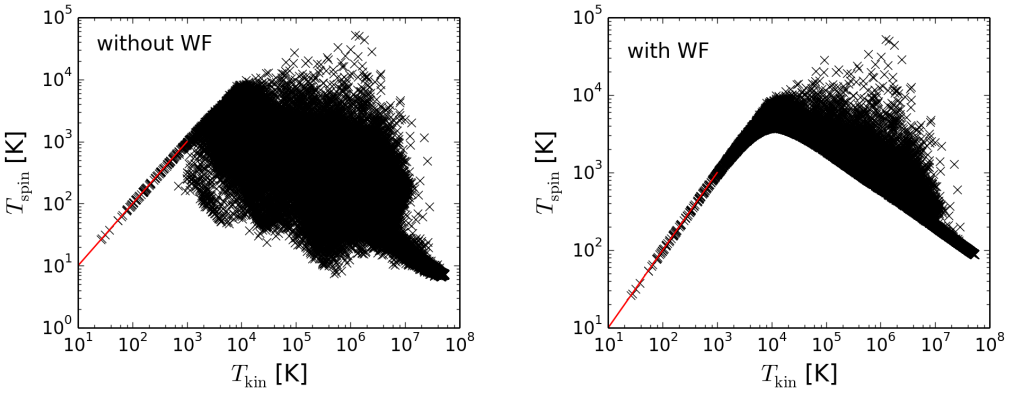

Figure 9.3: Scatter plot of the kinetic temperature $T_{\rm kin}$ and the spin temperature $T_{\rm spin}$ for the SILCC simulation *S10–KS–rand* at $t = 50$ Myr, calculated without (left) and with the Wouthuysen-Field effect. The red lines indicate the case of $T_{\rm kin} = T_{\rm spin}$.

Radiative background

Further, the brightness temperature of the background 21 cm radiation field influences the spin temperature, which includes the cosmic microwave background and the Galactic synchrotron emission near the 21 cm line (Draine, 2011). Both contributions together form the effective temperature of the Lyα field, T_R, as

$$T_R \approx T_{\rm CM} + 1.04\,{\rm K} = 3.77\,{\rm K}. \tag{9.7}$$

We follow this approach, as done in Kim et al. (2014).

Calculating the spin temperature

Taking all effects together, the spin temperature is calculated in equilibrium by

$$T_{\rm spin} = \frac{T_R + y_c T_{\rm kin} + y_\alpha T_\alpha}{1 + y_c + y_\alpha}, \tag{9.8}$$

as the weighted mean between the kinetic gas temperature $T_{\rm kin}$, the brightness temperature of the background field T_R, and the effective temperature of the Lyα field (Kim et al., 2014).

In Fig. 9.3 we show the distribution of $T_{\rm spin}$ as a function of $T_{\rm kin}$. In the left panel the Wouthuysen-Field effect is excluded, and in the right panel it is taken into account. Until $T_{\rm kin} < 10^3$ K, $T_{\rm spin} = T_{\rm kin}$ is fulfilled. For larger temperatures ($T_{\rm kin} > 10^3$ K), the spin temperature does not increase more with the kinetic temperature, and we find a large scatter in $T_{\rm spin}$. If we further neglect the contribution from collisions by setting $y_c = 0$, we can study the impact of the different contributions to $T_{\rm spin}$. The spin temperatures for $y_c = 0$ are shown in Fig. 9.4. If we further neglect the Wouthuysen-Field effect (left panel of Fig. 9.4), we simply are left with $T_{\rm spin} = T_R$. Including the Wouthuysen-Field effect (right panel of Fig. 9.4), causes the lower boundary of $T_{\rm spin}$, that we found in Fig. 9.3 in the right panel. The scatter in $T_{\rm spin}$ results from the contribution from the collisions.

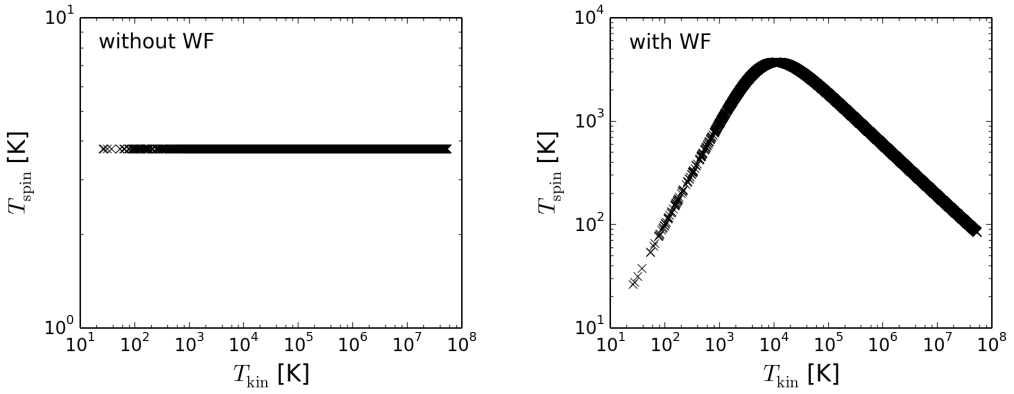

Figure 9.4: Same as Fig. 9.3, but neglecting the collisions ($y_c = 0$) when calculating $T_{\rm spin}$. Thus, in the left panel only the contribution from the T_R remains.

Table 9.2: List of the peak intensities of the H I line emission for *S10–KS–rand* at t = 50 Myr, and MC2 at t = 13.9 Myr at the resolution level L10 for all projections. The spin temperature $T_{\rm spin}$ is assumed as $T_{\rm spin} = T_{\rm kin}$, and calculated without (w/o WF) and with the Wouthuysen-Field effect (w WF). Since the luminosities for all three assumptions, it is only listed once in the fifth column of the table.

Run / Projection	$T_{\rm kin}$ $I_{\rm peak}$ [K km s^{-1}]	w/o WF $I_{\rm peak}$ [K km s^{-1}]	w WF $I_{\rm peak}$ [K km s^{-1}]	$L_{\rm tot}$ [L$_\odot$]
S10–KS–rand	1027.1	1025.7	1026.6	6×10^{-3}
xz	598.3	597.8	598.1	1.3×10^{-4}
xy	724.5	723.9	724.3	1.2×10^{-4}
yz	723.5	722.9	723.2	1.3×10^{-4}

9.1.3 Synthetic H I emission maps for the SILCC setup

For calculating the synthetic H I 21 cm emission maps, we assume as a first approach a local thermal equilibrium (LTE), and use the lines_mode parameter in RADMC-3D as lines_mode = 1 (see Section 4.1). Thus, RADMC-3D assumes the excitation temperature to be $T_{\rm ex} = T_{\rm spin} = T_{\rm kin}$. We calculate the synthetic emission maps for the simulation *S10–KS–rand* at t = 50 Myr, as presented in the left panel of Fig. 9.5. As a spectral resolution we take dv = 0.1 km s^{-1}, where we distribute 145 channels equally in velocity space in a velocity range of ±70 km s^{-1} around the rest frequency.

However, as discussed in Section 9.1, the excitation temperature is the spin temperature $T_{\rm spin}$, and can be calculated with Eq. (9.8). Since the kinetic temperature $T_{\rm kin}$ is used in RADMC-3D to calculate the level population as well as the thermal line width $a_{\rm tot}$, both $T_{\rm kin}$ and $T_{\rm spin}$ have to be given to RADMC-3D for the radiative transfer simulations. We introduce $T_{\rm spin}$ as a new input variable to RADMC-3D, and modify the code at those positions, where the level population is calculated. For the version 0.40 of the code, the changes were done in the camera_module, the source_module,

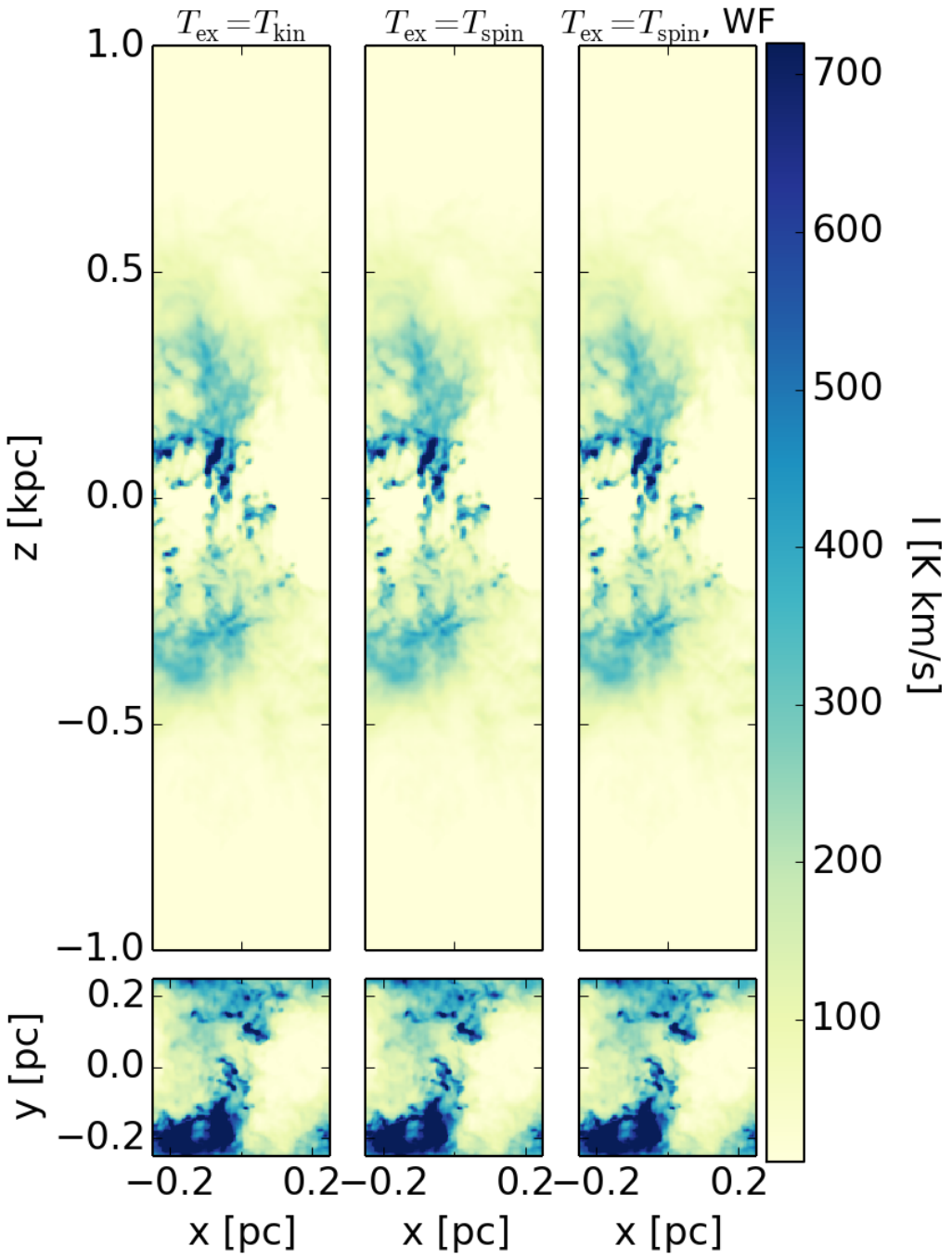

Figure 9.5: Synthetic H I emission maps for the simulation *S10–KS–rand* at $t = 50$ Myr, calculated assuming the excitation temperature to be equal to the kinetic temperature ($T_{ex} = T_{spin}$, left panels), and assuming the excitation temperature to be equal to the spin temperature, whereas the spin temperature was calculated without accounting for the Wouthuysen-Field effect (middle panels), and including it (right panels). The upper panels show the SILCC simulation boxes edge-on, and the lower ones face-on.

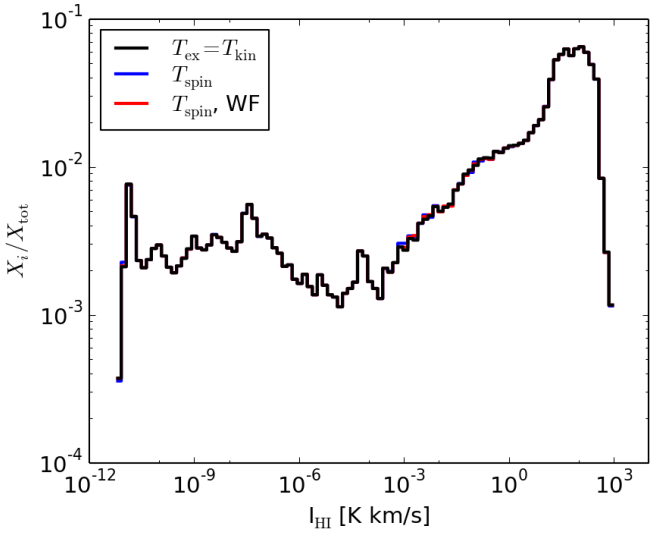

Figure 9.6: Histograms of the integrated H I intensities for the synthetic H I maps of the simulation *S10–KS–rand* at $t = 50$ Myr, as presented in Fig. 9.5. For all assumptions of the spin temperature the histograms are similar. X_i/X_{tot} indicates the fraction of pixels in each bin.

the userdef_module for reading in the new variable, and in the main of RADMC-3D.

With the modified version of RADMC-3D, we calculate the synthetic H I emission maps assuming a spin temperature. In the middle and right panel of Fig. 9.5 we show these maps, where we calculated T_{spin} once without the Wouthuysen-Field effect (middle) and once considering it (right). All maps show similar integrated intensities. The peak H I integrated intensities of all maps and the luminosity are listed in Table 9.2. Note, that since the maps are similar, the luminosity is not affected by the different approaches for setting the spin temperature. We confirm this by plotting the distributions of the integrated H I intensities for all three cases in Fig. 9.6. The histograms show only minor differences. This hints to the fact that the H I emission originates mainly from gas with spin temperatures similar or equal to the kinetic temperatures. As we found in Fig. 9.3, this is fulfilled for the gas especially at $T < 10^3$ K.

9.1.4 Synthetic H I emission maps for MC2

We further calculate the H I line emission maps for the molecular cloud MC2 at the refinement level L10. Figure 9.7 shows the synthetic H I emission maps, as calculated with a spin temperature, T_{spin}, taking the Wouthuysen-Field effect into account. The peak intensities for all three projections and for all three cases ($T_{spin} = T_{kin}$, and a calculated spin temperature without and with the Wouthuysen-Field effect) are summarized in Table 9.2. Since the luminosity remains unaffected by the different approaches, we list it only once in the fifth column of Table 9.2. The H I line emis-

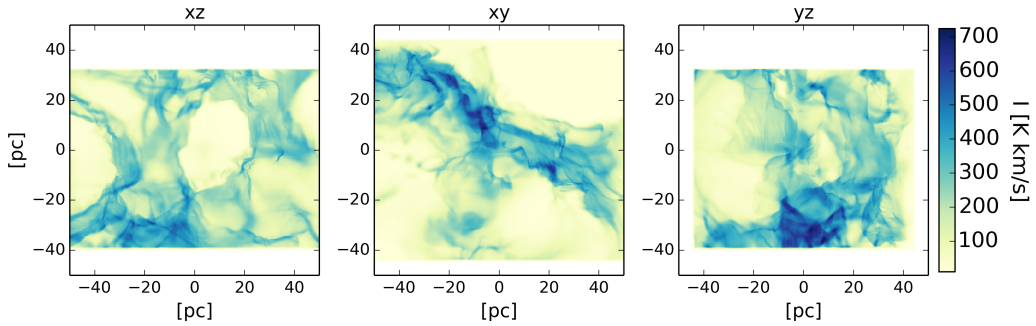

Figure 9.7: Synthetic H I emission maps for MC2 at L10, calculated with $T_{\rm spin}$, whereas the Wouthuysen-Field effect is taken into account.

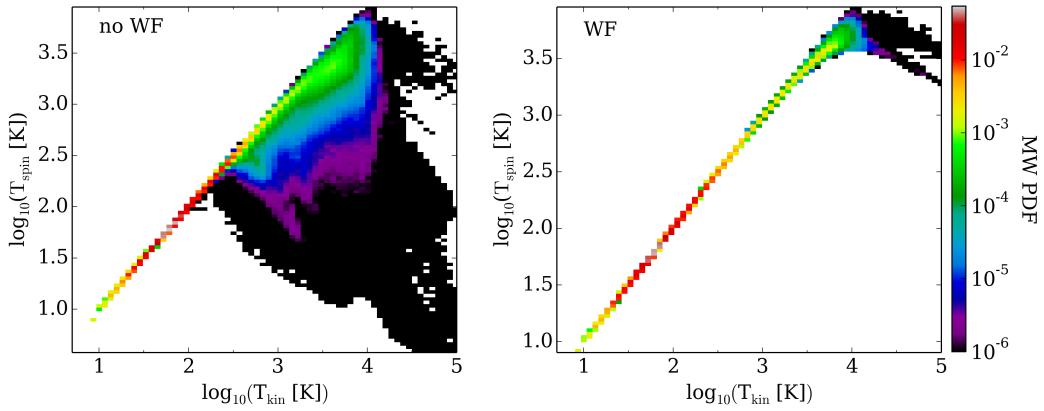

Figure 9.8: Comparison of the spin temperature, calculated without (left) and with (right) the Wouthuysen-Field effect, for MC2 at the refinement level L10 (see Table 4.3). The kinetic temperature is similar to the spin temperature for a large range of temperatures.

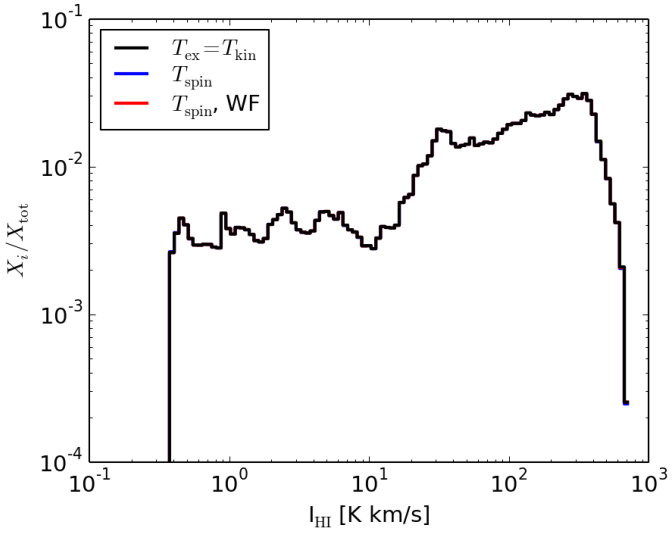

Figure 9.9: Histogram of the H I integrated intensities for MC2, calculated assuming T_{ex} to be equivalent to T_{kin}, or calculated as the spin temperature without and with the Wouthuysen-Field effect. We obtain similar synthetic emission maps for all assumptions.

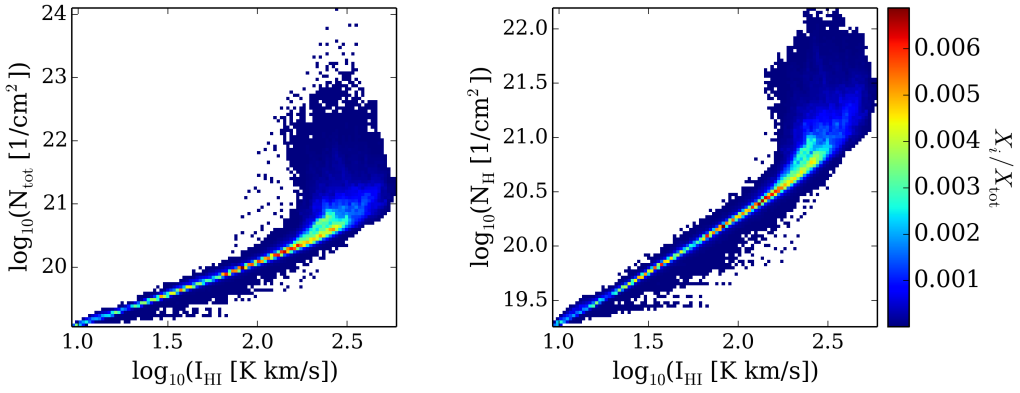

Figure 9.10: Two-dimensional histograms of the distribution of the H I line intensity with the total gas column density (left) and the H column density (right) for the xz-projection. Towards higher H I intensities the distribution steepens. The colour-coding indicates the fraction of pixels within the distribution.

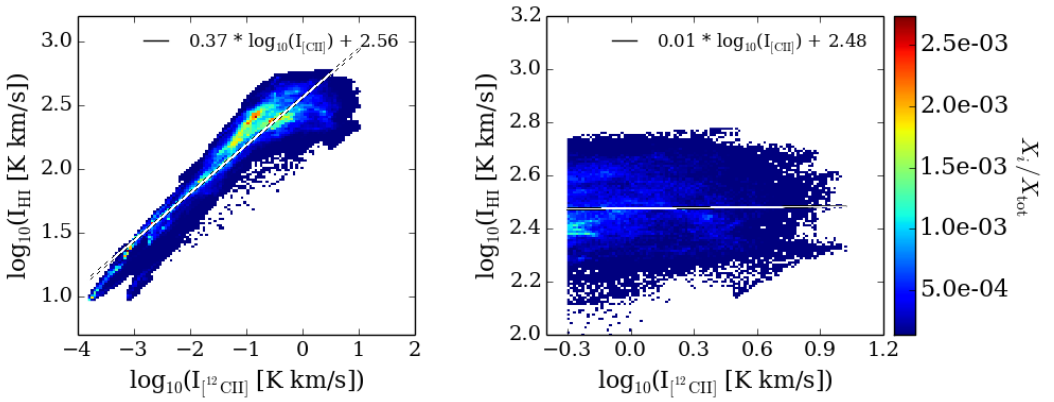

Figure 9.11: Two-dimensional histogram of the distribution of the H I and the [C II] line intensities for the xz-projection. The correlation follows a power-law over the whole parameter range. The colour-coding indicates the fraction of pixels within the distribution.

sion represents the extended density structure in the cloud.

We analyse the correlation between the integrated H I intensities with the total gas and H column densities in Fig. 9.10. Overall, we find the integrated H I intensities and the column densities to follow a power law. For high total column densities we expect in the dense regions hydrogen to be in the form of H_2. Therefore, less hydrogen in H is present along these lines of sight, so that the H I intensity does no longer increase with increasing column densities. Thus, the distribution shown in Fig. 9.10 steepens. Optical depth effects might boost the steepening even further.

In Section 6.3 we found the [C II] line emission to stem predominantly from the atomic gas phase. We therefore compare the integrated H I intensity with the [C II] intensity in Fig. 9.11 in a two-dimensional histogram. The distribution follows a power law when all pixels are taken into account (see left panel of Fig. 9.11). We fit the distribution of all pixels with a power law of

$$\log_{10}\left(\frac{I_{\rm HI}}{\rm K\,km\,s^{-1}}\right) = (0.3748\pm0.0002)\times\log_{10}\left(\frac{I_{[^{12}\rm CII]}}{\rm K\,km\,s^{-1}}\right)+(2.5619\pm0.0003) \quad (9.9)$$

Considering only the observable part of the data with respective to the [C II] line emission (where $I_{\rm [CII]} > 0.5$ K km s^{-1}, right panel of Fig. 9.11), we find only a slight dependency of the H I 21 cm line emission with the [^{12}C II] line emission, as the fitted power law is

$$\log_{10}\left(\frac{I_{\rm HI}}{\rm K\,km\,s^{-1}}\right) = (0.0077\pm0.0013)\times\log_{10}\left(\frac{I_{[^{12}\rm CII]}}{\rm K\,km\,s^{-1}}\right)+(2.4757\pm0.0004). \quad (9.10)$$

9.2 CO emission lines

9.2.1 Rotational CO emission lines

As further complementary data, we calculate the ^{12}CO, ^{13}CO, and C^{18}O lines, each for the rotational transition of $J = 1 - 0$ (see Table 9.1). The abundance of the ^{12}CO molecules are calculated within the chemical model NL99, used for the simulations (Nelson & Langer, 1997, Glover & Mac Low, 2007a,b). Excitations with molecular hydrogen (ortho-H_2 and para-H_2) can influence the level population of the CO molecules. Thus, we calculate the synthetic emission maps with RADMC-3D assuming the molecule not to be in local thermal equilibrium (lines_mode = 3, see Sections 3.1 and 4.1.1). We get the data for the energy levels, transition frequencies, Einstein coefficients, and the collisional rates for all CO isotopes from the Leiden Atomic and Molecular Database (LAMDA Schöier et al., 2005), which lists the data based on the work by Yang et al. (2010).

CO molecules are present in the molecular clouds, so that the interaction with dust grains plays an important role. In particular, CO molecules are expected to freeze-out on the surface of dust grains (Caselli et al., 1999, Redman et al., 2002, Savva et al., 2003, Christie et al., 2012). This happens for $T_{\rm dust} \lesssim 20$ K (Hollenbach et al., 2009). On the other hand, CO can be desorbed from the surface of dust grains by interactions with cosmic rays. This can be expressed with the cosmic ray ionization rate (CRIR). To estimate the fraction of CO in the gas phase considering that CO partially freezes out on dust grains, we follow the approximation by Hollenbach et al. (2009) and Seifried et al. (2017). The number density of CO in the gas phase is then calculated from the number density in the simulation ($n_{\rm CO\,Sim}$) as in Seifried et al. (2017) by

$$n_{\rm CO} = n_{\rm CO\,Sim} \frac{k_{\rm CR}}{k_{\rm CR} + k_{\rm ads}}, \tag{9.11}$$

where $k_{\rm CR}$ is the desorption rate of CO induced by cosmic rays as

$$k_{\rm CR} = 5.7 \times 10^{-13} \times \frac{\rm CRIR}{10^{-17}{\rm s}^{-1}}\ {\rm s}^{-1}{\rm molecule}^{-1} \tag{9.12}$$

(Herbst & Cuppen, 2006), with CRIR $= 10^{-16}$ s^{-1} , and $k_{\rm ads}$ is the adsorption rate due to collisions of CO with dust grains as

$$k_{\rm ads} = 3.44 \times 10^{-18} \sqrt{T_{\rm dust}} (2n_{\rm H_2} + n_{\rm H})\ {\rm s}^{-1}{\rm molecule}^{-1}. \tag{9.13}$$

We refer to Seifried et al. (2017) for a discussion of the impact of the considered components on the freeze-out of CO.

Further, the chemical network included in the simulations does not distinguish between the different CO isotopes. To do so in post-processing, we assume isotope ratios of ^{12}CO/^{13}CO = 69, and ^{12}CO/C^{18}O = 557 (Wilson & Rood, 1994, Wilson, 1999), so that

$$n_{^{13}{\rm CO}} = n_{^{12}{\rm CO}}/69, \tag{9.14}$$

Table 9.3: List of the peak intensities and luminosities of the ^{12}CO (1 – 0), ^{13}CO (1 – 0) and C^{18}O (1 – 0) line emissions, for MC2 at the resolution level L10 for all projections.

Projection	^{12}CO		^{13}CO		C^{18}O	
	$I_{\rm peak}$ [K km s^{-1}]	$L_{\rm tot}$ [$L_\odot$]	$I_{\rm peak}$ [K km s^{-1}]	$L_{\rm tot}$ [$L_\odot$]	$I_{\rm peak}$ [K km s^{-1}]	$L_{\rm tot}$ [$L_\odot$]
xz	302	0.52	117	0.08	48	0.02
xy	238	0.46	121	0.07	56	0.01
yz	269	0.83	137	0.09	54	0.02

and

$$n_{\rm C^{18}O} = n_{^{12}\rm CO}/557. \tag{9.15}$$

As we saw in Section 6, the CO abundances are better resolved for higher spatial resolutions (d$x \sim 0.122$ pc), so that we present in the following the synthetic CO maps for the zoom-in simulation MC2.

9.2.2 Synthetic CO emission maps for MC2

In Fig. 9.12 we show the synthetic emission maps for the CO emission lines of the ^{12}CO (1–0), ^{13}CO (1–0), and C^{18}O (1–0) transitions for MC2 at an resolution level of L10 for all three projections. In line with the CO column densities presented in Fig. 2.3, the CO emission of MC2 is restricted to the regions of dense gas, and thus, only present in distinct and small areas for all projections. Since the CO column densities are large once CO has formed ($10^{17} \lesssim N_{\rm CO} \lesssim 3 \times 10^{20}$ cm^{-2}), the integrated intensities along the lines of sight are likewise high. However, since CO is only present in a small area, the total CO luminosities are small. The peak integrated intensities as well as the luminosities of all presented CO emissions are listed in Table 9.3. The contours in the maps mark an integrated CO intensity of 0.1 K km s^{-1} in each line, to give an idea of the faint emission. This value corresponds to the typical detection sensitivity of ^{12}CO (1–0) in large-scale CO observations (Smith et al., 2014).

We likewise compare the integrated ^{12}CO (1–0) intensities with the total gas column densities and the CO column densities, aiming to characterize the parameter space we found for the intensities in our simulations. This might be helpful for further comparisons with observations, as it is at the moment done for observations in Draco (Schneider et al. in prep). We present the two-dimensional histogram of these parameters in Fig. 9.13, similar to the one of the H I line emission shown in Fig. 9.10. We find the ^{12}CO (1–0) line emission to be present from total gas column densities of $N \geq 10^{-19}$ cm^{-3} (left panel), as a result of the high shielding within the gas necessary for CO to form. We expect the ^{12}CO (1–0) line emission to be observable for $I_{\rm CO} \geq 0.1$ K km s^{-1}, and find for those intensities a power law dependence with the total column density, although the scatter of this distribution is

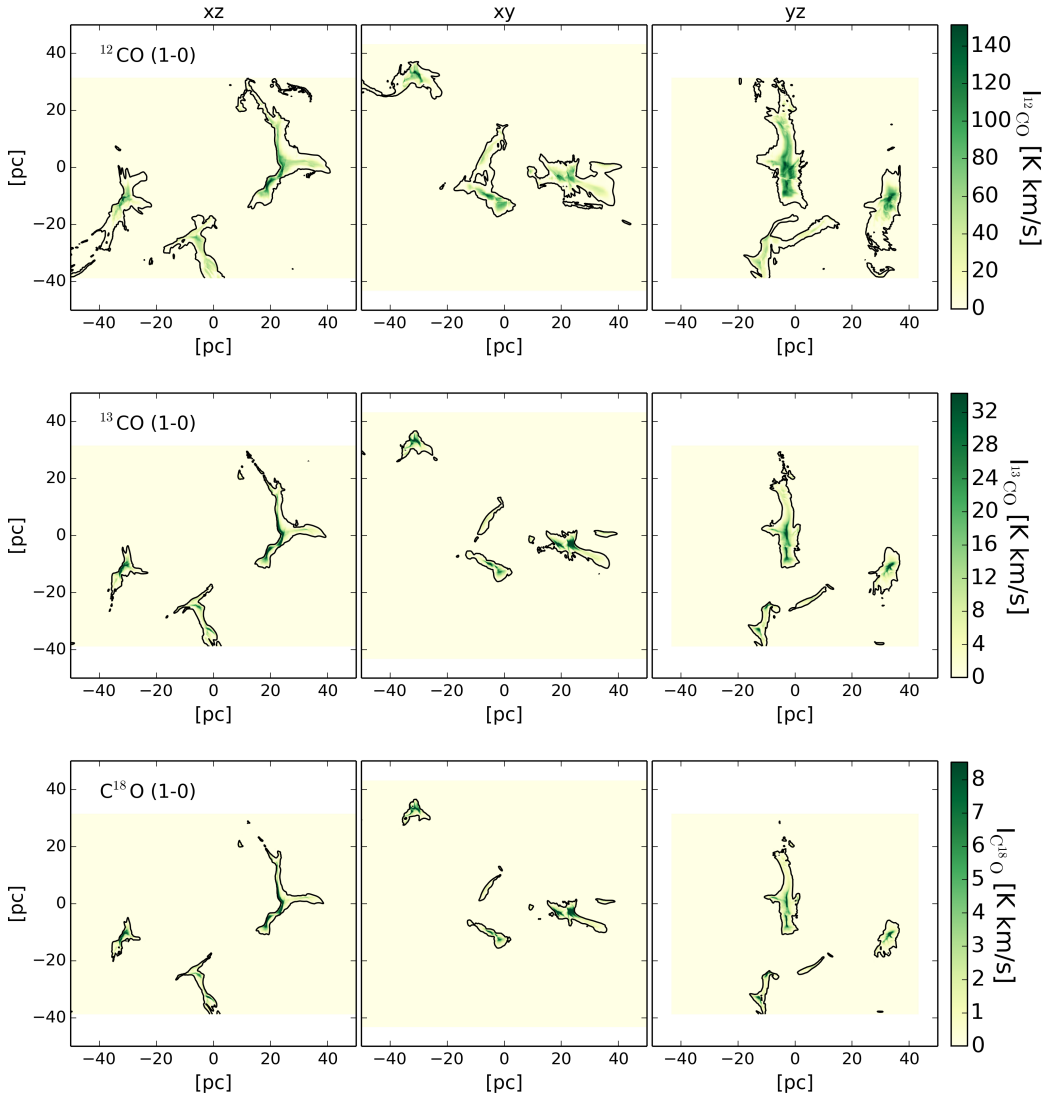

Figure 9.12: Synthetic ^{12}CO (1–0) (upper row), ^{13}CO (1–0) (middle row), andC^{18}O (1–0) (lower row) emission maps for MC2 at a resolution level of L10. The peak intensities and luminosities are summarized in Table 9.3. The contours indicate an integrated intensity of 0.1 Kkm s^{-1}, which is assumed to be detectable for the CO lines. Note, that the colour bars are saturated, since the regions if high integrated CO intensities are small.

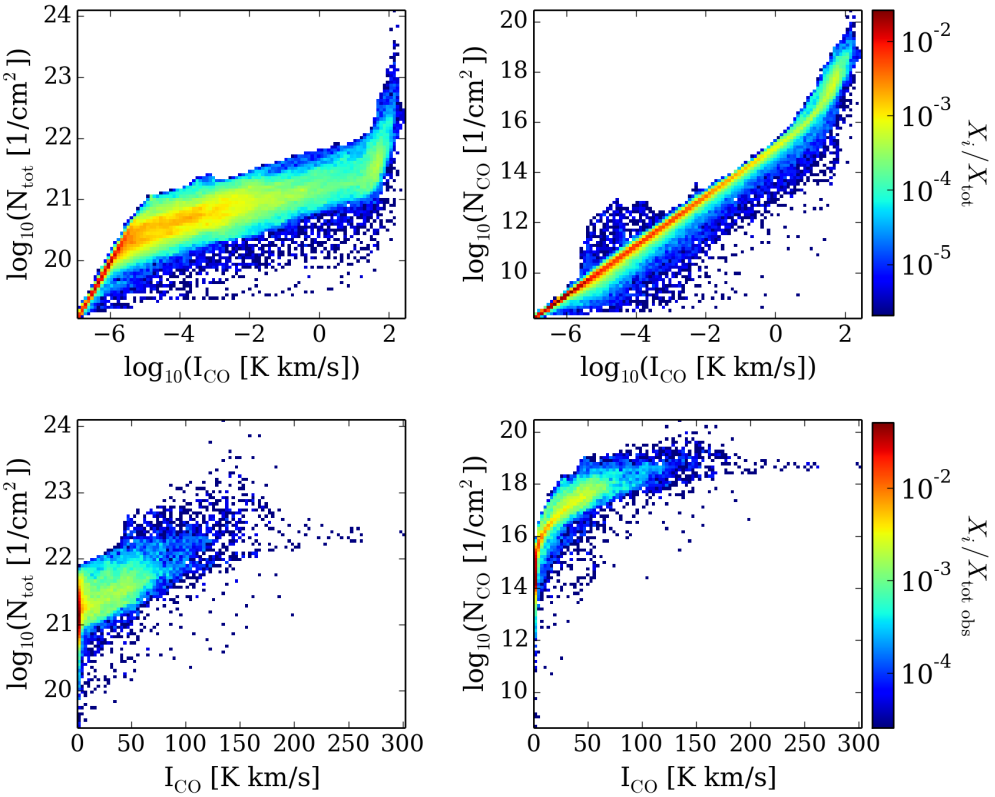

Figure 9.13: Same as Fig. 9.10, but for the integrated ^{12}CO (1–0) intensity in the upper row. The lower row shows the two-dimensional histograms for the observable pixels, for which $I_{\rm CO} \geq 0.1$ K km s^{-1} is fulfilled (Smith et al., 2014).

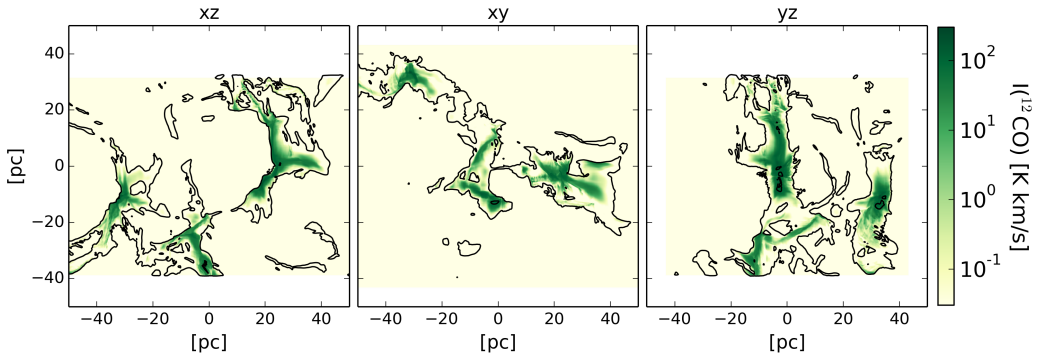

Figure 9.14: Synthetic ^{12}CO (1–0) maps for MC2. The overplotted contours show the integrated [C II] line emission at $I_{[^{12}\mathrm{CII}]} = 0.5$ K km s^{-1}, where we assume the detection limit.

large. For high integrated ^{12}CO (1–0) intensities the distribution steepens, probably caused by the optical depth of the ^{12}CO (1–0) line emission. In the right panel of Fig. 9.13 we show the correlation between the integrated ^{12}CO (1–0) intensities and the CO column densities. Note, that we took the CO column densities directly from the simulations, without considering the freeze-out of CO on dust grains, as taken into account for the CO radiative transfer simulations. Overall, we find a power-law correlation with a steepening of the distribution towards high integrated ^{12}CO (1–0) intensities, in line with the expected optical depth of this emission, and the findings in the correlation with the total gas column density in the left panel of Fig. 9.13.

Observations of CO are used to estimate the mass in H_2 in the ISM. Since CO needs a higher shielding to form compared to the conditions under which H_2 forms, there are regions, where H_2 is present, which is no longer traced by CO. With the simulation of MC2 we can investigate the correlation between the integrated ^{12}CO $(1-0)$ intensity and the H_2 column densities for all three projections, and thus, we can estimate which fraction of H_2 mass is traced by CO in its projection. We expect the integrated intensity of ^{12}CO $(1-0)$ to be detectable for $I \geq 0.1$ K km s^{-1} (Smith et al., 2014). In Fig. 9.12 this corresponds roughly to the green coloured area in the plots. We find that for all three projections about 80% of the total H_2 mass are situated within the regions assumed to be detectable in ^{12}CO $(1-0)$.

For CO-dark H_2 gas the suitability of other tracers as the [C II] line emission is discussed in literature. We found in Section 6.3 that the [C II] line emission stems from the atomic gas phase, in transition to the molecular gas, rather than from molecular gas. However, with the synthetic [C II] and CO emission maps, and the H_2 column density maps we investigate which fraction of H_2 mass coincides with the detectable [C II] line emission, and which fraction is aligned in regions with a detectable [C II], but not CO integrated intensity. Figure 9.14 shows the synthetic ^{12}CO (1–0) emission maps, with contours indicating the [C II] detectable regions, where $I_{[^{12}\mathrm{CII}]} \geq 0.5$ K km s^{-1}. Within the contours ~90% of the total H_2 mass are situated. Thus, around 10% of the H_2 mass can be referred to CO-dark H_2, which is aligned with detectable [C II] line emission, but not with ^{12}CO (1–0). The remaining

10% of H_2 mass are neither visible in [C II] nor in ^{12}CO (1–0).

9.3 Line profiles

To get an impression about the line profiles at different wavelengths, we present the line profiles for the [^{12}C II], [^{13}C II], ^{12}CO (1–0), and H I line emission for six different positions in Fig. 9.15. The positions P1 - P4 were already presented in Chapter 8. P5 and P6 are additional points. For a better comparison, the [^{12}C II] line profiles are scaled by a factor of 20, and the [^{13}C II] line profiles by an additional factor of 107. The last one takes into account the scaling of the number density for $n_{^{13}C^+}$, as described in Section 3.2.2. The scaled [^{13}C II] line intensities are comparable with the [^{12}C II] lines for P2, P5, and P6. For the other three points (P1, P3, P4), the peaks in the scaled [^{13}C II] line profiles are significant larger than for the [^{12}C II] lines. This is due to self-absorption, caused by optical depth effects of the [^{12}C II] line emission. To a small degree this occurs likewise in P2 for the component at $v \sim -3$ km s^{-1}, and in P6 for the component at $v \sim 3$ km s^{-1}. For P1, P3, and P4, the position ($\overline{v}$) and line width (σ) of the ^{12}CO (1–0) profile coincides with the ones of the [^{12}C II] and [^{13}C II] line profiles. For P6, only one component of the [^{12}C II] and [^{13}C II] lines have a counterpart in ^{12}CO (1–0). The profile at P2 differs from the others, as its line width in ^{12}CO (1–0) is larger. The H I line profiles have in general a larger line width compared to the ^{12}CO (1–0) and the [C II] line profiles. This also holds, if CO is not present, as shown in P5.

9.4 Discussion

We calculated as complementary data the H I 21 cm line emission of the hyperfine structure line in atomic hydrogen on the example of the SILCC-01 simulation *S10–KS–rand*, and for the zoom-in simulation MC2. For calculating the emission, the excitation temperature $T_{\rm spin}$ has to be estimated. We followed the approach described in Kim et al. (2014), Furlanetto & Furlanetto (2007), where $T_{\rm spin}$ is determined by collisions with other atomic hydrogen atoms and electrons, the Wouthuysen-Field effect, and the radiation from the background. We found for our simulation setups that a large mass fraction of the gas has spin temperatures equal to the kinetic gas temperature. Therefore, the integrated H I intensity maps show only slight differences when $T_{\rm spin}$ is calculated with the different approaches.

We found integrated H I intensities $I_{\rm HI} \leq 1000$ K km s^{-1} for both the simulation *S10–KS–rand* and MC2. This is in line with the observed H I intensities towards regions like W43, where Bihr et al. (2015) find integrated H I intensities between

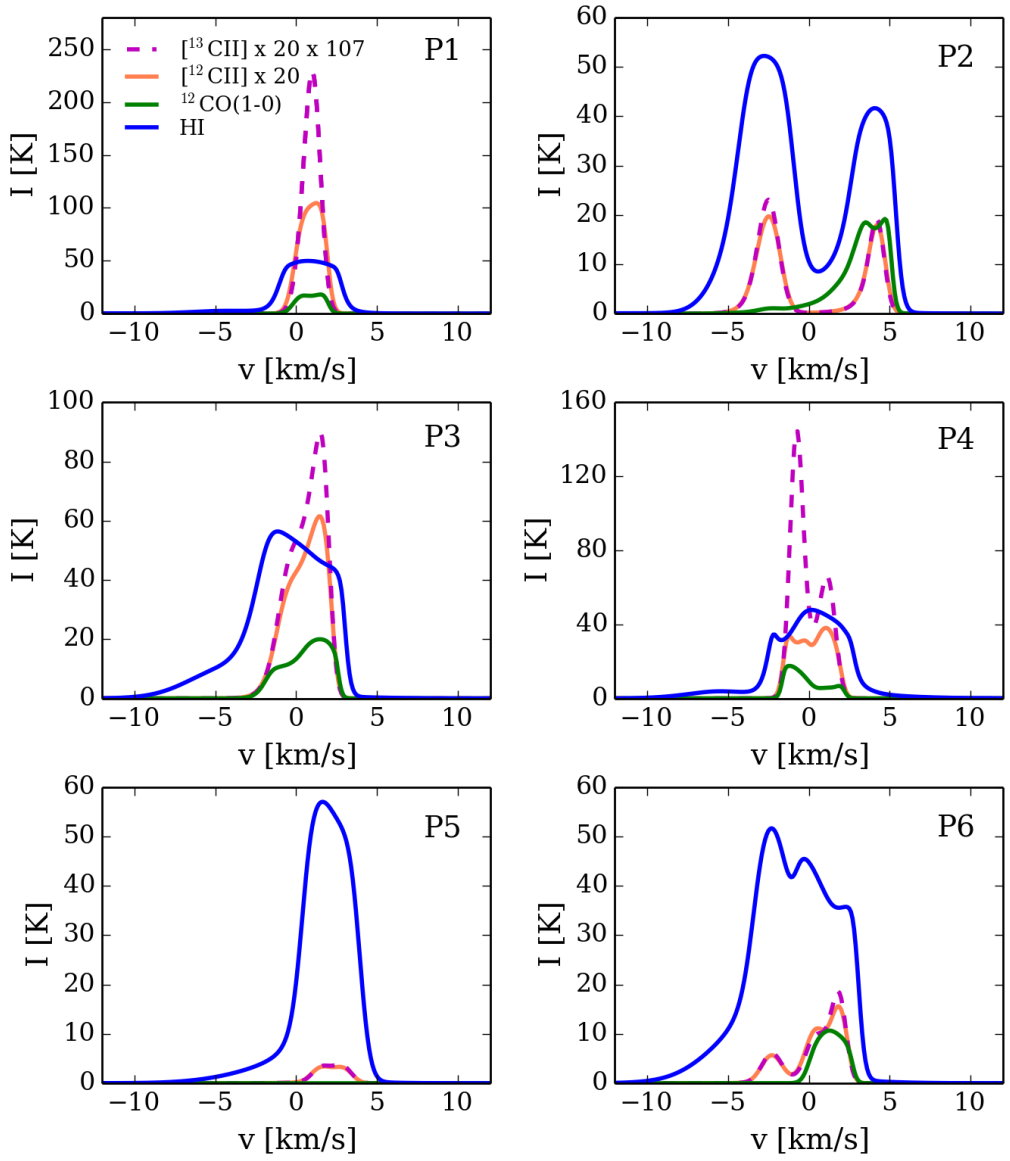

Figure 9.15: Comparison of the line profiles of the [C II], the ^{12}CO (1–0), and the H I emission line for the positions P1-P4, as introduced in Chapter 8, and on two further positions. Note, that the [^{12}C II] line is scaled by a factor of 20, and the [^{13}C II] line by an additional factor of 107, accounting for the scaling of the number density (see Section 3.2.2)

200 and 1000 K km s^{-1}. Additionally, we studied the correlation between the integrated H I and [^{12}C II] intensities in a two-dimensional histogram. When taking all data points in the map, we found the distribution describable by a power law with a slope of ∼0.4. For high integrated intensities, $I_{[^{12}\mathrm{CII}]} \geq 0.5$ K km s^{-1}, which corresponds to the expected observable part of the emission, the distribution flattens, and the H I intensity does no longer increase with an increasing [^{12}C II] intensity. Thus, we cannot confirm a power-law correlation for the observable range. This is surprising, since we found in Chapter 6 the [C II] line emission to be correlated with the atomic gas phase. Optical depth effects in the H I line could contribute the flattening of the distribution. Moreover, we can find a hint for the reason of this result when plotting the line profiles, as done for some example profiles in Fig. 9.15. Here we see, that the H I line profiles cover a larger range in velocity compared to the [^{12}C II] line profiles. Thus, although the [C II] line emission stems from the gas in which hydrogen is mainly in atomic form, there might be more contributions to the H I intensity along a line of sight as the gas emitting the [^{12}C II] line emission. For investigating this issue in more detail, we suggest to likewise analyse in future work the origin of the H I emission in the gas.

We carried out synthetic ^{12}CO (1–0), ^{13}CO (1–0), and C^{18}O (1–0) emission maps of MC2. The integrated intensities of these lines are less than $I_{^{12}\mathrm{CO}} \lesssim 300$ K km s^{-1}, $I_{^{13}\mathrm{CO}} \lesssim 120$ K km s^{-1}, $I_{\mathrm{C}^{18}\mathrm{O}} \lesssim 30$ K km s^{-1}. Note, that these are roughly the peak intensities in the integrated intensity maps, and that in general the integrated intensities are smaller in the maps. The intensities we find for the ^{13}CO (1–0) line emission are larger than in Taurus ($I_{^{13}\mathrm{CO}} \lesssim 7$ K km s^{-1}, integrated over a velocity of 2–9 km s^{-1}) reported in Goldsmith et al. (2008, fig. 1 therein), but are smaller than the ^{13}CO (1–0) intensities in Orion ($I_{^{13}\mathrm{CO}} \lesssim 200$ K km s^{-1}), presented in Kong et al. (2018, fig. 6 therein). Kong et al. (2018) further present integrated ^{12}CO (1–0) and C^{18}O (1–0) emission maps, that likewise cover a larger range of integrated intensities with $I_{^{12}\mathrm{CO}} \lesssim 1000$ K km s^{-1}(see Fig. 1.7), and $I_{\mathrm{C}^{18}\mathrm{O}} \lesssim 50$ K km s^{-1}. However, since Orion is a region of active star formation, we judge the differences to be reasonable.

Lastly, we analysed which fraction of the H_2 mass is aligned along line of sights with detectable ^{12}CO (1–0) and [^{12}C II] line emission. We found ∼80% of the total H_2 mass in the same area as observable ^{12}CO (1–0) intensities, and ∼90% in the area of observable [^{12}C II] intensities. Thus, ∼10% of the H_2 mass is CO-dark, and further ∼10% is not detectable in ^{12}CO (1–0) or [^{12}C II].

10

Conclusion and Outlook

10.1 Conclusion

In this work we carried out synthetic emission maps of simulated interstellar medium, focussing on the [C II] emission line. We used the radiative transfer code RADMC-3D to calculate the emission maps. They are the first step and the base in the process aiming to obtain synthetic observations. The [^{12}C II] line is emitted from the fine structure transition of the $^{12}C^+$ ion at a wavelength of $\lambda = 157.741\ \mu$m[1]. Since C^+ can be present in the molecular gas phase as well as still in the warm gas phase, the [C II] line emission can originate from various ISM phases. Therefore, the observed [^{12}C II] line emission can be associated with molecular clouds, tracing both the regions, in which stars are going to form soon, and the regions, in which stars already exist and ionize the surrounding gas. Following these considerations, one would like to estimate *(i)* the star formation rate by analysing the [C II] line emission (e.g. De Looze et al., 2011, 2014, Pineda et al., 2014, Herrera-Camus et al., 2015, Kapala et al., 2015), and *(ii)* the fraction of H_2 in the gas (e.g. Wolfire et al., 2010, Langer et al., 2014b). Studying H_2 in the ISM is important, since 20% of the hydrogen mass is present in form of H_2 in the ISM (Tielens, 2005), but it is hard to detect it directly because it does not have a permanent dipole momentum. Therefore, one uses other observations as tracers for H_2, normally the rotational transitions of CO. However, since CO needs larger shielding of the gas to form, compared to H_2, there might be H_2 not visible in CO. This gas, called CO-dark H_2, is hoped to be detectable in the [^{12}C II] line.

[1] In our notation the [^{12}C II] line refers especially to the emission line of the $^{12}C^+$ isotope, whereas we use the name [C II] line emission, when talking about the emission line from carbon ions in general.

Knowing about the hopes set into the analysis of the [C II] line emission, we address the question of the origin in the ISM of the [C II] line. With numerical simulations we can follow the evolution of the ISM and tackle this issue by having access to the three dimensional structure of the gas within the simulation setup. The models we take in this work are the SILCC setup with a spatial resolution of $\mathrm{d}x = 3.9$ pc (Walch et al., 2015, Girichidis et al., 2016b), and a simulation of a young, forming molecular cloud before the onset of star formation, MC2, with a spatial resolution of $\mathrm{d}x = 0.122$ pc (Seifried et al., 2017). The last mentioned is a zoom-in into a small region, embedded within the SILCC box (SILCC-Zoom project). For the SILCC simulations, the feedback process of supernova explosions (SNe) are considered, while the positioning of the SNe is varied. One run of the SILCC setups include additionally the feedback of stellar winds. The gas in the simulation MC2 experiences only the feedback from SNe before its formation process starts. In this manner, the forming molecular cloud stays within the simulation box, and gas keeps contracting to form the molecular cloud. According to their feedback processes, the ISM in all simulations represents gas before the onset of star formation.

However, as we presented in Chapter 2, and as it was found in Walch et al. (2015), Girichidis et al. (2016b), Peters et al. (2017), the composition of the gas phase changes with the kind of feedback the gas experience. The gas in the SILCC simulations has total gas number densities of $n \lesssim 10^4$ cm^{-3}, while the temperatures within the gas are between 10 and 10^8 K. For most of the SILCC simulations it consists of a warm gas phase with $T \geq 10^4$ K and $n \leq 10^{-2}$ cm^{-3}, a second phase of gas with $T \sim 10^4$ K and $10^{-2}\,\mathrm{cm}^{-3} \leq n \leq 10^{0}\,\mathrm{cm}^{-3}$, and a third phase of cold gas with $T \leq 100$ K and $n \geq 10$ cm^{-3}. For the zoom-in simulation MC2, the range of total gas number density has shifted to higher number densities $n \lesssim 10^6$ cm^{-3}, and slightly smaller temperatures $\gtrsim 5$ K. This is caused by the better spatial resolution in MC2. Further, due to the missing feedback of SNe once the zoom-in process has started, there is no more gas heated up, but continues contracting into the molecular cloud. Therefore, the composition of the gas changes towards the dense gas. Regions with densities of $n \geq 10^4$ cm^{-3} can be associated with the dense cores, in which star formation is expected to happen soon (Stahler & Palla, 2005, Snow & McCall, 2006). The details for the underlying simulations are presented in Chapter 2.

We carried out synthetic [C II] emission maps for the SILCC simulations with a spatial resolution of $\mathrm{d}x = 3.9$ pc, and a spectral resolution of $\mathrm{d}v \sim 1$ km s^{-1}, and for the zoom-in simulation MC2 in general with a spatial resolution of $\mathrm{d}x = 0.122$ pc, and a spectral resolution of $\mathrm{d}v \sim 0.1$ km s^{-1} (see Table 3.2). We expect the [C II] line emission to be observable for $I_{[^{12}\mathrm{CII}]} \geq 0.5$ K km s^{-1} in large scale studies (see Section 3.4). About 15 to 30% of the total field of the molecular cloud have integrated [C II] intensities above this limit. Thus, we conclude that one can observe a molecular could in the [C II] line emission before star formation sets in.

For MC2 we carried out further synthetic [C II] maps with lower spatial resolution, ranging from 3.9 pc to 0.122 pc (see Table 4.3). With those we tested the convergence of the [C II] line emission in the maps. The [C II] luminosity calculated

over the whole emission map differs only by a median deviation of 0.5%, when comparing the resolution levels of dx = 0.25 pc and dx = 0.122 pc. Thus, although the luminosity and the peak intensities still change slightly, the synthetic emission maps are about to converge. For more details, we refer to Section 4.2.2.

In the following, we summarize the results we found in the study of the [C II] emission maps, ordered by its Chapter, and close with ideas for future work.

Distribution of the emission

The SILCC setup simulates the evolution of the ISM in a piece of a galactic disc. We analysed the vertical distribution of the [^{12}C II] line emission around the disc's midplane. Overall, the profiles are not Gaussian, but have an asymmetric shape, with the dominant contribution from the molecular clouds situated in the midplane. We characterized its width by calculating the square root of the variance of the vertical [^{12}C II] emission distribution around the midplane. For a Gaussian shaped profile, this corresponds to the standard deviation of a Gaussian. We found the scale height within the SILCC simulations to change with time. If there is an continuously outflowing gas component, the scale height increases. In case of an asymmetric outflow, the scale height changes less, or even decreases with time if the outflowing gas becomes clumpy. The scale heights we find are in general $\lesssim$ 100 pc. We stress, that the SILCC simulation represent a small probe of a galactic plane, and therefore ask for caution, when comparing these numbers with observed scale heights, obtained from averaged observations of a whole galaxy. In observations of the vertical emission distribution on a local scale within the Milky Way, Glück (2017) find complex vertical profiles, with sharp emission peaks from molecular clouds. Although their molecular clouds are distributed on a larger vertical scale than in the SILCC simulations, their qualitative result is in agreement with our study. We discussed further aspects of determining the scale height, and the influence of observations on the result in Chapter 5.

Opacity of the [^{12}C II] emission line

We found the [^{12}C II] line emission to become optically thick along some lines of sight within all simulation setups. For the SILCC simulation, this affects the molecular clouds formed in the disc's midplane. For the zoom-in simulations we found between 35% and 40% of the observable area ($I_{[^{12}\mathrm{CII}]} \geq 0.5$ K km s^{-1}) to be optically thick. The opacity affects the emission *(i)* by resulting in stimulated [C II] emission, and *(ii)* by absorption effects. We analysed this in Section 4.2.1.

We model the [C II] emission line as optically thin, with a method inspired by the carbon isotope ^{13}C$^+$. For this isotope, the fine structure transition splits into three hyperfine structure lines. Its strongest line ($F = 2 - 1$) is at a frequency very close to the [^{12}C II] line emission. We mimic the [^{13}C II] ($F = 2 - 1$) line emission by scaling the number density n_{C^+} with a factor of 107, taking into account the isotope abundance of ^{12}C$^+$/^{13}C$^+$ and the intensity ratio among the hyperfine structure

transitions in $^{13}C^+$. The [^{13}C II] ($F = 2 - 1$) line, called [^{13}C II] hereafter, is optically thin, and originates from the same gas phase as the [^{12}C II] line emission. Therefore, it can be used to characterize the physical parameters of the [C II] emitting gas.

Origin of the [C II] emission

We studied the origin of the [C II] line emission using the optically thin [^{13}C II] line emission and found the dominant part in the SILCC simulations to stem from the molecular gas phase. A small contribution comes from the warm, neutral medium. This result differs from the findings we made in the simulation of MC2, with the better spatial resolution of 0.122 pc. Here, all the [C II] line emission stems from the cold gas phase with $T \leq 100$ K. We characterize the emission by its quartiles of the cumulative distribution and found parameter ranges of 43 K $\leq T \leq$ 64 K, 53 cm^{-3} $\leq n \leq$ 438 cm^{-3}, with a range of 16% to 44% of the hydrogen in molecular form, and a visual extinction A_V between $0.5 \leq A_V \leq 0.91$. Thus, the gas associated with the [C II] line emission is predominantly atomic gas. We tested further whether this result holds for different spatial resolutions, different time steps, and different simulations. We found that the characteristic temperature range of the [C II] emitting gas is unaffected, when carrying out the analysis for the different simulations. However, the range of number densities and fractional molecular hydrogen abundances in the [C II] emitting gas shifts towards higher values with increasing resolution. Despite the resolution, the SILCC simulations and the zoom-in simulations differ in their evolutionary time step that was taken for the analysis. Whereas we analysed the SILCC simulation at $t = 50$ Myr, we took a snapshot at $t = 13.9$ Myr for MC2. Since the results found for the zoom-in simulation MC2 at the same spatial resolution as the SILCC simulation differ from the results in the SILCC setup, we conclude that the result is also dependent on the analysed region taken from the simulation, and additionally influenced by the composition of the ISM, as this is determined by the feedback processes assumed for the simulation. We refer to Chapter 6 for details of the study of the origin of the emission, and to Chapter 2 for details in the underlying simulations.

Correlation with the column density

In Chapter 7 we studied the correlation between the integrated [^{12}C II] intensity and the column density of the total gas, H, and C^+ in MC2. For the observable range of [^{12}C II] intensities we fitted the correlations with power laws, and found slopes of ~0.7, ~0.5, and ~0.6, respectively. Additionally, we defined a factor $Y_{\rm CII}$ as the ratio between the total gas column density and the integrated [^{12}C II] intensity. The median value for the $Y_{\rm CII}$ factor estimated from all projections in MC2 is $Y_{\rm CII} \approx 1.1 \times 10^{21}$ cm^{-2} (K km s^{-1})$^{-1}$. However, as the [^{12}C II] intensity scales with the column density by a power law, it is better to use $Y_{\rm CII} \propto I_{[^{12}{\rm CII}]}^{-0.3}$ to constrain the column density or the mass of a cloud by the [^{12}C II] intensity. We note, that the value we found for $Y_{\rm CII}$ applies to our simulation of a young, molecular cloud before the onset of star formation, exposed to a uniform ISRF of $G_0 = 1.7$. For higher

/ lower ISRF we expect the Y_{CII} value to become lower / higher, respectively, since the radiation field would yield to an increase of the integrated [^{12}C II] intensity.

Line profiles

For the zoom-in simulation MC2 we studied the line profiles of the [^{12}C II] line emission, and tried to develop a tool to analyse the them in a statistical manner. For this, we compared the line profiles with a reference function, where we chose a Gaussian function, reflecting the case of an optically thin line, and a Boxcar function, reflecting an optically thick line. We calculated the quadratic mean of the differences between the reference function and the line profile, weighted it by the amplitude of the reference function, and call the result "Tauber value". In general we find the Tauber values calculated with the Gaussian reference function to be smaller than the Tauber values calculated with the Boxcar function. This hints to the fact, that a large fraction of the [^{12}C II] line profiles in MC2 is optically thin. Line profiles with several distinct velocity components have larger Tauber values, since their profiles are no longer describable with one single reference function. This tendency we found likewise, when comparing the Tauber values with the width σ of the profiles. Comparing the Tauber values with the integrated [^{12}C II] intensity did not show a clear correlation. These findings hold likewise for the different spatial resolution levels, and for the zoom-in simulation MC1. We further compared our Tauber values with those calculated from observations of infrared dark clouds by Beuther et al. (2014). We chose this data set, because this observation has comparable integrated [^{12}C II] intensities as we found in MC2. However, the widths of the line profiles are larger than those found for the majority of the profiles in our simulations. This can be caused by the observation with a beam. The Tauber values of the observations are in the same range as those found in the simulations. For further details we refer to Chapter 8.

Complementary emission maps

The chemical model in our simulations likewise follows the formation of H and CO. We therefore calculated in MC2 synthetic emission maps of the hyperfine transition in atomic hydrogen, which is the H I 21 cm line, and rotational transitions of ^{12}CO (1–0), ^{13}CO (1–0), and C^{18}O (1–0). These data can be used in future work as a complementary to the [^{12}C II] and [^{13}C II] line emission maps, and contribute to study the dynamics of the clouds with methods applied by observers. The aim of this part presented in Chapter 9 is to introduce this data.

For calculating the H I maps we used the spin temperature, T_{spin}, as excitation temperature for atomic hydrogen. We found T_{spin} to be similar to the kinetic temperature in most of the gas mass. Including the Wouthuysen-Field effect for calculating T_{spin} has only a small influence. Inspired by the result that the [^{12}C II] emitting gas is associated with the hydrogen gas in transition to its molecular phase, we compared the integrated [^{12}C II] line intensities with the integrated H I line intensities. For the assumed observable range in [^{12}C II] we did not found a clear correlation between these quantities. Thus, although the [^{12}C II] line emission is associated with the H I emission, the H I emission itself stems from a larger region of the simulation box

and can be optically thick, so that its intensity is not increasing with larger column density, and presumably larger integrated [^{12}C II] intensity.

Having calculated the CO emission maps, we can identify regions in the map that have a reasonable [^{12}C II] line emission to be detectable, but no ^{12}CO (1–0) line emission. These regions, since dark in CO, could contain molecular dark H_2 gas. Although we found that the [^{12}C II] line emission traces the atomic gas phase rather than the molecular one, we calculated the mass in H_2 along the line of sights, where [^{12}C II] could be detected, but not CO. We found about 10% of the total H_2 mass to be in these regions of CO-dark H_2. Further 10% of the total H_2 mass are not aligned with the ^{12}CO (1–0) or the [^{12}C II] line emission.

Finally, we presented some line profiles of the [^{12}C II], [^{13}C II], ^{12}CO (1–0), and the H I line emission. Here, we found the line widths of the [^{12}C II] and [^{13}C II] line profiles to be comparable with the ^{12}CO (1–0) line profiles, while the H I profile in general stems from gas over a larger velocity range. Further, when comparing the line profiles of the [^{12}C II] and [^{13}C II] line emission, we found the [^{12}C II] line to be self-absorbed.

10.2 Outlook

We found in this work that the evolution of the gas phases in the ISM and the resulting composition of the phases changes with the applied feedback processes. This was likewise analysed in Walch et al. (2015) and Girichidis et al. (2016b). Here we have seen, that this also affects the [C II] line emission, calculated with the radiative transfer code RADMC-3D. To judge, whether our findings are general ones, and how much they are affected by the simulation setup, it would be very interesting to vary some parameters, and improve some assumptions in the setup of the underlying simulation. Those changes could be

- including more and different feedback processes. We found the ISM in the zoom-in simulation MC2 to form dense cores, that could be the birth places of stars. As a next step, and already work in progress, one could include the radiation of the stars as a further feedback process. To analyse the effect on the [C II] line emission, it is necessary to couple the radiation to the chemical network included in the simulation.
- expand the chemical network within the simulation setup. The current chemical network follows the formation of C^+ and CO, but atomic carbon is not considered so far. Also in this field there is ongoing work in including the chemical network of Nelson & Langer (1999), which calculates likewise the formation of atomic carbon. Further, including more chemical species and molecules would allow to identify tracers for different environments.
- calculating different scenarios, as studying the evolution in a colliding flow

scenario. This would allow to investigate whether our findings apply to different dynamical conditions, or whether they change within different scenarios.
- carry out simulations by taking into account only a few feedback processes. By this, one could study the influence of one process to the system in a systematic way. This could strengthen the understanding of the evolution when seeing all processes interplaying in one simulation.

In addition to that, this work can be expanded with respect to the radiative transfer simulations. Carrying out synthetic emission maps is a good way to study and understand the physics within the simulations. So far we carried out synthetic emission maps, and benefited by the three-dimensional setup to study the physical properties of the [C II] emitting gas. We further analysed the correlation between the integrated intensity of several wavelengths, as well as with the column densities of the simulation. In future work, one could use the synthetic emission maps to carry out synthetic *observations*. For those, one would need to consider the instrumental effects like for example the beam size of the telescope, the influence of noise, as well as source-related parameters such as the distance. In the case of interferometric observations, the spatial filtering has to be also taken into account. Synthetic observations would allow us to evaluate on a sophisticated base, whether the emission is detectable under various circumstances.

Ongoing observations of the [C II] line emission will make comparisons possible in future work. There are recent [^{12}C II] and [^{13}C II] line observations in Orion obtained with SOFIA (PI: A. Tielens), further [^{12}C II] observations of molecular clouds as Draco (Schneider et al. in prep.), [C II] observations in other galaxies as in M33 and M51 (Pineda et al. in prep.), and the mapping of the galactic centre in our Galaxy, which was done recently with SOFIA. Further, future observation may provide us with more data from the molecular cloud complex of Taurus. Since the object of these observations are very different, this provides a good base to test different scenarios in the simulations.

With our models, we can provide scatter plots of the correlation between various characteristics of the line profiles, as its maximum intensity within the line profile (main beam temperature), the widths of the line profile, and its integrated intensity. These quantities can be collected for several wavelengths. Comparing the parameter range of the simulated line profiles with the ones obtained from the observations, can be the basis of a fruitful collaboration. If the parameter space of the observations and the simulations match, we might have found a good model to describe the object in the observations. A disagreement can hint to the fact that the underlying simulation describes a different object than observed, or it can show us the limitations of our model and assumption. Thus, from a comparison between simulations and observations, both sides can take profit.

Finally, a comparison of the Tauber values calculated for different emission lines might give in the future a suitable tool to analyse the line profiles in simulations and observations in a statistical manner.

Acknowledgements

The last years gave me a lot of new experiences, that I am thankful for. I learned a lot about me, about the life. I am very grateful for the fact that I did not need to go this way alone, but had many people around me to talk with both about the science and about the other things that we call life. Without their support I would not have been able to write this thesis. I also thank the anonymous person, that provided me the book "Momo" by Michael Ende, right at the moment when I needed it most to read.

I want to thank my supervisor Stefanie Walch-Gassner for the support I got for my work. I am very thankful, that she let me do this work in my way. I am also grateful for the support I got from my second supervisor Jürgen Stutzki. Likewise I am thankful for the help I got from Daniel Seifried. For proof-reading of the texts and further fruitful discussions I would like to thank a lot Seamus Clarke, Álvaro Sánchez-Monge, Volker Ossenkopf-Okada, and Juan Ibañez-Mejia. The discussions with them helped me to strengthen the purpose of the texts, and they motivated me to investigate additional aspects. Further, the comments from Franziska Franeck were very helpful. Likewise, the co-authors of the SILCC project contributed to the way of how the texts were written in the end. Many thanks to all of them.

A work is not done in a vacuum place, but needs a working group and an office, which provides in the best case a constructive working atmosphere. I am thankful that I found this in the working group of "Theoretical Astrophysics". I am thankful especially for the time I had the honour to share the office with Nassim, Seamus, Franta, Juan and Onix. Further, I am happy to had Prabesh, Sebastian, Dominik, Shash, Johanna, Paul and many more as friends and colleges. I experienced support in the context of work and as a person, and I enjoyed being with you. There are many things worth to note here, and I apologize of not mentioning more, or if I have forgotten someone.

At that point I also want to thank my family, especially my sister Franziska, Álvaro, and my friends Laura, Connie, Kathrin, Hannes, Eva and many others, that listened to me in good and less good times, that were there, when I needed them, and that turned the time into a good time. I am deeply thankful for all discussions that encouraged me to go my way. I am happy, that I could spent the last four years with all of you.

Bibliography

Accurso, G., Saintonge, A., Bisbas, T. G., & Viti, S. 2017, MNRAS, 464, 3315

Allison, A. C. & Dalgarno, A. 1969, ApJ, 158, 423

Andree-Labsch, S., Ossenkopf-Okada, V., & Röllig, M. 2017, A&A, 598, A2

Banerjee, A. & Jog, C. J. 2007, ApJ, 662, 335

Barinovs, Ğ., van Hemert, M. C., Krems, R., & Dalgarno, A. 2005, ApJ, 620, 537

Barnes, J. E., Wood, K., Hill, A. S., & Haffner, L. M. 2014, MNRAS, 440, 3027

Bennett, C. L., Fixsen, D. J., Hinshaw, G., et al. 1994, ApJ, 434, 587

Berger, M. J. & Colella, P. 1989, Journal of Computational Physics, 82, 64

Beuther, H., Bihr, S., Rugel, M., et al. 2016, A&A, 595, A32

Beuther, H., Ragan, S. E., Ossenkopf, V., et al. 2014, A&A, 571, A53

Bihr, S., Beuther, H., Ott, J., et al. 2015, A&A, 580, A112

Bisbas, T. G., Tan, J. C., Csengeri, T., et al. 2018, MNRAS, 478, L54

Boreiko, R. T., Betz, A. L., & Zmuidzinas, J. 1988, ApJ, 325, L47

Brand, J. & Blitz, L. 1993, A&A, 275, 67

Burton, M. G., Braiding, C., Glueck, C., et al. 2013, , 30, e044

Burton, W. B. & te Lintel Hekkert, P. 1986, A&AS, 65, 427

Buser, R. 2000, Science, 287, 69

Carney, B. W. & Seitzer, P. 1993, AJ, 105, 2127

Carroll, B. W. & Ostlie, D. A. 2006, An introduction to modern astrophysics and cosmology

Caselli, P., Walmsley, C. M., Tafalla, M., Dore, L., & Myers, P. C. 1999, ApJ, 523, L165

Chabrier, G. 2001, ApJ, 554, 1274

Christie, H., Viti, S., Yates, J., et al. 2012, MNRAS, 422, 968

Clark, P. C., Glover, S. C. O., & Klessen, R. S. 2012, MNRAS, 420, 745

Clarke, S. D., Whitworth, A. P., Spowage, R. L., et al. 2018, ArXiv e-prints [[arXiv]1806.08564]

Clarke, S. D. C. H. 2016, PhD thesis, Cardiff University

Croxall, K. V., Smith, J. D., Wolfire, M. G., et al. 2012, ApJ, 747, 81

Dalgarno, A. & McCray, R. A. 1972, ARA&A, 10, 375

Dame, T. M., Hartmann, D., & Thaddeus, P. 2001, ApJ, 547, 792

de Graauw, T., Helmich, F. P., Phillips, T. G., et al. 2010, A&A, 518, L6

De Looze, I., Baes, M., Bendo, G. J., Cortese, L., & Fritz, J. 2011, MNRAS, 416, 2712

De Looze, I., Cormier, D., Lebouteiller, V., Madden, S., et al. 2014, A&A, 568, A62

Dickey, J. M. & Lockman, F. J. 1990, ARA&A, 28, 215

Draine, B. T. 2011, Physics of the Interstellar and Intergalactic Medium

Dubey, A., Antypas, K., Calder, A., et al. 2013, SE-CSE 2013 – Proceedings, International Workshop on Software Engineering for Computational Science and Engineering, 1

Dubey, A., Daley, C., ZuHone, J., et al. 2012, ApJS, 201, 27

Dubey, A., Fisher, R., Graziani, C., et al. 2008, in Astronomical Society of the Pacific Conference Series, Vol. 385, Numerical Modeling of Space Plasma Flows, ed. N. V. Pogorelov, E. Audit, & G. P. Zank, 145

Dullemond, C. P. 2012

Dullemond, C. P. & Dominik, C. 2004, A&A, 417, 159

Dullemond, C. P., Juhasz, A., Pohl, A., et al. 2012, RADMC-3D: A multi-purpose radiative transfer tool, Astrophysics Source Code Library

Ekström, S., Georgy, C., Eggenberger, P., et al. 2012, A&A, 537, A146

Elias, J. H. 1978, ApJ, 224, 857

Ende, M. 1973, Momo oder Die seltsame Geschichte von den Zeit-Dieben und von dem Kind, das den Menschen die gestohlene Zeit zurückbrachte (Thienemanns Verlag, Stuttgart)

Ewen, H. I. & Purcell, E. M. 1951, Nature, 168, 356

Federrath, C., Roman-Duval, J., Klessen, R. S., Schmidt, W., & Mac Low, M.-M. 2010, A&A, 512, A81

Ferland, G. J., Porter, R. L., van Hoof, P. A. M., et al. 2013, , 49, 137

Field, G. B. 1959, ApJ, 129, 551

Fixsen, D. J., Cheng, E. S., Cottingham, D. A., et al. 1994, ApJ, 420, 457

Flower, D. R. 2001, Journal of Physics B: Atomic, Molecular and Optical Physics, 34, 2731

Flynn, C., Gould, A., & Bahcall, J. 1999, in Astronomical Society of the Pacific Conference Series, Vol. 165, The Third Stromlo Symposium: The Galactic Halo, ed. B. K. Gibson, R. S. Axelrod, & M. E. Putman, 387

Franeck, A., Walch, S., Glover, S. C. O., et al. 2015, in EAS Publications Series, Vol. 75, EAS Publications Series, 385–386

Franeck, A., Walch, S., Seifried, D., et al. 2018, MNRAS, 481, 4277

Fryxell, B., Olson, K., Ricker, P., et al. 2000, Astrophysical Journal, Supplement, 131, 273

Furlanetto, S. R. & Furlanetto, M. R. 2007, MNRAS, 374, 547

Furlanetto, S. R., Oh, S. P., & Briggs, F. H. 2006, Phys. Rep., 433, 181

Gatto, A., Walch, S., Naab, T., et al. 2017, MNRAS, 466, 1903

Genzel, R. & Stutzki, J. 1989, ARA&A, 27, 41

Genzel, R., Tacconi, L. J., Combes, F., et al. 2012, ApJ, 746, 69

Gingold, R. A. & Monaghan, J. J. 1977, MNRAS, 181, 375

Girichidis, P., Naab, T., Walch, S., et al. 2016a, ApJ, 816, L19

Girichidis, P., Walch, S., Naab, T., et al. 2016b, MNRAS, 456, 3432

Glover, S. C. O. & Clark, P. C. 2012, MNRAS, 421, 116

Glover, S. C. O. & Mac Low, M.-M. 2007a, ApJS, 169, 239

Glover, S. C. O. & Mac Low, M.-M. 2007b, ApJ, 659, 1317

Glover, S. C. O. & Smith, R. J. 2016, MNRAS, 462, 3011

Glück, C. B. 2017, PhD thesis, Universität zu Köln, Zülpicher Strasse 77

Gnat, O. & Ferland, G. J. 2012, ApJS, 199, 20

Goicoechea, J. R., Teyssier, D., Etxaluze, M., et al. 2015, ApJ, 812, 75

Goldsmith, P. F., Heyer, M., Narayanan, G., et al. 2008, ApJ, 680, 428

Goldsmith, P. F., Langer, W. D., Pineda, J. L., & Velusamy, T. 2012, ApJS, 203, 13

Goldsmith, P. F., Pineda, J. L., Neufeld, D. A., et al. 2018, ApJ, 856, 96

Gould, R. J. 1994, ApJ, 423, 522

Graf, U. U., Simon, R., Stutzki, J., et al. 2012, A&A, 542, L16

Grenier, I. A., Casandjian, J.-M., & Terrier, R. 2005, Science, 307, 1292

Habing, H. J. 1968, Bull. Astron. Inst. Netherlands, 19, 421

Hailey-Dunsheath, S., Nikola, T., Stacey, G. J., et al. 2010, ApJ, 714, L162

Haken, H. & Wolf, H. C. 2003, Atom- und Quantenphysik (Springer-Verlag, Berlin Heidelberg)

Hartigan, P. & Kenyon, S. J. 2003, ApJ, 583, 334

Herbst, E. & Cuppen, H. M. 2006, Proceedings of the National Academy of Science, 103, 12257

Herrera-Camus, R., Bolatto, A. D., Wolfire, M. G., et al. 2015, ApJ, 800, 1

Heyminck, S., Graf, U. U., Güsten, R., et al. 2012, A&A, 542, L1

Hill, A. S., Joung, M. R., Mac Low, M.-M., et al. 2012a, ApJ, 761, 189

Hill, A. S., Joung, M. R., Mac Low, M.-M., et al. 2012b, ApJ, 750, 104

Hollenbach, D., Kaufman, M. J., Bergin, E. A., & Melnick, G. J. 2009, ApJ, 690, 1497

Hollenbach, D. J. & Tielens, A. G. G. M. 1999, Reviews of Modern Physics, 71, 173

Hopkins, P. F. 2015, MNRAS, 450, 53

Hubber, D. A., Rosotti, G. P., & Booth, R. A. 2018, MNRAS, 473, 1603

Hughes, T. M., Foyle, K., Schirm, M. R. P., et al. 2015, A&A, 575, A17

Kapala, M. J., Sandstrom, K., Groves, B., et al. 2015, ApJ, 798, 24

Karachentsev, I. D., Karachentseva, V. E., Huchtmeier, W. K., & Makarov, D. I. 2004, AJ, 127, 2031

Kennicutt, Jr., R. C. 1998, ApJ, 498, 541

Kim, C.-G., Ostriker, E. C., & Kim, W.-T. 2014, ApJ, 786, 64

Klein, R., Poglitsch, A., Raab, W., et al. 2010, in Society of Photo-Optical Instrumentation Engineers (SPIE) Conference Series, Vol. 7735, Society of Photo-Optical Instrumentation Engineers (SPIE) Conference Series, 1

Klessen, R. S. & Glover, S. C. O. 2016, Star Formation in Galaxy Evolution: Connecting Numerical Models to Reality, Saas-Fee Advanced Course, Volume 43. ISBN 978-3-662-47889-9. Springer-Verlag Berlin Heidelberg, 2016, p. 85, 43, 85

Koepferl, C. M. & Robitaille, T. P. 2017, ApJ, 849, 3

Kolmogorov, A. 1941, Akademiia Nauk SSSR Doklady, 30, 301

Kong, S., Arce, H. G., Feddersen, J. R., et al. 2018, ApJS, 236, 25

Langer, W. D., Pineda, J. L., & Velusamy, T. 2014a, A&A, 564, A101

Langer, W. D., Velusamy, T., Pineda, J. L., et al. 2010, A&A, 521, L17

Langer, W. D., Velusamy, T., Pineda, J. L., Willacy, K., & Goldsmith, P. F. 2014b, A&A, 561, A122

Larson, R. B. 1981, MNRAS, 194, 809

Liszt, H. 2001, A&A, 371, 698

Lucy, L. B. 1977, AJ, 82, 1013

Madden, S. C., Geis, N., Genzel, R., et al. 1994, Infrared Physics and Technology, 35, 311

Makiuti, S., Shibai, H., Nakagawa, T., et al. 2002, A&A, 382, 600

May, J., Bronfman, L., Alvarez, H., Murphy, D. C., & Thaddeus, P. 1993, A&AS, 99, 105

McClure-Griffiths, N. M., Dickey, J. M., Gaensler, B. M., et al. 2005, ApJS, 158, 178

McKee, C. F. & Ostriker, J. P. 1977, ApJ, 218, 148

Mendoza, C. 1983, in IAU Symposium, Vol. 103, Planetary Nebulae, ed. D. R. Flower, 143–172

Micic, M., Glover, S. C. O., Federrath, C., & Klessen, R. S. 2012, MNRAS, 421, 2531

Mihalas, D. & Binney, J. 1981, Science, 214, 20

Möllenhoff, C., Appenzeller, I., Gässler, W., et al. 1999, A&A, 352, L5

Möller, T., Bernst, I., Panoglou, D., et al. 2013, A&A, 549, A21

Momany, Y., Zaggia, S., Gilmore, G., et al. 2006, A&A, 451, 515

Mookerjea, B., Israel, F., Kramer, C., et al. 2016, A&A, 586, A37

Mouhcine, M., Ibata, R., & Rejkuba, M. 2010, ApJ, 714, L12

Nakagawa, T. 1993, in Astronomical Society of the Pacific Conference Series, Vol. 41, Astronomical Infrared Spectroscopy: Future Observational Directions, ed. S. Kwok, 373

Nakagawa, T., Doi, Y., Yui, Y. Y., et al. 1995, ApJ, 455, L35

Nakagawa, T., Yui, Y. Y., Doi, Y., et al. 1998, ApJS, 115, 259

Nasonova, O. G., de Freitas Pacheco, J. A., & Karachentsev, I. D. 2011, A&A, 532, A104

Nelson, R. P. & Langer, W. D. 1997, ApJ, 482, 796

Nelson, R. P. & Langer, W. D. 1999, ApJ, 524, 923

O'Brien, J. C., Freeman, K. C., & van der Kruit, P. C. 2010, A&A, 515, A62

Okada, Y., Requena-Torres, M. A., Güsten, R., et al. 2015, A&A, 580, A54

Ossenkopf, V. 1997, New Astron., 2, 365

Ossenkopf, V., Röllig, M., Neufeld, D. A., et al. 2013, A&A, 550, A57

Palla, F. & Stahler, S. W. 2002, ApJ, 581, 1194

Peters, T., Naab, T., Walch, S., et al. 2017, MNRAS, 466, 3293

Pineda, J. L., Langer, W. D., & Goldsmith, P. F. 2014, A&A, 570, A121

Pineda, J. L., Langer, W. D., Velusamy, T., & Goldsmith, P. F. 2013, A&A, 554, A103

Pontoppidan, K. M., Meijerink, R., Dullemond, C. P., & Blake, G. A. 2009, ApJ, 704, 1482

Pritchard, J. R. & Furlanetto, S. R. 2006, MNRAS, 367, 1057

Rachford, B. L., Snow, T. P., Destree, J. D., et al. 2009, ApJS, 180, 125

Ragan, S., Henning, T., Krause, O., et al. 2012, A&A, 547, A49

Redman, M. P., Rawlings, J. M. C., Nutter, D. J., Ward-Thompson, D., & Williams, D. A. 2002, MNRAS, 337, L17

Reissl, S., Wolf, S., & Brauer, R. 2016, A&A, 593, A87

Rice, T. S., Goodman, A. A., Bergin, E. A., Beaumont, C., & Dame, T. M. 2016, ApJ, 822, 52

Risacher, C., Güsten, R., Stutzki, J., et al. 2015, IEEE, 39th International Conference on Infrared, Millimeter and Terahertz waves

Röllig, M., Abel, N. P., Bell, T., et al. 2007, A&A, 467, 187

Romano, D., Matteucci, F., Salucci, P., & Chiappini, C. 2000, ApJ, 539, 235

Rybicki, G. B. & Lightman, A. P. 1979, Radiative Processes in Astrophysics (Wiley-vch Verlag)

Salpeter, E. E. 1955, ApJ, 121, 161

Sandell, G., Mookerjea, B., Güsten, R., et al. 2015, A&A, 578, A41

Sanders, D. B., Solomon, P. M., & Scoville, N. Z. 1984, ApJ, 276, 182

Savva, D., Little, L. T., Phillips, R. R., & Gibb, A. G. 2003, MNRAS, 343, 259

Schmidt, M. 1959, ApJ, 129, 243

Schöier, F. L., van der Tak, F. F. S., van Dishoeck, E. F., & Black, J. H. 2005, A&A, 432, 369

Seifried, D., Sánchez-Monge, Á., Suri, S., & Walch, S. 2017, MNRAS, 467, 4467

Sembach, K. R., Howk, J. C., Ryans, R. S. I., & Keenan, F. P. 2000, ApJ, 528, 310

Shetty, R., Glover, S. C., Dullemond, C. P., & Klessen, R. S. 2011a, MNRAS, 412, 1686

Shetty, R., Glover, S. C., Dullemond, C. P., et al. 2011b, MNRAS, 415, 3253

Shibai, H., Okuda, H., Nakagawa, T., et al. 1991, ApJ, 374, 522

Shibai, H., Yui, M., Matsuhara, H., et al. 1994, ApJ, 428, 377

Smith, R. J., Glover, S. C. O., Clark, P. C., Klessen, R. S., & Springel, V. 2014, MNRAS, 441, 1628

Snow, T. P. & McCall, B. J. 2006, ARA&A, 44, 367

Sobolev, V. V. 1957, Soviet Ast., 1, 678

Spitzer, Jr., L. 1942, ApJ, 95, 329

Springel, V. 2010, ARA&A, 48, 391

Springel, V. 2011, in IAU Symposium, Vol. 270, Computational Star Formation, ed. J. Alves, B. G. Elmegreen, J. M. Girart, & V. Trimble, 203–206

Stacey, G. J., Viscuso, P. J., Fuller, C. E., & Kurtz, N. T. 1985, ApJ, 289, 803

Stahler, S. W. & Palla, F. 2005, The Formation of Stars, 865

Stark, A. A. & Lee, Y. 2005, ApJ, 619, L159

Sternberg, A. & Dalgarno, A. 1989, ApJ, 338, 197

Sternberg, A. & Dalgarno, A. 1995, ApJS, 99, 565

Stil, J. M., Taylor, A. R., Dickey, J. M., et al. 2006, AJ, 132, 1158

Sutherland, R. S. & Dopita, M. A. 1993, ApJS, 88, 253

Swinbank, A. M., Karim, A., Smail, I., et al. 2012, MNRAS, 427, 1066

Tammann, G. A., Loeffler, W., & Schroeder, A. 1994, ApJS, 92, 487

Tauber, J. A., Fridlund, C. V. M., & Pilbratt, G. 1996, in IAU Symposium, Vol. 170, CO: Twenty-Five Years of Millimeter-Wave Spectroscopy, 112

Taylor, A. R., Gibson, S. J., Peracaula, M., et al. 2003, AJ, 125, 3145

Tielens, A. G. G. M. 2005, The Physics and Chemistry of the Interstellar Medium

Tielens, A. G. G. M. & Hollenbach, D. 1985, ApJ, 291, 722

van de Hulst, H. C. 1945, Ned. Tijdschr. v. Natuurkunde

van der Kruit, P. C. & Searle, L. 1981a, A&A, 95, 105

van der Kruit, P. C. & Searle, L. 1981b, A&A, 95, 116

van der Tak, F. F. S., Black, J. H., Schöier, F. L., Jansen, D. J., & van Dishoeck, E. F. 2007, A&A, 468, 627

Velusamy, T. & Langer, W. D. 2014, A&A, 572, A45

Wakelam, V. & Herbst, E. 2008, ApJ, 680, 371

Walch, S., Girichidis, P., Naab, T., et al. 2015, MNRAS, 454, 238

Weigert, A., Wendker, H., & Wisotzki, L. 2016, Astronomie und Astrophysik (WILEY-VCH, Weinheim)

Wiese, W. L. & Fuhr, J. R. 2007, J. Phys. Chem. Ref. Data, 36, 1287

Wiesenfeld, L. & Goldsmith, P. F. 2014, ApJ, 780, 183

Wilson, N. J. & Bell, K. L. 2002, MNRAS, 337, 1027

Wilson, T. L. 1999, Reports on Progress in Physics, 62, 143

Wilson, T. L. & Rood, R. 1994, ARA&A, 32, 191

Wolfire, M. G., Hollenbach, D., & McKee, C. F. 2010, ApJ, 716, 1191

Wouthuysen, S. A. 1952, AJ, 57, 31

Wright, E. L., Mather, J. C., Bennett, C. L., et al. 1991, ApJ, 381, 200

Wünsch, R., Walch, S., Dinnbier, F., & Whitworth, A. 2018, MNRAS[[arXiv:1708.06142]1708.06142]

Yang, B., Stancil, P. C., Balakrishnan, N., & Forrey, R. C. 2010, ApJ, 718, 1062

Young, E. T., Becklin, E. E., Marcum, P. M., et al. 2012, ApJ, 749, L17

Zielinsky, M., Stutzki, J., & Störzer, H. 2000, A&A, 358, 723

Zygelman, B. 2005, ApJ, 622, 1356

Epilogue

"And now? Did you answer the questions? Do you know where the [C II] emission comes from?"
I characterized the gas more precise in temperature and density, and chemical composition. I found that [C II] traces atomic gas, that is about to become molecular. I found it to be correlated with atomic gas, not the molecular one. I saw how the model can influence the opinion. If the model was not spatially resolved, if it progressed further in time, my answer may have been different. I realised the importance to clarify the conditions under which the analysis was done. So, if you ask me where the [C II] line emission comes from, I would like to answer:
In the scenario of a forming molecular cloud, before the onset of star formation, and when the gas is contracting without being disturbed by feedback, our models tell us, that the [C II] line emission stems from the atomic gas phase. This atomic gas is just on the way to become molecular. Thus, the [C II] line emission traces this transforming gas. Within the picture of knowledge we have, this is the answer.

List of Abbreviations and constants

Table 1: List of constants.

Constant	Value	Unit	Description
	Physical constants		
c	2.9979×10^{10}	cm s^{-1}	speed of light
h	6.6262×10^{-27}	erg s	Planck constant
	6.6262×10^{-34}	J s	
k_B	1.3807×10^{-16}	erg K^{-1}	Boltzman constant
	1.3807×10^{-23}	J K^{-1}	
G	6.6726×10^{-11}	m^3 kg^{-1} s^{-2}	Gravitational constant
eV	6.242×10^{11}	erg	electron volt
au	1.6605×10^{-24}	g	atomic weight
	Astronomical constants		
pc	3.0856×10^{18}	cm	parsec
$M_\odot$	1.989×10^{33}	g	solar mass
$L_\odot$	3.828×10^{26}	W	solar luminosity

Table 2: List of physical quantities used in this work.

Quantity	Unit	Description
$A_{\rm ul}$	[s^{-1}]	Einstein coefficient of spontaneous emission
$B_{\rm lu}$, $B_{\rm ul}$	[s^{-1}]	Einstein coefficients for absorption, and stimulated emission, respectively
$C_{\rm lu}$, $C_{\rm ul}$	[s^{-1}]	Excitation rate coefficients for upwards, and downwards collision
$D_{\rm max}$	[K / (km s^{-1})]	Maximum of the absolute value of the derivative of a line profile
dv	[km s^{-1}]	spectral resolution of a simulation
dx	[pc]	spatial resolution of a simulation
$I_{\rm lp}$	[K], [erg/(s sr Hz cm^2)]	intensity in each velocity channel, building the line profile
$I_{\rm tot}$	[erg / (s sr cm^2)]	sum over the integrated intensity over all pixels in the map
I	[K km s^{-1}], [erg / (s sr cm^2)]	integrated intensity along the velocity, or the frequency
L	[W], [$L_\odot$]	luminosity
$L_{\rm tot}$	[W], [$L_\odot$]	total luminosity of a map
$L_{\rm max}$	[pc]	escape probability length scale
N	[cm^{-2}]	column density
n	[cm^{-3}]	volume density
s		standard deviation of a Gaussian kernel, for smoothing the line profiles
$\sigma_{\rm lp}$	[km s^{-1}]	width of a line profile (second moment)
$\sigma_{\rm Box}$, $\sigma_{\rm Gauss}$	[km s^{-1}]	width of the Boxcar and Gaussian reference functions
$T_{\rm ex}$	[K]	excitation temperature of a line
$T_{\rm kin}$	[K]	kinetic temperature of the gas
$T_{\rm spin}$	[K]	spin temperature, which is the excitation temperature for the H I line
$V_{\rm Box}$, $V_{\rm Gauss}$		Tauber values, calculated with a Boxcar and a Gaussian as reference functions
$\bar{\rm v}_{\rm lp}$	[km s^{-1}]	centroid of a line profile (first moment)
$\bar{\rm v}_{\rm Box}$, $\bar{\rm v}_{\rm Gauss}$	[km s^{-1}]	centroid of the Boxcar and the Gaussian reference functions
Var	[pc]	variance of the distribution of a vertical intensity profile, needed for calculating the scale height $\bar{z}$
$\bar{z}$	[pc]	scale height, quantifying the width of the vertical intensity profile around the galactic midplane

Table 3: List of abbreviations used in this work.

Abbreviation	Description
[^{12}C II]	opacity affected [C II] line emission denoting the fine structure emission line of the $^{12}C^+$ ion $^2P_{3/2} \rightarrow ^2 P_{1/2}$ at $\lambda = 157.74\ \mu$m
[^{13}C II]	optically thin [C II] line emission corresponding to the strongest hyperfine structure transition ($F = 2 - 1$) in the $^{13}C^+$ ion
CNM	cold neutral medium
CR	cosmic ray
GMC	giant molecular cloud
H I	hyperfine structure transition line of atomic hydrogen, denoting the H I 21 cm line
HIM	hot ionized medium
IMF	initial mass function
ISM	interstellar medium
ISRF	interstellar radiation field
LTE	local thermal equilibrium
LVG	large velocity gradient
MHD	magneto-hydrodynamic
PAH	Polycyclic aromatic hydrocarbons
PDR	photon-dominated region (or photo-dissociation region)
SN	supernova
SNR	supernova rate
WIM	warm ionized medium
WNM	warm neutral medium

“Er wandte sich an die Schildkröte zu seinen Füßen:
‘Kassiopeia, meine Teure! Was ist nach Deiner Ansicht
das Beste, das man während einer Belagerung tun kann?’
*‘*FRÜHSTÜCKEN*!’ erschien als Antwort auf deren Panzer.”*

Michael Ende

Erklärung zur Dissertation

Ich versichere, dass ich die von mir vorgelegte Dissertation selbständig angefertigt, die benutzten Quellen und Hilfsmittel vollständig angegeben und die Stellen der Arbeit — einschließlich Tabellen, Karten und Abbildungen — , die anderen Werken im Wortlaut oder dem Sinn nach entnommen sind, in jedem Einzelfall als Entlehnung kenntlich gemacht habe; dass diese Dissertation noch keiner anderen Fakultät oder Universität zur Prüfung vorgelegen hat; dass sie — abgesehen von unten angegebenen Teilpublikationen — noch nicht veröffentlicht worden ist sowie, dass ich eine solche Veröffentlichung vor Abschluss des Promotionsverfahrens nicht vornehmen werde. Die Bestimmungen der Promotionsordnung sind mir bekannt. Die von mir vorgelegte Dissertation ist von Professor Dr. Stefanie Walch-Gassner betreut worden.

Teilpublikationen:

- "[C II] synthetic emission maps of simulated galactic discs"
  A. Franeck, S. Walch, S.C.O. Glover, D. Seifried, P. Girichidis, T. Naab, R.S. Klessen, T. Peters, R. Wünsch, A. Gatto, P.C. Clark
  EAS Publications Series 2015, p. 385 – 386

- "Synthetic [C II] emission maps of a simulated molecular cloud in formation"
  A. Franeck, S. Walch, D. Seifried, S. Clarke, V. Ossenkopf-Okada, S.C.O. Glover, R.S. Klessen, P. Girichidis, T. Naab, R. Wünsch, P.C. Clark, E. Pellegrini, T. Peters
  submitted to MNRAS in May 2018, accepted September 2018, printed December 2018
  MNRAS, 481, 4277

Köln, Annika Franeck